Lubricated friction at the nano and mesoscale

CLODOMIRO CAFOLLA

Durham University

Lubricated friction at the nano and mesoscale

Author:
Clodomiro Francesco Cafolla

Primary Supervisor:
Dr. Kislon Voïtchovsky

A thesis presented for the degree of
Doctor of Philosophy

Centre for Materials Physics
Department of Physics and Astronomy

Stockton Road
Durham
DH1 3LE

August 28, 2020

Abstract

Friction is central to numerous natural processes and technological applications, from the motion of synovial joints to car engines and wind turbines. Despite its ubiquitous relevance, a comprehensive picture is still lacking and current models are largely semi-empirical. Experiments conducted at the atomic scale have shed light on the fundamental origins of friction, but linking findings on the single atom or molecule level to macroscale observations involving countless tribological contacts remains a considerable challenge. To bridge this gap, results are needed at the mesoscale, typically between 1 nm and 1 μm, where atomistic information is still tractable but macroscopic behaviour begins to emerge. The problem becomes even more complex when considering the presence of a fluid lubricant confined in a nanogap between the two sliding surfaces.

This thesis aims at bridging the current gap between atomistic models for lubricated friction and larger scale observations. This is done mainly using atomic force microscopy (AFM) which allows investigations of both the molecular level details and the mesoscale picture within the same experiment. Wherever possible, AFM measurements have been complemented by other experimental and computational techniques. Using a variety of model systems, the thesis studies the organisation and dynamics of lubricants under nanoconfinement at the solid/liquid interface. The investigations lead to some novel insights. First, polar and non-polar lubricants are shown to experience a structural transition under nanoconfinement, with the solid-like characteristics of the boundary layer being responsible for an increase in lubricated friction. Second, the lubricant molecular ordering can be modulated by surface singularities that limit the configurational entropy of the fluid molecules. This suggests surface defects indirectly influence the lubricant properties by inducing local molecular rearrangement. External factors, such as humidity and temperature, are also investigated. Some common threads in the different model systems suggest that atomistic models can be adapted at the mesoscale to describe lubricated friction based on a thermally activated process.

Acknowledgements

I thank Dr Kislon Voitchovsky for his invaluable guidance and suggestions throughout my PhD.
I am grateful to Dr Qing Helen He for the opportunity to conduct breakthrough research in her group.
This thesis is dedicated to my parents, Arturo and Rosa Maria, my grandparents, Miro, Francesco, Angela and Rosa and my grandaunt Sara. I will be always grateful for their love and support throughout my life. Dedico questo lavoro ai miei genitori, Arturo e Rosa Maria, ai miei nonni Miro, Francesco, Angela e Rosa e a zia Sara cui sono infinitamente debitore per il costante e incondizionato supporto.

Declaration

The work presented in this thesis has been developed under the supervision of Dr. Kislon Voitchovsky of the Department of Physics and Astronomy at Durham University. All text and figures are the work of the author, unless otherwise stated. The specific contributions of other researchers to the work presented is detailed in the next section. No part of this thesis has been presented for any other degree or qualification.

Contributions

Dr Amir Payam has developed the mathematical model presented in Chapter 3. The molecular dynamics simulations have been carried out either by Dr William Foster or with his help and guidance (Chapters 2 and 5).

Publications related to this thesis

- **Cafolla C**, Voitchovsky K. Impact of water on the lubricating properties of hexadecane at the nanoscale **Nanoscale 2020.** DOI: 10.1039/D0NR03642K.
  This article forms the basis of Chapter 6.

- **Cafolla C**, Foster W, Voitchovsky K. Lubricated friction around nanodefects. **Science Advances 2020**, 6: eaaz3673.
  This article forms the basis of Chapter 5.

- **Cafolla C**, Payam A, Voitchovsky K. A non-destructive method to calibrate the torsional spring constant of atomic force microscope cantilevers in viscous environments. **Journal of Applied Physics 2018**, 124: 154502. **Editor's Pick & Highlighted in SciLight**
  This article forms the basis of Chapter 3

- **Cafolla C**, Voitchovsky K. Lubricating properties of single metal ions at interfaces. **Nanoscale 2018**, 10: 11831. **2018 Nanoscale Hot Article Collection**
  This article forms the basis of Chapter 4

- Ricci M, Trewby W, **Cafolla C**, Voitchovsky K. Direct observation of the dynamics of single metal ions at the interface with solids in aqueous solutions. **Nature Scientific Reports 2017**, 7: 43234

- Miller EJ, Trewby W, Payam AF, Piantanida L, **Cafolla C**, Voitchovsky K. Sub-nanometer resolution imaging with amplitude-modulation atomic force microscopy in liquid. **Journal of Visualized Experiments 2016**, 118: e54924
  My contributions to this article (cleaning procedure and contamination) have been included in Chapter 2

This thesis focuses on presenting my investigations on lubricated friction. During my PhD, I have been involved in a number of studies on strongly correlated electron systems, astrophysics and bio-medical topics. These studies and other professional experience are detailed at the end of the Thesis within Chapter 8.

Contents

1.0 Introduction

Lubrication involves some interesting points...Let the bearings run dry!
Richard Feynmann, There is plenty room at the bottom, 1960

1.1 Overview

Since childhood, we have all acquired an intuitive understanding of the importance of friction [1, 2]. This is because friction emerges any time the surfaces of two objects enter in contact with each other, from walking in a room to writing on a piece of paper. Slipping on an icy sidewalk may have been an invaluable teaching on slippage [3]. Mastering friction is fundamental to successfully play a number of sports from spin balling [4] to goalkeeping a fast strike [5]. These examples taken from everyday life highlight the ubiquitous nature of friction which dominates over systems at first sight completely distant and unrelated to each other [1, 6]. Friction indeed plays a fundamental role in almost any interfacial phenomena across multiple scales, ranging from energy [7] and environmental science [8–10] to metallurgy [11, 12] and material sciences [13, 14], medicine [15, 16], design of touch display devices [5] and automated systems [17].

In spite of its wide relevance in nature, friction is still poorly understood. This is due to the complexity of the phenomenon which cannot be simplified using simple, mathematically solvable models [18]. Friction phenomena can be described by some empirical models, with enough accuracy when considering macroscale systems, corresponding to length scales above a few μm where optical techniques can already provide insightful information on surface phenomena [5]. Over the last two decades a number of investigations have elucidated the origins of friction at the atomic level (< 0.1 nm), where investigations focus on the motion of single atoms or molecules [5, 19–24]. However, the connections between the molecular description and the macroscale observations are still lacking, leaving significant scope for development [1, 3, 6, 25, 26].

Our understanding is further limited when considering lubricated friction. If the idea of using lubricating liquids and greases so as to reduce friction and wear has been applied

since antiquity, only about 150 years ago the pioneering works of Reynolds and Tower started setting the bases for a quantitative description of lubrication [5, 27, 28]. We have recently achieved a better picture of lubrication mechanisms at the atomic level [29–33], but bridging atomistic observations with the well known empirical laws governing friction at the macroscale remains a considerable challenge [34, 35].

The thesis will hence focus on the "mesoscale", this grey area in between scales where well-defined models return solid enough predictions. In this thesis, mesoscale typically corresponds to a length scale between 1 nm and 1 μm (see Fig. 1.1), where lubricated friction emerges as a consequence of group effects due to the specific interactions of the lubricant molecules with each other and with the sliding solid surfaces.

In this chapter, I will explore the key concepts in friction and our current understanding, as well as introducing the most challenging, still fascinating, questions I will contribute to answering within the next chapters.

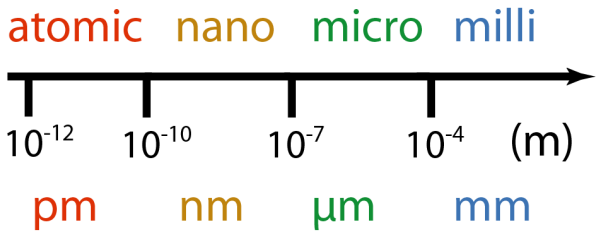

Fig. 1.1: Pictorial representation of the length scales most relevant for friction phenomena. One of the current challenges in friction studies is to bridge the gap between fundamental mechanisms at the atomic scale and macroscopic observations (larger than a few μm). The focus of the thesis is on this intermediate length scale, that is, the mesoscale (for the purposes of this research, typically between 1 nm and 1 μm).

1.2 Why friction studies?

Friction studies have a crucial importance not only in unravelling the fundamental mechanisms behind a wide variety of natural phenomena, but above all in allowing technological advances in mechanical and electronic systems. The extent of systems dominated by friction forces ranges from the flow of red blood cells in vessels [36] and the functioning of articular cartilage [37] to slider-disk interfaces in hard disk drives [38] and the motion of car engine components [39, 40]. In these examples as well as in the vast majority of cases, friction is undesired as it leads to significant energy waste and surface wear. A progress in friction studies would lead to a marked improvement in energy efficiency and enabling component operations within extreme conditions [41]. For example, in the automotive industry, friction forces account for more than 25% of fuel energy consumption [9, 39, 42, 43]. A reduction in friction forces by a few percentages has been estimated

to result in annual electricity savings of 36,000 GWh and CO_2 emission reduction of 10.6 million tonnes per year [9, 10, 39].

A better understanding of friction has also the potential of enabling breakthrough technologies at the nano and mesoscale. At such a small scale, devices become more sensitive to the friction forces and solutions which may work on macroscale systems are often inadequate [5]. In macroscale machines, friction can be reduced using a lubricant film with a typical thickness between hundreds of microns and a few millimeters. For miniaturised technologies, the gap between contacting parts is markedly smaller leading to the fluid behaviour being significantly affected by the confinement [44, 45]. In nanogaps, the capillary and adhesion forces tend to dominate over gravity and inertial forces [46]. Microelectromechanical systems and slider-disk interfaces in disk drives provide striking examples. In the latter, an improvement in controlling friction has contributed to the development of the technology. These innovations include more efficient lubricant formulations so as to preserve at least a monolayer of lubricant on the disk surface throughout the lifetime of the device [47].

From these examples, it is clear that friction studies have stunning potential for driving the next generation technologies and contributing to positively reshaping our world by reducing anthropogenic greenhouse emission.

1.3 Fundamental concepts

Friction studies focus on three main phenomena: friction, wear and lubrication. Friction is defined as the force opposing the relative motion of two objects (i.e. solid surfaces, fluid layers, and single atoms) sliding against each other [1, 3, 6, 25]. The progressive material loss due to the body contact and motion against, or within, another medium is called wear. The control and reduction of friction and wear are defined as lubrication [25, 26]. The research field of friction, wear and lubrication is defined as tribology [26]. This term is derived from combining the ancient greek verb τρίβω (to rub) with the noun λόγος (discourse) and was used for the first time in 1966, becoming so popular as to be accepted as the scientific name for the field [1, 26].

Wear has a crucial importance in friction studies, and interestingly it may be both beneficial and detrimental depending on the particular scenario. Wear may be a desired phenomenon as it helps manufacture and polish components with a roughness of a few Angstroms. On the other hand, there are cases when wear should be reduced to a minimum. For example, a train derailed in Hatfield (UK) and killed four people, as a consequence of rail cracking due to surface wear over the years [48]. In this Chapter, we will however focus on friction and lubrication as these have been the major topics of investigation within the thesis.

Friction is usually divided into two main categories: dry and lubricated, according to the

absence or the presence of any lubricating film between the two sliding objects. Dry friction is further divided into static and kinetic friction, the former describing the interactions between non-moving surfaces, and the latter between the moving surfaces [3].

1.3.1 Dry friction

At the macroscopic level, dry friction is described by Amontons-Coulomb's laws which provide a description precise enough for an empirical understaning of the phenomenon [1, 2, 49]. The first two laws of the model were formulated in 1699 by Guillaume Amontons (1663-1705); eight years later, Charles-Augustin de Coulomb (1736-1806) provided the third law [49–51]. The Italian polymath Leonardo da Vinci (1452-1519) had already formulated the first two laws two centuries before, but their authorship is given to Amontons who was the first to publish them [50]. According to the first law of this model, the relationship between the normal force exerted, F_N, by each of the two sliding surface on the other, and the resulting lateral friction force, F_L, is described by a linear equation of the form:

$$\mu = \frac{F_L}{F_N} \tag{1.1}$$

where the coefficient of proportionality, μ, is defined as the coefficient of friction, and is an empirical property of the contacting materials [2, 19, 51, 52]. Friction force, and consequently the friction coefficient are divided into two categories: static and dynamic (or kinetic). Static friction force describes the mechanical resistance a body must overcome in order to start moving. Dynamic friction force accounts for the resistance a body experiences when moving [3, 26]. The static friction coefficient, μ_s, is typically greater than the kinetic one, μ_k [5, 52]:

$$\mu_k \leq \mu_s \tag{1.2}$$

According to the second law of the Amontons-Coulomb's model, the static force of friction is independent of the apparent contact area [2, 51]. The first two laws are graphically represented in Fig. 1.2.

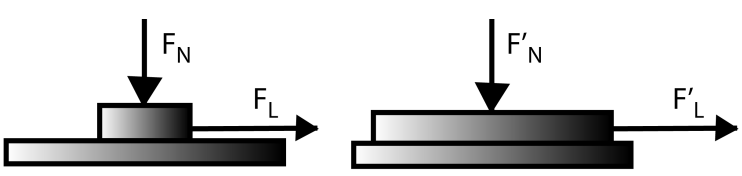

Fig. 1.2: Pictorial representation of the Amontons-Coulomb's model of friction. The friction force, F_L, is proportional to the applied normal force, F_N, but is independent of the apparent contact area. Given that F_N and F'_N are equal and acting on systems of two bodies made of the same materials, the resulting forces, F_L and F'_L, are also equal.

The third law states that the kinetic force of friction is independent of the sliding velocity

[26, 51]. Strictly speaking, this is not a law as it is never true. The independence of the kinetic friction force from the sliding velocity should be seen as a weak dependence of the former on the latter [5]. Amontons explained the laws in terms of microscopic contacts and roughness of the sliding surfaces. In the case of rigid contacts, friction would be due to the force to lift the surfaces up the rough asperities (Fig. 1.3a); whereas in the case of deformable asperities, the friction would arise from the work to bend them (Fig. 1.3b) [51, 53]. The French scientist Philippe de La Hire (1640-1718) added that breaking off some of the contacts would also account for the measured friction force (Fig. 1.3c) [53, 54]. This framework would explain the observed dependence of the friction on the load and its independence from the apparent contact area [2, 51]. Currently, the independence of the friction force from the apparent contact area is interpreted as a result of bodies being generally characterised by such a high degree of roughness that the actual points of contact are single nanoscopic or microscopic asperities [5]. When considering these asperities, it can be seen that the friction force becomes proportional to the actual contact area [55]. The measurement of the real contact area is not a trivial task, but can be indirectly calculated using the resistance between two conductors, and their specific resistivity [26].

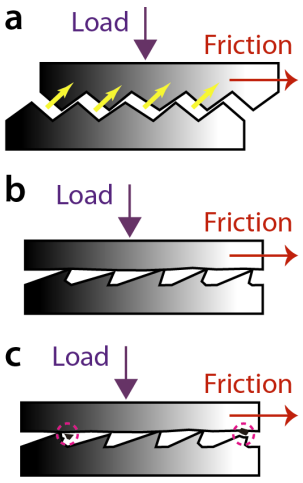

Fig. 1.3: Early explanation of the observed macroscale friction. (**a**) The friction force is due to an energy cost associated with pulling the sliding objects up the surface irregularities. (**b**) In case of plastic surfaces, the energy cost is associated to deforming them. (**c**) A contribution to the friction forces was thought to be due to breaking off the asperities as highlighted by the dashed purple circles.

The simplistic explanation provided by Amontons has significantly evolved over the centuries. It is currently accepted that friction is a complex phenomenon originating from several contributions ranging from adhesion [2, 56] and capillary forces [56] up to contact elasticity [24], surface chemistry [57] and topography [58].

The two main mechanisms are considered to be the adhesion and the three body deformation (ploughing) components [2, 25, 26, 56, 58–61]. Adhesion forces were described

as a main contribution to friction for the first time in the 1930-40s by Bowden and Tabor [62]. The surfaces of two solids in contact with each other undergo a series of plastic and elastic deformations, as described above (see also Fig. 1.3). Interatomic bonds form between the two surfaces due to attractive forces of electrostatic origin [5]. The bonds are usually classified by increasing order of strength: weak van der Waals interactions between transient dipoles in neutrally charged molecules [63]; hydrophobic interactions so as to limit the contact between a hydrogen-bonding body and non-hydrogen-bonding molecules; hydrogen bonds between electropositive hydrogen and electronegative oxygen; ionic bonds between particles with opposite charges; and covalent bonds between atoms with a negligible difference in electronegativity leading to almost equally sharing the valence electrons [64]. Independently from the strength of the bonds, applying a tangential force, F_t, so as to slide one object over the other results in a shear stress, S, over the contact junction cross-sectional area A [64]:

$$S = \frac{F_t}{A} \tag{1.3}$$

If S exceeds the sum of all the interatomic bonds between the two surfaces in contact, the two bodies will start moving with respect to each other. This critical shear stress to initiate and sustain sliding is defined as the shear strength, s. The force needed to generate s is the adhesion friction force, F_{adh}:

$$F_{adh} = \overline{s} A_r \tag{1.4}$$

where A_r is the total real area of contact, and $\overline{s}$ is the average shear stress for the surface junctions. A_r is the sum of the areas of all the single contact junctions ($A_r = \sum_1^i A_i$). The real contact area can be approximated as a linear function of the applied load F_N [33], and, in the case of elastic deformations of surfaces with a Gaussian distribution of the asperity heights, takes the form of:

$$A_r \approx 3 \left(\frac{R}{\sigma_h} \right)^{\frac{1}{2}} \frac{F_N}{E} \tag{1.5}$$

where R is the mean radius of curvature of the surface irregularities, σ_h is the standard deviation of the asperity heights distribution, and E is the composite elastic modulus of the two contacting materials [65, 66]. Recent works have shown that this model, formulated in 1966 by Greenwood and Williamson, holds true once the correct mean radius is used and provided that the real contact area is a small fraction of the apparent one, that is, below 0.01% [5, 65–69]. For markedly compliant materials like rubber, more complex theories have been developed [68, 69] but their detailed discussion is beyond the aims of this work. For plastic deformations, A_r is

$$A_r \approx \frac{F_N}{H} \tag{1.6}$$

where H is the hardness of the softer material [70, 71]. H defines the ability of a material to resist an applied load before undergoing a surface plastic deformation under the action of an indenter [72]. For metals, the surface plastic deformation tends to take place when the mean applied pressure is three times greater than the yield stress, Y:

$$H \simeq 3Y \tag{1.7}$$

where Y corresponds to the tensile or compressive force per unit area to start a plastic deformation [73]. This approximation holds true when the surface plastic deformation takes place as a homogeneous flow under the action of an indenter of almost any shape (conical, cylindrical or spherical) [5]. Within the elastic range, the equivalent of hardness is the stiffness or elastic modulus, that is, the ability of a material to temporarily change its shape [3, 74].

For both the elastic and the plastic deformations, the friction force due to adhesion interactions is linearly dependent on the load (Eqs 1.4-1.6). If the shear strength is independent from the contact pressure, then F_{adh} is independent from the apparent contact area [5]. Thus, the model confirms Amontons' observations on the role of the applied load, but it is also able to capture the contribution of the surface roughness (Fig. 1.4a).

Alongside the adhesion contribution, the other main component to friction is the ploughing force, F_{plow}. This force is due to a deformation of the softer surface by the harder one [59]. F_{plow} can be seen as a dynamic case of the adhesion friction force for plastic interfaces where the deformation of one of the two materials in contact is irreversible [75]. In other words, F_{plow} arises when moving a hard asperity through a markedly more compliant substrate (Fig. 1.4b):

$$F_{plow} = Hx^2 tan\,(\phi) \tag{1.8}$$

where $x^2\ tan(\phi)$ is the cross-sectional area of the groove as shown in Fig. 1.4b. Here, F_N is supported by the hardness of the material over a cone area of $\pi a^2/2$ [5, 76]:

$$F_N = \frac{1}{2} H \pi x^2 tan^2\,(\phi) \tag{1.9}$$

The adhesion and ploughing contributions are not completely independent from each other. It is however convenient to express the friction force as the sum of these two components [76]:

$$F_L = F_{adh} + F_{plow} \tag{1.10}$$

Combining Eqs 1.1, 1.4, 1.6, 1.8-1.10, the total friction coefficient is [5]

$$\mu = \frac{F_L}{F_N} \approx \frac{s}{H} + \frac{2}{\pi} cot\,(\phi) \tag{1.11}$$

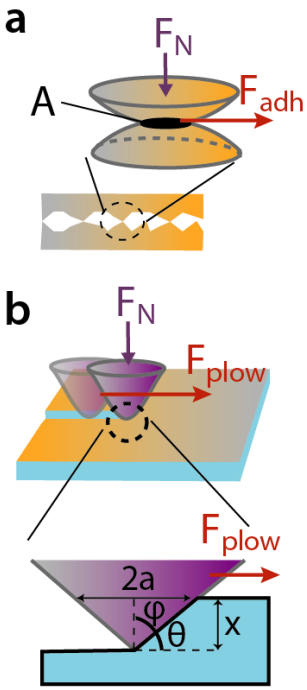

Fig. 1.4: Adhesion and ploughing contribution to the friction force. (**a**) Two solids sliding over each other undergo elastic and plastic deformations resulting in adhesion friction force, F_{adh}. The zoomed in view shows the real contact area, A, which is proportional to the applied load, F_N. (**b**) A difference in the compliance between the two sliding surfaces results in the asperities of the harder deforming the softer one. The expanded view shows the geometry of the asperity, here modelled as a cone ploughing through a cross-sectional groove area ax, which can be also expressed as $x^2 tan(\phi)$.

Experimental values for μ in metals are however found markedly greater in comparison with the predictions from Eq. 1.11 [52]. This is due to the fact that the model works under the assumption of the material hardness and contact area being constant with respect to an applied shear. In most plastic materials, hardness changes with increasing deformation. This phenomenon is defined as work hardening. The process is due to the applied shear creating dislocations, that are, line defects within the crystal lattice of the material. Dislocations accumulate or interact with other surface impurities such as grain boundaries. This results in pinning points which prevent a smooth sliding of the surfaces. A higher shear stress hence needs to be applied so as to allow a plastic flow. Thus, the material shows an increased yield stress and hardness [72, 77]. The model of Eq. 1.11 furthermore ignores the dynamic evolution of the contact area under combined normal and tangetial loading [78]. This phenomenon takes place when, in plastic materials, the acting forces deform the materials increasing the real contact area under shear [78]. In Eq. 1.6, the real contact area was assumed to depend only on F_N. In reality, tangential forces have also an impact on asperities, flattening them and thus contributing to plastically deforming the contact area [78]. The contact area however does not increase indefinitely, but it is

limited by the plasticity of the material and by any interfacial film, such a lubricant layer, reducing the shear stress [5].

Static friction and the stick-slip phenomenon

The model becomes even more complex when considering static friction force, that is, the force required to start sliding an object [79]. Due to surface imperfections, static friction tends to be greater than kinetic: the force needed to slide one object over another depends on the commensurability between the surfaces of the two bodies, with pinning effects accounting for the strong resistance to motion [3]. In other words, when brought in contact, the atoms of the two surfaces tend over time to minimize their interfacial energy by moving towards more energetically favourable locations within the junction edge [80]. Furthermore, capillary force may attract molecules from the surrounding environment towards the points of contact, thus further increasing the effective contact area [81]. This is the case for water molecules adsorbed to the surface asperities at high humidity conditions [82]. Thus, considering the synergistic effect of adhesive forces and normal load, the static friction force, F_s, is given by:

$$F_s(t) = \mu \left[F_{adh}(t) + F_N \right] \tag{1.12}$$

where μ is the static friction coefficient and t is the contact time [5]. As shown in Fig. 1.5a, the evolution of static friction with respect to contact time rapidly becomes asymptotic. This explains why static friction force for a combination of two materials is assumed to be a constant value [80].

The same mechanisms behind the dependence of $F_s(t)$ on contact time account for the kinetic friction force decreasing with increasing sliding velocity, v. For low sliding velocities, the contact junctions are allowed more time to grow and oppose to motion. As it can be expected, kinetic friction shows an asymptotic behaviour with respect to v [3, 5, 83] (see Fig. 1.5b). The model breaks down when considering lubricated friction where viscous forces account for energy dissipation [5].

The static friction force being greater than the kinetic one and the dependence of the latter on the sliding velocity are the fundamental mechanisms behind the so-called stick-slip phenomenon [84]. As shown in Fig. 1.5c-d, the motion of the two surfaces alternates between them sticking to and smooth sliding over each other [3, 85]. Stick-slip is often an undesired phenomenon coming from the system not sliding at constant velocity, and resulting for example in the unpleasant sound of a braking train [86, 87].

The phenomenon can be modelled in terms of a body of mass m sitting on a belt and connected to a spring of stiffness k and a damper with dampening constant η (see Fig. 1.5c). The belt moves with velocity v. An applied load F_N resulting from the body weight mg

and any adhesive forces, pushes the body against the belt; the resulting friction force F_L opposes to the motion between the object and the belt [88]. The body will move at the same velocity of the block ($\dot{x} = v$) for small displacements x of the object from its equilibrium position such that $F_L < \mu_s F_N$, where μ_s is the static friction force coefficient [88].

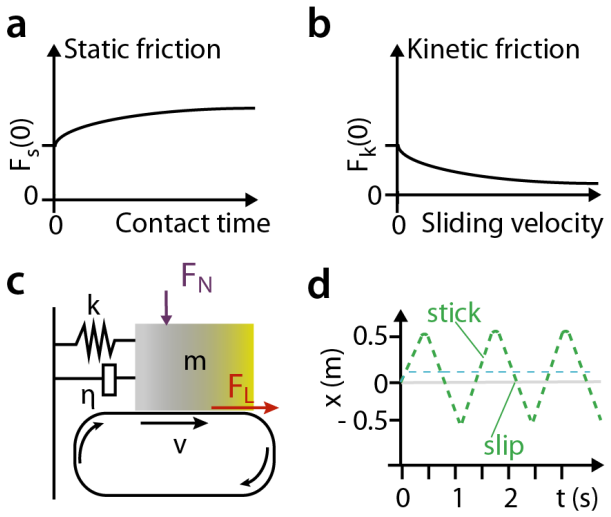

Fig. 1.5: The evolution of static and kinetic friction force with respect to contact time and sliding velocity is behind the stick-slip phenomenon. (**a**) Static friction, F_s, increases as a function of contact time rapidly reaching an asymptotic value. (**b**) The sliding velocity reduces the kinetic friction, F_k, towards an asymptotic value. Given the small range of rest times and velocities near zero to achieve the asymptotes, F_s and F_k for a combination of materials are usually taken to be constant values. (**c**) The static friction being larger than the kinetic friction and the latter being influenced by sliding velocity are behind the stick-slip phenomenon. Stick-slip can be modelled as an oscillatory motion of a body of finite mass m on a belt moving with velocity v. The motion is restrained by a spring of stiffness k and a damping element η. (**d**) Representative position and time values for a system of $m = 1$ kg, $k = 100$ N/m, $\mu_s = 0.5$, $\alpha = 0.2$ s/m, $v = 1$ m/s and $\eta = 20$ kg/s. As the applied load F_N increases, stick-slip instabilities dominate the motion of the object. F_N is 50 and 150 N for the blue and green dashed lines, respectively.

The tangential force will be then equal to

$$F_L = |\eta v + kx| \tag{1.13}$$

As the displacement increases, the spring will elongate exerting a greater restoring force, kx, on the body eventually becoming larger than the static friction force. At this stage, the body will slide with a relative velocity:

$$v_{rel} = v - \dot{x} \tag{1.14}$$

The body motion can be described by an equation of the form:

$$m\ddot{x} + \eta\dot{x} + kx = F_L \tag{1.15}$$

where F_L is the kinetic friction force and for a small velocity range can be approximated as

$$F_L = (\pm\mu - \alpha v_{rel})\, F_N \tag{1.16}$$

where α is a coefficient of proportionality between the kinetic friction force and the relative velocity and the $\pm$ sign depends on whether v_{rel} is greater or smaller than 0, respectively [5, 88]. Rearranging Eqs 1.15 and 1.16 gives

$$m\ddot{x} + (\eta - \alpha)\,\dot{x} + kx = (\pm\mu - \alpha v)\, F_L \tag{1.17}$$

Here, $(\eta - \alpha)$ represents an effective dampening coefficient for the system. Stick-slip behaviour takes place when this term is negative, that is, when the energy dissipated due to the dampening is smaller than the energy provided by the friction force. No oscillatory behaviour is observed when the dampening allows a smooth sliding without any instabilities.

Stick-slip motion is influenced by the contact time between the two sliding surfaces [89]. This time dependent stick-slip is particularly relevant in geology. The phenomenon takes the name of aging and is characterised by the fact that the increase in static friction during the stick phase is markedly greater than the increase in the kinetic friction during the slip stage [90].

Stick-slip motion can be also displacement controlled. In this case, the phenomenon depends on the friction force changing with the position of one sliding surfaces with respect to the other. For a macroscale system as in Fig. 1.5c, the body on the belt may encounter singularities. A non-uniform interface results in a position dependent evolution of the balance between the friction force and the restoring force due to the spring element [5, 91]. At the atomic level, displacement controlled stick-slip is described by the Prandtl-Tomlinson model, as discussed in the next section.

1.3.2 Lubricated friction

Dry friction between metals and ceramics is usually characterised by friction coefficients μ of at least 0.5, resulting in a significant wear of the sliding surfaces and marked loss of energy. Excluding a few scenarios where such a high friction coefficient is required (i.e. automotive brakes), a wide variety of liquids and greases have been used since antiquity as *lubricants* so as to reduce friction between sliding elements [49]. Lubricants are layers of either solid, liquid or vapour form, which introduced between two rolling objects allow

a smoother rolling [5]. Depending on their mechanism of action, lubricants are classified within six main lubrication categories [5]:

- Hydrostatic lubrication. The lubricant separating the two bodies is subject to an external pressure thus allowing enough lifting force for the asperities of the two surfaces not to touch each other [92].
- Hydrodynamic lubrication. Here, the lifting force is provided by viscous drag of the lubricant fluid within a confined gap [5, 92].
- Elastohydrodynamic lubrication (EHL). This regime is characterised by an increase of lubricant viscosity with pressure and elastic deformation of the confining surfaces. The former mechanism may be however negligible for elastically compliant solids, whereas the second mechanism may be minimum at high loads and high speeds [93].
- Mixed lubrication. The phenomenon arises from an interaction of solid-solid contact and hydrodynamic (or EHL) action. This is due to the lubricant thickness being comparable to the surfaces roughness, thus resulting in some asperities sliding against each other as in the case of dry friction [5, 94].
- Boundary lubrication. The asperities of the surfaces are in contact with each other but fully covered with a strongly adhered layer of lubricant [5]
- Solid lubrication. The sliding bodies are separated by a solid lubricant with a low shear strength, for example graphite and molybdenum disulfide [95]

In the vast majority of technological applications, liquid lubricants are used without any external source of pressure. The lubricating mechanisms within these systems can be summarised in the so called Stribeck curve as shown in Fig. 1.6 [5, 96]. Here, the friction coefficient of a lubricated system changes according to the sliding parameters, that are, the lubricant dynamic viscosity, η, the sliding speed, v_s, and the applied load, F_N [96]. The lubricating parameter, λ_s, is an useful measurement to classify the different lubricating regimes:

$$\lambda_s = \frac{\eta\, v_s}{F_N} \tag{1.18}$$

For high values of λ_s, the lubricant film has enough lifting force to separate the sliding forces. This is the case of regimes characterised by a viscous lubricant subject to low confining pressure and high sliding speed [5, 96]. For any lubricants, there usually exist an ideal combination of lubricating parameters such that the lubricant reaches an optimal thickness to sustain the sliding. As the film thickness decreases due to an increase of confining pressure or decrease in sliding speed, we enter a regime of mixed lubrication. In this case, alongside regions of hydrodynamic lubrication, some solid-solid contacts occur

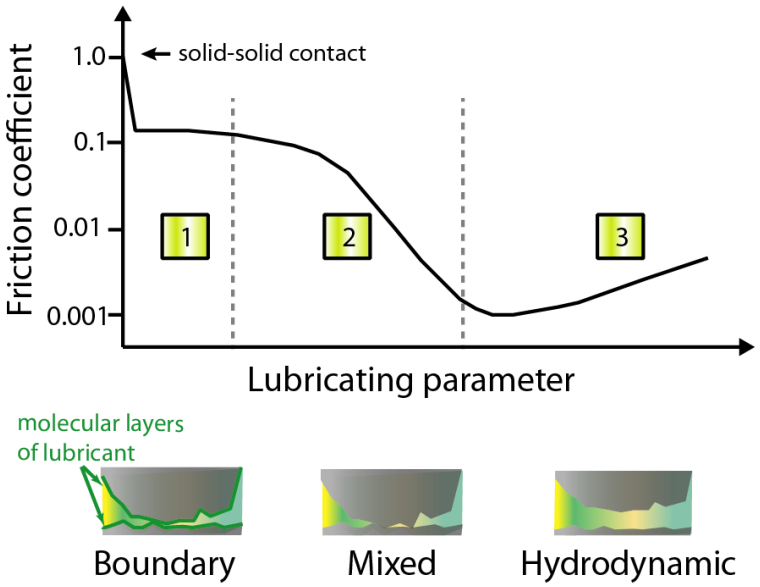

Fig. 1.6: The friction coefficient depends on the lubricating parameter, that is, the ratio between lubricant thickness and roughness height. The lubricating parameter can be also expressed as the product of lubricant dynamic viscosity and sliding speed divided by the applied load. Based on the evolution of the curve, three main regimes can be identified: 1. boundary; 2. mixed; 3. hydrodynamic.

resulting in a higher friction coefficient. A further decrease in λ_s leads to reducing the lubricant film thickness such that asperities are separated only by molecular layers of lubricant. Typically commercial lubricants are formulated with additives so that they can still effectively reduce friction even in this regime of boundary lubrication [5].

Viscosity

As highlighted by Eq. 1.18, alongside the sliding parameters, the principal characteristic behind a lubricant efficiency is its viscosity [91]. For a fluid confined between two surfaces and subject to a shear stress, τ_f, the viscosity is

$$\eta = \frac{\tau_f}{v(d)/d} \tag{1.19}$$

where d the distance between the two confining surfaces and $v(d)$ is the sliding velocity of the top place as a function of d (see Fig. 1.7a). The denominator of Eq. 1.19 is the strain rate, $d\gamma/dt$, or flow the fluid undergoes when subject to a shear stress [64]. In fluid dynamics, viscosity is indeed the equivalent of the shear modulus, G, for a linear elastic solid subject to a shear stress, τ_s:

$$G = \frac{\tau_s}{\gamma} = \frac{\tau_s \, d}{x} \tag{1.20}$$

where γ is the strain, x the distance the top surface moves sideways and d the separation between the top and the bottom surface. In other words, a solid displays the characteristic of rigidity, that is, an ability to oppose an applied shear stress by deforming, whereas a fluid does not have this property and flows in response to a shear force (see Fig. 1.7) [64].

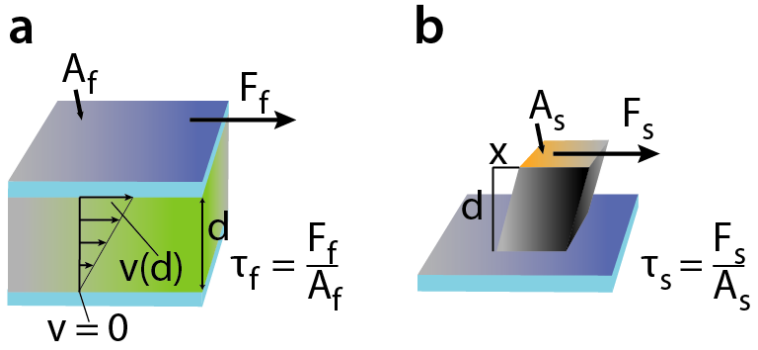

Fig. 1.7: (**a**) Fluid and (**b**) solid response to an applied shear stress. (**a**) The fluid is sheared between two plates. The bottom plate is in a stationary position and the top one of area A_f is subject to a tangential force, F_f. This results in the fluid flowing with velocity, $v(d)$. (**b**) When a shear force F_s is applied to the top surface, A_s, of a linear elastic solid, the object deforms by a quantity x.

A dimensional analysis of Eq. 1.19 shows that viscosity is measured in N s/m^2 or Pa s. Rearranging Eq. 1.19, the lubricated friction force is found to be directly proportional to η:

$$F_L = \frac{A_f \; v(d) \; \eta}{d} \tag{1.21}$$

In situations where the fluid flow is markedly dominated by gravity, the density, ρ, of the fluid should be taken into account. In this case, the fluid is characterised by a kinematic viscosity [5]

$$\nu = \frac{\eta}{\rho} \tag{1.22}$$

The physical model mathematically represented by Eq. 1.21 however holds true provided that no-slip boundary condition is valid. As shown in Fig. 1.8, such a condition is met when fluid molecules in contact with the solid surface move at the same velocity of the solid [97]. In reality, fluid molecules almost always show some slip in proximity of the confining surfaces [98], but for the vast majority of macroscopic Newtonian liquids this effect is negligible [99, 100]. The slip velocity, v_s, of the fluid at the surface is characterised by the slip length, b, that is, the distance between the solid-fluid interface and the point where the velocity profile extrapolates to zero :

$$v_s = b \; \frac{dv_x(z)}{dz} \tag{1.23}$$

where $dv_x(z)/dz$ is the gradient of the fluid velocity in the direction perpendicular to the

plate [98]. The mechanisms behind slip length are mainly due to surface defects: molecules jump to nearby vacancies created by thermal activation (defect slip) [101]. For polymer melts subject to high shear rates, slippage arises as a global effect due to the polymer being entangled in a structure with a high viscosity. Thus, the shear is favoured at the solid interface, rather than all over the polymer melt [5, 101, 102].

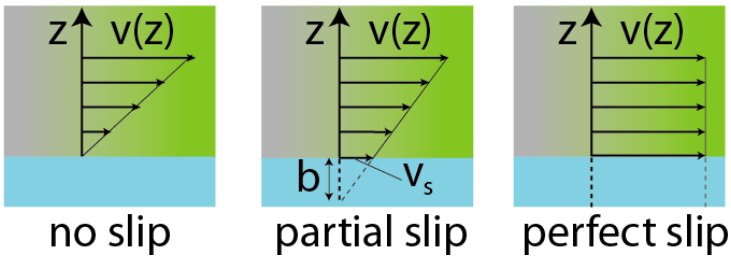

Fig. 1.8: Different regimes of fluid flow velocity in the proximity of a confining surface. The velocity is a function of the distance, z, from the surface. b is the slip length and characterises the three regimes: $b = 0$ (no slip); $0 < b = \infty$ (partial slip); $b = \infty$ (perfect slip).

It is possible however to implement the model of Eq. 1.21 including the slip length b. This can be done by correcting the denominator of Eq. 1.21 as the sum of d and b. Furthermore, the model of Eq. 1.21 assumes that viscosity does not change with the strain or shear rate, $d\gamma/dt$. For shear rates below 10 s^{-1}, this is true for a wide variety of fluids, the so-called Newtonian fluids. Shear-thickening and shear-thinning fluids are instead characterised by a viscosity dependence on the shear rate:

$$\tau_f = \frac{d\gamma}{dt}\,\eta\left(\frac{d\gamma}{dt}\right) \tag{1.24}$$

Shear-thickening fluids, such as cornstarch, show an increase in viscosity as the shear rate increases [64]. The fluid contains particles which are well ordered at low shear rates. At high shear rates, the particles are brought out of their equilibrium positions, thus resulting in a disordered structure opposing greater resistance to flow [64]. For shear-thinning fluids, such as blood or paint, the high shear rates result in breaking the aggregates of the blood cells or the paint particles and align them into a uniform direction thus allowing a smoother flow [5, 64].

Temperature and pressure dependence of viscosity

The thermodynamic phase of fluid lubricants directly influences the interactions among the constituent molecules, thus modulating the fluid response to external stimuli. This is the case also for viscosity which shows a strong dependence on temperature and pressure. Taking water as an example, the viscosity almost doubles at 273 K in comparison to 298 K [5]. Intuitively, the flow response of molecules to an applied shear is reduced as their

thermal agitation decreases. Analytically, the viscosity dependence on temperature can be modelled using an Arrhenius-like relationship:

$$\eta = \eta_0 \exp\left(\frac{E_a}{k_b T}\right) \tag{1.25}$$

where η_0 is a pre-exponential factor (approximated as the infinite-temperature viscosity); and E_a, and k_b are the activation energy, and the Boltzmann constant, respectively. Within this framework, lubrication can be seen an activated process characterised by bond breaking/making between the lubricant molecules: a network of tightly bonded molecules at low temperatures strongly resistant to a shear force [103]. This framework is also confirmed by viscosity having an exponential dependence on pressure P as described, in first approximation, by the so-called Barus model:

$$\eta = \eta_0 \exp\left(\alpha P\right) \tag{1.26}$$

where η_0 and α are the viscosity at one atmosphere and a constant parameter for the given lubricant, respectively [5]. From a molecular point of view, the pressure would confine the lubricant molecules in a solid-like layer where their mobility is reduced. From a macroscopic point of view, the exponential rise of viscosity in oil-based lubricants counterbalances the high pressure and maintains an effective hydrodynamic lubrication. For mechanical parts lubricated by mineral oil, the confining pressure can achieve even a few GPa. Thus, Eq. 1.26 would predict an increase in viscosity by 8 orders of magnitude. Such an extreme enhancement of the effective viscosity is however not usually observable due to shear thinning and solidification at high confining pressure [5, 104]. High local pressure within the lubricant film contributes to keeping the surfaces out of solid-solid contacts also through another mechanism, that is, inducing elastic deformation of the surfaces themselves. This allows the lubricant film to maintain an efficient thickness so as to generate a lifting force able to push the two surfaces away from contact [105, 106].

1.4 The problem of length and time scales in friction studies

The Amontons-Coulomb's laws for dry friction and the model for lubricated friction as described by Eqs 1.19-1.26 provide a semi-empirical framework for macroscopic phenomena. Such an approach is able to predict the evolution of linear systems, but only over a limited range of parameters. Their predictive power markedly decreases when tackling non-equilibrium disordered systems with interacting degrees of freedom [34]. This explains why over the last thirty years there has been an increasing number of theoretical

and experimental works attempting to understand the fundamental origins of macroscopic friction. This has been also possible thanks to developments both in computational power and in nanotechnology extending the study of friction to atomic, nanoscale and microscale systems (see Fig. 1.1) [5, 34, 107–109]. At these length scales, friction is currently addressed by a number of different approaches: minimalistic models (MM) [34, 110–114], atomistic molecular dynamics (MD) simulations [115, 116], mesoscopic multicontact models [113] and experimental studies based on atomic force microscopy (AFM) [21, 44, 98], surface force apparatus (SFA) [117, 118] and quartz crystal microbalance (QCM) [19, 26].

Minimalistic models

MM models provide an explanation for simple systems at the atomic and nano-scale. The two most popular approaches include the Prandtl-Tomlinson (PT) and the Frenkel-Kontorova (FK) models [5, 34, 116].

The PT model was developed in the 1920s. It represents a sliding surface in terms of a single point-like atom subject to an interfacial periodic potential due to the substrate. The sliding atom is coupled to a rigid slider through a spring element of spring constant k_{eff} (Fig. 1.9) [110, 116]. The atom, originally located in a configuration of minimum potential energy, moves along the x direction when the work done by the pulling force of the slider overcomes the energy barrier of the substrate potential. In other words, motion takes place by converting the stored elastic energy into kinetic energy [34, 113, 114]. The kinetic energy is then dissipated as heat which is modelled as a damping constant within the atom-spring system [5, 113, 114]. The total potential experienced by the atom hence consists of two contributions, the atom-substrate interaction and the elastic interaction with the slider. The sum of these two components can be modelled as:

$$U(x,t) \; = - \, U_0 \; cos\left(\frac{2\,\pi}{a}\;x\right) \; + \; \frac{k_{eff}}{2}\;(x - vt)^2 \tag{1.27}$$

where v is the velocity of the slider, and U_0 and a are the magnitude and periodicity of the substrate potential, respectively. The effective spring constant, k_{eff}, is defined by including the cantilever and the tip lateral stiffness, and the lateral stiffness of the the tip-sample elastic contact [5, 119]. Motion of the atom can be characterised by stick-slip transistions between adjacent minima as in Fig. 1.9, or it can be continuous depending on whether the potential well is greater or smaller than the energy provided by the spring element, respectively. This condition is described by the parameter:

$$\lambda = \frac{2\,\pi^2\,U_0}{k_{eff}\;a^2} \tag{1.28}$$

where the numerator represents the potential energy barrier, and the denominator the work done by the slider connected to the spring [113, 114]. Not only does the PT describe the molecular basis behind stick-slip motion, but it also explains the fundamental mechanisms behind the Arrhenius-type relationship between friction and temperature, as described by Eq. 1.25. The jump from one minimum to an adjacent one can be modelled by transition state theory with a probability rate, p, of a slip event:

$$p = p_0 \; exp\left(-\frac{\Delta E}{k_B T}\right) \tag{1.29}$$

where p_0 is a constant describing the attempt frequency of a jump [21]. Notably, a decrease in the friction force at very low temperature may be observed due to the thermal energy not being enough strong to facilitate interfacial bonds between the sliding atom and the substrate [113, 114].

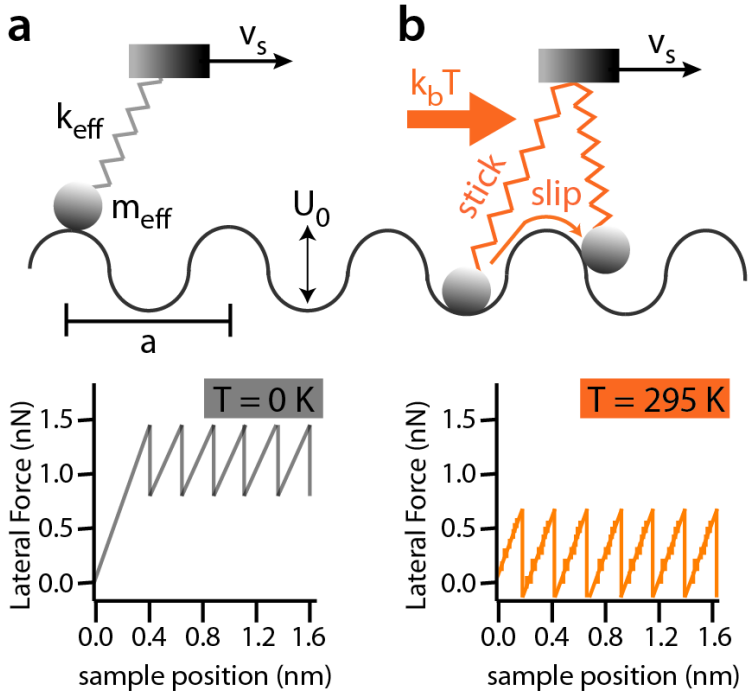

Fig. 1.9: Prandtl-Tomlinson model for a one-dimensional system. An atom of effective mass m_{eff} is connected, through a spring of effective spring constant k_{eff}, to a rigid slider moving at velocity v_s in the x direction. The atom moves in a sinusoidal potential of periodicity a. In the case of a soft spring constant, a stick-slip behaviour takes place, with the friction force jumping from a minimum to another when the spring tension is able to provide enough energy to overcome the potential well of magnitude U_0. (**a**) This regime is clear at $T = 0K$, with the friction force being a sawlike function of the atom displacement. (**b**) Thermal activation favours the motion of the atom thus reducing the friction force. At this higher temperature regime, thermal noise appears visible.

The PT model also confirms a dependence of the friction force on the sliding velocity. This relationship is not however linear as observed at the macroscale for both dry stick-slip

and lubricated friction (Eqs 1.16 and 1.21, respectively). At temperatures such that the thermal energy is sufficient to overcome the potential energy barrier (i.e. $E_a \approx k_B T$), the friction force depends logarithimically on the velocity. This is because, the faster the sliding, the less time the atom has to do a thermally activated jump from one minimum to the next [5]. When the thermal energy is not enough to allow a jump event, the friction force follows a power-law v^β regime with β =2/3 [20]. A further transition happens for velocities above 1 μs, with friction force showing a linear dependence on this variable [20]. This explains the observations at the macroscale where the sliding velocity is indeed greater than the aforementioned value.

The PT model has been successful in exploring numerous complex systems, such as elucidating the thermally activated nature of the friction process. The PT model is however limited to the atomic scale with no immediate links to nano and mesoscale tribological phenomena and to a velocity range which is not directly applicable to real-life devices [20]. In this regard, the Frenkel-Kontorova (FK) model allows investigations of nanoscale friction, thus at a length scale larger than that of the PT scheme. Within the FK framework, the top sliding surface is modelled as a chain of N harmonically coupled atoms subject to an interfacial sinusoidal potential of magnitude U_0 and periodicity a (see Fig. 1.10a) [34]. The interactions between nearest atoms within the chain are modelled as springs. The sliding motion of the two surfaces is represented as the chain of atoms being subject to a lateral force generated from the gradient of the periodic potential [5]. Fig. 1.10a shows a configuration when all the atoms are located at the minima of the potentials wells and no lateral force is applied. In the case of infinitely stiff springs, the chain moves in unison under the action of a lateral force, thus all the atoms reach at the same time the maxima of the interfacial potential and then slide to the next minima. The lateral force to move the chain is equal to the force needed to overcome each individual potential well, multiplied by the number of atoms. Such a condition is defined as atomic locking [34]. When the elastic layer is of finite extension, an applied lateral force generates, at one end of the chain, kinks which propagate along the chain and disappear at the other end (see Fig. 1.10b) [34]. This results in a smaller lateral force needed to initiate the motion, as the energy to move a kink is markedly smaller than the potential U_0 [5, 111, 112]. Thus, the motion of the chain is facilitated by the density of kinks [5, 111].

One of the most remarkable outcomes of the FK model is the prediction of zero-static friction for the so-called incommensurate surfaces, where the atom chain is out of proportion with the interfacial potential [5, 111, 120]. Frictionless sliding in incommensurate substrates requires the atoms chain to be unpinnned. Such a condition is achieved when the interfacial potential is significantly smaller than the spring stiffness, thus allowing atoms to maintain a distance close to their original spacing from each other [111]. For an atom moving to the maximum of the interfacial potential well, another atom

will go down to the minimum. For an infinitely long chain, the total sum of the forces will be zero leading to frictionless sliding [5]. Above a critical depth of the interfacial potential over the pinning threshold and provided that the chain stiffness is below a limit value, an Aubry transition takes place. The atoms move in a periodic arrangement, each close to a local minimum and separated from its neighbours by kinks. Here, motion needs a finite force, which is however smaller in comparison with moving an atomic-locked system [5, 121]. The FK model has been also applied to study lubricated friction confirming that a lubricant layer would remarkably decrease friction [122].

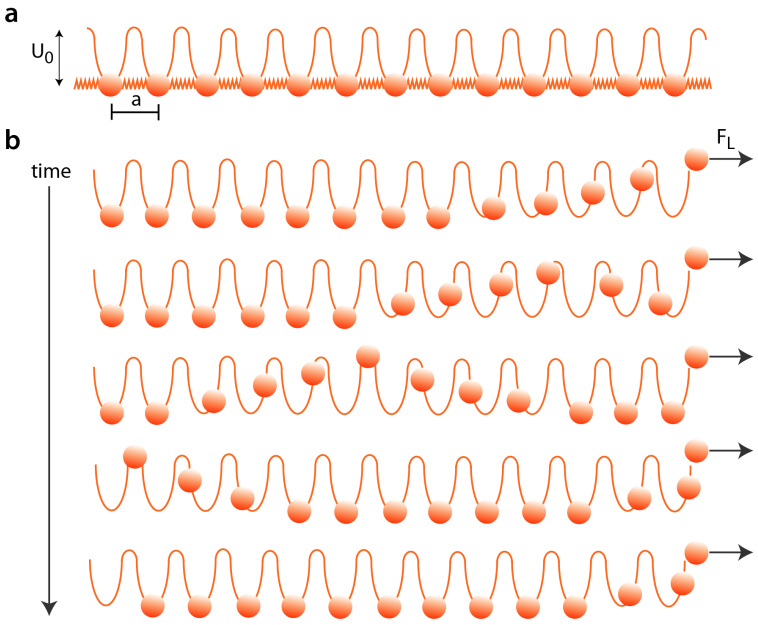

Fig. 1.10: Frenkel-Kontorova model. (**a**) The sliding of a surface over a substrate is modelled with the former as a chain of atoms interacting with each other through springs and subject to a potential from the latter. (**b**) Applying a lateral force results in a kink which develops at the right end and move towards the left. Once the kink has reached the end of the chain, the latter has moved by a lattice spacing.

In the case of both the two sliding surfaces being incommensurate, the FK model predicts structural lubricity (often misdescribed as superlubricity), that is, sliding with no energy dissipation through atomic scale stick-slip. Phonon and electronic contributions to friction remain as dissipative channels, but overall the dynamic dry and lubricated friction forces markedly decrease [34]. Even if the FK can be extended to two-dimensional scenarios [112], it is still unable to capture three dimensional scenarios [5].

Results from molecular dynamics simulations

Atomistic MD simulations can describe the atomistic structural details of sliding interfaces with a high degree of accuracy for three dimensional systems [123]. These investigations are based on computational studies where the dynamics of all the atoms at the interface

is calculated by solving Newtonian equations of motion given appropriate interatomic potentials [34]. MD simulations have confirmed the findings of the PT and FK models for commensurate surfaces: a lateral force is needed to overcome the static friction associated with the pinned atoms. In the case of incommensurate sliding surfaces, MD results show a frictionless behaviour unless the deformation of one of the interacting body allows accommodating the atoms of the other body [115, 116]. For incommensurate and atomically flat surfaces, MD simulations have also shown that adsorbed molecules account for a non-zero static friction rather than the expected structural lubricity. Adsorbates may also explain the adhesion hysteresis observed at the macroscale: the energy to bring in contact two surfaces is lower than the work to separate them. This is because adsorbed molecules tend to diffuse over the surface and end up trapped in local minima positions thus "locking" the sliding surfaces [5, 115].

MD simulations have furthermore contributed to showing that under extreme temperature and speed conditions, macroscopic models for dry friction do not hold true. This is the case of high temperature regimes for no-melting solid surfaces such as NaCl(100) where a rigid diamond tip apex slides over the surface [124]. Here, a progressive softening of the outermost layer of the solid substrate is responsible for the dry friction varying as a function of the applied load. For high loads, the friction coefficient is large at low temperature and markedly decreases close to the melting point. In proximity of this phase transition value, the probe determines local melting of the substrate, and its motion is facilitated by its own tiny liquid droplet, as it happens in ice skating. In the case of a low load, wear-free sliding on a hard surface takes place. Friction increases as temperature reaches the melting point where the surface, still solid, is progressively softer due to increasing anharmonicity [34, 124].

A non-linear regime diverging from Amontons-Coulomb's laws characterises also high speed nanofriction of atomically flat surfaces. Gold clusters rolling over graphite show a low-speed drift sliding regime, whereas at speed higher than 10 m/s, there is a ballistic frictional behaviour, so-called in analogy with the damped motion of a projectile. This is because at high speed, the substrate corrugation is averaged out [34, 125].

MD simulations have been also able to elucidate some of the fundamental mechanisms behind lubricated friction, in particular for fluid lubricants confined by two surfaces in a gap of a few nanometers. For such nanoconfined liquids, an enhanced viscosity and eventually solidification occurs as a result of the fluid layering and reduced mobility [34, 126, 127]. Within such a small length scale, surface defects play a major role in modifying lubricated friction due to pinning effects and nonzero static force [115].

MD simulations are not able however to provide a comprehensive understanding of tribological phenomena due to a number of limitations. The choice of suitable interatomic forces between atoms is one of the major problems [128]. MD simulations are usually

based on empirical force fields. *Ab initio* MD simulations taking into account the quantum mechanics of the electrons are not ideal as they can handle only a few hundreds of atoms for a time scale shorter than 1 ns [34, 129]. Even using reliable empirical force fields accurately parametrized for a given tribological problem, MD studies can explore a limited number of atomic interactions within a relatively short time frame. Typical simulations investigate 10^5-10^6 atoms progressing at a rate of a few μs per simulation day [34, 130]. Further limitations arise as MD simulations do not take into account the aging of contacts due to substrate relaxation [131].

Mesoscopic multicontact models

Multicontact models aim at filling in the gap between atomistic models and macroscale friction. This is done extending the single contact PT model of friction to multi-asperity contacts, thus providing a theoretical framework for friction phenomena at length scales between a few nm up to μm and time scales of tens of ms [34, 68, 114, 132]. Within this framework, friction is modelled in terms of dynamical formation and rupture of elastically coupled contacts [113]. The contacts, described in terms of elastic constants, do not represent only interactions among rough asperities but may also represent molecular bonds, capillary bridges and solid lubricant patches [34]. Multicontact models have shown that the overall smooth sliding emerges from uncorrelated stick-slip events or from smooth motion of the single contacts. A mesoscale stick-slip regimes is given by a cooperative behaviour of the contacts [34, 113]. Even if multicontact models allow investigating length and time scales more relevant to real-life tribological measurements, they still fail to accurately describe liquid lubricant. Another unsolved problem within the model is the microscopic origin behind the formation and rupture events [34]. These events may be qualitatively interpreted as reversible interactions of surface atoms, but first-principle calculations would be needed to quantitatively understand the nature of these instabilities [34].

Experimental approaches

The development of experimental techniques since the 1980s has allowed testing the predictions of theoretical models. As shown in Fig. 1.11, the main experimental approaches to study friction forces at these length scales include quartz crystal microbalance (QCM) [19, 26, 133], surface force apparatus (SFA) [118], and atomic force microscopy (AFM) [21, 44, 134].

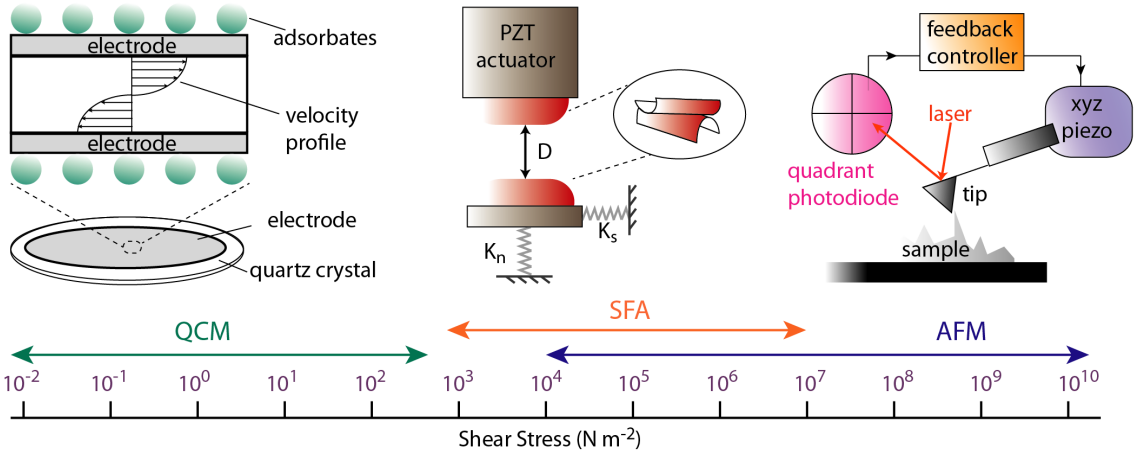

Fig. 1.11: Experimental methods to investigate friction and lubrication at the nanoscale and mesoscale. All together the three techniques allow exploring friction phenomena over a range of shear stress spanning 12 orders of magnitudes [19]. **QCM** measures the friction dissipation of adsorbed layers sliding over the surface. The enlarged image shows a cross-sectional area of the QCM highlighting the motion of the crystal and the electrode surface coverage by an adsorbed monolayer. Within a **SFA**, the PZT actuator brings in contact the upper surface with the lower one, and induces a lateral shear stress. The two surfaces are separated by a distance D. The applied pressure and the lateral friction force are measured incorporating two springs of elastic constant K_n and K_s at the bottom and at the side of the bottom surface, respectively. The inset shows how the two surfaces are placed in a crossed cylinder geometry. Within an **AFM**, the motion of a vibrating tip on the sample surface is detected recording the laser normal and lateral deflection on a quadrant photodiode. The xyz piezo scanner controls the position and motion of the cantilever. A feedback loop allows maintaining constant the tip oscillation amplitude or the applied force by the tip, while raster-scanning.

Quartz crystal microbalance

A QCM consists of a thin single crystal of quartz and metal electrodes attached to the top and bottom surfaces of the crystal. The choice of quartz is due to its small internal dissipation. Thus, a driving voltage applied by the electrodes results in oscillations with a sharp resonance frequency between 5 and 10 MHz [5, 19]. QCM is able to study friction phenomena measuring the frequency shift of the quartz crystal resonator induced by the adsorption of a thin film. When the adsorbed layer is subject to a shear stress, it can slide over the electrode surface thus dissipating its kinetic energy via friction. This results in broadening the resonance frequency of the oscillation [133]. Remarkably, the method can explore small shear stress ($\approx$ within the range 10^{-2} - 10^{2} N m^{-2}) over a relatively broad range of time scale, from a few seconds up to hours [19, 26, 133, 135, 136]. QCM has been able to show that phononic and electronic excitations are fundamental mechanisms behind frictional dissipation [137], confirming the results of analytical studies [138] and MD simulations [115]. QCM studies investigated the phononic contribution using systems with similar lattice spacing but different amplitude of surface corrugation, U_0. QCM studies

hence showed that the viscous coefficient of friction can be expressed as

$$\eta_m = \eta_{subs} + c\, U_0^2 \tag{1.30}$$

In Eq. 1.30, η_{subs} is the damping of the adsorbate sliding energy within the substrate, thus accounting for both phononic and electronic contributions. The second term of the Equation represents the dissipation from phononic contribution in the adsorbed layer, and c is a constant depending on temperature and lattice spacing [137]. Furthermore, QCM has shown how conduction electrons contribute to friction [139]. The motion of adsorbate atoms result in collisions with the surface atoms, exciting conduction electrons and creating electron-hole pair. The recombination of electron-hole pairs results in dissipating the excess energy in phonons, that is, heat [5, 140, 141]. QCM showed this, by studying how η_m for various adsorbates on a lead substrate markedly decreases to a minimum following the lead substrate transition to a superconducting state [139].
The technique is significantly limited to weakly adsorbed layers, such as rare gases and small physisorbed molecules [5, 19]. Furthermore, static friction force cannot be studied as the molecules easily slide on the QCM surface without any threshold force to start motion [5].

Surface force apparatus

SFA allows investigating fluids confined between atomically flat surfaces over an area of typically several μm^2 [117, 118, 142]. The distance between the confining solid surfaces is measured absolutely using interferometry, and dynamical measurements of the viscoelastic properties of confined fluids are performed over a range of frequencies (1-3 Hz) using surface force balances (SFB) [117], or SFA with resonance detection [142]. Within such length and time scales, SFA has shown that friction can be influenced by adhesion hysteresis due to the interdigitation of molecules at the interface, an effect particularly pronounced for soft and amorphous thin films [5, 143]. SFA techniques are however limited to atomically flat surfaces, and their results tend to average over multiple locations thus not allowing an accurate correlation between measured friction forces and molecular level details of the interface [5, 45]. This prompts questions relative to the extent the phenomena observed by SFA are valid in less idealised contexts [5]. Furthermore, the presence of any contaminant between the two confining surfaces cannot be ruled out, leading to potentially ambiguous results [118].

Atomic force microscopy and friction force microscopy

The limitations of SFA techniques are overcome by AFM based investigations. AFM offers the unique possibility of combining high-resolution imaging of the surface topography with

highly precise lateral force detection [5, 107, 144]. As shown in Fig. 1.11, a tip is mounted at the end of a compliant cantilever and raster-scans the sample surface. The cantilever position in the three dimensions is controlled by a piezoelectric element. Laser light is reflected on the top surface of the probe and detected on a quadrant photodiode (PD). The changes in light position on the PD are electronically analysed and transmitted to a feedback loop so as to keep constant the tip-sample distance or the force applied by the probe [45]. The surface topography of the sample is then reconstructed from the feedback loop adjustements [19, 26].

AFM can also measure lateral forces (friction force microscopy, FFM). When moving laterally along the surface (with respect to the cantilever axis) the friction force exerted on the tip by the interactions with the sample results in twisting the cantilever beam. As a result, the laser moves laterally on the four quadrants of the PD with an amplitude proportional to the friction force experienced by the tip [5]. The vertical deflection of the light beam in the upper and lower quadrants of the PD allows simultaneously recording the applied normal load. Remarkably, the method detects even angular deflections of a few angstroms, thus allowing atomic-level investigations of the static and kinetic friction. The technique is highly versatile allowing using sharp and blunt probes, that are, tips with a radius below and above 10 nm, respectively. In this way, friction forces can be investigated for systems of a few hundreds or thousands of atoms in contact with the substrate. Tips may also be functionalised, thus exploring the impact of chemical interactions and adhesion forces on the friction forces, respectively [5].

This flexibility and the ability to investigate friction and lubrication at the fundamental level have made AFM a popular choice for nano and mesoscale friction studies [5, 145].

At the nanoscale, FFM has experimentally confirmed structural lubricity on numerous incommensurate atomically clean crystalline substrates, as predicted by the FK model [146]. Furthermore, it has clarified that structural lubricity over scales larger than a few nanometers needs to meet three criteria: (i) the sliding bodies should be atomically smooth and crystalline surfaces; (ii) no contaminants between the surfaces in contact, a condition often achievable only in vacuum; (iii) no surface dislocations should take place [5].

FFM-based techniques have further demonstrated the validity of the PT and multicontact approaches modelling friction as a thermally activated process. Scanning a NaCl surface with a silicon tip in ultrahigh-vacuum conditions, slip and stick events were observed when the force exerted by the AFM spring constant was greater or smaller than the interfacial periodic potential, respectively. Also, when the tip alternatively scanned in two opposite directions, a friction hysteresis loop was generated with the loop area corresponding to the energy dissipated by friction in sampling back-and-forth the substrate [5, 147]. Remarkably, ultralow dissipation can be achieved at loads approaching 0 nN, suggesting that the potential corrugation depends on the normal force: the greater the normal force,

the greater the barrier height between adjacent atomic positions as the atoms are pushed closer towards the surface lattice [147]. FFM has also confirmed the temperature and velocity dependence of atomic friction as predicted by the PT model (see Eqs 1.27-1.29) [5, 148], with experiments conducted using a silicon tip scanning over graphite (0001) or gold (111) surfaces in ultra-high vacuum. The sliding velocities and temperatures probed were within the range of 10^{-9} - 10^{-6} m/s and 100-300 K, respectively [85, 149]. Similar experiments have been also performed on mica at room temperature and ambient pressure exploring velocities of $\sim 10^{-6}$ m/s [150].

Remarkably, FFM has not just confirmed theoretical and computational predictions, but it allowed further extending our understanding of how friction is influenced by sliding and environmental conditions. The logarithmic increase of friction over velocity has been shown to be valid only in dry environments, whereas a logarithmic decrease appears in humid conditions. These two regimes share a common origin as they are both thermally activated processes, but other mechanisms are responsible for their differences. In dry conditions, the friction increase with sliding velocity is due to the latter reducing the time atoms have so as to jump from one site to the adjacent one. In humid environments, a water meniscus forms around the AFM tip and opposes to its smooth sliding; as the probe velocity increases, the water meniscus has however less time to fully form around the probe [5].

AFM based investigations have been invaluable in showing the mechanisms of lubricated friction within nanoscale gaps. Here, the reduced mobility of the lubricant molecules and their interactions with the confining surfaces result in solid-like behaviour of the lubricant, thus questioning the validity of standard fluid lubricant models as described in Section 1.3.2 [5, 44, 98, 107].

Still, the majority of AFM based investigations, such as FFM, tend to sample lateral forces over multiple locations, thus averaging out atomistic details and not allowing achieving a clear picture of the links between molecular-level details and mesoscale tribological phenomena. Furthermore, FFM tends to focus on homogeneous samples. Thus, it does not allow investigating the impact of defects and singularities which may markedly influence the friction force [107].

1.5 Open questions

From the limitations behind experimental and computational approaches, it is clear why a proper theory of friction is still lacking. Such a theory should be able to quantitatively describe tribological phenomena in all the cases when linear-response continuum models as expressed by Amontons-Coulomb's laws are not applicable [34, 107]. Analytical approaches can overcome these limitations but they require an accurate knowledge of all the relevant

parameters, thus being markedly time consuming and highly prone to divergent results. This may also explain why tribology is often perceived as an empirical "black art" rather than a solid scientific discipline [5]. Fully capturing the complexity of friction into a model with solid predictive power is however crucial for the relevance of tribological phenomena in energy and technology [39, 151]. Such a goal relies on developing investigations able to access the molecular details of the interface while at the same time retaining a mesoscale picture of the system. This would allow bridging the current gap between, on the one hand, highly accurate atomistic models with limited applicability to real systems, and, on the other hand, macroscale semi-empirical laws valid over a limited range of parameters [152].

Lubricated systems pose a number of additional questions. Also here, the most challenging problems arise at the mesoscale: (i) elucidating the impact of lubricant molecular ordering on the friction force; (ii) and achieving a comprehensive description of the mechanisms by which ambient conditions modulate the shear response.

There is currently an intense debate on whether or not lubricants confined within such a length scale presents a different behaviour with respect to the properties of the fluid in the bulk. MD simulations [153, 154] and AFM based experiments [44, 107, 155] suggest an enhanced viscosity under nano-confinement due to the reduced entropy and mobility of the liquid molecules, which are organised in a more ordered, or glassy way [156]. On the other hand, SFA investigations revealed no molecular ordering for both aqueous solutions [157] and organic lubricants [158]. There is hence the need for techniques able to reconcile such a discrepancy which may be due to the different length and time scales considered.

Another area of intense research is to capture the nano- and mesoscale processes whereby ambient conditions influence lubricated friction. This is a crucial question given that for the majority of technological applications, contacts between surfaces do not take place in vacuum [38–40]. Thus, friction results markedly affected by the surrounding environment including temperature [159], airborne contaminants [160] and humidity [161]. Among these factors, humidity is often ignored given the difficulty in visualising and studying water adsorption [162]. The role of humidity is also underestimated as there are a number of dry systems (i.e. graphite, graphene and ultra-nanocrystalline diamond) where physisorbed water molecules may act as a lubricant [5, 162]. In many real-life scenarios, water however plays a significantly negative role on lubrication [161, 163, 164]. Water molecules easily enter the lubricated system from a high humid environment and reduce the adsorption of organic [161] and ionic liquid based [165] lubricants, thus modifying the interfacial chemistry and functionality of the protective lubricant thin film and further promoting the physisorption of both polar compounds and organic molecules containing hydrophilic groups [162, 163, 165]. Some recent studies have suggested that a global picture for humidity effects on lubrication requires a molecular description of the chemical

and physical events at the sliding interface, and directly relating such adsorption events with the larger meso and macroscale tribological observations [5, 165]. However, adsorbed water molecules cannot be easily detected due to their high mobility thus preventing from a full understanding of humidity impact on lubricity [5, 165].

Answering these questions has a crucial role in fundamental science, but most importantly will help develop lubricants whose molecular-level effects may be used so as to accurately tune macroscale friction [5, 38, 107]. A comprehensive understanding of lubricated friction forces at the mesoscale will also help further develop mechanical and electronic nano-technologies where the confined length scales result in limiting the efficiency of macroscale tribological solutions [5, 38, 44, 45, 107, 166].

Thus, the aims of this thesis are to characterise lubricated friction at the mesoscale (1 nm-1 μm), in particular studying the behaviour of lubricants in nano-confined gaps, and the impact of environmental conditions and chemical-physical surface singularities in modulating the sliding motion of two solids in contact. The investigations are performed in a number of model systems, including aqueous and organic lubricants at the interface with atomically flat surfaces and substrates with well-defined defects. This will allow studying any common threads in mesoscale lubrication. Hereafter, a description of the thesis structure:

Chapter 2- Methods will describe the rationale and the characteristics of the main tools used to address these questions. The Chapter will hence provide specific details of AFM based imaging and spectroscopy, as well as introducing the general aspect of scanning electron microscopy used to study AFM probes. The Chapter will also describe some key aspects of MD simulations used as a complementary tool when investigating lubricated friction in an organic model lubricant (Chapter 5).

Chapter 3- AFM torsional calibration. Here, I address the methodology developed within this thesis so as to quantitatively characterise the lubricated friction force with a precision down to the pN range. The Chapter will present a non-invasive and non-destructive *in situ* calibration method to determine the torsional spring constants of AFM cantilevers in viscous environments.

Chapter 4- Lubricating properties of single metal ions at interfaces. The Chapter will present some of the most relevant findings for lubricated friction in ionic aqueous solutions at nano-confinement. These model systems are relevant both for biomedical applications and for the development of green water-based lubricants for machinery and industrial engines. AFM imaging and spectroscopy results show that the shear response of ionic solutions can be captured by the Prandtl–Tomlinson model: the ions motion is described via a thermally-activated process resisted by the ion's hydration water.

Chapter 5- Lubricated friction around surface nano-defects. The Chapter will investigate the role of surface singularities in modulating the lubricant ordering and the

resulting impact on lubricated friction. Here, AFM and MD simulations are used to study the structural and dynamical behaviour of a model lubricant (squalane) near atomic steps of a graphite substrate. The results show that surface asperities induce a local organisation of the lubricant molecules into solid-like domains due to a loss of configurational entropy. This provides a molecular-level insight into the the mechanisms whereby roughness affects lubricated friction.

Chapter 6- Impact of water on the lubricating properties of hexadecane at the nanoscale. Here, AFM imaging, contact angle measurements and highly localized nano-rheology are used to track *in situ* the behaviour of a model organic lubricant (hexadecane) when exposed to ambient humidity. The results show that real-life conditions promote the formation, at the lubricant-solid interface, of water nanodroplets from ambient humidity. This does not occur on intrinsically hydrophobic materials, but on the hydrophilic surfaces typically found in engines and industrial machinery. The nanodroplets appear through a thermally-nucleated process and dramatically impact the lubricating properties of the system. The Chapter also shows that the detrimental impact of humidity on lubrication can be fully mitigated by addition of small amounts of surfactant (here oleic acid) to the oil.

Chapter 7- Conclusions and outlook. The final Chapter will summarise the key findings of this thesis and discuss challenges and ways forward in lubricated friction. The Chapter will in particular highlight the fact that, at the nano and mesoscale, the organisation and dynamics of lubricating fluids at the interface with solid surfaces depend on the particular chemical and physical characteristics of the lubricant/solids combination, with external factors (for example ambient humidity) playing a key role. This heterogeneity of factors may seem to prevent from inferring any general laws for nano and mesoscale tribology. Within all the model systems explored here, the lubricated friction is however characterised by some similar aspects, first of all the lubricant molecules behaving according to a thermally activated process (Prandtl-Tomlinson model). The Chapter will suggest investigations to further confirm this, and elucidate unanswered questions with potential technological applications.

References: Chapter 1

[1] M. Urbakh et al., *Nature* **2004**, *430*, 525–528.

[2] J. Gao et al., *The Journal of Physical Chemistry B* **2004**, *108*, 3410–3425.

[3] B. N. Persson et al., *Physics of sliding friction*, Springer Science & Business Media, **2013**.

[4] S. Goodwill et al., *Experimental Mechanics* **2004**, *44*, 195–206.

[5] C. M. Mate et al., *Tribology on the small scale*, Oxford University Press, **2019**.

[6] Y. Mo et al., *Nature* **2009**, *457*, 1116–1119.

[7] H.-J. Kim et al., *Scientific Reports* **2015**, *5*, 17034.

[8] L. Pirjola et al., *Environmental Science & Technology* **2015**, *49*, 3644–3652.

[9] O. P. Taylor et al., *SAE Technical Paper* **2016**, *2016-01-0892*.

[10] R. Amirante et al., *International Journal of Engine Research* **2017**, 1468087417706602.

[11] J. A. Schey, *Tribology in metalworking: friction, lubrication, and wear*, Springer, **1984**.

[12] A. Fuji et al., *Journal of materials science* **1995**, *30*, 5185–5191.

[13] I. M. Hutchings et al., *Tribology: friction and wear of engineering materials*, CRC Press, **1992**.

[14] N. Myshkin et al., *Tribology International* **2006**, *38*, 910–921.

[15] T. Kawano et al., *Arthritis & Rheumatism* **2003**, *48*, 1923–1929.

[16] R. W. Forsey et al., *Biomaterials* **2006**, *27*, 4581–4590.

[17] Z. Q. Mei et al., *The International Journal of Advanced Manufacturing Technology* **2006**, *30*, 693–699.

[18] A. Vanossi et al., *Nature Materials* **2012**, *11*, 97–98.

[19] J. Krim, *Scientific American* **1996**, *275*, 74–80.

[20] C. Fusco et al., *Physical Review B* **2005**, *71*, 045413.

[21] E. Gnecco et al., *Physical Review Letters* **2000**, *84*, 1172.

[22] W. W. Chong et al. in Key Engineering Materials, *Vol. 642*, Trans Tech Publ, **2015**, pp. 3–7.

[23] A. Dayo et al., *International Journal of Thermophysics* **1998**, *19*, 827–834.

[24] O. Braun et al., *Tribology Letters* **2012**, *48*, 11–25.

[25] B. Bhushan, *Fundamentals of tribology and bridging the gap between the macro-and micro/nanoscales*, Springer Science & Business Media, **2012**.

[26] H.-J. Butt et al., *Physics and chemistry of interfaces*, John Wiley & Sons, **2006**.

[27] N. Rott, *Annual Review of Fluid Mechanics* **1990**, *22*, 1–12.

[28] O. Pinkus, *Journal of Tribology* **1987**, *109*, 2–15.

[29] J. Krim, *Langmuir* **1996**, *12*, 4564–4566.

[30] C. M. Mate, *IBM Journal of Research and Development* **1995**, *39*, 617–627.

[31] A. Socoliuc et al., *Science* **2006**, *313*, 207–210.

[32] E. Meyer, *Progress in Surface Science* **1992**, *41*, 3–49.

[33] B. Bhushan et al., *Nature* **1995**, *374*, 607–616.

[34] A. Vanossi et al., *Reviews of Modern Physics* **2013**, *85*, 529.

[35] W. H. Thompson, *The Journal of Chemical Physics* **2018**, *149*, 170901.

[36] H. Turlier et al., *Nature Physics* **2016**, *12*, 513–519.

[37] Y. Song et al., *Journal of Biomechanics* **2012**, *45*, 524–530.

[38] J. Krim, *Frontiers in Mechanical Engineering* **2019**, *5*, 22.

[39] K. Holmberg et al., *Tribology International* **2012**, *47*, 221–234.

[40] B. K. Sharma et al., *Green Materials from Plant Oils* **2014**, 269–.

[41] R. Chattopadhyay, *Green tribology, green surface engineering, and global warming*, ASM International, **2014**.

[42] P. Lee et al., *US Department of Energy* **2017**.

[43] M. McManus et al. in Proceedings IMechE Seminar S673, *Vol. 2*, **1999**.

[44] K. Voitchovsky, *Nanoscale* **2016**, *8*, 17472–17482.

[45] C. Cafolla et al., *Nanoscale* **2018**, *10*, 11831–11840.

[46] Z. Bo et al., *Nanoscale Horizons* **2017**, *2*, 89–98.

[47] C. M. Mate, *Tribology Letters* **2013**, *51*, 385–395.

[48] H. P. Jost, *Tribology & Lubrication Technology* **2005**, *61*, 18.

[49] D. Dowson, *History of tribology*, Addison-Wesley Longman Limited, **1979**.

[50] A. A. Pitenis et al., *Tribology Letters* **2014**, *56*, 509–515.

[51] E. Popova et al., *Friction* **2015**, *3*, 183–190.

[52] P. J. Blau, *Tribology International* **2001**, *34*, 585–591.

[53] F. P. Bowden et al., *Proceedings of the Royal Society of London* **1939**, *169*, 371–391.

[54] K. Senetakis et al., *Soils and Foundations* **2013**, *53*, 746–755.

[55] I. Szlufarska et al., *Journal of Physics D: Applied Physics* **2008**, *41*, 123001.

[56] E. Broitman, *Friction* **2014**, *2*, 40–46.

[57] C. Gachot et al., *Tribology Letters* **2013**, *49*, 193–202.

[58] B. Bhushan et al., *Acta materialia* **2004**, *52*, 2461–2474.

[59] J. J. Mazo et al., *Physical Review Letters* **2019**, *122*, 256101.

[60] M. Mishra et al., *Tribology Letters* **2012**, *45*, 417–426.

[61] X. Ling et al., *Langmuir* **2007**, *23*, 8392–8399.

[62] F. Bowden et al., *The friction and lubrication of solids*, Oxford University Press, **1950**.

[63] R. H. French, *Journal of the American Ceramic Society* **2000**, *83*, 2117–2146.

[64] R. A. L. Jones et al., *Soft condensed matter*, Oxford University Press, **2002**.

[65] M. Ciavarella et al., *Journal of the Mechanics and Physics of Solids* **2006**, *54*, 2569–2591.

[66] M. Ciavarella et al., *Wear* **2008**, *265*, 729–734.

[67] J. A. Greenwood et al., *Proceedings of the Royal Society of London* **1966**, *295*, 300–319.

[68] B. N. Persson, *The Journal of Chemical Physics* **2001**, *115*, 3840–3861.

[69] B. Persson, *Physical Review Letters* **2007**, *99*, 125502.

[70] J. T. Busby et al., *Journal of Nuclear Materials* **2005**, *336*, 267–278.

[71] P. Zhang et al., *Materials Science and Engineering: A* **2011**, *529*, 62–73.

[72] P. Sarker et al., *Nature Communications* **2018**, *9*, 1–10.

[73] E. Pavlina et al., *Journal of Materials Engineering and Performance* **2008**, *17*, 888–893.

[74] E. Riedo et al., *Applied Physics Letters* **2003**, *83*, 1986–1988.

[75] T. Zhu et al., *Progress in Materials Science* **2010**, *55*, 710–757.

[76] P.-z. Zhu et al., *Tribology Letters* **2011**, *41*, 41–46.

[77] Y.-T. Cheng et al., *Journal of Applied Physics* **1998**, *84*, 1284–1291.

[78] A. Ovcharenko et al., *Wear* **2008**, *264*, 1043–1050.

[79] A. Vanossi et al., *Proceedings of the National Academy of Sciences* **2012**, *109*, 16429–16433.

[80] N. V. Gitis et al., *Journal of Physics D: Applied Physics* **1992**, *25*, 605.

[81] S. Malamut et al., *Tribology Letters* **2009**, *35*, 159–170.

[82] H. Tian et al., *Journal of Tribology* **1993**, 28–35.

[83] T. Baumberger et al., *Physical Review B* **1999**, *60*, 3928.

[84] C. Gao et al., *Journal of Tribology* **1990**, *112*, 354–360.

[85] L. Jansen et al., *Physical Review Letters* **2010**, *104*, 256101.

[86] J. Behrendt et al., *Journal of Sound and Vibration* **2011**, *330*, 636–651.

[87] P. A. Thompson et al., *Science* **1990**, *250*, 792–794.

[88] R. Leine et al., *Nonlinear Dynamics* **1998**, *16*, 41–54.

[89] J. H. Dieterich in *Rock friction and earthquake prediction*, Springer, **1978**, pp. 790–806.

[90] E. Rabinowicz, *Proceedings of the Physical Society* **1958**, *71*, 668.

[91] B. N. Persson, *Sliding friction: physical principles and applications*, Springer Science & Business Media, **2013**.

[92] J. C. Su et al., *Industrial Lubrication and Tribology* **2001**, *53*, 261–269.

[93] D. Dowson et al., *Elasto-hydrodynamic lubrication: international series on materials science and technology*, Elsevier, **2014**.

[94] H. Christensen, *Proceedings of the Institution of Mechanical Engineers* **1972**, *186*, 421–430.

[95] K. Miyoshi, *Solid lubrication fundamentals and applications*, CRC Press, **2019**.

[96] D. Dowson, *Journal of Physics D: Applied Physics* **1992**, *25*, A334.

[97] C. Wang, *Chemical Engineering Science* **2002**, *57*, 3745–3747.

[98] D. Ortiz-Young et al., *Nature Communications* **2013**, *4*, 1–6.

[99] B. E. Rapp, *Microfluidics: modeling, mechanics and mathematics*, William Andrew, **2016**.

[100] R. I. Tanner et al., *Rheology: an historical perspective*, Elsevier, **1998**.

[101] A. Martini et al., *Journal of Fluid Mechanics* **2008**, *600*, 257–269.

[102] E. C. Achilleos et al., *Journal of Vinyl and Additive Technology* **2002**, *8*, 7–24.

[103] S. G. E. Giap, *Journal of Physical Science* **2010**, *21*, 29–39.

[104] S. Bair et al., *Tribology Transactions* **2003**, *46*, 289–295.

[105] H. Åstrom et al., *Proceedings of the Institution of Mechanical Engineers* **1994**, *208*, 191–198.

[106] J. Skotheim et al., *Physical Review Letters* **2004**, *92*, 245509.

[107] C. Cafolla et al., *Science Advances* **2020**, *6*, eaaz3673.

[108] A. Vanossi et al., *Beilstein Journal of Nanotechnology* **2018**, *9*, 1995–2014.

[109] I. A. Lyashenko et al., *Beilstein Journal of Nanotechnology* **2017**, *8*, 1889–1896.

[110] U. D. Schwarz et al., *ACS Nano* **2016**, *10*, 38–41.

[111] M. Weiss et al., *Physical Review B* **1996**, *53*, 7539.

[112] Y. Yang et al., *Physical Review E* **2010**, *82*, 051119.

[113] I. Barel et al., *Physical Review Letters* **2010**, *104*, 066104.

[114] I. Barel et al., *Tribology Letters* **2010**, *39*, 311–319.

[115] M. H. Muser et al., *Physical Review B* **2000**, *61*, 2335.

[116] M. Hirano, *Surface Science Reports* **2006**, *60*, 159–201.

[117] U. Raviv et al., *Science* **2002**, *297*, 1540–1543.

[118] A. Gaisinskaya-Kipnis et al., *Langmuir* **2016**, *32*, 4755–4764.

[119] V. L. Popov et al., *ZAMM-Journal of Applied Mathematics and Mechanics* **2012**, *92*, 683–708.

[120] C. Wang et al., *Physical Review Letters* **1988**, *60*, 2661.

[121] A. Bylinskii et al., *Nature Materials* **2016**, *15*, 717–721.

[122] Y. Yang et al., *Communications in Nonlinear Science and Numerical Simulation* **2015**, *20*, 154–158.

[123] M. Robbins et al., *Modern tribology handbook*, **2001**.

[124] T. Zykova-Timan et al., *Nature Materials* **2007**, *6*, 230–234.

[125] R. Guerra et al., *Nature Materials* **2010**, *9*, 634–637.

[126] B. Persson et al., *Physical Review B* **1994**, *50*, 5590.

[127] B. Persson et al., *Journal of Physics: Condensed Matter* **2004**, *16*, R295.

[128] J. H. Los et al., *Physical Review B* **2005**, *72*, 214102.

[129] R. Car et al., *Physical Review Letters* **1985**, *55*, 2471.

[130] X. Liu et al., *Tribology Letters* **2012**, *46*, 167–178.

[131] Q. Li et al., *Nature* **2011**, *480*, 233–236.

[132] B. N. Persson et al., *Journal of Physics: Condensed Matter* **2004**, *17*, R1.

[133] M. Abdelmaksoud et al., *Langmuir* **2006**, *22*, 9606–9609.

[134] H. Lee et al., *Nanotechnology* **2009**, *20*, 325701.

[135] C. Keller et al., *Biophysical Journal* **1998**, *75*, 1397–1402.

[136] F. Meyer et al., *Review of Scientific Instruments* **2019**, *90*, 115108.

[137] T. Coffey et al., *Physical Review Letters* **2005**, *95*, 076101.

[138] M. Tomassone et al., *Physical Review B* **1997**, *56*, 4938.

[139] M. Highland et al., *Physical Review Letters* **2006**, *96*, 226107.

[140] L. Bruch, *Physical Review B* **2000**, *61*, 16201.

[141] B. Persson, *The Journal of Chemical Physics* **1993**, *98*, 1659–1672.

[142] H. Sakuma et al., *Physical Review Letters* **2006**, *96*, 046104.

[143] J. N. Israelachvili et al., *Journal of Adhesion Science and Technology* **1994**, *8*, 1231–1249.

[144] E. J. Miller et al., *Journal of Visualized Experiments* **2016**, e54924.

[145] B. Cappella, *Mechanical properties of polymers measured through AFM force-distance curves*, Springer, **2016**.

[146] E. Meyer et al., *Friction* **2014**, *2*, 106–113.

[147] A. Socoliuc et al., *Physical Review Letters* **2004**, *92*, 134301.

[148] S. Y. Krylov et al., *Physica Status Solidi (b)* **2014**, *251*, 711–736.

[149] X.-Z. Liu et al., *Physical Review Letters* **2015**, *114*, 146102.

[150] E. Riedo et al., *Physical Review Letters* **2003**, *91*, 084502.

[151] B. Marchon et al., *IEEE Transactions on Magnetics* **2014**, *50*, 137–143.

[152] O. Braun, *Tribology Letters* **2010**, *39*, 283–293.

[153] Y. Leng et al., *Physical Review Letters* **2005**, *94*, 026101.

[154] M. Tsige et al., *Chemical Physics Letters* **2008**, *457*, 357–361.

[155] T. Li et al., *Physical Review B* **2007**, *75*, 115415.

[156] W. D. Kaplan et al., *Annual Review of Material Research* **2006**, *36*, 1–48.

[157] W. H. Briscoe et al., *Nature* **2006**, *444*, 191–194.

[158] C. Drummond et al., *Physical Review E* **2001**, *63*, 041506.

[159] A. Filippov et al., *Physical Review Letters* **2004**, *92*, 135503.

[160] Z. Li et al., *ACS Nano* **2016**, *10*, 349–359.

[161] J. Lancaster, *Tribology International* **1990**, *23*, 371–389.

[162] Z. Chen et al., *Lubricants* **2018**, *6*, 74.

[163] A. Arcifa et al., *ACS Applied Materials & Interfaces* **2016**, *8*, 2961–2973.

[164] O. Y. Fajardo et al., *ACS Nano* **2017**, *11*, 6825–6831.

[165] X. Gong et al., *Chemical Science* **2015**, *6*, 3478–3482.

[166] J. D. Kiely et al., *MRS Bulletin* **2018**, *43*, 119–124.

2.0 Methods

The methods of science, like everything else under the sun, are themselves objects of scientific scrutiny, as method becomes methodology, the analysis of methods.
Daniel Dennett, Postmodernism and truth, 1998

2.1 Overview of the Chapter

In order to explore and contribute to answering the open questions of lubricated friction at the nano and mesoscale, I conducted experimental measurements combining atomic force microscopy (AFM) high resolution imaging with nanoscale localised shear spectroscopy measurements. Scanning electron microscopy (SEM) of the AFM probes ensured reproducibility of the results. Atomistic molecular dynamics (MD) simulations were used so as to conduct investigations at the atomic level and complement the AFM findings at the nano and mesoscale. In order to allow a better understanding of the physics behind the measurements, the present Chapter will review the fundamental aspects and modelling of these three techniques: AFM, SEM and MD simulations. The focus will be on AFM which has been the main tool to conduct the research studies of the project.

2.2 Atomic force microscopy

AFM belongs to the family of scanning probe microscopy (SPM) techniques. Following the invention of scanning tunneling microscopy (STM) by Gerd Binning and Heinrich Rohrer, AFM was developed in 1986 still by Binning, in collaboration this time with Christoph Gerber and Calvin Quate [1]. SPM techniques are based on reconstructing the sample topography and physical properties by raster-scanning a probe over the sample surface and studying their interactions. In the case of AFM, the main parameter to study the sample is the force between the probe and the sample itself. Unlike its STM predecessor, AFM allows investigating potentially any type of surfaces and not just conductive or semiconductor

materials [1–3]. The technique operates both in dry and liquid environment, providing vertical and lateral resolution down to a few picometers, and allowing measuring forces potentially down to the picoNewton range [4–6]. The essential aspects of an AFM have been mentioned in Chapter 1 Section 1.4. Here, I will present, in detail, the technique analysing its main electric and mechanical components, fundamental parameters, and its operational modes.

2.2.1 *Fundamentals of AFM*

AFM provides a highly versatile tool to conduct atomic and nano-scale measurements of various properties of a sample, including for example topography, friction, adhesion, visco-elasticity, electric polarization and magnetization [7–9]. Furthermore, the technique can be applied to modify surfaces and manipulate individual atoms and molecules [7]. Measurements are based on the interactions between a nanometric tip and the sample's surface, thus overcoming optical diffraction limit.
As shown in Fig. 2.1, the tip is mounted at the end of a flexible cantilever whose motion works as a transducer of the tip-sample interactions.

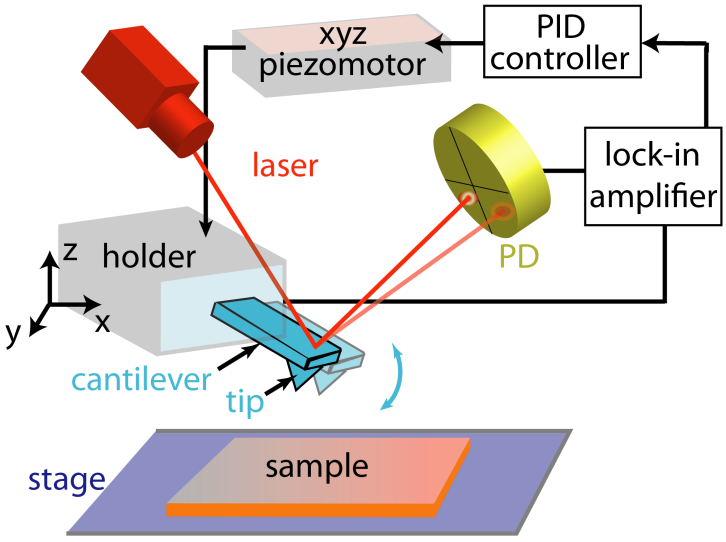

Fig. 2.1: Simplified representation of an atomic force microscopy (AFM). The interactions between the tip and the sample are detected by a photodetector (PD) recording the laser beam deflection. The cantilever can be maintained statically or oscillated by an excitation system. Feedback electronics is based on a lock-in amplifier transmitting information on the cantilever position and oscillation to a proportional integral derivative (PID) controller. The motion of the cantilever is actuated, usually, by a xyz piezomotor moving the probe in the three dimensions.

As the tip scans over the sample surface, the motion of the cantilever is usually detected by a laser beam which, upon reflection on the backside of the cantilever, is recorded by a photodetector (PD). The PD has four quadrants so as to monitor lateral and vertical

changes in the reflected light within a timescale ≤ 5 MHz [5, 10]. The PD converts the light signal into a voltage [11, 12]. A feedback loop re-adjusts the tip-sample distance through the piezoelectric motor so as to keep the cantilever position or its motion constant (see Fig. 2.1). The feedback corrections are used to image the sample surface. Here, the versatility of AFM emerges as, depending on the tip-sample interactions probed, surface imaging spans from topographical analysis to the distribution of electric charges and magnetic domains [7].

Furthermore, AFM also allows investigations of a localised area of the sample by force spectroscopy. Keeping the feedback loop off, the interactions between the tip and the sample are explored as a function of their separation. Also here, a number of different interactions can be studied depending on the tip material and sample characteristics, ranging from friction to conductive measurements.

The versatility of the AFM results in a number of different operational modes, which are typically divided into static (for example contact), and dynamic (e.g. amplitude or frequency modulation). The former identifies scanning approaches where the cantilever is kept static at its base [13, 14]. In this case, the main observable is the cantilever deflection and, when imaging, the feedback loop maintains the cantilever position constant. Dynamic modes are based on imposing a periodic motion to the cantilever, and applying a feedback loop on the changes of the vibration parameters (amplitude, frequency and phase). The oscillation is typically achieved by acoustically driving the cantilever through a piezoelectric acoustic oscillator, or optically exciting it with a pulsed laser (usually of ~ 1 mW) focused at the base of the cantilever. In the latter case, the driving laser wavelength is usually in the blue range so as to minimise any interference with the red laser used for detection [15–17].

Table 2.1 presents a brief summary of the most commonly used operational modes. A complete review goes beyond the scope of this thesis, and I would suggest the work by Song and Bhushan [8], as well as the book by Bellitto [18] for a detailed description of the different operational modes.

Static modes					
Mode	**Cantilever deflection**		**Feedback**	**Typical Measurable**	**Operation**
Contact	Vertical bending		Deflection	Norm. deflection	Raster-scanning, & spectroscopy
Friction force microscopy	Vert. bending, torsion, & lateral bending		Load	Norm. deflection, & twist angle	Raster-scanning, & spectroscopy
Dynamic modes					
Mode	**Cantilever deflection**	**Excitation Source**	**Feedback**	**Typical Measurable**	**Operation**
Amplitude Modulation	Vertical bending	Holder	Amplitude	Norm. deflection, amp., freq. & phase	Raster-scanning, & spectroscopy
Frequency Modulation	Vertical bending	Holder	Amp., freq. & phase	Norm. deflection, amp., freq. & phase	Raster-scanning, & spectroscopy
Shear Spectroscopy	Torsion	Sample	Off	Norm. deflection, shear amp. & phase	Spectroscopy

Tab. 2.1: Summary of some of the most common static and dynamic modes. For each operational mode, the main parameters under control, the feedback loop channel and the outputs are highlighted. For a complete review on AFM operational modes, please see refs [8] and [18].

Within this thesis, the molecular organisation and dynamic response of lubricants nano-confined between two solid surfaces were characterised with amplitude modulation (AM) AFM imaging and shear spectroscopy, respectively. Fig. 2.2 pictorially compares the two modes.

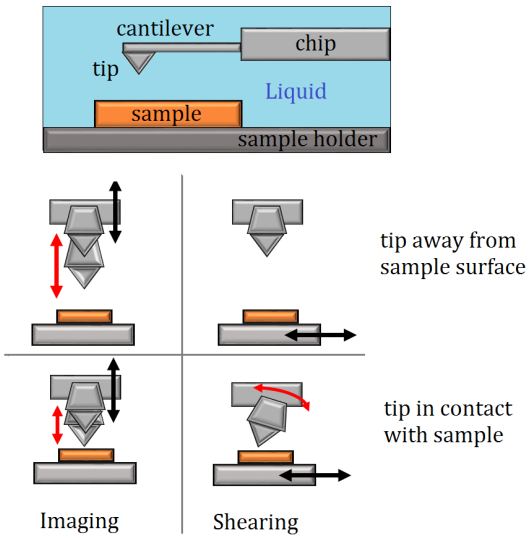

Fig. 2.2: Pictorial representation of the differences between imaging and shear spectroscopy. The top panel shows a lateral view of the cantilever and the sample immersed in the liquid. The bottom panel shows a front view of the cantilever in imaging (on the left) and shearing mode (on the right). The black arrows represent the external oscillation applied either vertically to the cantilever base (imaging mode) or laterally to the sample holder (shearing). The red arrows represent the consequent motion of the tip.

The images in Fig. 2.3 show the potential of AM-AFM imaging in finely distinguishing

atomic details, as well as mesoscopic organisation, thus representing an invaluable tool in merging molecular details and microscopic information on the interface between two surfaces in contact. Shear spectroscopy allows using AFM as a nanoscopic linear rheometer. In this way, we can conduct highly localised measurements on the lubricated friction with a precision down to the pN range. The rationale for preferring these operational modes will be completely clear after discussing the details of the methods (see Section 2.2.3 below). Hereafter, I will hence describe the fundamental parameters of these operational modes, and their modelling so as to allow extracting quantitative information from the measurements.

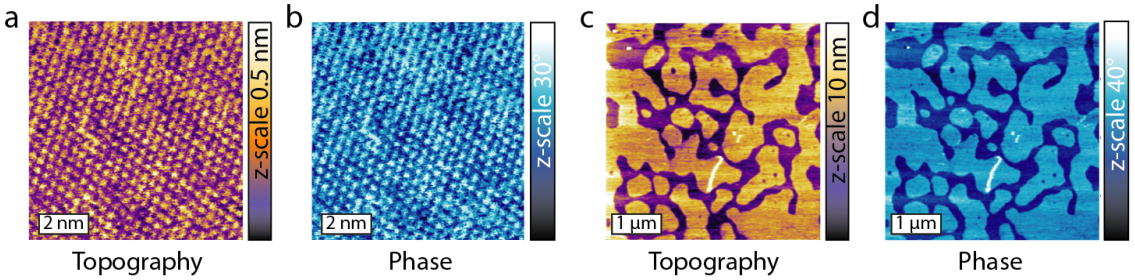

Fig. 2.3: Representative amplitude-modulation AFM imaging. (**a-b**) High resolution images of the interphase between mica and 1 mM KCl aqueous solution. The lighter areas in the topography (**a**) show an epitaxial arrangement of the cations on the negatively charged mica surface. (**c-d**) High resolution AFM images of the mesoscale interface between mica and hexadecane at relative humidity > 90 %. The high humidity results in water molecules organised into large domains, that are, the lighter areas in the topography (**c**). (**b, d**) The phase lag between the driving signal and the tip oscillation is allowed to vary freely and changes depending on the local tip-sample interactions, F_{ts} (see Sections 2.2.3 and 2.2.4 below.)

2.2.2 AFM key parameters

The main AFM parameters depend on the characteristics of the cantilever whose motion over the sample surface can be, in first approximation, described as a damped harmonic oscillator. There are, however, other relevant factors related to the environmental conditions and the detection system of the AFM. Here, I will review the main operational parameters controlled during the experiments as discussed in the following Chapters 3-6.

AFM probe

Among the main components of an AFM, the probe plays a key role as the information extracted by the technique is based on the interactions between the probe itself and the sample. The probe is composed of a cantilever with a tip attached to its free end. The cantilever has micrometric sizes with length, width and thickness usually within the ranges $10-500$ μm, $1-100$ μm and $0.1-5$ μm, respectively. A wide combination of materials

(e.g. silicon nitride, diamond, diamond-like carbon), sizes and geometries (for example, triangular, rectangular, V or T-shape) result in a broad spectrum of cantilevers with different mechanical characteristics so as to allow investigating potentially any samples from highly compliant lipid bilayers to stiff metallic oxides [5, 16]. The sensitivity of the cantilever in detecting sub-nanometric features is improved by a nanometric tip with a typical height range between 3−20 μm [5, 16, 19]. This allows investigating the interfacial forces only for a small numbers of atoms at the tip edge. Also here, nanoscale manufacturing provides tips made of different materials and with diverse shapes, thus resulting in further distinctive mechanical properties [5, 16, 19–22].

Cantilever spring constant

Calibrating the cantilever flexural spring constant, k_f, has a crucial importance in both static and dynamic mode so as to quantify the tip-substrate interfacial forces. In first-approximation, the cantilever can be modelled as a spring displaced from its equilibrium position and experiencing an acceleration due to a restoring force. Thus, using Hooke's law, the force, F_{ts}, exerted by the tip on the sample can be modelled as a function of the tip-sample distance, z [23–25]:

$$F_{ts} = k_f \; z \tag{2.1}$$

where k_f is a constant of proportionality, the so-called flexural spring constant. The model represented by Eq. 2.1 holds true for small z displacements [26]. k_f is an intrinsic property of the cantilever depending on its material and geometry. For the case of a rectangular cantilever beam, k_f is given by [27]:

$$k_f = \frac{Ewt^3}{4L^3} \tag{2.2}$$

where E is the Young's modulus of elasticity for the cantilever material; and w, t, and L describe the shape of the probe, defining its width, thickness and length, respectively [23]. The combination of the parameters results in a broad range of cantilever stiffness, from very soft ($k_f < 0.01$ N/m) up to markedly stiff probes ($k_f > 100$ N/m) [5, 16, 20].
The calibration of the flexural spring constant, alongside that of the inverse optical lever sensitivity (InvOLS, see below), represents a key step so as to convert the voltage signal detected by the photodiode into nanoNewtons of applied force. A number of calibration methods have been developed. The Sader and thermal methods are both based on analysing the thermal fluctuations of the cantilever in the surrounding environment. These two methods have become some of the most popular approaches for beam-shaped and rectangular cantilevers. This is due to the methods being able to return solid predictions in a wide range of conditions and environments. Furthermore, both the methods need a

limited number of input parameters which are relatively easy to determine: cantilever's geometry, resonance frequency and quality factor [28–32]. This leads to discussing the cantilever resonance frequency and quality factor.

Angular resonance frequency

The angular resonance frequency, ω_0, has a crucial role in dynamic mode where the probe motion is subject to a periodic vibration. ω_0 is given by [33]:

$$\omega_0 = \sqrt{\frac{k_f}{m}} \tag{2.3}$$

where m describes the effective mass of the cantilever in the medium of interest. It may be difficult to directly determine m. This leads to using the value of ω_0 in vacuum, ω_{vacuum}, and combine it with the cantilever mass per unit length, μ, the density of the medium, ρ, and the real part of the so-called hydrodynamic function characterising the response of the body in the fluid, $\Gamma_r(\omega)$ [26, 34]:

$$\omega = \omega_{vacuum}\left(1 + \frac{\pi\rho w^2\Gamma_r(\omega)}{4\mu}\right)^{-1/2} \tag{2.4}$$

Quality factor

The Quality factor, or Q-factor, is a dimensionless parameter, which describes how underdamped an oscillator is. The Q-factor characterizes the resonator's bandwidth relative to its center frequency [5, 33]. Mathematically, it is defined as [33]

$$Q = \frac{\omega}{\delta\omega} \tag{2.5}$$

where $\delta\omega$ is the angular half-power bandwidth. Oscillators with high Q-factors have low dampening: this corresponds to a lower rate of energy loss in comparison with the stored energy. Fig. 2.4 shows the dependence of Q-factors on the bandwidth [5, 26, 35].
The oscillation of a cantilever in liquid presents some important differences in comparison with vibrations in air, or vacuum. Firstly, the cantilever tends to have an increase in the effective mass by a factor of 10-40, and a corresponding decrease in the resonance frequency, f_0. This effect is due to the higher density of the surrounding liquid in comparison with the density of air [36, 37]. The natural frequency, f_n, and the resonance one are related by the following equation [26, 38]:

$$f_0 = f_n\sqrt{1 - \frac{1}{4Q^2}} \tag{2.6}$$

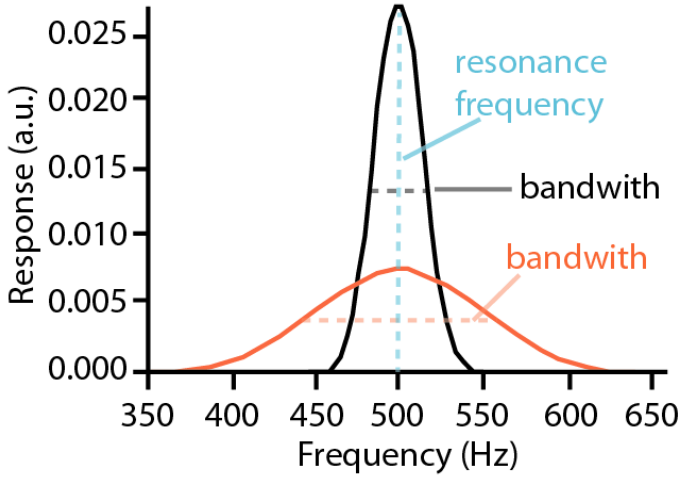

Fig. 2.4: Given the same resonance frequency, a larger bandwidth corresponds to a lower Q-factor, and vice versa. The frequency x-scale is set arbitrarily.

Hence, the strong hydrodynamic interaction between the cantilever and the liquid results in reducing the value of the Q-factor, even by two orders of magnitudes [5].

Inverse optical lever sensitivity

We have seen that the motion of the cantilever is optically detected by a laser beam deflected on the probe top surface and tracked by a photodiode which records a signal in voltages. The measured voltage needs to be converted into nanometers of displacement through the inverse optical lever sensitivity (InvOLS). The InvOLS hence expresses the relationship between nanometers and volts (nm V^{-1}). The knowledge of the spring constant allows then using Eq. 2.1 so as to quantify the force applied by the AFM probe. The InvOLS depends on the particular combination of photodiode, cantilever and medium where the reflection takes place [34, 39]. Calibration of the InvOLS is usually performed with a force-distance measurement on a hard surface. This allows measuring the voltage response of the detector as a function of the known distance moved by the z-piezomotor. When the cantilever is pushed against the substrate, the laser deflection can be assumed to be equivalent to the distance moved by the z-piezomotor. Thus, within the probe-surface contact region, the voltage versus distance curve shows a linear behaviour. The inverse of the curve slope returns the InvOLS [34, 39, 40].

2.2.3 Modelling the motion of an AFM cantilever

The section presents some fundamental models describing the motion of the cantilever. The modelling will provide a basis for correctly interpreting the results of the measurements presented in Chapters 3-6, and give quantitative information on the interactions between

the tip and the sample.

Static modes

The most common static mode is the so-called contact mode with the tip in contact with the sample. Here, modelling of the probe motion allows using the cantilever deflection and the spring constant to extract the force exerted by the tip on the sample. The vertical detector records the displacement of the free end of the cantilever while the feedback loop acts on the probe height. For small dispacements, the tip-sample interaction, F_{ts}, can be described using Eq. 2.1. Fig. 2.5 shows a typical force-distance curve acquired in air in contact mode.

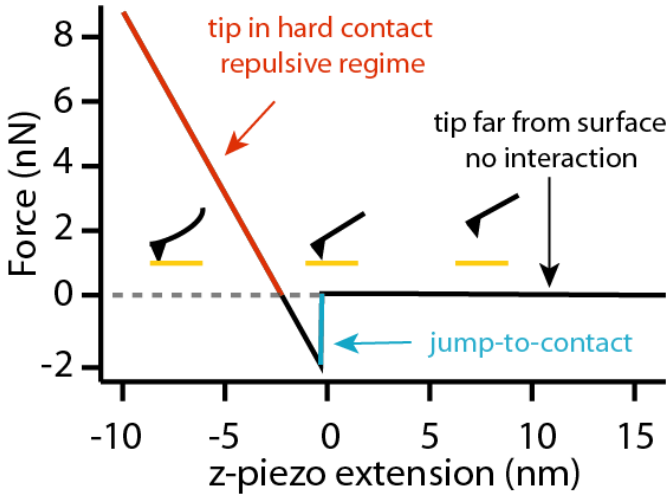

Fig. 2.5: Representative force spectroscopy in contact mode. The jump-to-contact phenomenon is particularly strong in air due to, for example, capillary forces.

Experiments conducted with static mode in air are typically affected by the so-called jump-to-contact instability [38]. As shown in Fig. 2.5, this instability is due to the attractive force gradient being markedly greater than the flexural spring constant: $\frac{\partial F_{ts}}{\partial z} \gg k_f$. Thus, the AFM suddenly jumps to contact with the substrate. This limits the force resolution and may further contribute to damaging both the tip and the substrate. The discontinuity can be reduced by using stiffer probes. However, as shown in Eq. 2.1, this leads to a reduction in the sensitivity of the measurement of the vertical displacement for the same applied force [10]. The jump-to-contact may be reduced by fully immersing the AFM probe and sample in liquid so as to reduce any attractive capillary forces. Contact mode may however damage the tip and the sample, thus making it non-ideal for soft interfaces, as it is the case for lubricant thin films investigated in this thesis [6, 17, 20, 41, 42].

Dynamic modes

Dynamic modes have been developed so as to solve the limitations of the static operational approaches. Here, the probe is subject to an oscillation, thus modelling aims at studying the amplitude, frequency and phase response of the cantilever for such a periodic motion [38]. For dynamic modes, the non-linear dynamics response of the AFM cantilevers requires a complex mathematical development [43, 44]. In first approximation, we can model the motion of the cantilever-tip ensemble as a damped point-like mass harmonic oscillator under the excitation of a driving force, F_{exc}. The model ignores any contributions to the cantilever motion from high flexural modes of the lever as well as any changes in the hydrodynamic damping of the probe motion [45, 46]. In spite of the limitations, the approach has been shown to be helpful for basic predictions [33]. Within this model, the motion of a cantilever of effective mass m is then described by a non-linear second-order differential equation [45, 46]:

$$m\ddot{z}(t) + \gamma\dot{z}(t) + k_f z = F_{exc} + F_{ts} \tag{2.7}$$

where z is the displacement of the free edge of the cantilever as a function of time t, γ is a damping term, and F_{ts} describes the tip-sample interaction forces [10, 47]. γ is given by [38, 46]:

$$\gamma = \frac{m\omega_0}{Q} \tag{2.8}$$

where ω_0 and Q are the natural angular resonance frequency and the quality factor of the cantilever [5, 38, 46]. In Eq. 2.7, the effective mass takes into account the hydrodynamic loading from the surrounding fluid the cantilever may be immersed into. The driving force F_{exc} has a sinusoidal periodicity:

$$F_{exc} = F_d \; cos\,(\omega_d t) \tag{2.9}$$

where F_d and ω_d are the driving force amplitude and angular frequency, respectively [33, 47].

In the absence of any tip-surface interactions ($F_{ts} = 0$), and approximating the cantilever as a point-mass object of homogeneous density and subject to a motion of small magnitude, Eq. 2.7 can be solved using the classic solution for a harmonic oscillator with damping [38]:

$$z = B \; exp(-\frac{\omega_0}{2Q}) \; cos(\omega_r t - \beta) - A \; cos(\omega_d t) \tag{2.10}$$

where B and β are constants and ω_r is given by:

$$\omega_r = \omega_0\sqrt{1 - \frac{1}{4Q^2}} \tag{2.11}$$

The first addendum of Eq. 2.10 decays exponentially. Thus, after the rapid extinction of this transitory part of the solution, the dynamics of the cantilever is dominated by the second term describing a steady-state motion. As shown in Fig. 2.6, the amplitude, A, of the steady-state term has a Lorentzian dependence on the driving frequency [38]:

$$A = \frac{F_d/m}{\left[\left(\omega_0^2 - \omega_d^2\right)^2 + \left(\omega_d\ \omega_0/\ Q\right)^2\right]^{1/2}} \tag{2.12}$$

The phase shift between the steady-state motion of the cantilever and the driving force has a sigmoidal shape (see Fig. 2.6) and is given by:

$$tan\left(\phi\right) = \frac{\omega_d\ \omega_0/\ Q}{\omega_0^2 - \omega_d^2} \tag{2.13}$$

The convention is that $\phi = 90°$ at resonance, that is, when $\omega_d = \omega_0$ [33, 45, 47].
In the current scenario of the cantilever not interacting with the sample surface and when driving the cantilever at resonance frequency ($\omega_d = \omega_0$), the oscillation amplitude is defined as free amplitude, A_0 [38, 45]:

$$A_0 = \frac{F_d\ Q}{k_f} \tag{2.14}$$

Equations 2.12 and 2.14 show that the larger the dampening (the smaller Q-factor), the smaller the maximum amplitude [5, 38]. The dependence of the phase lag on the dampening is shown by Eq. 2.13: lowering the Q-factor results in a smoother transition of the phase response.
We can now introduce the effect of the tip-sample interaction, thus in Eq. 2.7 F_{ts} is no longer equal to zero. F_{ts} accounts for both conservative and dissipative contributions. For small oscillation amplitudes, A, of the tip with respect to its equilibrium position, z_c, we can approximate F_{ts} by [38]:

$$F_{ts}(z) = F_{ts}(z_c) + \left(\frac{dF_{ts}}{dz}\right)_{z_c}(z - z_c) \tag{2.15}$$

We can use Eq. 2.15 to derive an effective spring constant, k_{eff} [38]:

$$k_{eff} = k_f - \left(\frac{dF_{ts}}{dz}\right)_{z_c} = k_f - k_{int} \tag{2.16}$$

The new effective angular resonance frequency, ω_{eff}, is then:

$$\omega_{eff} = \left(\frac{k_{eff}}{m}\right)^{1/2} \tag{2.17}$$

Within this framework, ω_{eff} for a weakly perturbed harmonic oscillator depends on the gradient of the tip-sample interaction.

ω_{eff} is shifted by $\Delta\omega$ from the natural frequency: [26, 38]:

$$\Delta\omega = \omega_{eff} - \omega_0 \approx -\frac{\omega_0\ k_{int}}{2k_f} \tag{2.18}$$

Thus, when interacting with the subtrate, the AFM probe behaves as a harmonic oscillator with an effective resonance frequency and a frequency shift as described by Eqs 2.17 and 2.18, respectively. The interaction oscillation amplitude, A_{int}, and phase, ϕ_{int}, can be described by the following equations [26, 38]:

$$A_{int} = \frac{F_d/m}{\left[\left((\omega_0 + \Delta\omega)^2 - \omega_d^2\right)^2 + (\omega_d\ \omega_0/\ Q)^2\right]^{1/2}} \tag{2.19}$$

$$tan\,(\phi_{int}) = \frac{\omega_d\ \omega_0/\ Q}{(\omega_0 + \Delta\omega)^2 - \omega_d^2} \tag{2.20}$$

As shown in Eq. 2.19, the amplitude depends on the excitation and effective resonance frequency. This allows explanations of the changes in oscillation amplitude changes as a function of the interaction forces between the tip and the surface. Under the effect of weak conservative forces, the shape of $A_{int}(\omega)$ is preserved but shifted in the frequency domain (see Fig. 2.6).

At the driving frequency, ω_d, the oscillation amplitude is however reduced as a result of the interactions with the substrate. This is the case in both the attractive and the repulsive regime. The decrease in the oscillation amplitude is then used so as to derive the force gradient and hence reconstruct the height variations. The frequency shift is negative or positive depending on whether the tip-surface interaction is attractive or repulsive, respectively. Thus, the phase shifts with the new resonance frequency keeping the maximum dissipated power at ω_{eff} [38].

Some limitations however affect the model of a weakly perturbed harmonic oscillator, mathematically represented by Eqs 2.19- 2.20. First, the model works under the assumption of the interaction with the sample surface resulting in a frequency shift but not an energy transfer. Secondly, the force gradient is neither independent nor a linear function of the tip-sample separation and furthermore can vary depending on the approach/retraction portions of the oscillation cycle [48]. The first limitation is overcome by taking into account a dissipative component so that the tip-sample interaction force is given by [26, 49]:

$$F_{ts} = F_{ts}(z_c) - k_{int}z - \gamma_{int}\frac{dz}{dt} \tag{2.21}$$

where γ_{int} is the interaction damping coefficient. Thus, the differential equation becomes:

$$m\ddot{z}(t) + (\gamma + \gamma_{int})\dot{z}(t) + (k_f + k_{int})z = F_d\ cos(\omega_d t) \tag{2.22}$$

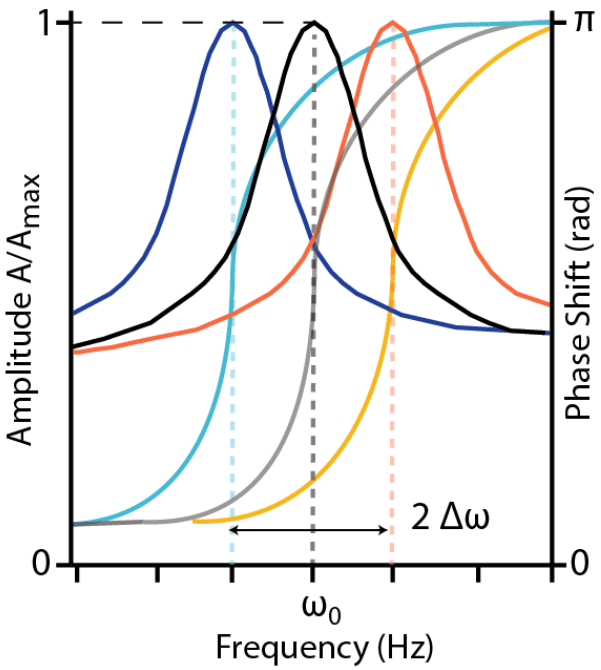

Fig. 2.6: The amplitude and phase have a Lorentzian and sigmoidal behaviour with respect to the driving frequency, respectively. The oscillation amplitude and phase for the unperturbed damped harmonic oscillator are shown in black and grey, respectively. The amplitude and phase responses of the cantilever change under the effect of a small conservative force due to the interaction of the tip with the sample. Under the effect of a repulsive force, the amplitude and phase are shifted as shown by the red and orange curves, respectively. An attractive interaction results in shifting the system as shown by the blue and cyan curves.

We can express the damping and stiffness terms as:

$$k_{eff} = k_f + k_{int} \tag{2.23}$$

$$\gamma_{eff} = \gamma + \gamma_{int} \tag{2.24}$$

Using Eqs 2.23-2.24, the steady-state solution of Eq. 2.22 is identical to the SHO solution for free motion (see Eq. 2.10). As shown in Fig. 2.7, the extra dampening term however results in broadening the curve of the oscillation amplitude:

$$\Delta\omega = \omega_{eff} - \omega_d = \sqrt{\frac{k_{eff}}{m}} - \sqrt{\frac{k_f}{m}} \approx -\frac{\omega_d\ k_{int}}{2k_f} \tag{2.25}$$

$$A_{int} = \frac{F_d/m}{\left[\left(\left(\omega_{eff}^2 - \omega_d\right)^2\right)^2 + \left(\omega_{eff}\ \omega_d/\ Q_{eff}\right)^2\right]^{1/2}} \tag{2.26}$$

$$tan\left(\phi_{int}\right) = \frac{\omega_{eff}\ \omega_d/\ Q_{eff}}{\omega_{eff}^2 - \omega_d^2} \tag{2.27}$$

where the effective Q-factor is decreased by $Q_{eff} = \frac{m\ \omega_{tot}}{\gamma_{tot}}$. This results in the resonance curve for the oscillation amplitude decreasing for the same value of F_d (Fig. 2.7).

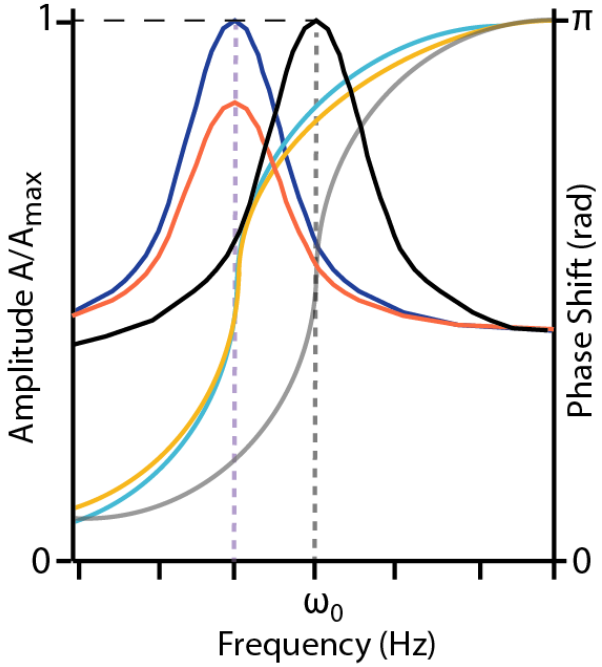

Fig. 2.7: The amplitude and phase change under the effect of small conservative and dissipative forces due to the interaction of the tip with the sample. The oscillation amplitude and phase for the unperturbed damped harmonic oscillator are shown in black and grey, respectively. An attractive interaction results in shifting the system as shown by the blue and cyan curves. Under the effect of a small dissipative interaction, the shift in amplitude and phase is shown by the red and orange curves, respectively.

The phase shows a smooth dependence around the new effective frequency [26, 49]. The model represented by Eqs 2.26 - 2.27 can be further improved including the dependence of the force gradient on the tip-sample separation. This can be done assuming a periodicity in the separation with the equilibrium position, z_c, being constant over time [48, 49]. Thus, $F_{ts}(z(t))$ can be expressed as a Fourier expansion in the time domain [48, 49]:

$$F_{ts}(z(t)) = F_{ts}(t) = \frac{a_0}{2} + \sum_{i=1}^{\infty} a_i\ cos(i\omega_d t) + \ b_i\ sin(i\omega_d t) \tag{2.28}$$

Equation 2.28 can be simplified keeping only the first order term:

$$F_{ts}(t) = \frac{a_1}{A} z(t) - \frac{b_1}{A\omega_d} \frac{dz(t)}{dt} \tag{2.29}$$

Thus, the differential equation for motion is given by [50]:

$$m\ddot{z}(t) = -\left(k_f - \frac{a_1}{A}\right) z(t) - \left(\gamma + \frac{b_1}{A\omega_d}\right) \dot{z}(t) + F_{exc}(t) + F_{ts}(t) \tag{2.30}$$

The model mathematically represented by Eq. 2.30 is very similar to that of Eq. 2.22. In the former, the tip motion is however influenced by the interaction force averaged over an entire oscillation cycle, whereas in the latter model the motion depends only on the force gradient at the mean tip-sample distance.

More sophisticated models have been introduced taking into account that in reality the cantilever is not a simple point-mass object subject to a damped oscillatory motion. An intensive field of research is focusing on re-constructing the force-distance behaviour without any *a priori* assumptions on the geometry of the cantilever and on a linear behaviour for the tip-sample interactions [8, 47, 51]. The so-called multi-frequency force approach reconstructs the interfacial forces by exciting and/or detecting several frequencies of the cantilever oscillation [51]. Analytical and numerical models have been implemented so as to describe the probe as a 1D, 2D, and 3D beam. These models better address the cantilever dynamics in particular when higher-order flexural modes of the cantilever are excited. Point-mass models provide a solution for the vertical displacement of the cantilever, but the experimental set-up usually detects the rotation angle of the cantilever. Thus, some inaccuracy in data explanation may appear because, for high-order modes, there is not a simple proportional relationship between vertical displacement and rotational angle [8]. These advanced models however go beyond the scope of this thesis where small amplitude oscillations were applied and no higher-order excitation modes were used. In this scenario, the analytical modelling of the cantilever as a point mass has been shown to provide insightful understanding of the physics behind the motion of probe [8, 26, 33, 50].

Two main dynamic modes are currently used: amplitude modulation (AM) and frequency modulation (FM). The former is based on using a fixed amplitude and frequency for the driving signal. The cantilever can be driven near or off-resonance, depending on whether or not ω_d/ω_0 is approximately equal to unity [6, 26, 38]. Thus, the changes in the oscillation amplitude of the cantilever ΔA are detected and used to re-construct the tip-sample interactions [38]. AM-AFM allows studying the nanoscopic details of interfaces. This is done by using small oscillation amplitudes (for example, $\sim$ 1-2 nm), which are comparable to the size of the features under investigation [17]. In AM-AFM, the second main observable is the phase lag. The phase can vary freely [6, 17], and is used to characterise the energy dissipation of the system, depending on its mechanical properties. Thus, phase-contrast images can provide an insightful channel to observe, for example, the organisation of nano-confined liquid molecules whose height features are comparable to the substrate defects [6].

In FM-AFM, the driving frequency ω_d is adjusted so as to match the resonance frequency of the cantilever ω_0 [52, 53], thus the phase lag is kept at 90° (see Eqs 2.20 and 2.27). This is the first main difference with AM-AFM where instead the oscillation frequency is kept constant. Furthermore, in FM-AFM, a feedback loop ensures that the oscillation

amplitude of the cantilever is kept constant, whereas in AM-AFM this can vary under the influence of the tip-sample interactions [50]. Remarkably, FM-AFM allows measuring conservative and dissipative forces in a decoupled manner. This can be done as the two contributions result in changing $\Delta\omega$ (conservative forces, represented by $F_{ts}(z_c)$ in Eq. 2.21) and ΔA (dissipative forces, mathematically given by $\gamma_{int}\frac{dz}{dt}$ in Eq. 2.21) [50, 53]. Force reconstruction from AM-AFM is more troublesome and it is still an active field of research [47, 50].

Comparing AM and FM-AFM, the former is more robust than the latter having fewer feedback loops [38, 53]. One major drawback of AM-AFM is the response time which can be modelled as $\tau = 2Q/\omega_0$ [38]. Thus, AM-AFM is not ideal when investigating systems with low dampening, typically measurements performed in air. When conducting AFM studies in liquid, there is however no marked difference between the two operating modes given that $Q \sim 1$ [5, 26, 38]. Within this thesis, we probed the organisation and dynamics of fluid lubricants whose large resonance frequency bandwidths [5] limit the reliability of FM-AFM imaging. It is true that AM-AFM does not allow an accurate characterisation of dissipative and conservative forces. Still, AM-AFM is preferred over FM-AFM as the latter appears significantly limited due to difficulties in precisely tracking the resonance frequency [38].

Visco-elastic measurements with shear spectroscopy

Before modelling the tip motion in shear spectroscopy, it is useful to review the fundamental technical aspects of the method. The technique has been pioneered in the labs of E. Riedo [54, 55], and further developed by K. Voitchovsky [20] and within this project [5, 6, 17].

Shear measurements are conducted as follows. Lateral oscillations are imposed to the sample using the AFM scanner. To ensure locality of the measurement, the imposed oscillation amplitude is kept below 1 nm (here 0.5 nm). The frequency is set at 1.1 kHz, below the resonance frequency of the scanner ($\sim$ 2 kHz) so as to avoid hardware damage. Both, the amplitude and the frequency can be changed externally; the parameters used here represent a compromise between accuracy and rapidity. As the tip approaches the sample's surface, the cantilever experiences some lateral torsion due to coupling through the confined liquid. This occurs typically in the last nanometer before contact, and increases progressively as the tip presses on the surface. Detection of the amplitude and phase of torsion are achieved using the AFM lock-in amplifier set on the lateral oscillation frequency. Given the geometry of the system, the torsional amplitude and phase represent the shear amplitude, A_S, and phase, ϕ_S, respectively. Simultaneously, the normal force exerted by the tip on the confined liquid is obtained from the average vertical cantilever deflection. A typical shear-extension curve is shown in Fig. 2.8.

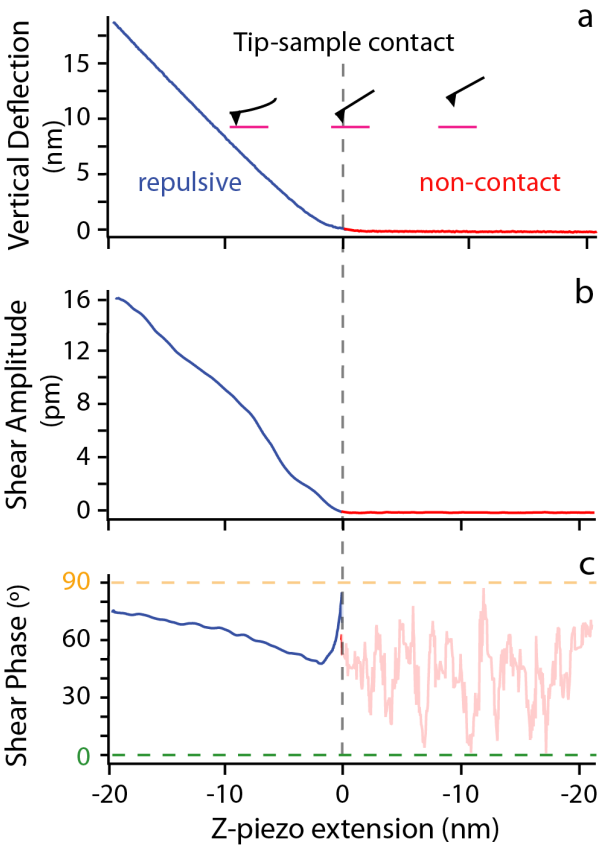

Fig. 2.8: Example of a single shear force spectroscopy measurement. The vertical cantilever deflection (**a**), the torsional amplitude (**b**) and the associate torsional phase (**c**) as measured simultaneously as functions of the vertical extension of the cantilever base (AFM Z-piezo). The shear amplitude is always taken as peak to peak. The cartoons in the top subplot illustrate the position of the tip with respect to the sample surface at different Z-piezo extensions. The dotted vertical line marks the beginning of a permanent vertical deflection (repulsive) and the Z-piezo extension is arbitrarily set to zero, marking the measured point of contact between the tip and the sample. The induced torsional (or shear) amplitude being too small before the point of contact, the phase is undefined (semi-transparent region in the bottom subplot) and randomly oscillates between the extreme values of perfectly elastic (0°) and viscous couplings (90°). The experiment was performed on hexadecane adsorbed on mica and using an Arrow UHF silicon nitride cantilevers (Nanoworld, Switzerland). The RH and temperature were 46 ± 2% and 298.0 ± 0.1 K, respectively.

Positive values of the base extension (Z-piezo) indicate the true tip-sample distance, whereas negative values describe the region where the tip does not move vertically but the applied vertical load increases. When the tip-surface is larger than a few nanometers, no liquid confinement occurs and no coupling exists between the tip and the moving solid surface. The shear amplitude is close to zero and the phase exhibits random oscillations between 0° and 90°. As the tip moves to the surface, viscoelastic coupling start to occurs through the liquid. The shear amplitude increases (here linearly) with the confining force; and the shear phase evolves from an almost perfectly viscous coupling (90°) to a viscoelastic regime as more load is applied, consistently with the reduction in configurational entropy

of the confined liquid [6, 17]. In this repulsive regime, and for small z-displacements, the cantilever follows a Hookean behaviour thus allowing extracting the force applied, F_L, by the tip during the shearing using Eq. 2.1, that is:

$$F_L = k_f \; d \tag{2.31}$$

where k_f and d are the flexural spring constant and the vertical deflection, respectively [6, 17, 20]. The same reasoning can be used for the small induced torsional (or shear) amplitude, A_S, which is related to the shear force, F_S, through:

$$F_S = k_t \; A_S \tag{2.32}$$

where k_t is the torsional spring constant.

Furthermore, we can also extract the average energy dissipated per shear cycle, E_{diss}. E_{diss} can be calculated from the viscous part of the work carried out by the tip over an oscillation cycle:

$$E_{diss} = 2 \; A_t \; F_S \; sin(\phi_S \; t) \tag{2.33}$$

It should be noted that Eq. 2.33 relies on averaged quantities since the instantaneous (oscillating) shear forces and phases are not accessible with our setup. As such, the energy dissipated over a cycle is simply modelled as the product of the viscous component of the shear force and the total distance, $2A_t$, travelled by the tip over a full shear cycle, with the model holding true for the small torsional amplitudes used here.

When focusing on the repulsive region, it is convenient to plot A_S, ϕ_S, and hence F_S and E_{diss} as functions of the vertical deflection (or applied load). This approach offers two main advantages. First it allows for an estimate of the confining pressure between the tip and the mica surface. Second, the non-contact region, when no coupling takes place, is reduced to a single point, thus focusing on the most meaningful part of the data set.

In a typical experiment, measurements were taken over at least 5 locations, with at least 20 individual sets of force curves per location. A Python code was used to sort out automatically all the acquired data curves into relevant folders. The curves were then suitably plotted, adjusted (force calculation) and averaged using a bespoke routine in Igor Pro (Wavemetrics, Lake Oswego, OR, USA). Only the extension curves (tip approaching the surface) are considered for the analysis in order to be systematically probing the interface from its equilibrium arrangement and allow for better comparability and reproducibility. Retraction curves were also acquired and usually exhibit an identical behaviour to the extension curves aside for occasional variations likely induced by tip-induced transient changes in the interfacial molecular arrangement.

The present shear force measurements contrast with standard friction force microscopy.

First, the measurements are highly localised (within a few squared nanometers) allowing probing a small number of molecules, including the lubricating properties of single ions (Chapter 4) [17] and surface nano-defects (Chapter 5) [6]. Second, a spectroscopic approach allows probing a whole range of applied loads in a same measurement at any given location and simultaneously tracking the viscoelastic response of the system [56].

In order for the AFM to operate in this mode, it is crucial to ensure that there is no delay between the reference signal driving the lateral oscillation and the actual motion. Technical limitations in the AFM set-up may, in principle, introduce an additional phase lag between the reference oscillation applied to the scanner and the measured tip torsion. Such a delay would induce a phase offset, δ, so that even when the tip is moving completely in phase with the sample (perfectly elastic motion), the measured shear phase is δ and not zero. This would prevent using the torsional phase as an accurate parameter to quantitatively study the viscoelastic properties of the fluid. The torsional phase is interpreted as the equivalent of shear phase in standard rheology measurements conducted with a linear rheometer. In order to ensure that this interpretation can be used in the present context, there is the need for a test on a system where the phase can be predicted.

Here, this test is conducted on a mica surface immersed in pure water as the control sample. Shear curves are acquired continuously while progressively increasing the Z-piezo extension and hence the applied load. The experiment is presented in Fig. 2.9, with all the curves appearing in different colours on the same graphs. Before the tip experiences any coupling with the oscillating surface (Z-piezo > 0), the shear force is close to zero and the shear phase is undefined. This is consistent with the behaviour visible in Fig. 2.8. When the tip reaches the surface (Z-piezo extension close to zero), the tip starts experiencing some coupling (dotted vertical line); the shear force increases and the shear phase is $\sim 90°$ within error. This is in agreement with the hypothesised perfectly viscous behaviour of water for such a soft nano-confinement [17, 57]. As the Z-piezo extends (negative values), the applied load increases and the shear phase decreases, indicating an increase of the confined liquid's elastic component. At loads > 100 nN, the tip is pinned into the mica surface. The shear force reaches a maximum and the shear phase goes to zero. This is expected for a perfectly elastic behaviour [6, 17, 20, 54, 55], here artificially created by pinning the tip into the sample. Given the high loads (~ 350 nN) applied to the tip, significant damage was done to both the tip and the sample. This type of measurement was hence conducted only once as a control.

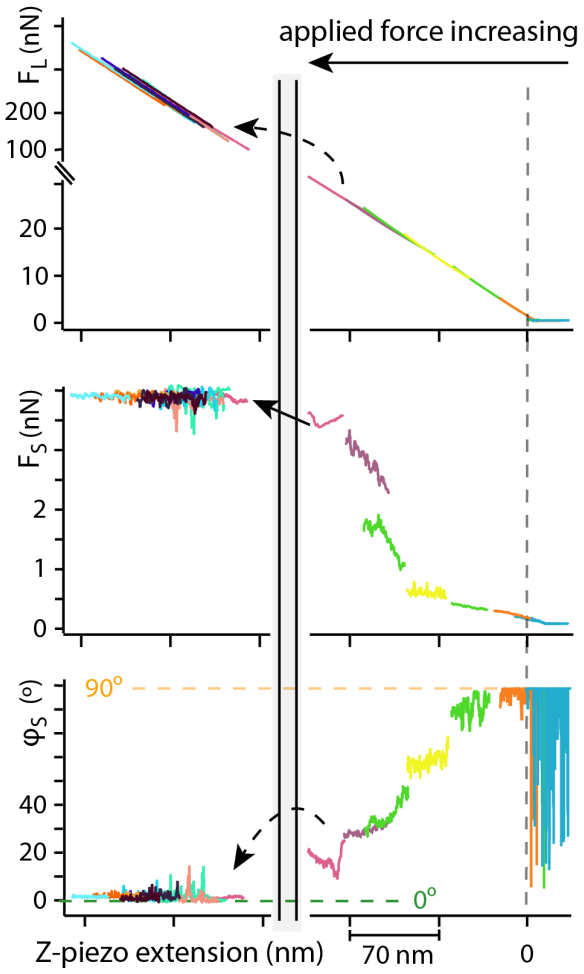

Fig. 2.9: Shear measurement with increasing confining forces in pure water at the interface with mica. The applied force, F_L, the shear force, F_S, and the shear phase, ϕ_S, were acquired simultaneously for each spectroscopic curves (all different colours). Multiple curves are acquired as the Z-piezo is progressively extended to increase the applied load. In proximity of the point of contact (vertical dotted line), $F_S > 0$ and $\phi_S \sim 90°$. As F_L increases, the shear force eventually reaches a plateau due to the tip pinned into the mica (left region of the graphs). The transition to the plateau coincides with the shear phase converging to zero within error. This confirms the validity of the data interpretation and the reliability of the shear phase to characterise the viscoelasticity of the system. The RH and temperature were 46 ± 2% and 298.0 ± 0.1 K, respectively.

2.2.4 AFM probe-sample interactions

In vacuum, the AFM tip probes mainly F_{ts} due to the interactions with the solid substrate: van der Waals interactions, short range repulsive interactions, electrostatic interactions, and adhesive and capillary forces. Within this thesis, the investigations aimed at charactering the behaviour of solid-liquid interfaces. Thus, F_{ts} were typically due to interactions between the liquid molecules and the confining surfaces. The interactions between model lubricants and solid surfaces at equilibrium were characterised using AFM high-resolution imaging. The dynamic behaviour of fluid molecules at the interface was

studied using shear spectroscopy. As shown in Fig. 2.10, when nano-confined between an AFM tip and a solid substrate, liquid molecules typically restructure at the interface due to multiple types of F_{ts}.

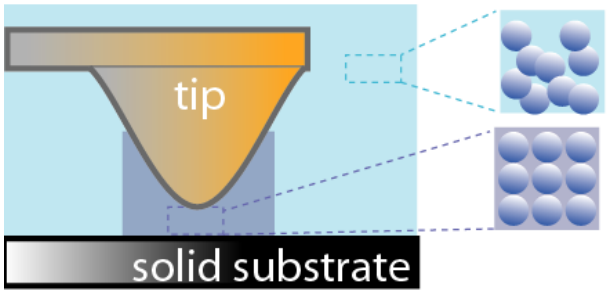

Fig. 2.10: Schematics of the typical solid-liquid interface explored in this thesis. Because of the interactions with the confining solid substrate and AFM tip, liquid molecules tend to restructure. Likewise, the interactions experienced by the AFM tip tend to be dominated by the fluid re-structuring (solvation forces).

This adds some layers of complexity when accurately characterising F_{ts} and distinguishing among all the different contributions. Conducting AFM experiments in liquid has however the advantage of reducing capillary forces due to condensation of contaminants and water vapour. This is highly desiderable as the formation of a meniscus may be markedly detrimental to the imaging lateral resolution [58, 59]. Hereafter, I will review the nature and characteristics of the main F_{ts} at the solid-liquid interface.

van der Waals interactions

van der Waals (vdW) interactions arise between electric dipoles. The dipoles can be either permanent or induced by thermal and quantum fluctuations [60, 61]. vdW interactions are in general some of the weakest forces within the spectrum of F_{ts} involved in our experiments. In general, vdW magnitude is within $\sim$ 0.5-5 k_BT, thus significantly smaller than electrostatic interactions whose strength can achieve even a few hundreds of k_BT for ionic and covalent bonds [56]. In the absence of any strong electrostatic forces, vdW interactions however may dominate the system, for example in the case of nano-confined alkanes [6]. These forces will be hence relevant in the work presented in Chapters 5 and 6. vdW interactions are usually short ranged scaling as r^{-6} where r is the distance between two atoms or molecules. The total interactions between the AFM tip and the sample result from adding all dipole-dipole forces. This can be done integrating over a volume of fixed density. Thus, for a spherical tip of radius R, vdW potential scales as [62]:

$$U_{vdW} = -\frac{HR}{6r} \tag{2.34}$$

where H is the Hamaker constant accounting for the polarizability of the materials. In liquid, U_{vdW} can be attractive or repulsive depending on the value of H.
The vdW model can furthermore provide insightful information on the weak interactions between a solid and a liquid separated by another liquid. This will become particularly relevant in Chapter 6 when discussing how the absorption of water nanodroplets from ambient humidity may influence the interactions of a model lubricant with the solid surface. For two media 1 and 2, separated by a distance L through a third medium 3, the potential is described by [63]:

$$U_{vdW} = -\frac{H_{132}}{12\pi L^2} \tag{2.35}$$

with H_{132} being:

$$H_{132} = \frac{3k_BT}{4}\frac{\epsilon_1-\epsilon_3}{\epsilon_1+\epsilon_3}\frac{\epsilon_2-\epsilon_3}{\epsilon_2+\epsilon_3} + \frac{3h\nu_\epsilon}{8\sqrt{2}}\frac{\left(n_1^2-n_3^2\right)\left(n_2^2-n_3^2\right)}{\sqrt{n_1^2+n_3^2}\,\sqrt{n_2^2+n_3^2}\left(\sqrt{n_1^2+n_3^2}\,\sqrt{n_2^2+n_3^2}\right)} \tag{2.36}$$

where k_B, T, h, ν_ϵ, ϵ_i and n_i are the Boltzmann constant, the temperature, the Planck constant, the electronic absorption frequency, the dielectric constant and the refractive index, respectively [63, 64].

Electrical double layer forces

These forces play a fundamental role when a charged solid surface is in contact with a fluid containing ions. This is the scenario of Chapter 4 when studying the behaviour of ionic aqueous solutions adsorbed on a negatively charged mica surface. The density distribution of the ions in close proximity of the charged surface deviates from that in the bulk. The fluid counterions tend to accumulate in proximity of the charged surface and form an electrical double layer (EDL): the first layer corresponds to the charged surface and the second to the neutralizing counterions. This process is aimed at maintaining electric neutrality and, hence, minimizing the energy of the system. According to the most widely used model, that is the Gouy-Chapman-Stern model (GCS), immediately after the charged surface, there is a dense monolayer of solvated ions, tightly adsorbed onto the surface. The electric double layer can be modelled as a capacitor. As shown in Fig. 2.11, in close proximity to the charged surface (Stern or Helmoltz layer), the capacitor potential, ψ, linearly decreases with the distance from the surface, x [10, 56, 61]. Given the fact that the ions have a finite size, they cannot approach the surface any closer than their radius. Thus, it is useful to define an outer Helmholtz plane (OHP) considering the distance of the center of the ions from the surface. The Stern layer is followed by a diffuse layer, described using Maxwell−Boltzmann statistics. In the diffuse layer, the charge distribution decays exponentially from the solid surface [10, 56, 61]. Notably, the Stern layer has been the focus of the experiments of this thesis with the AFM tip nano-confining the ionic aqueous

solutions within a few nanometers from the charged mica.

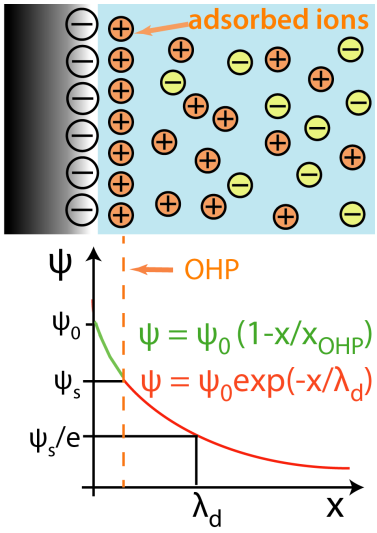

Fig. 2.11: Schematic representation of how a charged surface induces a re-organisation of the ionic species in a liquid solvent. The negative charges on the solid surface are counter-balanced by positive ions whose finite size determines the outer Helmholtz plane (OHP). The electrostatic potentials, ψ, in the Stern and diffuse layer are highlighted in green and red, respectively. In the diffuse layer, ψ depends exponentially on the Debye screening length, λ_d, corresponding to the thickness of the diffuse double layer.

Generally, both the AFM probe and the sample have a surface charge density, σ_t and σ_s, respectively. This gives rise to a double layer force, F_{dl}, between the tip of radius R and sample which can be modelled as [10, 65]:

$$F_{dl} = \frac{2\pi R}{\epsilon_0 \epsilon_s} \lambda_d \left[\left(\sigma_t^2 + \sigma_s^2 e^{-d/\lambda_d} \right) + 2\sigma_t^2 + \sigma_s^2 e^{-d/\lambda_d} \right] \tag{2.37}$$

Equation 2.37 shows F_{dl} between two bodies may be attractive or repulsive depending on the sign of the bodies' surface charges. Combining the repulsive contribution from F_{dl} and the attractive one from vdW interactions leads to the Derjaguin-Landau-Verwey-Overbeek (DLVO) theory [10]. The model accurately describes the behaviour of two approaching surfaces provided their distance is larger than a few nanometers. Below this length scale, the assumptions, on which the DLVO model relies, break down. This is because the DLVO theory considers only the electrostatic interactions between the surface and the counter-ions as the main forces within the Stern layer. The model ignores thermal motion, ion diffusion, adsorption onto the surface and other solvent/surface interactions due to enthalpy [56]. Thus, the theory cannot accurately describe the results of the experiments presented in this thesis, characterised by an AFM-solid surface gap of a few nanometers. In order to capture the nature of the main interactions behind the experiments of this thesis, non-DVLO forces should be introduced.

Solvation forces

The most important solid-liquid interactions for this thesis are solvation forces. This type of forces are due to the solvent interactions with the solid surfaces and have a predominant effect for separations below a few nanometers [56, 66, 67]. Solvation forces depend on the specific physical and chemical properties of the liquid, as well as on on the characteristics of the confining solids, i.e. if the surfaces are hydrophobic or hydrophilic [17, 42, 68], smooth or rough [6, 69], crystalline or amorphous [17]. These factors affect the reorientation or restructuring of fluid molecules as shown in Fig. 2.10. This leads to local density variations with fluid molecules organised in quasi-discrete layers [17, 56, 66, 67]. Solvation forces tend to very rapidly increase with nano-confinement. As the separation between the solid surfaces decreases, the configurational entropy of liquid molecules decreases leading to strongly cohesive solid-like layers [6, 10, 17, 70]. The rapid increase in solvation forces is often modelled as an exponential function of the surface separation [10, 56]. Thus, as the liquid molecules are squeezed out, the changes of the molecular ordering and density give rise to an oscillatory solvation force, F_{sol} [10, 56]:

$$F_{sol} = f_0 \; cos\frac{2\pi}{D} \; e^{-D/D_m} \tag{2.38}$$

where f_0 is a prefactor that takes into account the contact energy between the two surfaces; D is the spacing between the two identical confining surfaces and D_m is the liquid molecular diameter. The complexity of factors influencing solid-liquid interactions however results in limiting the generality of the model represented by Eq. 2.38. For example, solvation forces have been reported to be characterised by a monotonic behaviour as the surfaces separation decreases [71]. In other words, solvation forces provide a general framework describing the liquid molecular rearrangement due to the action of the AFM tip approaching the substrate surface. These forces can be attractive or repulsive depending on the characteristics of both the liquid and the solids. If the tip squeezes out fluid molecules with a strong affinity for both the confining surfaces (for example water confined between two hydrophilic surfaces as described in Chapter 4), solvation forces will be on average repulsive, giving rise to the so-called hydration repulsive behaviour [59]. On the other hand, liquid molecules are spontaneously repelled from nano-gaps between surfaces with a low affinity for the fluid itself (i.e. water confined between two hydrophobic surfaces). Associated to this spontaneous removal of the fluid, there is an attractive force between the solid surfaces [10, 56].

Steric repulsion

As the tip-substrate distance reduces, the probe will experience short-range repulsive forces strong enough to prevent any further approach towards the surface. In vacuum, such

repulsive F_{ts} are explained in light of the Pauli exclusion principle, with the atoms of the tip not being able to penetrate the substrate due to an overlap of the electron clouds (Pauli exclusion principle) [56]. At the solid-liquid interaces, a number of additional interactions may prevent the probe from reaching the surface, for example steric repulsion due liquid layers strongly bound to the surface [59]. The AFM probe may experience Pauli repulsion forces in the case where all fluid molecules are removed from between the two solid surfaces. Within this thesis, it is only possible to deduce that the tip experiences permanent repulsion from the deflection of the cantilever. In this case, the tip is assumed to be in contact with the "sample" (see for example Fig. 2.8a). Here, the term "sample" is used with a general meaning also including any liquid layers strongly adsorbed to the bottom solid surface. Further pressing on the "sample" may result in deforming and indenting the "sample" itself. The deformation can be in principle described by contact mechanics models, such as the Derjaguin-Muller-Toporov model [60]. In case of liquid molecules organised in solid-like layers, this approach would however require the confined fluid to have such a high viscosity that the resulting long relaxation timescale would lead to an almost perfectly elastic behaviour.

2.3 Equipment and protocols used within this project

The AFM measurements were performed using a commercial Cypher ES AFM system (Oxford Instruments, Santa Barbara, CA, USA), equipped with temperature control. The AFM measurements are highly sensitive to any contamination which manifests itself in the form of anomalous results and inconsistent data [16]. In order to avoid any contamination of either the sample or the cantilever/tip, all aqueous and organic solutions were prepared using borosilicate glass beakers, cylinders and bottles. The glass material was purchased from Pyrex, Corning, NY, USA. A careful cleaning procedure for each glass container was performed in order to remove any polar and nonpolar contaminant. Four washing steps were carried out sequentially: (i) tap water and soap, followed by rinse with tap water 20 times, (ii) ultra-pure water (18.2 $M\Omega$, Merck Millipore, Billerica, MA, USA), (iii) $> 98\%$ pure propan-2-ol (Merck Millipore, Billerica, MA, USA), and (iv) ultra-pure water again. The glass containers were then extensively flushed with nitrogen in order to remove remaining water. The propan-2-ol was used as purchased, without further purification [17]. The cantilevers were immersed in a bath of ultrapure water, followed by propan-2-ol, and finally ultrapure water, for 60 minutes at each step [17]. A nitrogen flux was used to dry the cantilevers. The AFM stage was cleaned firstly with ultra-pure water, then pure propan-2-ol (Merck Millipore, Billerica, MA, USA), and finally with ultra-pure water again. The

stage was heated to $\sim$ 393 K for 30 minutes before each experiment to evaporate residual water and possible contaminants from previous experiments [6, 17].

2.3.1 Sample preparation

Substrates. High-quality V1 muscovite mica and highly orientated pyrolytic graphite (HOPG) were purchased from SPI Supplies (West Chester, PA, USA) and Ted Pella Inc (Redding, CA, USA), respectively. Mica discs (12 mm diameter) and HOPG substrates were attached to a steel plate using epoxy glue (Araldite, Basel, Switzerland). Overnight curing at 335 K was carefully performed in order to obtain a good thermal contact between the mica disc and the steel plate in temperature controlled experiments. Mica and HOPG substrates were freshly cleaved with adhesive tape before each experiment. After cleaving, mica was rinsed copiously with ultra-pure water (Water AnalaR NORMAPUR, VWR International Ltd, Leicestershire, UK) when studying aqueous solutions. This was done so as to remove the K^+ ions initially occupying half of the ditrigonal cavities of mica. The rationale and details of the rinsing procedure are further described within Chapter 4 [17].
Aqueous and organic solutions. Aqueous solutions were prepared in ultrapure water with 99.9% pure salts purchased from Sigma- Aldrich and used without any further purification (St. Louis, MO, USA). Solutions with controlled pH were prepared by adding a diluted solution of fuming 37% hydrochloric acid (HCl, Merck Millipore, Billerica, MA, USA) to the desired ionic solution while stirring with a magnetic stirrer and tracking the solution's acidity with a pH meter (Mettler Toledo Columbus, OH, USA). No buffering agent was used to avoid interfering with the measurements [72]. In the absence of buffering agent, the pH is susceptible to change rapidly in response to changes in the solution's environment and the care was taken to conduct the experiments immediately after the pH adjustment and at controlled temperature. Testing of the pH was also conducted immediately after conducting experiments so as to ensure stability [17].
Organic liquids (squalane, hexadecane, and oleic acid) with a purity $\geq$ 99% were purchased from Sigma-Aldrich (St. Louis, MO, USA) and used without any further purification. They were stored in borosilicate glass beakers cleaned as previously described [6].

2.4 Scanning electron microscopy

Within this thesis, SEM has been used to confirm the stability of the tip apex. Variations in the AFM tip geometry due to wear may indeed affect the reliability and accuracy of imagining and spectroscopy data [73, 74]. Hence, it is fundamental to verify the conditions of the scanning probes before and after imaging/shear spectroscopy. SEM of the cantilevers has been suggested as a solid tool so as to ensure that AFM measurements are not affected

by any changes in the tip geometry [5, 6, 17, 73].

SEM is based on using a beam of electrons as a detection tool. The electrons are thermoionically fired by an electron gun, focused through a series of electromagnetic lenses and impinge on the specimen surface interacting with its atomic structure. The electrons lose their energy as they are randomly scattered and absorbed by the sample. The volume over which the energy loss takes place is the interaction volume measuring the diffusion of the primary electron beam into the sample. The size and depth of this volume depend on the beam energy, and the sample characteristics (density; mass and atomic number of the constituent molecules) [75].

The interactions of the primary electrons with the specimen atoms result in emitting radiation: secondary electrons, back-scattered electrons, Auger electrons, transmitted electrons and other contributions such as visible light and X-rays. Even if these components are simultaneously produced, they are independently detected: the secondary and back-scattered electrons represent the standard signals to reconstruct surface topography and chemical composition, respectively [76–78].

Samples are usually prepared so as to increase or stabilise their electrical conductivity. This is particularly important for non-conductive samples which are coated with electrically conducting material so as to prevent the accumulation of electric charges and hence the formation of image artefacts. Samples are typically observed in vacuum, as the atmospheric gas would significantly attenuate the electron beam. Environmental SEM (ESEM) however allows investigating wet samples (for example biological speciments, or oil-bearing minerals) at low pressure (a few torr) and high humidity (up to 100%). ESEM divides the column into differential pressure zones so as to separate the gun from the sample chamber [79].

Within the thesis, SEM has been used so as to conduct topographical imaging of AFM probes. For each experimental investigation, five cantilevers were randomly selected and imaged, either before or after conducting the AFM experiments (including imaging and shear force spectroscopy). The SEM analysis was performed with a commercial FEI Helios SEM system (Dawson Creek Drive Hillsboro, Oregon 97124 USA). Images were collected using a 3 kV electron beam in vacuum and the current set to 0.17 nA. The low voltage markedly decreases the electron range and the interaction volume enhancing surface sensitivity and decreasing sample charging. This allows high-spatial resolution and distinguishing features of a few nanometers [75]. The current used here results in a small probe diameter while still maintaining a good signal to noise ratio [80–83].

2.5 Molecular dynamics simulations

In this thesis, MD simulations have been used in Chapter 5 examining the behaviour of a model lubricant (squalane) at an atomistic defect, that is, a step edge on HOPG. This allowed investigating a region of a few nanometers, which is difficult to experimentally characterise with an AFM probe, as well as ruling out any AFM tip convolution effects on the results.

Molecular simulations started in the 1950s and have since then grown exponentially providing an insight into the interacting forces among individual molecules or atoms [84, 85]. Simulations can be divided into stochastic and deterministic. The former methods (e.g. Monte Carlo) are based on simulating one molecule per time by a trial displacement. The resulting position is accepted only if in agreement with the potential energy of the system [84, 86]. Deterministic approaches, such as MD simulations, determine the trajectories of the molecules solving numerically Newtonian or Langevin differential coupled equations of motion over a series of time steps and using a suitable interparticle interaction potential [84, 85]. Stochastic methods are ideal for gas and low density systems where large potential barriers can lead to molecules in a MD simulation being trapped into a few low energy configurations, thus leading to poor configurational sampling. Deterministic methods are preferred for tribological studies as they allow calculating time-dependent thermodynamic properties of the system, such as viscosity and transport coefficient [59]. Furthermore, MD simulations can study hundreds of thousands of atoms within a time frame of microseconds. This is a key advantage as it allows addressing one of the hottest questions in tribology: the behaviour of lubricant molecules at nano-confinement [6, 59]. Here, MD simulations present further advantages given their complementarity to AFM studies. Recent AFM developments have led to atomic level resolution [6, 87] thus allowing a direct comparison with MD results. In addition, MD simulations can rule out any AFM probe convolution effects affecting the reliability of AFM observations [6, 88]. Still, the time and spatial scales MD simulations can explore are significantly smaller in comparison with experimental systems. The choice of appropriate intermolecular forces further limits the accuracy of MD simulations [88]. *Ab initio* MD simulations are able to characterise also intramolecular forces [89]. The advantages of this method providing an insight into the quantum mechanics of the molecules are however counterbalanced by high computational costs, limiting their use to small systems of a few hundreds of atoms over a short time scale [85] (see also Chapter 1 Section 1.4). Thus, *Ab initio* MD simulations are not used here. The details of the force field used to simulate the intermolecular interactions are discussed in the next section.

2.5.1 Geometrical parameters

The geometry of MD simulations is usually based on a box with periodic boundary conditions (PBC). Such a system is based on periodically replicating the simulation cell so as to prevent the system from having any abrupt borders with vacuum [90]. PBC furthermore allows approximating an infinitely large system as molecules passing through one of the box sides reappear on the opposite side. This saves computational time and leads to results closer to experimental conditions [88, 91]. Particular attention should be anyway paid to the molecules not interacting with their images in an adjacent box. Artefacts due to non-physical interactions are prevented using the minimum image convention, that is, ensuring that the simulation box size is at least twice in comparison with the minimum distance for any interacting potentials to take place [88]. Fig. 2.12 shows an example of a PBC simulation where squalane molecules are deposited on a 4 layers graphite surface. The HOPG substrate is modelled as an electrically neutral system [6, 87]. A net dipole moment of the HOPG substrate has been reported in the literature, potentially resulting in long-range electrostatic interactions [92]. Thus, further work should take in account these effects so as to study a system as realistic as possible.

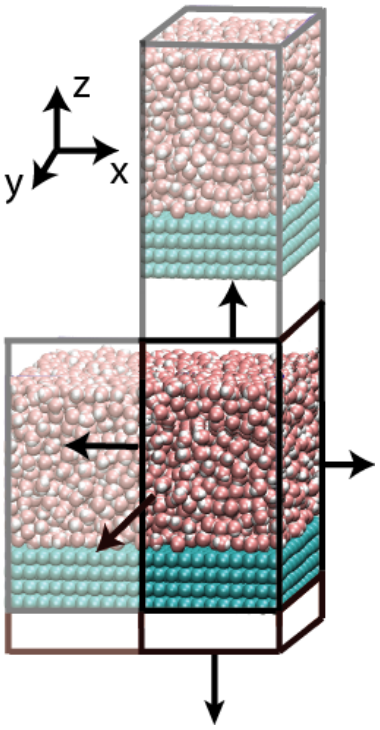

Fig. 2.12: An example of a simulation with periodic boundary condition. Vacuum regions prevent any artefacts due to the liquid molecules, confined between two adjacent boxes, interacting with each other. The periodic conditions are applied on the x, y and z planes.

2.5.2 The equations of motion

MD simulations study the time evolution of a system with N interacting bodies, by solving Newton's equations of motion for each molecule:

$$\mathbf{F}_i = m_i \mathbf{a}_i, \ i = 1...N \tag{2.39}$$

where $\mathbf{F}_i$ is the force exerted on the i^{th} molecule; and m_i and $\mathbf{a}_i$ are its mass and acceleration, respectively. $\mathbf{F}_i$ can be calculated as the infinitesimal change of potential energy function, U, with respect to the position:

$$\mathbf{F}_i = \frac{\partial U_i}{\partial \mathbf{r}_i} \tag{2.40}$$

Equations 2.39 and 2.40 are usually solved using the Verlet leapfrog method [84, 85, 93]. Within this framework, the position $\mathbf{r}$ and velocity $\mathbf{v}$ are updated every time step Δt:

$$\mathbf{v}_i(t_i + \frac{1}{2}\Delta t) = \mathbf{v}_i(t_i - \frac{1}{2}\Delta t) + \frac{\Delta t}{m_i}\mathbf{F}_i \tag{2.41}$$

$$\mathbf{r}_i(t_i + \Delta t) = \mathbf{r}_i(t_i) + \mathbf{v}_i(t_i + \frac{1}{2}\Delta t) \tag{2.42}$$

It is important to choose a short time step so as to realistically capture the atomic interactions [88]. Bond-vibrations in hydrogen atoms represent a lower limit for the time step which needs to be at least ≈ 1 fs. Here, the bonds were constrained so as to allow a time step of 2 fs. The constraints were applied using the Linear Constraint Solver algorithm [94]. The calculations were performed using the simulation package GROMACS version 2016 [95, 96] whose key aspects are covered in the following subsections. A full description can be found in the package manual [96].

2.5.3 Atomic interaction potential

The potential energy function U used to calculate $\mathbf{F}_i$ in Eq. 2.40 involves the contributions from bonded and nonbonded interactions:

$$U(r) = U_{bonded} + U_{unbonded} \tag{2.43}$$

U_{bonded} includes 2-, 3- and 4- body interactions of covalently bonded atoms:

- U_{bonds}, the spring body potential, representing the covalent bond-stretching between 2 bodies.

- U_{angles}, the bending angle potential, accounting for the angular vibrational motion occurring between a triple of covalently bonded bodies.

- $U_{dihedral}$, the 4-body torsion (or dihedral angle) potential. This term describes the energy associated to 4 consecutive bonded molecules (proper dihedral angle) or to torsions of 3 bodies centered around a forth one (improper dihedral angle). An example of improper dihedral potential is the energy cost due to preventing planar aromatic rings from switching to the opposite chirality configuration [88].

U_{bonds}, U_{angles} and improper $U_{dihedral}$ are modelled as harmonic potential, whereas a sinusoidal function is used for proper $U_{dihedral}$.
$U_{unbonded}$ involves electrostatic interactions, weak dipole attractions and hard-core repulsions between all the pairs of molecules excluding those involved in a bonded term. $U_{unbonded}$ is given by [88]:

$$U_{unbonded}(r) = U_{Coulomb} + U_{Lennard-Jones} \tag{2.44}$$

Here, the electrostatic potential energy between each pair of molecules, i and j, is described by Coulomb's law [88, 97]:

$$U_{Coulomb} = \sum_{i,j} \frac{1}{4\pi} \frac{q_i q_j}{\epsilon_0 r_{ij}} \tag{2.45}$$

where q_i and q_j are the charges of molecules i and j; $r_{i,j}$ is the charge separation; and ϵ_0 is the free space dielectric constant. $U_{Coulomb}$ is modelled using the particle mesh Ewald (PME) approach so as to overcome issues due to evaluating the long-range electrostatic forces [98, 99]. The PME method sets a threshold: below the cut-off, electrostatic interactions are calculated according to Eq. 2.45; above this value, electrostatic potential is given by a summation in Fourier space [98, 99].
Weak dipole attractions (London forces) and hard core repulsions due to Pauli exclusion principle are described by the Lennard-Jones model:

$$U_{Lennard-Jones} = 4\epsilon \left[\left(\frac{\sigma}{z}\right)^{12} - \left(\frac{\sigma}{z}\right)^{6} \right], \tag{2.46}$$

where ϵ, σ and z are the depth of the potential well, the effective molecular tip diameter and the interatomic tip-sample distance, respectively.
The choice of suitable force fields between atoms or molecules is one of the most crucial aspects in MD simulations so as to ensure reliable results [100]. Here, we use the Optimised Potentials for Liquid Simulations-All atom (OPLS-AA) force field [101, 102]. OPLS-AA force field offers an accurate representation of organic molecules [101, 102] and in particular of alkanes [103, 104], which were our main object under investigation through MD simulations (see Chapter 5). OPLS-AA was also used so as to describe the graphite

layers on which squalane, our model alkane, was deposited [87, 92, 105, 106].

2.5.4 Pressure and temperature

The key parameters defining the ensemble are the number of molecules, N, the pressure, P, and the temperature, T. These parameters are assumed to be constant over time [107]. The boundary conditions of an NPT ensemble are achieved using a barostat and thermostat scheme. The former allows the volume to vary freely so as to maintain P constant [108]. The latter controls the velocities of the molecules in order to achieve the desired temperature [109].

Barostat

The two most common barostat schemes are the Berendsen [88, 110] and Parrinello-Rahman [111, 112]. In the Berendsen method, the pressure is defined by [88, 110]:

$$P = \frac{2}{3V}\left(E_{kin} - \Theta\right) \tag{2.47}$$

where E_{kin} and Θ are the kinetic and the internal virial energy for pair-additive potentials, respectively [110]. Given the relationship between P and V in Eq. 2.47, a scaling factor, μ_P, allows proportional scaling of the box dimensions so as to achieve the desired P_0 [88, 110]:

$$\mu_P = 1 + \frac{\Delta t}{\tau_p}\beta\left[P(t) - P_0(t)\right]^{1/3} \tag{2.48}$$

where β and τ_p are the isothermal compressibility of the system and the pressure coupling constant, respectively. The Berendsen algorithm is computationally efficient, but leads to inaccurate results as it drastically suppresses pressure fluctuations [113]. Thus, it is usually applied to equilibrate the simulation box, but other barostat schemes should be preferred for the production runs [88]. Here, production runs are based on the Parrinello-Rahman barostat. This scheme describes the simulation box as a matrix and accordingly modifies the equations of motion [88, 112].

Thermostat

In order to ensure the ensemble to maintain the desired temperature, T_0, we used two thermostats schemes: the Berendsen method for equilibrating the simulation box [114], and the Nosé - Hoover for the production runs [115]. Both the two methods are based on controlling T using the velocities of the molecules. This can be done as the two variables

are related according to the equipartion theorem as follows [88, 116]:

$$\sum_i \frac{1}{2} m_i \left\langle \mathbf{v}_i^2 \right\rangle = \frac{3}{2} N k_B T \tag{2.49}$$

Every n_{TC} time steps, the Berendsen method scales all the velocities of the molecules by a same amount through a time-independent factor. The scheme is computationally efficient ensuring the ensemble to rapidly achieve the desired temperature [88, 114, 116]. Kinetic energies fluctuations are however suppressed. The lack of a Maxwell-Boltzman distribution for velocities leads to an incorrect ensemble [88, 114, 116]. We took advantage of the efficient and fast Berendsen scheme when initially equilibrating the simulation box. The Nosé - Hoover method was then applied when recoding the data [117, 118]. The latter scheme modifies the equations of motion introducing a thermal reservoir and a thermodynamic friction term, ζ:

$$\frac{d^2 \mathbf{r}_i}{dt^2} = \frac{\mathbf{F}_i}{m_i} - \mathbf{v}_i \zeta \tag{2.50}$$

ζ evolves in time according to the mass parameter of the reservoir so as to accommodate changes in the reference temperature [118].

2.5.5 *Protocols and analysis of MD simulations*

Hereafter, I will review the main aspects relative to the methodology, including validity benchmarks and observables. The physics behind the results will be discussed in Chapter 5. The simulation box size was (34.1 nm × 7.2 nm × 11.8 nm) unless otherwise specified, with ∼ 3000 squalane molecules and 8 layers of graphite. Surface defects, here atomic step edges, were simulated with additional 4 layers of graphite whose y-dimension size was three times smaller than the bottom layers. The 4 layers simulating the step-edge include only carbon atoms. The simplification is also based on the fact that there is no unanimous consensus on the chemistry of the step edge terminal groups [6, 87, 119, 120].

The reliability of the results was assessed considering the density of squalane in bulk, that is, without any confinement in the HOPG box. In this case, the squalane molecules were found to have a density of 803 kg/m^3 at 298 K (see Fig. 2.13), in agreement with the experimental value of 804 kg/m^3 [121].

The NpT ensemble was maintained at 298.0 K and 100 kPa using a velocity-rescale thermostat [116] and Parrinello-Rahman barostat [111, 112] with coupling times of 0.5 and 5 ps, respectively. The pressure coupling was semi-isotropic with the box free to fluctuate only along the z direction. During the simulations, the HOPG atoms were not allowed to move. All simulations were performed with a 0.002 ps time step. Before use, the squalane box was equilibrated for 20 ns. After combining with the stepped HOPG, the

system was equillibrated for 17 ns before collecting the data over a further 12 ns. Gromacs built-in functions and Python home-made algorithms have been used so as to analyse the trajectories of the molecules, spatial distribution and their thermodynamic parameters [95]. Visual Molecular Dynamics complemented the data analysis allowing visual inspection of the time evolution of the molecular ensemble (see for example Fig. 2.12) [122]. Three main quantitative parameters were extracted from the simulations.

- The density, ρ, of the squalane molecules as a function of lateral and vertical confinement. Representative results are shown in Fig. 2.13.

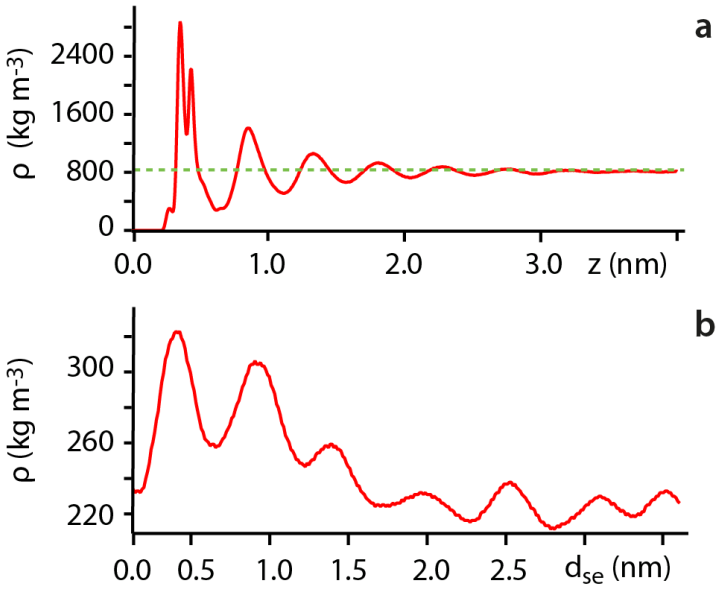

Fig. 2.13: Average density profiles of squalane as functions of z-distance from the substrate (**a**) and from the step edge, d_{se}, (**b**) showing molecular layering. In the vertical profile (**a**), a characteristic oscillatory profile can be observed, progressively vanishing over ~ 3 nm past which the confined fluid ρ is the same as in the bulk (804 kg/m^3, green dotted line). The split peak in the first layer is an artefact due to sampling. Along the surface (**b**), interfacial effects lead to an oscillatory profile near the step but ρ is noisy due to the limited number of molecules (~ 3) being probed at each distance from the step.

ρ was used as a benchmark for the validity of the simulations. This observable furthermore allowed studying the layering of squalanes at nano-confinement as typically expected due to the constrained geometry under nanoconfinement.

- The diffusion constant, D, corresponding to the mobility of the molecules. Similarly to ρ, also this observable is expected to be influenced by local re-ordering. Thus, the variable may work as an indirect benchwark for the validity of MD simulations. D was calculated using the Einstein relation by least squares fitting of the mean square displacement of the squalane molecules [123]. D was averaged over a 1.2 nm thick band above the HOPG surface.

Different box sizes were tested so as to verify the generality of the findings. Fig. 2.14 shows representative results.

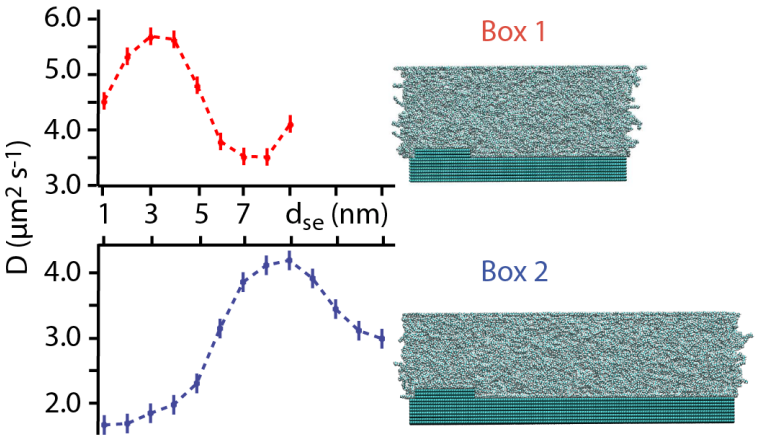

Fig. 2.14: Effects of box sizes on the diffusion constant, D. Box 1 and box 2 size are (24.1 × 7.2 × 12.9) nm and (34.1 × 7.2 × 11.8) nm, respectively. The confinement along the z-direction has a clear impact on D, but does not affect the trend of greater molecular mobility as the distance d_{se} from the step edge increases.

Because of the large size of the squalane molecules compared with the size of the simulation box, the relatively small size of the box induces an overall reduction in the diffusion constant. This does not affect, however, the observed trend of increased molecular mobility away from the step edge, which appears in all the simulations. As shown in Fig. 2.14, smaller nano-gaps result in reducing D. The squalane molecules within Box 1 (red) reach a value for D of about 5.5 μm^2/s. Reducing by about 1 nm the size of the box along the z-direction significantly reduces D (see Box 2 and the corresponding diffusion constant values in blue). The degree of vertical nano-confinement does not affect, however, the trend of increased molecular mobility away from the step edge. As discussed in detail in Chapter 5, this confirms the role of surface defects on limiting the configurational entropy of lubricant molecules. When d_{se} is greater than 4 nm and 9 nm for Box 1 and 2, respectively, D shows an apparent decrease. This is due to the periodicity of the MD simulations along the x and y directions. In other words, molecules at the right edge of the two boxes in Fig. 2.14 are undergoing confinement effects due to another step edge.

- As discussed in the previous Section 2.2.4, fluid molecules tend to restructure at nanoconfinement. Thus, MD simulations are expected to show some re-ordering of squalane particularly in close proximity of the surface defects due to a reduction in the configurational entropy of the liquid molecules. The average orientation of squalane molecules was quantified using an orientation order parameter, S_y, as a

function of the distance from the step [95]:

$$S_y = \frac{3}{2}\langle cos^2\ \theta_y\rangle - \frac{1}{2} \tag{2.51}$$

where θ_y is the angle formed by the y-axis of the step edge (lateral orientation of the step in the plane of the surface) and the molecular axis of squalane. Defined in this way, the order parameter can vary between $S_y = 1$ and $S_y = -1/2$ for an arrangement of the squalane molecule parallel and perpendicular to the step edge, respectively. A value of $S_y = 0$ indicates no preferential order [95]. Here, S_y is calculated from the squalane molecules whose center of mass lies within 1.2 nm of the surface ($\sim$ 3 molecular layers). As visible in Fig. 2.15, S_y progressively decreases from positive values at the step edge to almost zero past distances $d_{se} > 6$ nm. This shows that the squalane molecules undergo a rearrangement as expected for nano-confined fluids. The molecules are preferentially oriented parallel to the step edge when in close proximity, with this preferential order progressively being lost away from the step where no molecular orientation is preferred.

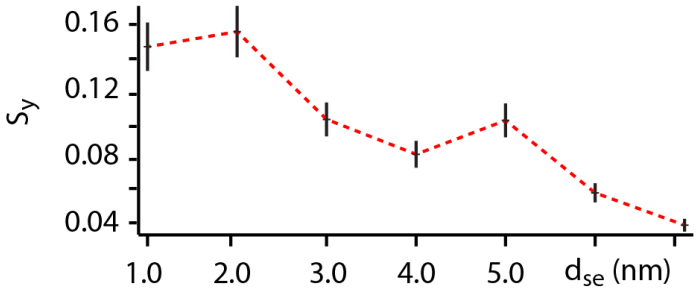

Fig. 2.15: Average orientation of squalane molecules as a function of distance from the step edge, d_{se}. In close proximity to the step edge, squalane molecules are preferentially oriented parallel to the step axis ($S_y > 0$), favouring the orientation of the row-like domains observed by AFM. As the distance from the step edge increases, the molecules become randomly oriented ($S_y \sim 0$).

Notably, even at the step edge, the order parameter tends to be small (< 0.2). This is because a value of 1 would indicate the squalane molecules perfectly extended and exactly aligned along the step. In practice, this almost never occurs due to the fact that the squalane molecules are not rigid rods. Squalane molecules can bend and accommodate multiple curvatures, especially at room temperature. As such, even molecules visually oriented along the step will fluctuate thermally and see their S_y parameter reduced from 1. However, the clear trend visible in Fig. 2.15 and the fact $S_y > 0$ near the step unambiguously indicate a preferred molecular orientation along the step axis.

Chapter 5 will discuss in detail the relevance of these findings also in light of the AFM

imaging and shear experiments.

2.6 Summary

The Chapter has discussed the two main methods used within this research project: AFM imaging and shear spectroscopy. I have also introduced the key features of SEM imaging and MD simulations which have been applied as complementary tools so as to further investigate AFM probes (Chapter 3-6) and the molecular arrangement of a model lubricant (Chapter 5).

References: Chapter 2

[1] N. Pavlivcek et al., *Nature Reviews Chemistry* **2017**, *1*, 1–11.

[2] H.-J. Butt et al., *Physics and chemistry of interfaces*, John Wiley & Sons, **2006**.

[3] J. Krim, *Scientific American* **1996**, *275*, 74–80.

[4] D. Ortiz-Young et al., *Nature Communications* **2013**, *4*, 1–6.

[5] C. Cafolla et al., *Journal of Applied Physics* **2018**, *124*, 154502.

[6] C. Cafolla et al., *Science Advances* **2020**, *6*, eaaz3673.

[7] C. Gerber et al., *Nature nanotechnology* **2006**, *1*, 3–5.

[8] Y. Song et al., *Journal of Physics: Condensed Matter* **2008**, *20*, 225012.

[9] N. Jalili et al., *Mechatronics* **2004**, *14*, 907–945.

[10] B. Cappella et al., *Surface Science Reports* **1999**, *34*, 1–104.

[11] H. Xie et al., *IEEE Sensors Journal* **2008**, *8*, 1478–1485.

[12] C. Quate, *Surface Science* **1994**, *299*, 980–995.

[13] N. M. Kuruppu Arachchige et al., *ACS Applied Nano Materials* **2019**, *2*, 2193–2203.

[14] B. J. Rodriguez et al., *Nanotechnology* **2009**, *20*, 195701.

[15] G. C. Ratcliff et al., *Applied physics letters* **1998**, *72*, 1911–1913.

[16] E. J. Miller et al., *Journal of Visualized Experiments* **2016**, e54924.

[17] C. Cafolla et al., *Nanoscale* **2018**, *10*, 11831–11840.

[18] V. Bellitto, *Atomic force microscopy: imaging, measuring and manipulating surfaces at the atomic scale*, InTech, **2012**.

[19] S. Akamine et al., *Applied Physics Letters* **1996**, *68*, 579–581.

[20] K. Voitchovsky, *Nanoscale* **2016**, *8*, 17472–17482.

[21] K. Voitchovsky, *Nanotechnology* **2015**, *26*, 100501.

[22] S. Akrami et al., *Nanotechnology* **2014**, *25*, 455701.

[23] D. Walters et al., *Review of Scientific Instruments* **1996**, *67*, 3583–3590.

[24] M. Rief et al., *Science* **1997**, *275*, 1295–1297.

[25] P. A. Wiggins et al., *Nature Nanotechnology* **2006**, *1*, 137.

[26] R. Garcia, *Amplitude modulation atomic force microscopy*, John Wiley & Sons, **2011**.

[27] A. Torii et al., *Measurement Science and Technology* **1996**, *7*, 179.

[28] J. E. Sader et al., *Review of Scientific Instruments* **1995**, *66*, 3789–3798.

[29] T. Pettersson et al., *Review of Scientific Instruments* **2007**, *78*, 093702.

[30] J. E. Sader et al., *Review of Scientific Instruments* **2014**, *85*, 113702.

[31] C. T. Gibson et al., *Nanotechnology* **2005**, *16*, 234.

[32] M. L. Palacio et al., *Nanotribology and Nanomechanics*, Springer, **2017**, pp. 95–134.

[33] A. San Paulo et al., *Physical Review B* **2001**, *64*, 193411.

[34] R. Proksch et al., *Nanotechnology* **2004**, *15*, 1344.

[35] J. Tamayo, *Journal of Applied Physics* **2005**, *97*, 044903.

[36] D. J. Tritton, *Physical fluid dynamics*, Springer Science & Business Media, **2012**.

[37] C. K. Batchelor et al., *An introduction to fluid dynamics*, Cambridge University Press, **2000**.

[38] R. Garcia et al., *Surface Science Reports* **2002**, *47*, 197–301.

[39] M. Higgins et al., *Review of Scientific Instruments* **2006**, *77*, 013701.

[40] V. Pukhova et al., *Nanotechnology* **2013**, *24*, 505716.

[41] A. M. Baro et al., *Atomic force microscopy in liquid: biological applications*, John Wiley & Sons, **2012**.

[42] M. Ricci et al., *Nature Communications* **2014**, *5*.

[43] W. Xiang et al., *Precision Engineering* **2020**, *64*, 269–279.

[44] S. Lee et al., *Physical Review B* **2002**, *66*, 115409.

[45] T. R. Rodriguez et al., *Applied Physics Letters* **2002**, *80*, 1646–1648.

[46] R. Garcia et al., *Physical Review B* **1999**, *60*, 4961.

[47] A. F. Payam et al., *Nanotechnology* **2015**, *26*, 185706.

[48] J. E. Sader et al., *Nanotechnology* **2005**, *16*, S94.

[49] K. Schroter et al., *Macromolecules* **2009**, *42*, 1114–1124.

[50] A. J. Katan et al., *Nanotechnology* **2009**, *20*, 165703.

[51] R. Garcia et al., *Nature nanotechnology* **2012**, *7*, 217.

[52] T. Albrecht et al., *Journal of Applied Physics* **1991**, *69*, 668–673.

[53] X. Xu et al., *Journal of Applied Physics* **2007**, *102*, 034303.

[54] T. Li et al., *Physical Review Letters* **2008**, *100*, 106102.

[55] T. Li et al., *Physical Review B* **2007**, *75*, 115415.

[56] J. N. Israelachvili, *Intermolecular and surface forces*, Academic Press, **2015**.

[57] C. Cafolla et al., *Nanoscale* **2020**.

[58] T. Ondarçuhu et al. in *Surface Tension in Microsystems*, Springer, **2013**, pp. 279–305.

[59] C. M. Mate et al., *Tribology on the small scale*, Oxford University Press, **2019**.

[60] B. V. Derjaguin et al., *Journal of Colloid and Interface Science* **1975**, *53*, 314–326.

[61] R. A. L. Jones et al., *Soft condensed matter*, Oxford University Press, **2002**.

[62] H. C. Hamaker, *Physica* **1937**, *4*, 1058–1072.

[63] J. M. Fernandez-Varea et al., *Journal of Colloid and Interface Science* **2000**, *231*, 394–397.

[64] F. L. Leite et al., *International Journal of Molecular Sciences* **2012**, *13*, 12773–12856.

[65] M. Bostrom et al., *Advances in Colloid and Interface Science* **2006**, *123*, 5–15.

[66] K. Okada et al., *International Journal of Engineering Science* **2016**, *101*, 110–114.

[67] D. A. Welch et al., *ACS Nano* **2016**, *10*, 181–187.

[68] R. Lim et al., *Physical Review Letters* **2002**, *88*, 246101.

[69] J. Gao et al., *Tribology Letters* **2000**, *9*, 3–13.

[70] W. Hofbauer et al., *Physical Review B* **2009**, *80*, 134104.

[71] M. Dijkstra, *Thin Solid Films* **1998**, *330*, 14–20.

[72] L. Piantanida et al., *Biophysical Journal* **2017**, *113*, 426–439.

[73] M. Kopycinska-Muller et al., *Ultramicroscopy* **2006**, *106*, 466–474.

[74] S. B. Velegol et al., *Langmuir* **2003**, *19*, 851–857.

[75] J. Liu, *Materials Characterization* **2000**, *44*, 353–363.

[76] G. Danilatos et al., *Scanning* **1979**, *2*, 72–82.

[77] D. Stokes, *Principles and practice of variable pressure/environmental scanning electron microscopy*, John Wiley & Sons, **2008**.

[78] S. Amelinckx et al., *Electron microscopy: principles and fundamentals*, John Wiley & Sons, **2008**.

[79] A. Bogner et al., *Ultramicroscopy* **2005**, *104*, 290–301.

[80] T. Ichimura et al., *Microelectronic Engineering* **2014**, *113*, 109–113.

[81] L. Reimer, *Scanning electron microscopy: physics of image formation and microanalysis*, Springer, **2013**.

[82] N. Dellby et al., *Microscopy* **2001**, *50*, 177–185.

[83] R. Keyse, *Introduction to scanning transmission electron microscopy*, Routledge, **2018**.

[84] J. Ewen et al., *Friction* **2018**, *6*, 349–386.

[85] A. Vanossi et al., *Reviews of Modern Physics* **2013**, *85*, 529.

[86] C. L. Brooks, *Computer simulation of liquids*, Springer, **1989**.

[87] W. Foster et al., *Nanoscale* **2020**, *12*, 5452–5463.

[88] A. R. Leach et al., *Molecular modelling: principles and applications*, Pearson Education, **2001**.

[89] E. Paquet et al., *Advances in Chemistry* **2018**, *2018*, 14.

[90] T. Hansson et al., *Current Opinion in Structural Biology* **2002**, *12*, 190–196.

[91] I.-C. Yeh et al., *The Journal of Physical Chemistry B* **2004**, *108*, 15873–15879.

[92] X. Tang et al., *Physical Chemistry Chemical Physics* **2017**, *19*, 31168–31176.

[93] R. W. Hockney et al., *Journal of Computational Physics* **1974**, *14*, 148–158.

[94] B. Hess et al., *Journal of Computational Chemistry* **1997**, *18*, 1463–1472.

[95] M. J. Abraham et al., *SoftwareX* **2015**, *1*, 19–25.

[96] D. van der Spoel et al., *Nijenborgh* **2005**, *4*, 9747.

[97] H. D. Young et al., *University physics with modern physics*, Addison-Wesley, **2012**.

[98] T. Darden et al., *The Journal of Chemical Physics* **1993**, *98*, 10089–10092.

[99] U. Essmann et al., *The Journal of Chemical Physics* **1995**, *103*, 8577–8593.

[100] J. H. Los et al., *Physical Review B* **2005**, *72*, 214102.

[101] W. L. Jorgensen et al., *Journal of the American Chemical Society* **1996**, *118*, 11225–11236.

[102] J. L. MacCallum et al., *Journal of Computational Chemistry* **2003**, *24*, 1930–1935.

[103] B. Chen et al., *The Journal of Physical Chemistry B* **1998**, *102*, 2578–2586.

[104] S. W. Siu et al., *Journal of Chemical Theory and Computation* **2012**, *8*, 1459–1470.

[105] C. Mucksch et al., *Chemical Physics Letters* **2011**, *510*, 252–256.

[106] J. Vilhena et al., *Nanoscale* **2016**, *8*, 13463–13475.

[107] G. Kalibaeva et al., *Molecular Physics* **2003**, *101*, 765–778.

[108] C. Gattinoni et al., *Physical Review E* **2014**, *90*, 043302.

[109] P. H. Hunenberger in *Advanced Computer Simulation*, Springer, **2005**, pp. 105–149.

[110] H. J. Berendsen et al., *The Journal of Chemical Physics* **1984**, *81*, 3684–3690.

[111] S. Nose et al., *Molecular Physics* **1983**, *50*, 1055–1076.

[112] M. Parrinello et al., *Journal of Applied physics* **1981**, *52*, 7182–7190.

[113] S. Rogge et al., *Journal of Chemical Theory and Computation* **2015**, *11*, 5583–5597.

[114] A. Lemak et al., *Molecular Simulation* **1994**, *13*, 177–187.

[115] D. J. Evans et al., *The Journal of Chemical Physics* **1985**, *83*, 4069–4074.

[116] G. Bussi et al., *The Journal of Chemical Physics* **2007**, *126*, 014101.

[117] S. Nose, *The Journal of Chemical Physics* **1984**, *81*, 511–519.

[118] W. G. Hoover, *Physical Review A* **1985**, *31*, 1695.

[119] Z. Chen et al., *Science advances* **2019**, *5*, eaaw0513.

[120] L. Chen et al., *Carbon* **2019**, *154*, 67–73.

[121] V. I. Korotkovskii et al., *High Temperature* **2012**, *50*, 471–474.

[122] W. Humphrey et al., *Journal of Molecular Graphics* **1996**, *14*, 33–38.

[123] M. P. Allen et al., *Computer simulation of liquids*, Oxford university press, **2017**.

3.0 AFM Torsional Calibration

According to my views, aiming at quantitative investigations, that is at establishing relations between measurements of phenomena, should take first place in the experimental practice of physics.
Heike Kamerlingh Onnes, The Significance of Quantitative Research in Physics, 1882

3.1 Overview

This Chapter will provide the details of a non-invasive and non-destructive calibration method for the torsional spring constant of atomic force microscopy (AFM) cantilevers. Torsional calibration is fundamental to a range of applications, from nanoscale friction and lubrication measurements to the characterization of micro-electromechanical systems and the response of biomolecules to external stimuli. Torsional calibration has a crucial role in this thesis, as it is extensively applied in the research studies presented in Chapters 4-6. Existing calibration methods are either time consuming and destructive (*ex situ* static approaches), or rely on models using the frequency and quality factor (Q-factor) of the cantilever torsional resonance as input parameters (*in situ* dynamical approaches). While *in situ* approaches are usually preferred for their easy implementation and preservation of the cantilever, their dependence on the torsional resonance Q-factor renders calibration in highly viscous environments challenging. This is problematic, for example, in many nanoscale tribological applications. Here, I propose a calibration method that does not depend on the cantilever torsional Q-factor and show how the cantilever deflection can be converted into a lateral force. The method is tested with six cantilevers of different shapes and material composition and in six fluid media. The derived spring constants are compared with predictions from existing methods, demonstrating a higher precision, in particular, for highly viscous liquids. The proposed method will allow quantitatively investigating lubricated friction at the nano and mesoscale by using highly localised and accurately calibrated shear force spectroscopy measurements.
The bulk of this Chapter has been published as an article: A non-destructive method to

calibrate the torsional spring constant of atomic force microscope cantilevers in viscous environments. Journal of Applied Physics 2018, 124: 154502. The article was *Editor's Pick* and highlighted in *SciLight*.

3.2 Importance and challenges in AFM torsional calibration

In the previous Chapters, we have seen that AFM is an ideal tool for surface characterization, allowing both imaging at nanometer scales and measuring forces in the nano- to piconewton range [1–3]. While the most common AFM operation relies on measuring the flexural bending of a rectangular cantilever [4, 5] that quantifies forces normal to a sample, torsional measurements are becoming increasingly popular for their ability to extract in-plane forces such as the frictional force with nanoscale lateral precision [6–9]. Chapter 2 Sections 2.2.1 and 2.2.3 described how, in torsional measurements, the sample is moved laterally with respect to the main axis of the cantilever, making the cantilever twist as the AFM tip rubs against the sample's surface. The shear force between the tip and the sample can be accurately determined from the twisting angle of the cantilever, provided that the torsional spring constant and the inverse optical lever sensitivity (InvOLS) of the system are known. The InvOLS depends on the geometry of the system, and allows conversion of the raw photodiode measurement, taken in volts, into nanometers of lateral torsion at the tip. While the flexural calibration of the cantilever is relatively straightforward (see Chapter 2 Section 2.2.2 and further comprehensive reviews [10, 11]), the torsional calibration is usually more complex and often cannot be achieved *in situ*, or without specialist, homebuilt equipment [12–14]. The torsional calibration has however a crucial importance in this thesis to quantitatively describe lubricated friction forces at the nano and mesoscale.

Methods for the calibration of torsional forces can be broadly classified into three main categories [15]: (i) theoretical [16–18], (ii) static [13, 19–32] and (iii) dynamic [15, 33, 34]. Theoretical methods typically calculate the spring constant analytically from parameters characterizing the cantilever's geometry and its mechanical properties [16–18]. Such methods are particularly sensitive to errors originating from manufacturing variations in cantilevers' dimensions and material properties.

Static methods, in contrast, offer a direct measure of the lateral spring constant. These rely on a well-defined lateral force or displacement being applied to the AFM tip which generates torsional bending, thereby allowing the calculation of the torsional spring constant [13, 19–21]. For example, in the "wedge" method, the calibration is performed scanning the AFM tip over a wedge-shaped sample with known geometrical parameters, and analysing the

recorded normal and lateral forces with a suitable friction model [12, 13]. While static methods do not usually require many assumptions about cantilever's geometry or material properties, they often require extra equipment and hard mechanical contact with a sample surface, leading to tip damage. These techniques are hence considered *ex situ* and time consuming.

Finally, dynamic calibration methods usually rely on the torsional resonance frequency of the cantilever to find its spring constant [12, 33, 34]. Arguably, the best known torsional dynamic calibration methods are the so-called Cleveland method [33] and Sader method [33–35]. The Cleveland method measures the torsional frequency changes of the cantilever induced by the on-axis loading of added masses in order to deduce its torsional spring constant. In contrast, the Sader method determines the cantilever's torsional spring constant from its interactions with the surrounding medium, as quantified by the cantilever hydrodynamic function. The Sader method is particularly straightforward because it only requires the frequency and associated quality factor (Q-factor) of the cantilever torsional resonance as input parameters. As a result, the Sader method has become one of the most popular approaches in the scientific community to calibrate microcantilevers. While highly successful in most common conditions, the dependence of the Sader method on the cantilever's hydrodynamic function can become problematic in highly viscous environments. Practically, this difficulty comes from the need to know the Q-factor of the cantilever, a quantity difficult to measure accurately in highly viscous liquids where the resonance can significantly broaden in the frequency domain. Additionally, the method assumes a Q-factor significantly larger than unity. This assumption, although commonly verified in air, tends to fail in liquids, especially for those with high viscosity [34]. As a result, the calculated torsional spring constant can vary significantly when derived in different viscous media, despite being an intrinsic property of the cantilever [34]. An alternative method that does not rely on the Q-factor is hence highly desirable.

Here, I propose an alternative torsional calibration method that requires knowledge of five easily accessible parameters: the fundamental torsional resonance frequencies of a cantilever in air and in the medium of interest, the cantilever width and length, and the tip height. Significantly, the method is independent of the cantilever Q-factor, non-destructive and can be carried out on commercial AFMs without any further modifications. Since in most cases, the spring constant is only useful if the InvOLS is known, we adapt an existing InvOLS calibration methodology described elsewhere (ref. [34]) to also derive the system's InvOLS. The InvOLS calculation is based on the same five aforementioned parameters, on the Q-factor and on the power spectrum density of the cantilever torsional motion at DC (P_{DC}), obtained from the cantilever's thermal torsional vibration spectrum. This allows for a more accurate value of the InvOLS because the quantity now depends on the inverse of the square root of the Q-factor, as opposed to the inverse of the Q-factor with the Sader

formula. To validate the approach, results derived with the proposed method are compared to the Sader method using different cantilevers in different media.

3.3 Experimental

This section firstly describes the details about the materials and methods of the experimental measurements; secondly, it derives expressions for the cantilever's torsional spring constant and InvOLS based on suitable observables.

3.3.1 Materials and methods for the experimental measurements

The frequency response of six widely used commercially available cantilevers was investigated, each in six different media. The cantilevers were OMCL-RC800PSA (4 different cantilevers on a same chip, Olympus, Tokyo, Japan), AD-2.8AS (Adama Innovations LTD, Dublin, Ireland), and HQ-NSC18/HARD AL-BS (Windsor Scientific, Slough, UK). For clarity, the nominal geometrical and physical characteristics of the different cantilevers (hereafter referred to as C1–C6) are summarized in Table 3.1.

Fig. 3.1a highlights the different geometrical characteristics of the cantilevers used: C1-4 have a rectangular shape; C5 and C6 are a combination of a rectangle at the chip end and a triangle at the tip end.

As measurement media, air, ultrapure water, isopropanol, methanol, dimethyl sulfoxide (DMSO), hexadecane and squalane were used. The ultrapure water (AnalaR Normapur) was purchased from VWR International Ltd (Lutterworth, UK). All the other chemicals were purchased from Sigma-Aldrich (Dorset, UK) with a purity $> 99\%$ and used without any further purification. The tabulated density and viscosity of each fluid at the experimental temperature are shown in Table 3.2.

The measurements were conducted on a commercial Cypher ES AFM (Asylum Research, Santa Barbara, CA) equipped with a temperature-controlled sample stage. For each

Cantilever	**Commercial Name**	**Length (μm)**	**Width (μm)**	**Tip Height (μm)**	**Material**
C1	OMCL-RC800PSA	100.0	20.0	2.9	Silicon Nitride
C2	OMCL-RC800PSA	100.0	40.0	2.9	Silicon Nitride
C3	OMCL-RC800PSA	200.0	20.0	2.9	Silicon Nitride
C4	OMCL-RC800PSA	200.0	40.0	2.9	Silicon Nitride
C5	AD-2.8-AS	225.0	35.0	12.5	Diamond
C6	HQ-NSC18/HARD AL-BS	225.0	27.5	15.0	Diamond-like carbon

Tab. 3.1: Summary of the characteristics of the cantilevers (C1–C6) used for this study.

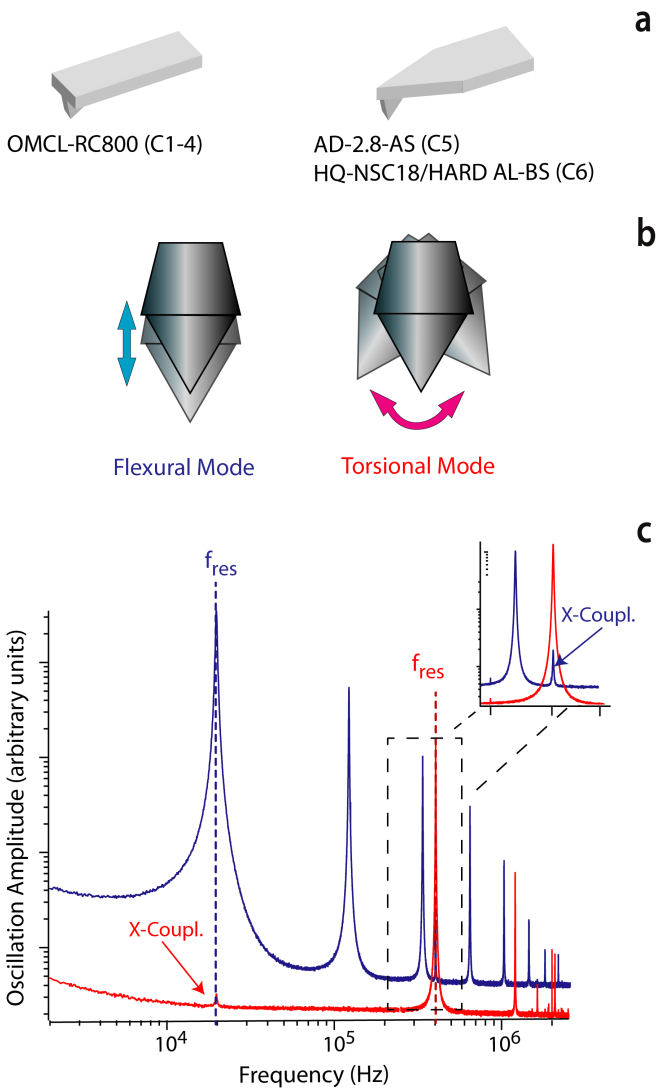

Fig. 3.1: Cantilever types and calibration details for flexural vs torsional modes. (**a**) Geometry of the cantilevers used in the study. (**b**) Pictorial representation of the different motion of the cantilever in flexural and torsional mode. (**c**) Representative example of flexural (blue) and torsional (red) thermal spectra for a given cantilever. In each case, the resonance frequency, f_{res}, of the first eigenmode is shown. Cross-coupling between the two modes is negligible for our purposes.

medium and for each cantilever, thermal spectra were recorded at 298 K. To minimize any errors associated with changes in the laser alignment in different fluids, all the media were explored in the same session for each cantilever. When exchanging fluids within a given series, the tip was thoroughly washed with isopropanol (20 times with 100 μm) and then with the new solution of interest (40 times with 100 μm).

The frequency response of the cantilevers in the different media was investigated by recording the thermal spectrum of each cantilever in each medium. The Brownian motion of the fluid surrounding the cantilever results in naturally exciting the cantilever itself and determining a flexural and a torsional motion. The two different types of motion can be

Medium	Density (kg/m^3)	Viscosity (Pa s)
Air	1.18	1.83 x 10^{-5}
Methanol	787.00	5.43 x 10^{-4}
Water	998.00	8.90 x 10^{-4}
DMSO	1095.00	1.99 x 10^{-3}
Isopropanol	785.00	2.10 x 10^{-3}
Hexadecane	769.00	3.08 x 10^{-3}
Squalane	805.00	2.80 x 10^{-2}

Tab. 3.2: Density and viscosity values for all the media at 298 K [36–38].

selectively detected using the AFM laser. Fig. 3.1(b) schematically shows the different dynamics between flexural and torsional motion of the cantilever. The two motions result in different thermal spectra, as shown in Fig. 3.1(c).

3.3.2 Deriving an expression for the torsional spring constant

Let's consider a cantilever of length L, width b and thickness h. Assuming that L is much greater than b and h, the torsional spring torque at the cantilever end is given by [33]:

$$k_\phi = \frac{1}{3\pi^2}\rho_c h b^3 L \omega_{t,a}^2 \tag{3.1}$$

where ρ_c is the cantilever density and $\omega_{t,a}$ is the torsional resonance frequency of the cantilever in air. While it is possible to directly use Eq. 3.1 to calculate the torsional spring constant of the cantilever, there are in practice two main limitations.

- Firstly, Eq. 3.1 requires knowledge of the cantilever thickness, a parameter that often carries a large variability with respect to the nominal value. This is confirmed by scanning electron microscopy (SEM) analysis of the cantilevers. SEM was performed on 6 different cantilevers (C1-C4, C6 and C7, see Section 3.5 below for details on C7). Before SEM imaging, the cantilevers were gold-coated (sputtering of a 15 nm thick gold layer) to prevent any charge accumulation. The images were acquired with a commercial FEI Helios SEM system (Dawson Creek Drive Hillsboro, Oregon 97124 USA). The machine operated at 3 kV electron beam in vacuum with a current set to 0.17 nA (see Chapter 2 Section 2.4 for further details on SEM). Representative images are presented in Fig. 3.2 for cantilever C4. The errors on the nominal values for length and width (200 μm and 40 μm, respectively) are in the range of 100-200 nm resulting in a negligible error ($< 0.5\%$). However, the thickness of the cantilever (nominal value of 800 nm) exhibits an error of more than 300 nm with a measured value of about 500 nm. This represents an error close to 40%, making the thickness

of the cantilever the geometrical parameter with by far the largest uncertainty. For all the cantilevers analysed, the length and width are in good agreement with the manufacturer's specifications (± 200 nm). This uncertainty is in agreement with the literature [34].

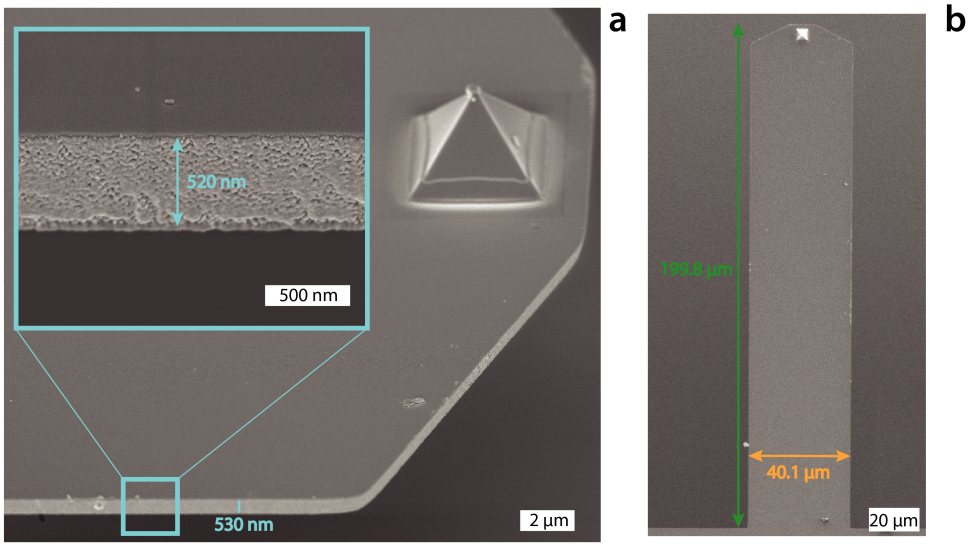

Fig. 3.2: Representative scanning electron microscopy images of cantilever C4. The cantilever is shown at different magnifications and at different angles. The manufacturer's specifications for the length, the width and the thickness are 200 μm, 40 μm and 800 nm, respectively. The thickness is affected by the largest relative and absolute error. The thickness measurements were corrected for the parallax shift considering the relative tilt angle [39].

- Secondly, Eq. 3.1 relies on the assumption of the cantilever's density being homogeneous. This is not always valid, with local inhomogeneities potentially affecting both the geometry and the density of the cantilever.

This is why the areal mass density is chosen to derive an effective cantilever density. We assume, then, that the cantilever dynamics in a dense fluid can be described by a simplified hydrodynamic function of torsional motion, $\Gamma_{tors}(\omega)$, characterized by two real (a_1, a_2) and one imaginary (b_1) regression coefficients as [40, 41]:

$$\Gamma_{tors}(\omega) \sim \left(a_1 + \frac{a_2}{\sqrt{Re}}\right) + i\left(\frac{b_1}{\sqrt{Re}}\right) \tag{3.2}$$

a_1, a_2 and b_1 are the regression coefficients of the hydrodynamic function for the torsional motion of a rectangular cantilever in fluid environments. The values of a_1, a_2 and b_1 are 0.0634, 0.388 and 0.4, respectively [40, 41]. Here, the fluid parameters are encapsulated by the Reynold's number, $Re = \rho_l \omega b^2/4\eta$, where ρ_l and η are the fluid density and viscosity, respectively. Using Eq. 3.2, we can relate the torsional resonance frequency

of the cantilever in air, $\omega_{t,an}$, with that in liquid, $\omega_{t,fn}$, for any given vibration eigenmode, n [33, 42]:

$$\omega_{t,an}^2 = \omega_{t,fn}^2 \left(\frac{3\pi a_1 \rho_f b}{2\rho_c h} + 1 \right) + \omega_{t,fn}^{3/2} \left(\frac{6\pi a_2 \sqrt{\eta}\sqrt{\rho_f}}{2\rho_c h} \right) \tag{3.3}$$

Using Eq. 3.3, the areal mass density of the cantilever, $\rho_c h$, can be calculated as follows:

$$\hat{\rho_c h} = \frac{3\omega_{t,f1}^2 \pi a_1 \rho_f b + 6\pi a_2 \sqrt{\omega_{t,f1}^3 \rho_f \eta}}{2\left(\omega_{t,a1}^2 - \omega_{t,f1}^2\right)} \tag{3.4}$$

Equation 3.3 can be used along with Eq. 3.1 to acquire the torsional torque constant (in Newton per meter) of the cantilever:

$$k_\phi = \frac{3\omega_{t,f1}^2 \pi a_1 \rho_f b^4 + 6b^3 \pi a_2 \sqrt{\omega_{t,f1}^3 \rho_f \eta}}{6\pi^2 \left(\omega_{t,a1}^2 - \omega_{t,f1}^2\right)} L\omega_{t,a1}^2 \tag{3.5}$$

which requires the beam width and length, and the torsional resonance frequencies in air and liquid as input parameters, alongside the density and viscosity of the fluid. The torsional spring constant (in N/m) of the cantilever can then be obtained from the torsional torque constant using the following equation [34]:

$$k_t = \frac{k_\phi L}{(L - \Delta L)\, h_t^2} \tag{3.6}$$

where ΔL is the distance between the position of the tip and the end of cantilever, and h_t is the tip height. The spring constant can be used alongside the torsional InvOLS, γ_t, as formulated in ref. [34], so as to multiply the cantilever deflection in volts and obtain the lateral force:

$$\gamma_t = h\sqrt{\frac{2k_B T}{\pi k_\phi f_0 P_{DC} Q}} \tag{3.7}$$

where k_B is the Boltzmann's constant, T is the temperature, and P_{DC} is the power spectrum density of the cantilever torsional motion at DC, measured on the cantilever's thermal torsional vibration spectrum.

Error calculation for the torsional spring constant

The error on the torsional spring constant is calculated using the standard quadrature approach and functional analysis for error propagation [43, 44]. The process is detailed below.

Error calculation for the proposed method

Following the SEM analysis (see representative images in Fig. 3.2), the error on the

geometrical parameters of the cantilevers is taken to be 200 nm with respect to the nominal value. The error on the resonance frequency, and on the Q-factor are taken to be 0.1 kHz and 0.2, respectively, judging by the uncertainties resulting from fitting of the thermal spectra. Both these variables, but especially the Q-factor, are highly sensitive to the choice of fitting interval due to the relatively broad resonance peaks in viscous environments (see Fig. 3.4 below). The uncertainty on the density and the viscosity of the medium are taken as 0.1 kg/m^3 and 1 μPa s, respectively. The uncertainty, α_k, on k_t is calculated using the quadrature approximation for multivariate functions [43, 44]:

$$\alpha_k^2 = \left(\frac{\partial k}{\partial \rho}\right)^2 \alpha_\rho^2 + \left(\frac{\partial k}{\partial \eta}\right)^2 \alpha_\eta^2 + \left(\frac{\partial k}{\partial b}\right)^2 \alpha_b^2 + \left(\frac{\partial k}{\partial h_t}\right)^2 \alpha_{h_t}^2 + \left(\frac{\partial k}{\partial L}\right)^2 \alpha_L^2 + \left(\frac{\partial k}{\partial f_a}\right)^2 \alpha_{f_a}^2 + \left(\frac{\partial k}{\partial f_1}\right)^2 \alpha_{f_1}^2 \tag{3.8}$$

where α_ρ, α_η, α_b, α_{h_t}, α_L, α_{f_a}, α_{f_1} are the errors on the density, the viscosity, the cantilever width, the tip height, the cantilever length, the resonance frequency in air and the resonance frequency in the medium of interest.

Error calculation for the Sader method

Certain input parameters appear both explicitly and implicitly in the Sader method, rendering a direct quadrature derivation challenging. A simplified multivariate functional approach is hence used [43, 44]. According to the Sader method, the torsional spring constant is given by [34]:

$$k_t = \frac{0.1592 \rho b^4 L Q \left(2\pi f_{res}\right)^2 \Gamma}{h_t^2} \tag{3.9}$$

where Q and Γ are the Q-factor and the hydrodynamic function, respectively. The uncertainty, α_k, on the torsional spring constant, k_t, is then [43, 44]:

$$\alpha_k = \sqrt{\left(\frac{\alpha_\rho}{\rho}\right)^2 + \left(4\frac{\alpha_b}{b}\right)^2 + \left(\frac{\alpha_L}{L}\right)^2 + \left(\frac{\alpha_Q}{Q}\right)^2 + \left(2\frac{\alpha_{f_{res}}}{f_{res}}\right)^2 + \left(\frac{\alpha_\Gamma}{\Gamma}\right)^2 + \left(2\frac{\alpha_{h_t}}{h_t}\right)^2} \tag{3.10}$$

When computing the error on the Sader method, an error of 5% is estimated to affect the hydrodynamic function [34].

3.4 Results and discussion

Tables 3.3 shows, for each cantilever, the values of the resonance frequency, Q-factor, and spring constants within the different media.

C1	**f_0 (kHz)**	**Q-factor**	**Proposed k_t (N/m)**	**Sader k_t (N/m)**
Air	821	324.0	$*$	250 ± 40
Methanol	475	6.3	260 ± 40	250 ± 40
Water	433	5.1	270 ± 40	260 ± 40
DMSO	405	3.7	270 ± 40	270 ± 40
Isopropanol	446	3.5	270 ± 40	260 ± 40
Hexadecane	447	3.1	290 ± 40	290 ± 50
Squalane	340	1.2	300 ± 40	340 ± 80
Mean Value $\pm$ Stand. Dev.	-	-	277 ± 15	278 ± 33
Coef. of Var.	-	-	0.054	0.119
C2	**f_0 (kHz)**	**Q-factor**	**Proposed k_t (N/m)**	**Sader k_t (N/m)**
Air	436	261.0	$*$	570 ± 90
Methanol	203	6.1	620 ± 90	550 ± 80
Water	184	5.5	630 ± 90	620 ± 90
DMSO	170	3.9	630 ± 90	610 ± 90
Isopropanol	191	3.6	630 ± 90	590 ± 90
Hexadecane	190	3.2	650 ± 90	640 ± 100
Squalane	142	1.0	640 ± 90	550 ± 130
Mean Value $\pm$ Stand. Dev.	-	-	633 ± 10	593 ± 37
Coef. of Var.	-	-	0.016	0.062
C3	**f_0 (kHz)**	**Q-factor**	**Proposed k_t (N/m)**	**Sader k_t (N/m)**
Air	416	219.0	$*$	130 ± 20
Methanol	236	4.7	140 ± 20	130 ± 20
Water	214	3.9	140 ± 20	140 ± 20
DMSO	197	2.7	140 ± 20	140 ± 20
Isopropanol	216	2.7	140 ± 20	150 ± 20
Hexadecane	215	2.4	150 ± 20	160 ± 30
Squalane	146	1.0	140 ± 20	210 ± 50
Mean Value $\pm$ Stand. Dev.	-	-	142 ± 4	155 ± 29
Coef. of Var.	-	-	0.028	0.187
C4	**f_0 (kHz)**	**Q-factor**	**Proposed k_t (N/m)**	**Sader k_t (N/m)**
Air	214	173.0	$*$	280 ± 50
Methanol	96	4.4	290 ± 40	260 ± 40
Water	87	4.1	310 ± 40	300 ± 40
DMSO	79	3.0	300 ± 40	310 ± 50
Isopropanol	88	2.8	300 ± 40	300 ± 50
Hexadecane	88	2.4	320 ± 40	320 ± 60
Squalane	78	0.2	490 ± 70	100 ± 100
Mean Value $\pm$ Stand. Dev.	-	-	335 ± 77	265 ± 83
Coef. of Var.	-	-	0.230	0.313
C5	**f_0 (kHz)**	**Q-factor**	**Proposed k_t (N/m)**	**Sader k_t (N/m)**
Air	524	460.1	$*$	107 ± 10
Methanol	266	8.5	79 ± 3	93 ± 4
Water	244	8.0	83 ± 3	111 ± 5
DMSO	229	5.5	85 ± 3	110 ± 6
Isopropanol	254	5.1	83 ± 3	104 ± 6
Hexadecane	255	4.3	88 ± 3	108 ± 7
Squalane	208	1.7	100 ± 4	131 ± 16
Mean Value $\pm$ Stand. Dev.	-	-	86 ± 7	110 ± 12
Coef. of Var.	-	-	0.081	0.109
C6	**f_0 (kHz)**	**Q-factor**	**Proposed k_t (N/m)**	**Sader k_t (N/m)**
Air	997	434.0	$*$	89 ± 8
Methanol	511	7.1	77 ± 3	70 ± 3
Water	473	7.5	82 ± 3	95 ± 5
DMSO	450	5.4	86 ± 3	99 ± 5
Isopropanol	499	3.8	84 ± 3	72 ± 5
Hexadecane	503	3.4	89 ± 3	79 ± 6
Squalane	417	1.3	101 ± 4	92 ± 15
Mean Value $\pm$ Stand. Dev.	-	-	87 ± 8	85 ± 12
Coef. of Var.	-	-	0.092	0.141

Tab. 3.3: Torsional resonance frequency, Q-factor and spring constant for all the cantilevers in the different media. The values for the spring constants are given for the proposed method and the Sader method. $*$ In the proposed method, the resonance frequency in air is used to compute the spring constant in the medium of interest.

The spring constant is calculated using the proposed method and compared to that obtained by the Sader method. The SEM analysis show that b and L are in good agreement with the nominal values ($\pm$ 200 nm), and the manufacturer's specifications for the geometry of the cantilevers are used when calculating the spring constant. Furthermore, the greatest sources of error are the resonance frequency and the Q-factor (see later in this section for a comprehensive discussion). For the Sader method, the mean value and the standard deviation are calculated without the value of the spring constant in air so as to allow fair comparison between the two methods. The coefficient of variation is the the ratio between the standard deviation and the average value of the spring constants across the six fluids and describes the relative variability of the predictions. Figure 3.3 pictorially represents the data shown in Table 3.3 so as to allow visually comparing the new method proposed here with the Sader method.

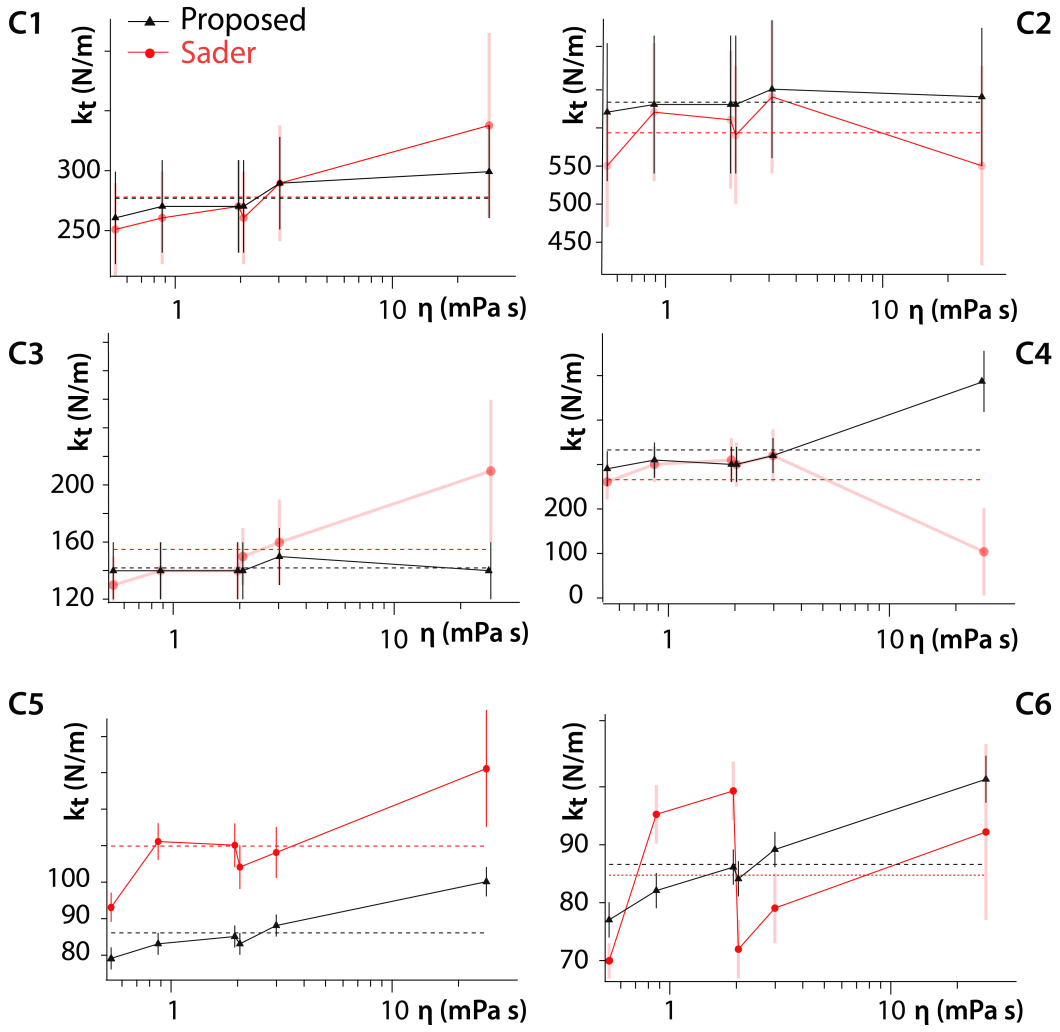

Fig. 3.3: Comparison of predictions from the proposed method and the Sader method in the different fluids for all the cantilevers. The dashed lines represent the average spring constant for each method; the data points and error bars relative to the Sader method have been shadowed and enlarged for clarity.

For all the cantilevers studied, the proposed method is found to be significantly less sensitive to viscosity in determining the spring constant. The robustness of the approach is particularly obvious in highly viscous media (see for example cantilever C3 in Fig. 3.3) where the dependence of the Sader method on the cantilever Q-factor hinders predictions. Accurate determination of the Q-factor is strongly dependent on the fitting interval selected in the thermal spectrum, especially since Q may be close to unity [34] (see Fig. 3.4). As shown in Fig. 3.3, for cantilevers C2 and C6, the proposed method appears more robust than the Sader method also in low viscous media. This is not surprising since the Sader method relies on the assumption of a Q-factor much greater than unity, a condition which is typically met for stiff cantilevers in air [33, 34, 45]. However, applying the method can be challenging even in media with viscosity as low as water [34]. Fig. 3.4 confirms this: representative thermal spectra for cantilever C3 in water and squalane highlight how changes in the Q-factor may markedly affect the Sader method limiting the accuracy in the fitting procedure.

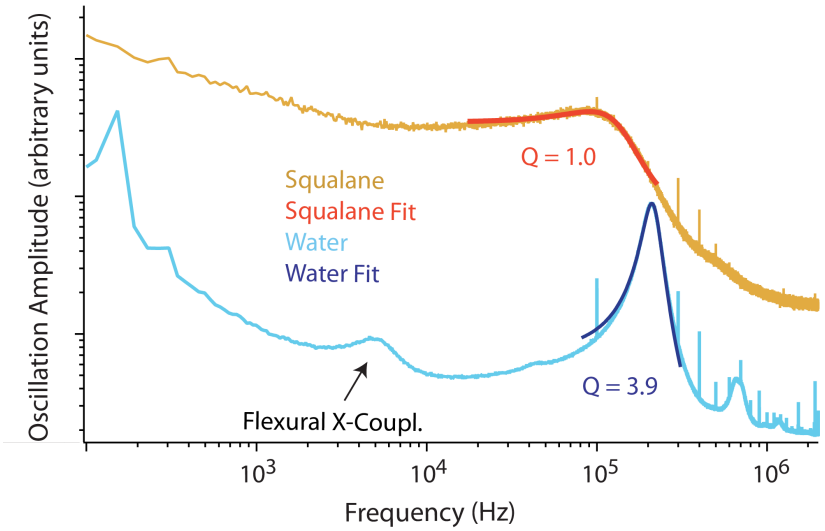

Fig. 3.4: Representative thermal spectra for cantilever C3 in low and high viscosity media (water and squalane, respectively). In both cases, the first eigenmode is fitted with the thermal noise method [4, 5, 34, 45–48]. In high viscosity media, the Q-factor significantly decreases and approaches unity, rendering the fitting procedure prone to large variations in the derived Q value depending on the fitting interval. The thermal spectrum of squalane has been offset vertically for clarity.

As illustrated in Table 3.3 and Fig. 3.3, the proposed approach shows also greater precision in comparison to the Sader method: for highly viscous media, the error is significantly smaller and, in some cases, reduced up to four times. For cantilevers C5 and C6, the uncertainty is smaller in all the media considered.

The robustness of the proposed method is quantitatively assessed calculating the relative variability of predictions for each cantilever across the different media (Fig. 3.5).

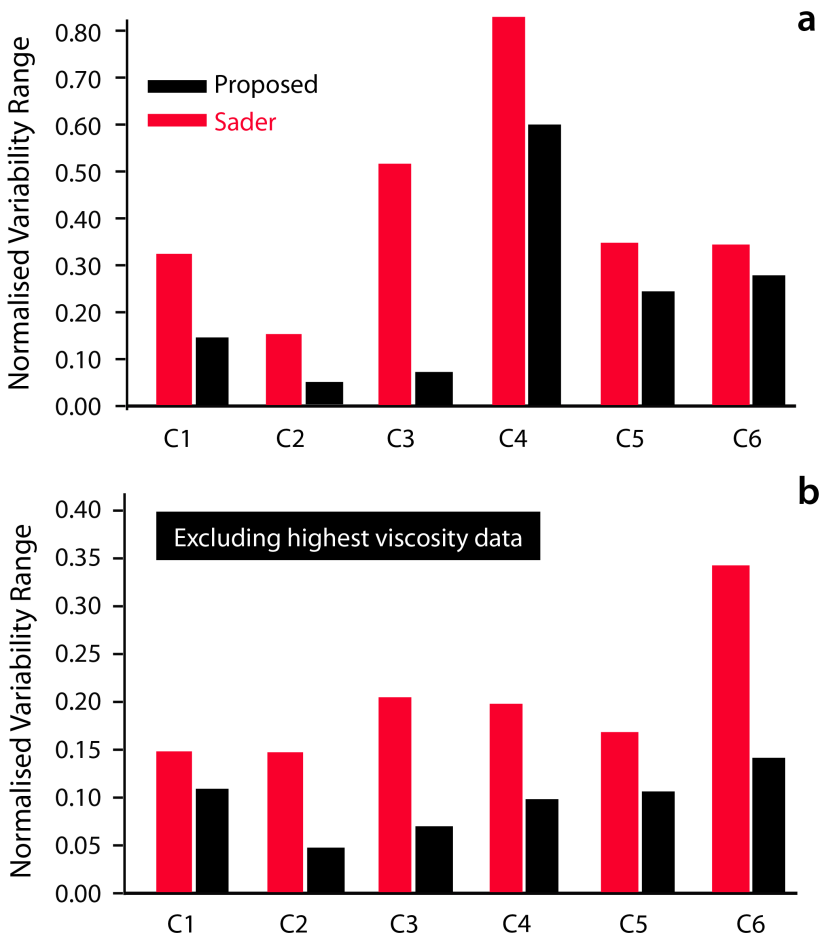

Fig. 3.5: Quantification of the variability across media for each cantilever's torsional spring constant for the proposed and the Sader methods. In (**a**) the variability is calculated using the data in all the media, whereas in (**b**) the data relative to the highest viscosity medium (squalane) have been excluded. For each cantilever, the variability of the spring constant across media is calculated as the difference between the maximum and the minimum spring constant normalized by the average value.

Here, the relative variability is defined as the difference between the maximum and the minimum spring constant normalized by the average value. The results clearly confirm the robustness of the method against the impact of the surrounding fluid's viscosity with the normalized variability range being, in some cases, even more than 4 times smaller with the proposed method. In Fig. 3.5b, a reduced set is considered, excluding the highest viscosity data point (squalane) given its possible biasing of the results. Again, the proposed method remains significantly less sensitive to viscosity changes in comparison with the Sader method.

The proposed method is validated by further statistical analysis on the relative variability of predictions for each cantilever across the different media (Fig. 3.6). In this case, the relative variability is defined as the coefficient of variation (COV), that is, the ratio between the standard deviation and the average value of the spring constants across the six fluids

[49]. The analysis further validates the robustness of the method against the influence of the surrounding fluid's viscosity. This is true independently from the viscosity range considered. For some of the cantilevers probed here, the calculated COV is even more than 4 times smaller with the proposed method.

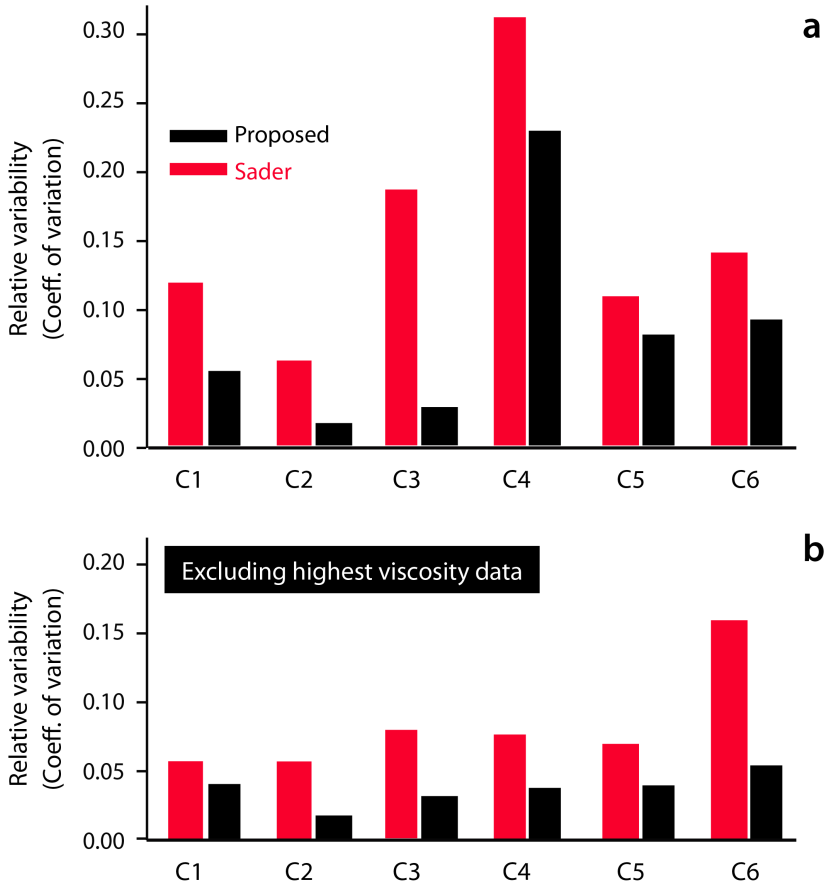

Fig. 3.6: Quantification of the variability across media for each cantilever's torsional spring constant for the proposed and Sader methods. For each cantilever, the variability of the spring constant across media is calculated as the coefficient of variation, the ratio between the standard deviation and the mean. In (**a**), the data points for all the liquids analysed are included, whereas in (**b**) the viscosity range does not include the most viscous liquid, that is, squalane. In both scenarios, the proposed method shows to be more robust than the Sader.

Combining Eqs. 3.5 and 3.7, it is possible to calculate easily the torsional InvOLS of the cantilevers, hence allowing a straightforward derivation of the lateral shear force experienced by the AFM tip. Hence, the proposed method would also potentially increase the accuracy of the torsional InvOLS calculation. This is because in the proposed method the torsional InvOLS depends on the inverse of the square root of the Q-factor, whereas in currently used models there is a linear dependence of the InvOLS on the inverse of the Q-factor [34]. It is important to note that the proposed method relies on knowledge of P_{DC} from the thermal spectrum of the cantilever. While the value of P_{DC} can be readily

obtained in most commercial AFMs, it is worth mentioning that additional gains and filters are often applied to the lateral deflection signal by commercial software in default settings. This may lead to an unexpectedly high or low InvOLS due to the P_{DC} value being incorrect.

3.5 Extending the method to arbitrarily shaped cantilevers

To test the proposed calibration method on non-rectangular cantilevers, I selected the widely-used and commercially available Arrow UHF (Nanoworld, Switzerland). The Arrow cantilevers are by design perfectly triangular, 42 μm wide at the base and 35 μm long. Its thickness is non-uniform with thinner edges and a trapezoidal cross section. For the sake of clarity, the cantilever is labelled as C7 and its characteristics are summarised in Table 3.4.

The proposed method can be in principle applied to any arbitrarily-shaped cantilever, but this require knowledge of the effective cantilever width, b_{eff}, for torsional purposes. There is no simple way of calculating b_{eff} because the torsion is not uniform across the cantilever. One possibility would be to use an approach similar to that previously developed for calculating the effective flexural width of arbitrarily shaped cantilevers (see Eq. 4 of ref. [50]), but this would require being able to access the higher torsional eignemodes of the cantilever, something beyond the detection bandwidth of most commercial machines. Here, in the absence of any obvious strategy to determining b_{eff}, this quantity is arbitrarily taken to be a third of the cantilever base width ($b_{eff} = 14$ μm). It is true that this choice, although intuitively reasonable, is speculative and does not allow for an accurate prediction of the torsional spring constant. In any case, it is not possible to assess the accuracy of our predictions since to the best of our knowledge, there exists no dynamic independent measurement of torsional spring constant for the Arrow (or any other commercially

C7	**f_0 (kHz)**	**Q-factor**	**Proposed k_t (N/m)**	**Sader k_t (N/m)**
Air	3884	272.0	$*$	220 $\pm$ 40
Methanol	1740	7.2	220 $\pm$ 30	230 $\pm$ 30
Water	1570	6.2	220 $\pm$ 30	240 $\pm$ 40
DMSO	1444	4.0	220 $\pm$ 30	220 $\pm$ 30
Isopropanol	1651	3.9	220 $\pm$ 30	230 $\pm$ 40
Hexadecane	1629	3.3	230 $\pm$ 30	230 $\pm$ 40
Squalane	1292	1.0	250 $\pm$ 40	210 $\pm$ 50
Mean Value	-	-	227	227
Stand. Dev.	-	-	12	10

Tab. 3.4: Torsional resonance frequency, Q-factor and spring constant for Cantilever C7 in the different media. $*$In the proposed method, the resonance frequency in air is used to compute the spring constant in the medium of interest.

available triangular cantilever). The analysis therefore focuses on the predictions variability across the different media rather than on the absolute value of the derived torsional spring constant. The choice of b_{eff} yields remarkably similar predictions from both methods for the torsional spring constant (Table 3.4 and Fig. 3.7), but the values should be taken with caution given the issues described above. Generally, using the proposed method, the variability for the torsional spring constant of triangular cantilevers tends to be smaller than that derived with the Sader method (Fig. 3.8).

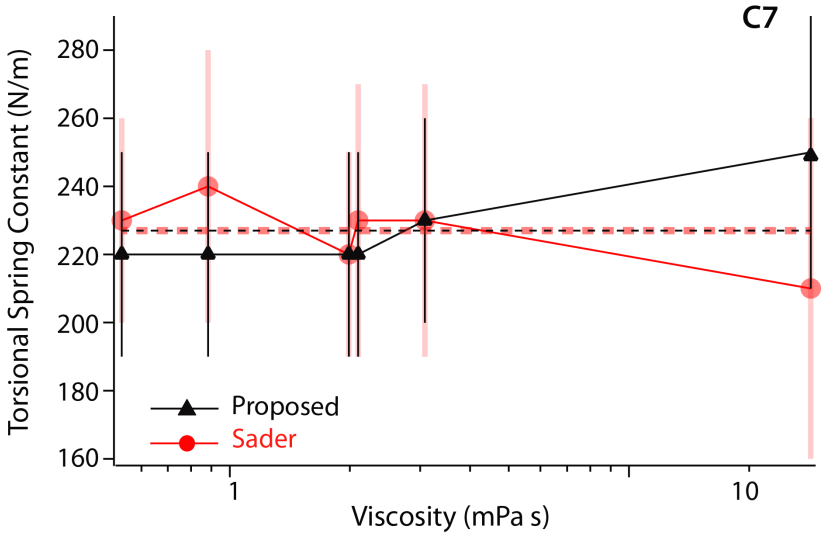

Fig. 3.7: Comparison of predictions from the proposed method and the Sader method in the different fluids for cantilever C7. The dashed lines represent the average spring constant for each method. The data points, error bars and average values relative to the Sader method have been shadowed and enlarged for clarity.

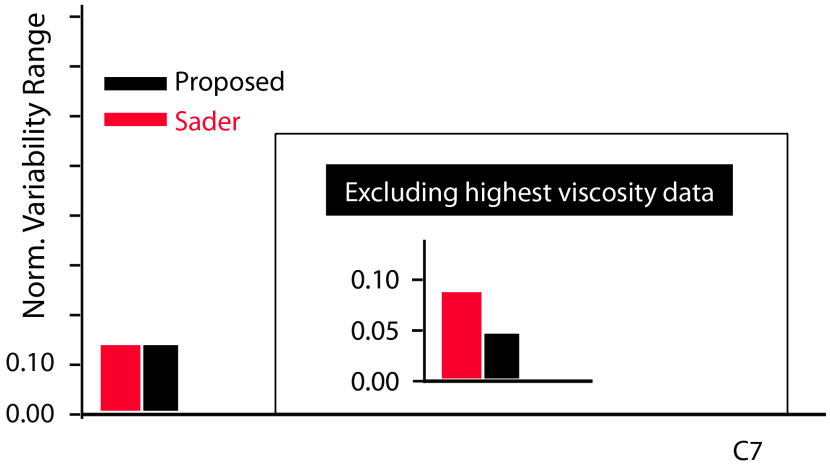

Fig. 3.8: Analysis of the variability in the torsional spring constant predictions for triangular cantilevers across the different liquids. The main graph comprises the data from all the media, whereas the graph in inset excludes the data relative to the highest viscosity medium (squalane). For each cantilever, the variability of the spring constant across media is calculated as the difference between the maximum and the minimum spring constant normalized by the average value.

3.6 Summary

The Chapter has presented a non-destructive and non-invasive method to determine the torsional spring constant of a cantilever, and to calculate the lateral shear force experienced by the AFM tip from the raw deflection as obtained from the photodetector. The method requires the following input parameters: the fundamental torsional resonance frequencies of the cantilever in air and in the medium of interest, the cantilever width and length, and the tip height. Significantly, the method is independent from the cantilever Q-factor which renders the approach particu larly effective in high viscosity media. The proposed approach is validated with cantilevers exhibiting different geometries and in six different media. The method can be carried out on commercial AFMs without the need for any extra equipment. The proposed method could be useful for quantitative high-resolution torsional imaging in solution [51] and in the field of nanoscale friction and tribology, for example when investigating ionic liquids [52], organic lubricants [9], surfactants layers [53] and functional nano-interfaces [54]. The method will be, in particular, invaluable in order to quantitatively investigate, in the following Chapters, the lubricating properties of nanoconfined aqueous solutions and organic liquids by using highly localised shear force spectroscopy measurements with a precision down to the pN range.

References: Chapter 3

[1] J. M. Fernandez et al., *Science* **2004**, *303*, 1674–1678.

[2] M. Grandbois et al., *Science* **1999**, *283*, 1727–1730.

[3] R. Garcia et al., *Nature Materials* **2007**, *6*, 405–411.

[4] M. Higgins et al., *Review of Scientific Instruments* **2006**, *77*, 013701.

[5] J. E. Sader et al., *Review of Scientific Instruments* **1999**, *70*, 3967–3969.

[6] K. Voitchovsky, *Nanoscale* **2016**, *8*, 17472–17482.

[7] T. Li et al., *Physical Review Letters* **2008**, *100*, 106102.

[8] C. Cafolla et al., *Nanoscale* **2018**, *10*, 11831–11840.

[9] C. Cafolla et al., *Science Advances* **2020**, *6*, eaaz3673.

[10] C. T. Gibson et al., *Nanotechnology* **2005**, *16*, 234.

[11] M. L. Palacio et al., *Nanotribology and Nanomechanics*, Springer, **2017**, pp. 95–134.

[12] M. Munz, *Journal of Physics D: Applied Physics* **2010**, *43*, 063001.

[13] R. J. Cannara et al., *Review of Scientific Instruments* **2006**, *77*, 053701.

[14] K.-H. Chung et al., *Langmuir* **2010**, *26*, 1386–1394.

[15] J. D. Parkin et al., *Nanotechnology* **2014**, *25*, 225701.

[16] R. Alvarez-Asencio et al., *Review of Scientific Instruments* **2013**, *84*, 096102.

[17] J. M. Neumeister et al., *Review of Scientific Instruments* **1994**, *65*, 2527–2531.

[18] J. Hazel et al., *Journal of Tribology* **1998**, *120*, 814–819.

[19] M. G. Reitsma et al., *Review of Scientific Instruments* **2011**, *82*, 093706.

[20] E. Liu et al., *Wear* **1996**, *192*, 141–150.

[21] E. Tocha et al., *Langmuir* **2007**, *23*, 7078–7082.

[22] A. Feiler et al., *Review of Scientific Instruments* **2000**, *71*, 2746–2750.

[23] G. Bogdanovic et al., *Colloids and Surfaces B: Biointerfaces* **2000**, *19*, 397–405.

[24] H. Xie et al., *Review of Scientific Instruments* **2008**, *79*, 096101.

[25] M. Reitsma, *Review of Scientific Instruments* **2007**, *78*, 106102.

[26] D. Ogletree et al., *Review of Scientific Instruments* **1996**, *67*, 3298–3306.

[27] D. Choi et al., *Journal of Microscopy* **2007**, *228*, 190–199.

[28] M. Varenberg et al., *Review of Scientific Instruments* **2003**, *74*, 3362–3367.

[29] X. Ling et al., *Langmuir* **2007**, *23*, 8392–8399.

[30] D. B. Asay et al., *Review of Scientific Instruments* **2006**, *77*, 043903.

[31] S. Ecke et al., *Review of Scientific Instruments* **2001**, *72*, 4164–4170.

[32] R. G. Cain et al., *Review of Scientific Instruments* **2001**, *72*, 3304–3312.

[33] C. P. Green et al., *Review of Scientific Instruments* **2004**, *75*, 1988–1996.

[34] N. Mullin et al., *Review of Scientific Instruments* **2014**, *85*, 113703.

[35] C. P. Green et al., *Journal of Applied Physics* **2002**, *92*, 6262–6274.

[36] J. Kestin et al., *Journal of Physical and Chemical Reference Data* **1978**, *7*, 941–948.

[37] C. Cafolla et al., *Journal of Applied Physics* **2018**, *124*, 154502.

[38] H. D. Young et al., *University physics with modern physics*, Addison-Wesley, **2012**.

[39] Helios SEM Operation Manual, https://rsc.aux.eng.ufl.edu/_files/documents/820.pdf.

[40] T. Cai, *ProQuest Dissertation Publishing* **2013**, *1*, 3601316.

[41] T. Cai et al. in International Frequency Control Symposium Proceedings, IEEE, **2012**, pp. 1–6.

[42] C. A. Van Eysden et al., *Journal of Applied Physics* **2006**, *100*, 114916.

[43] H. Ku, *Journal of Research of the National Bureau of Standards* **1966**, *706*, 263.

[44] A. A. Clifford, *Multivariate error analysis: a handbook of error propagation and calculation in many-parameter systems*, Applied Science Publications, **1973**.

[45] T. Pirzer et al., *Review of Scientific Instruments* **2009**, *80*, 035110.

[46] J. L. Hutter et al., *Review of Scientific Instruments* **1993**, *64*, 1868–1873.

[47] H.-J. Butt et al., *Nanotechnology* **1995**, *6*, 1.

[48] S. Cook et al., *Nanotechnology* **2006**, *17*, 2135.

[49] C. E. Brown, *Applied multivariate statistics in geohydrology and related sciences*, Springer, **1998**.

[50] A. F. Payam et al., *Applied Physics Letters* **2018**, *112*, 083101.

[51] N. Mullin et al., *Physical Review Letters* **2011**, *107*, 197801.

[52] F. Endres et al., *Faraday Discussions* **2012**, *154*, 221–233.

[53] R. Atkin et al., *Journal of the American Chemical Society* **2005**, *127*, 11940–11941.

[54] K. Voitchovsky et al., *Nature Communications* **2016**, *7*, 1–9.

4.0 Lubricating properties of single metal ions at interfaces

Thousands have lived without love, not one without water.
Wystan H. Auden, Juvenilia: Poems 1922-1928

4.1 Overview

The behaviour of ionic solutions confined in nanoscale gaps is central to countless processes, from biomolecular function to electrochemistry, energy storage and lubrication. However, no clear link exists between the molecular-level behaviour of the liquid and macroscopic observations. The problem mainly comes from the difficulty to interrogate a small number of liquid molecules. As discussed in the Introduction, these experimental limitations are also behind the intense debate on whether the organisation and dynamics of confined liquids would be different from the bulk. Here, I use atomic force microscopy to investigate the viscoelastic behaviour of pure water and ionic solutions down to the single ion level. The results show a glassy-like behaviour for pure water, with single metal ions acting as lubricants by reducing the elasticity of the nano-confined solution and the magnitude of the hydrodynamic friction. At small ionic concentration (< 20 mM) the results can be quantitatively explained by the ions moving via a thermally-activated process resisted by the ion's hydration water (Prandtl–Tomlinson model). The model breaks down at higher salt concentrations due to ion-ion interaction effects that can no longer be neglected. The correlations are confirmed by direct sub-nanometre imaging of the interface at equilibrium. The results provide a molecular-level basis for explaining the tribological properties of aqueous solutions and suggest that ion-ion interactions create mesoscale effects that prevent a direct link between nanoscale and macroscopic measurements.
The bulk of this Chapter has been published as an article: Lubricating properties of single metal ions at interfaces. Nanoscale 2018, 10: 11831-40. The article was included in the *2018 Nanoscale Hot Article Collection*

4.2 Introduction

Interfaces between solids and aqueous solutions are ubiquitous in nature [1], often confined to nano-gaps, inside or between solids [2]. Examples range from biomolecules folding [3] and microcirculation of metabolites in cells [4] to the growth of minerals [5] and geochemistry [6, 7]. In technology, the role played by this so-called nano-confined [8] water is arguably even more central with applications in electrochemistry and energy science [9], colloidal science [10], biomedical sciences [11], heterogeneous catalysis [12], tribology and lubrication [13]. Nano-confined water does not, generally, behave like its bulk counterpart; water molecules tend to be more ordered due to their interactions with the surface [2, 14] and reduced configurational entropy [15]. This molecular ordering vanishes over a few molecular diameters (typically $<$ 1-2 nm) in the bulk liquid [16], but the specific organisation and dynamics of the interfacial water molecules depend on the details of each system [2, 16–18]. Parameters such as the chemical nature and the geometry of the confining surfaces [9, 16], as well as the presence of dissolved molecules and ions [19], can markedly influence the behaviour of interfacial water [20]. The importance of interfacial effects is further emphasised for nano-confined water in systems where every liquid molecule can be seen as belonging to one or more interfaces. Additionally, the pressure and the temperature within the nano-confined gap [20–22], as well as a possible relative motion of the confining surfaces [23], can influence both the molecular arrangement and the dynamics of the nano-confined solution.

Numerous studies [2, 6, 8, 13–16, 18, 21–38] have examined the behaviour of nano-confined aqueous solutions in various systems and under different circumstances. Experimentally, the two main approaches are based on the surface force apparatus (SFA) and atomic force microscopy (AFM) with each family of methods offering different modes of operation. As discussed in Chapter 1 Section 1.4, the SFA-related methods rely on a well-defined confinement geometry between atomically flat surfaces over a large area (typically several μm^2) [23, 29, 32, 34, 39–42]. The distance between the confining surfaces can be measured in an absolute manner using interferometry, and dynamical measurements of the viscoelastic properties of confined aqueous solutions are possible over a range of frequencies (typically 1-3 Hz) using surface force balances (SFB) [43], or SFA with resonance detection [34, 39, 41, 42]. In contrast, AFM-based methods probe a small number of liquid molecules, typically located between a nanometre sharp tip and an atomically surface [2, 44, 45]. The exact confinement geometry is less well controlled, unless the tip radius is artificially increased [46]. This is both a drawback and an advantage over SFA-based methods. On the one hand, AFM is able to probe systems locally, with minimal area averaging, and with sub-nanometre precision in all directions [25, 45]. AFM allows for molecular-level imaging of the confined liquid [45, 47], direct identification of possible contaminant [48], and avoids

mesoscale averaging effects [49]. On the other hand, the small confinement area and poor control of the tip geometry can render interpretation of results challenging, especially in the absence of an absolute measurement of the confining gap's thickness.

Recently, both techniques have been used to investigate the effects of dissolved metal ions on the behaviour of nano-confined water [32, 33, 40, 43, 50–52]. SFB studies indicate that ultrapure water remains mostly fluid even when confined to gaps < 3.5 nm, retaining its bulk viscosity or close to it [23, 43, 51]. This result is supported by some theoretical studies [53, 54], and explained by a fast rotational and translational dynamics of water molecules under extreme confinement [53]. In contrast, AFM measurements suggest anomalous behaviour of nanoconfined water, with an effective viscosity that increases by orders of magnitude for nanoscale gaps between hydrophilic surfaces [18, 29]. This is also supported by some theoretical studies: Monte Carlo simulations showed that water molecules in contact with mica's ditrigonal cavities exhibit a residence time almost 10 times greater than that of bulk water [31].

Dissolving metal salts into the water does not reconcile the techniques. SFB studies show a general tendency for metal ions to increase the lubrication of water films confined between negatively charged mica surfaces, at least for ionic concentrations in the order of 100 mM NaCl [40, 43, 51]. This was interpreted as due to the shear rate being smaller than the hydration shell relaxation rate [52]: rapid exchange of water molecules between ions and the mica (in the order of 10^9 s^{-1}) ensures that the surface-bound hydration layer remains fluid at the shear rates (up to 10^3 s^{-1}) [50]. Different ions give rise to a wide range of lubricating properties, usually more effective for ions with a higher charge density [40, 43] suggesting a more robust Stern layer. In contrast, AFM experiments on various concentrations of NaCl suggest the confined ions act as pinning centres for water molecules, restricting their mobility and increasing the effective elasticity of the system [33].

The discrepancies between techniques highlight gaps in our understanding of the behaviour of nano-confined aqueous solutions. The confining constraints and the spatial scale of observations are just but two potential factors responsible for the divergent findings, in particular when taking into account the observed molecular arrangement of the sheared liquid film [34]. Ions do not necessarily arrange randomly at the surface of solids, but instead can form organised nanoscale clusters through water-mediated correlations [25], and with millisecond dynamics at the single ion level [24, 55]. While only a handful of reports evidence mesoscale order (1-100 nm) [25, 26], its origin would suggest mesoscale effects to be the rule rather than the exception. In nano-shearing experiments, mesoscale order could have significant consequences for the dynamics and lubrication properties of the system depending on the scale considered [24–26, 56]. Molecular-level measurements also need to address boundary effects [57] and any surface singularities that prevent mean field simplifications.

This Chapter investigates the tribological properties of aqueous solutions confined between an AFM tip and a flat mica surface at the single ion level. I explore the impact of charge density and pH on the viscoelastic response of the nano-confined liquid. The results provide quantitative insights into the lubrication properties of nano-confined solutions, including the conditions leading to the breakdown of the simple molecular-level descriptions that neglect system-specific effects.

4.3 Experimental

The mica substrates were prepared as described in Chapter 2 Section 2.3.1. Hereafter, I will recall the key aspects, and the underlying rationale.

Before conducting any measurements, the mica samples were cleaved and rinsed copiously with ultra-pure water. When a fresh surface of mica is revealed, immediately after cleaving, half of the ditrigonal cavities exposed are filled with K^+ ions. The ions originate from the bulk of the crystal where they form a cleavable layer that ensures electrostatic neutrality of the crystal. These K^+ ions can, in principle, interfere with the measurements conducted in this study and their removal and replacement by the desired ions was ensured through extensive rinsing. Hereafter, I estimate their final concentration in the solution during the different experiments. This will confirm the effectiveness of the rinsing procedure.

The cleaved mica surface is a disc of 12 mm diameter, with a total area of $\sim$ 113 mm^2. Considering the area of a hexagonal lattice site ($\sim$ 2.2 x 10^{-19} m^2, see Fig. 4.2f), a total of $\sim 3 \times 10^{14}$ K^+ ions are initially on the surface. This represents $\sim$ 1 nanomole of K^+. The surface is then rinsed sequentially 20 times with 100 μl of ultrapure water, and then 40 times with 100 μl of the experimental solution. Dividing the amount of K^+ by the total volume of the rinsing liquid yields a K^+ concentration of $\sim$ 0.2 μM. This concentration is an overestimate because sequential rinsing is more efficient at removing dissolved species than the single rinsing implicitly assumed in our estimate. Nonetheless, 0.2 μM is four orders of magnitude smaller than the 5 mM metal salt used in the ionic solutions probed here and the probabilty to find a K^+ ion adsorbed at the surface of mica is negligible. In ultrapure water, the lowest concentration of H^+ occurs at the highest pH investigated (5.38) where its concentration is still about 4 times that of K^+. Given the fact that the binding constant of H^+ to mica is an order of magnitude larger than that of monovalent metal ions [58], it is reasonable to expect a vanishingly small probability to find K^+ ions at the surface of mica even in pure water.

4.3.1 AFM measurements

Chapter 2 Section 2.2 described the details of AFM imaging and shear spectroscopy. Here, all the experiments were conducted with silicon nitride cantilevers originating from a same wafer (Olympus RC800 PSA, Olympus, Tokyo, Japan) with a nominal flexural spring constant, $k_f = 0.39$ N m^{-1}. Each cantilever was calibrated using its thermal spectrum [59] yielding a typical stiffness of 0.33 ($\pm$ 0.05) N m^{-1} in solution. Calibration of the torsional cantilever inverse optical lever sensitivity (InvOLS) and spring constant, k_t, was performed as described in Chapter 3. k_t was 200 ($\pm$ 20) N m^{-1}.

Particular attention was paid to avoid any possible sources of contamination (see cleaning procedures detailed in Chapter 2 Section 2.3). Imaging of the confined Stern layer and hydration landscape was conducted with sub-nanometre resolution. As described in Chapter 2 Section 2.2.3, the AFM was operated in amplitude-modulation using photothermal excitation. The ratio A/A_0, between the imaging amplitude and the free amplitude (away from the surface) was kept as high as possible [25], with A between 0.8-1.5 nm allowing for atomic level resolution of the interface [26, 48, 49, 60].

At least, three full sets of shear measurement ($>$ 100 curves each) were obtained in any given solution. For a given series, measurements were first conducted in ultrapure water, followed by monovalent, and then divalent salts. The monovalent ion solutions were tested in no particular order between the different sets in order to minimize the risk of systematic errors. When exchanging solutions within a given series, the tip was thoroughly washed with pure water (20 times with 100 μl) and then with the new solution of interest (40 times with 100 μl). This ensured that only the metal ions of interest were present on the mica surface.

Scanning electron microscopy (SEM) was used to evaluate whether, after conducting the experiments, the probes had undergone any marked changes in their geometry. In total, five cantilevers were randomly selected and imaged either before or after the experiments (including imaging and shear-force measurements). Prior to SEM imaging, the cantilevers were gold-coated by sputtering with a 15 nm thick film to prevent charge accumulation (see Chapter 2 Section 2.4 for further details on SEM). Representative images are presented in Fig. 4.1. No detectable changes in the tip shape or radius of curvature before and after the AFM experiments are visible within error. Since the tip is not perfectly spherical, objective determination of its radius can be problematic. Here, the tip apex on the SEM image is fitted with circles, the fitting weight being placed either on the very apex (smaller circle) or on the overall tip (larger circles). This provides with lower and upper estimates for the tip radius. The smallest/largest circles are shown on each figure. The procedure is repeated in magnified images of the same tips to ensure its reliability and accuracy. All the radii are found between 15 nm and 19 nm. SEM analysis also allows calculating

the confinement area ($\sim$ 10 nm^2) [61], and thus expressing F_S and E_{diss} as functions of the confining pressure. Here, the confining pressure increases by $\sim$ 100 MPa for every nanonewton load (nN) applied.

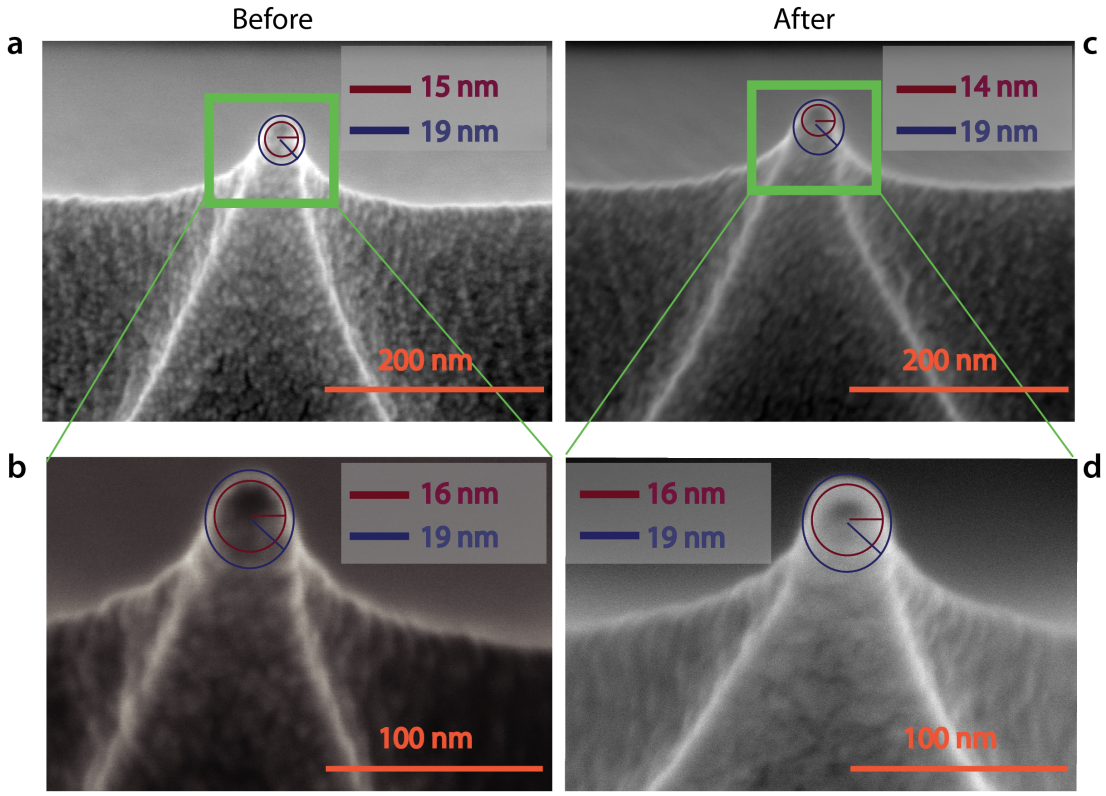

Fig. 4.1: Representative scanning electron microscopy images showing the analysis of a selected tip. The tip is shown at different magnifications immediately before (**a-b**) and after the AFM experiments (including both imaging and shearing) (**c-d**). The circles used to determine the lower and upper values of the tip radius are shown in each case. The radius of the tip was within manufacturer's specifications.

4.4 Results and discussion

4.4.1 High-resolution imaging of the confined interface

Figure 4.2 presents some high-resolution images of the mica surface in the different solutions. In all cases, atomic-level details are visible, but the quality of the image and the existence of mesoscale order depends on each imaging solution. The mesoscale patterns for the different ions are reproducible over multiple independent experiments. In pure water, the pseudo-hexagonal crystal structure appears clearly both in the topography and phase images. Water molecules form well-ordered hydration layers that extend up to 1 nm in the bulk solution [62] and follow the mica lattice arrangements. Adsorbed K^+ and

Rb^+ ions tend to form small domains due to water-mediated attractive lateral interactions when at the interface [24, 25], inducing near-uniform looking layer in 5 mM RbCl [25] and ordered longitudinal domains in KCl at the same concentration. This is consistent with the hydration structures of K^+ and Rb^+ ions, with both ions adsorbing mainly in a single hydration state to the mica substrate. In contrast, Na^+ ions can adopt different hydration states (inner and outer shell coordination) [63], rendering the AFM images less uniform (Fig. 4.2d). Marked localised height variations are visible resulting in noisier images due to the higher mobility of adsorbed Na^+ ions. Divalent Ca^{2+} ions can also adopt multiple hydration states and adsorb at both the centre of the ditrigonal cavities (position 1 the cartoon in Fig. 4.2f) and at interstitial sites [63] (position 2 in Fig. 4.2f). Domains similar to those induced by K^+ are visible, but Ca^{2+} ions are bound more strongly to the mica and cannot be easily removed [63].

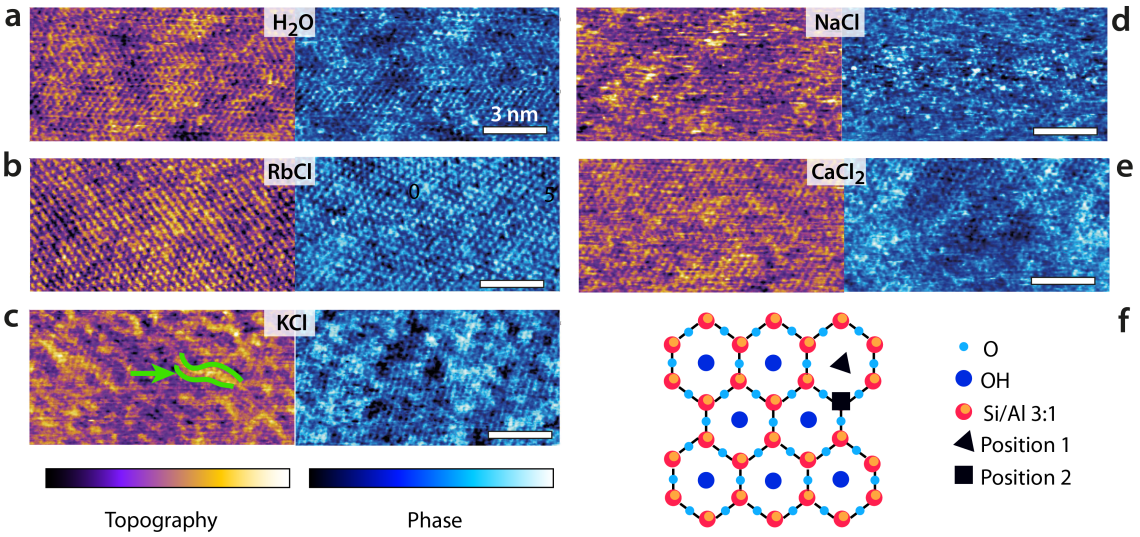

Fig. 4.2: High-resolution AFM images of the interface between mica and different experimental solutions. In each solution, both the topographic (purple-orange colour scale) and phase (blue colour scale) information are shown. (**a**) Hydration landscape of the mica surface in pure water. The lighter (higher) areas indicate regions where water molecules form an epitaxial lattice-like arrangement, with 2-3 nm wide domains. (**b**) In RbCl, the Rb^+ ions tend to form large correlated epitaxial domains, leading to an interface appearing almost uniform at this concentration. (**c**) K^+ ions behave in a similar fashion as Rb^+ (attractive correlation interactions at the interface), resulting in distinctive elongated domains (green arrow). (**d**) Na^+ ions exhibit no clear structural organization due to higher mobility and multiple solvation states. (**e**) Ca^{2+} ions also organise into domains but with many defects due to the multiple hydration states and adsorption to interstitial sites (position 2 in **f**). (**f**) Cartoon representation of the cleaved mica surface. The scale bar is 3 nm in all images. The colour scale represents height variations of 0.5 nm in topography and 30° in phase. All the ionic solutions with added salt (5 mM) are at pH 5.38. The temperature is 298.0 (± 0.1) K.

4.4.2 Shear-spectroscopy: hard confinement

The high-resolution images shown in Fig. 4.2 highlight the importance of local hydration effects on the organisation and the behaviour of the different ions at the interface. Order can exist both at the molecular (single-ion) level and at the mesoscale, inducing variations in the hydration landscape of the interface. To single out the impact of single ions on the lubrication of the interface, we conducted shear-force spectroscopy measurements [63] with a shearing amplitude $A_t \sim 0.5$ nm, significantly smaller than mesoscale structures. A_t is also comparable to the smallest distance ions would diffuse when moving between adjacent lattice sites of the mica. Given the ion coverage of mica shown by the high resolution images, we expect, on average, at most one ion to be present between the confining tip and the mica surface, effectively conducting single ion-level nano-tribological measurements.
The results, presented in Fig. 4.3, confirm the lubricating effect of the added ions on the system where they reduce the shear force, F_S, for a given applied force. The magnitude of the effect depends on the ion's charge density, following a standard Hofmeister series. The phase information shows that while the ions reduce F_S, they increase the viscosity of the sheared liquid, with the shear phase, ϕ_S, moving closer to 90° (Fig. 4.3b). This and the fact that the energy dissipation, E_{diss}, also decreases when ions are added to the solution suggest that pure water adopts a glassy-like behaviour. Substantial friction between ordered hydration water layers increases the energy dissipated in the system following a mechanism analogous to boundary friction. Consistently, the system exhibits a significant elastic response in pure water. Adding ions ruptures this order and decreases the friction through an increase in local viscosity. In other words, the system appears to evolve towards a more liquid-like behaviour of the interface, better described by hydrodynamic friction. Both theoretical [64, 65] and experimental studies [66, 67] have shown that water molecules on mica tend to acquire a crystalline, or ice-like arrangement in the first layer due to the approximate lattice matching between the mica surface and the hexagonal ice basal plane. When under nano-confinement, the diffusion of the water molecules markedly decreases [24, 64]. Added ions frustrate the otherwise highly structured hydrogen bond network, limiting the range of intermolecular correlations and competing with the ordered mica surface for water molecules. This results in an increase in mobility for the water molecule in the nano-confined gap [52, 68], rendering the sheared solution more viscous. Ions with a larger charge density, ρ, exhibit a more cohesive hydration shell and tend to strongly restructure the water's hydrogen bond network [69–71], leading to better lubrication properties. This is obvious from the difference in the friction coefficients derived for Rb^+ and Ca^{2+} (Fig. 4.3c). Na^+ exhibits a slightly anomalous behaviour that partly challenges this simple description due to its complex adsorption profile [25, 63, 72, 73]. The contribution of anions can be neglected here given the important negative surface charge of both confining surfaces.

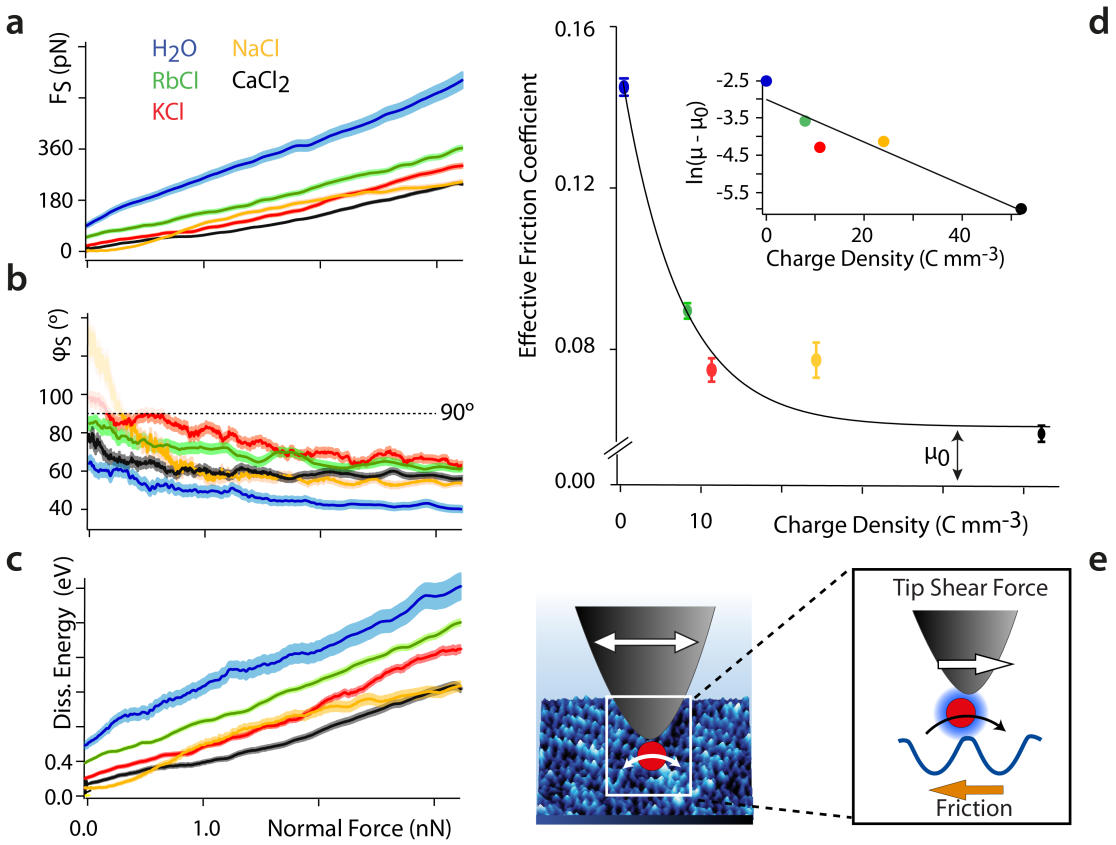

Fig. 4.3: (**a**) Averaged shear force, F_S, (**b**) shear phase, ϕ_S, and (**c**) energy dissipated per shear cycle as functions of the confining force for the different aqueous solutions. The thickness of the curves represents the standard error. Added ions decrease the magnitude of F_S at any given confining force by comparison with pure water, and ϕ_S increases to values closer to 90°, indicating a more viscous behaviour of the sheared liquid. At low confining forces (< 0.2 nN), the shear amplitude and hence force are close to the experimental noise level and the phase becomes undefined ($\phi_S > 90°$, semi-transparent region). The energy dissipation, E_{diss}, also decreases with added ions, indicating less friction. The effective friction coefficients derived from (**a**) are shown in (**d**) with their standard errors ($\mu_{water} = 0.142 \pm 0.002$, $\mu_{Rb} = 0.089 \pm 0.001$, $\mu_K = 0.074 \pm 0.003$, $\mu_{Na} = 0.077 \pm 0.004$, $\mu_{Ca} = 0.059 \pm 0.002$). The magnitude of the coefficients decreases exponentially with the ion's charge density (inset in **d**) as expected from Eq. 4.1 (see text). (**e**) The tip-driven shear motion of the ions at the surface of the mica lattice is captured by the Prandtl-Tomlinson model: the tip pulls ions between adjacent sites, over an energy barrier related to their hydration energy. All the solutions are at pH 5.38 and ionic solutions contain 5.0 mM salt. The temperature is 298.0 ($\pm$ 0.1) K.

Anions may gather in the upper hydration layers, but X-ray scattering and AFM show a rapid decrease of the degree of ordering in this region, indicating limited impact [74, 75]. The linear increase of F_S with the confining force suggests that the system follows a simple hydrodynamic friction that can be characterised by a single, ion-dependent coefficient. We empirically find an exponential relationship between the hydrodynamic friction coefficient

and the charge density of the cations in the solution:

$$\mu = \mu_0 + \mu_H e^{-\lambda\rho} \tag{4.1}$$

where $\mu_0 = 0.061 \pm 0.002$ represents the minimal achievable friction coefficient; $\mu_H = 0.082 \pm 0.002$ is the maximum contribution to friction that depends on added ions, and $\lambda = 1.38\ (\pm 0.09) \times 10^{-10}$ C^{-1} m^3 is an empirical parameter. In this framework, μ_0 describes the friction in the absence of a cohesive hydrogen-bond network within the sheared layer, aside from the immediate hydration structure of mica. The amount of friction induced by reorganizing the cohesive hydrogen-bond network due to added ions is described by μ_H which has a magnitude comparable to μ_0. When under shear, ions move between adjacent adsorption sites (potential minima) by overcoming an energy barrier, E_a, related to the disruption of the hydrogen bond network and to their interaction energy with the surface. The ions move through a thermally activated process [24], here enhanced by the shearing tip that effectively "pulls" ions to adjacent sites (Fig. 4.3e). Conceptually, this interpretation is captured by the Prandtl–Tomlinson model [76, 77] that describes the atomistic friction between a single atom and a periodic surface (see Chapter 1 Section 1.4 for a full description of the model). Here, this translates as the tip being assimilated to a point mass that pulls single hydrated ions via an elastic spring over the periodic mica lattice. Because of the small amplitude used, ions are repeatedly dragged back and forth between adjacent sites of the lattice. While the Prandtl–Tomlinson model has become famous for its description of the atomistic stick-slip friction, its theoretical framework can also describe smooth sliding friction. This occurs when the energy barrier experienced by the atom moving between two adjacent lattice sites is significantly lower than the energy provided by the pulling spring:

$$\gamma_{spring} = \frac{2\pi^2 U_0}{k_{eff}\ a^2} \tag{4.2}$$

with γ_{spring} the ratio between the energy barrier, U_0, and the spring pulling energy. The latter is characterised by the effective spring constant, k_{eff}, and the lattice parameter, a. Smooth sliding is hence expected to occur when $\gamma_{spring} \ll 1$.

In the present case, the energy barrier, E_a, experienced by hydrated ions moving between adjacent lattice sites of the mica lattice can be deduced from the parameter λ in Eq. 4.1. λ effectively captures the thermally-activated motion of the ions and must hence take the following form:

$$\lambda = \frac{E_a/q}{k_B T/a^3} \tag{4.3}$$

where E_a/q is the activation energy per unit charge q. The thermal energy (4.11×10^{-21} J or 25 meV at 298.0 K) is taken per volume a^3 of the system, with a being a relevant length scale [78], here half of mica's lattice parameter ($a = 0.26$ nm). E_a is found to be

$\sim 1.26\ k_BT$ which corresponds to about half the energy needed to dehydrate the mica surface over an area of a^2. From Eq. 4.2 and assuming $U_0 \sim E_a$, γ_{spring} is found to be $\sim 10^{-3} \ll 1$, confirming the validity of the interpretation.

Overall, the model works remarkably well and provides a consistent interpretation of the molecular processes dominating the nano-shearing measurements. The applicability of the model also suggests a profound connection between the solid–solid boundary friction implicitly assumed by the Prandtl–Tomlinson model and the hydrodynamic friction observed here for ions at interfaces: at the nanoscale, hydrodynamic friction can be understood as an extreme case of boundary friction where ions and molecules are pulled across the interface in a low γ_{spring} regime that enables smooth motion. In this framework, the friction force can then be understood in terms of local solvation effects and disruption of the hydrogen bond network that oppose the motion of the molecule considered at the interface, similarly to U_0 in the Prandtl–Tomlinson model.

From a thermodynamics perspective, the same process can be explained by the reduced entropy of the confined system whereby the imposed shear force precludes ions from moving randomly at the interfaces and freely probe all the available configurational states. This explains the fact that, for a given applied force, a decrease in the charge density of the added ion increases F_S and E_{diss}: ions with lower ρ exhibit a weaker solvation shell that can be easily disrupted by the confining tip. More work is hence needed to compensate for the associated tip-induced entropy reduction.

The ionic sequence found here for the effective friction coefficients contrasts with SFB findings [32]. This discrepancy could suggest that the two techniques probe different physical phenomena, due to the different sizes in the nano-confined areas they explore. The mesoscale order visible for K^+ ions in Fig. 4.2 is likely to influence SFB measurements, for example inducing local jamming and overlap during the lateral motion of ions and water molecules within the confined layer. Additionally, the ionic concentration probed here is relatively low, to ensure single ion level measurements. At higher concentrations, the confined hydrogen bond network becomes saturated with ions and other effects can take place such as ion-ion friction or the sliding past of dense Stern layers. These effects are explored, quantifying the dependence of F_S, ϕ_S and E_{diss} on KCl concentration (Fig. 4.4). At low ionic concentration (< 75 mM KCl), the adjunction of ions enhances the lubricating properties of the confined solution, but the solution becomes progressively more elastic under a given applied load already past 5 mM KCl (inset Fig. 4.4b). Around 75 mM KCl, the system reaches minimum of friction, but through an almost completely elastic behaviour. This could be interpreted as "dry" boundary friction with the K^+ ions arranged in such a manner that the confined hydrogen bond network plays a minimal role. At such high concentration, the mica is saturated with cations [24, 79] and multiple layers of ions may exist between the tip and the surface. Past 75 mM KCl, the lubrication properties

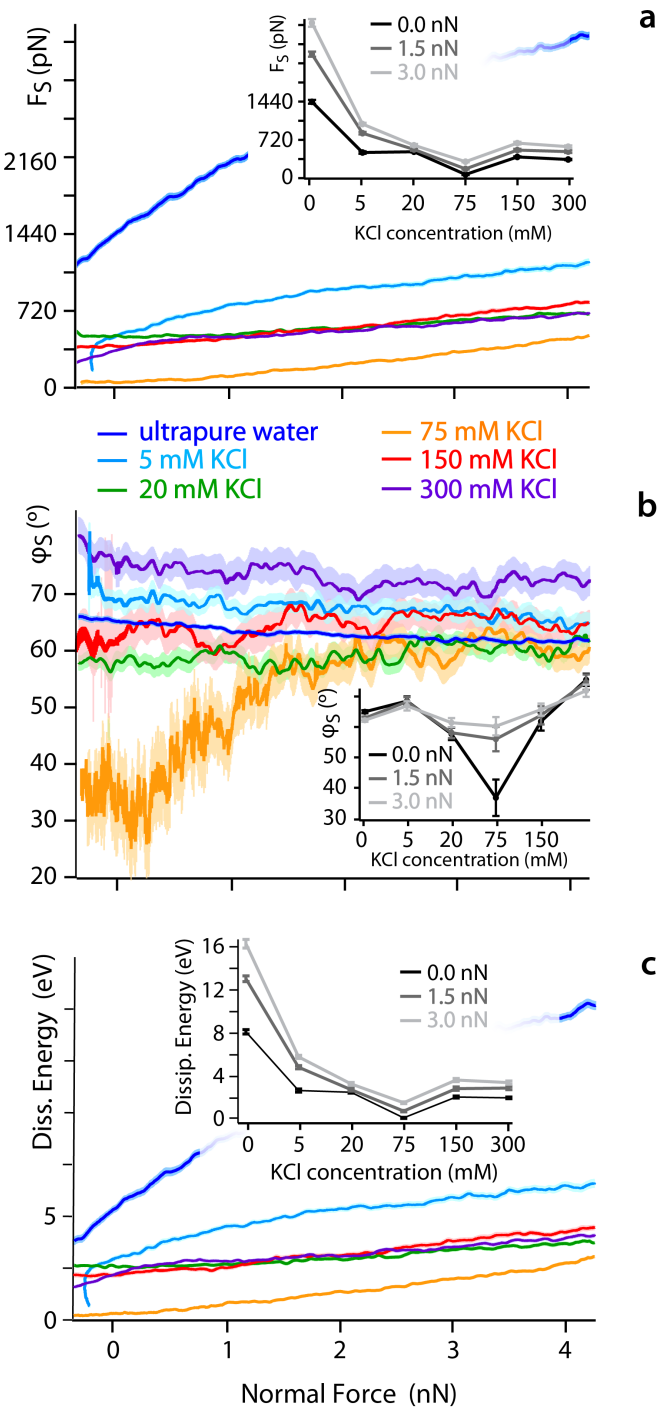

Fig. 4.4: Evolution of the shear force (**a**), shear phase (**b**) and energy dissipated per shear cycle (**c**) as functions of the confining force for different concentrations of KCl in aqueous solutions. The evolution is non-monotonous with a minimum in F_S and E_{diss} at 75 mM KCl, coinciding with a strongly elastic behaviour of the confined liquid. This is clearly visible at low confining pressures (~ 0 nN). For easier comparison, the insets (**a**–**c**) show respectively F_S, ϕ_S and E_{diss} as functions of ionic concentration for given applied forces.

of the solution deteriorate, and the response under shear becomes again more viscous. The ionic concentration corresponding to the friction minimum is only approximately

identified, but the results clearly indicate a non-monotonic behaviour, also confirming previous studies in NaCl [80]. Qualitatively, this non-monotonicity should be expected since ions can no longer behave as dissolved "point perturbations" to the hydrogen bond network past a certain concentration, but rather become the dominating feature with its own characteristics. Overall, these results highlight the importance of both spatial and temporal scales as well as ionic concentration when characterising the behaviour of confined fluids.

4.4.3 Shear-spectroscopy: soft confinement

The impact of the cations on the behaviour of the nano-confined water's hydrogen bond network can also be observed further away from the mica surface, with several layers of water and ions between the tip and the surface. This is done by examining changes in F_S, ϕ_S and E_{diss} as functions of the tip–sample distance. The results of this experiment are shown in Fig. 4.5. In pure water, F_S increases already when the tip is still ~ 2 nm away from the mica surface. In contrast, F_S increases only at distances smaller than ~ 0.5 nm when salt is added to the solution. No clear trend links ρ and F_S or E_{diss} except for an increase in the effective viscosity, consistent with better-ordered interfacial water layers. As discussed in Chapter 1 (see Eqs 1.21 and 1.23 in Section 1.3.2), the effective viscosity, η_{eff}, of the nano-confined liquid under shear can be quantified as follows [30]:

$$\eta_{eff} = \frac{F_S \; sin\,(\phi_S) \;\; (d+b)}{A \; v} \tag{4.4}$$

where $F_S \; sin\,(\phi_S)$ is the viscous component of the shear force, A the tip-sample contact area, b the slip length of the liquid at the interface with mica, and v the shearing velocity. Here, $v \sim 0.5$ μm s^{-1} and $b = 0$ (no-slip) [30]. In order to further highlight the different behaviour of water at nano-confinement, η_{eff} is normalised by the bulk solution viscosity, η_{bulk}, at 298.0 K (890 μPa s) [81]. The significant increase in η_{eff} for ultrapure water supports the hypothesised glassy-like behaviour under nano-confinement (Fig. 4.32) and agrees with previous AFM studies in similar conditions [82]. Equation 4.4 implicitly assumes a continuous fluid, a hypothesis that tends to break down at very short tip–sample distances where the molecular nature of water can no longer be ignored [18]. In pure water, this breakdown is observed for nano-confinement distances smaller than about two water molecules (dotted vertical blue line in Fig. 4.5b), characterised by a subsequent decrease in η_{eff}. Interestingly, a second step-like decrease in η_{eff} can be seen at a distance of ~ 0.25 nm (dotted yellow line), the approximate thickness of a single water layer. These observations suggest that the apparent decrease in η_{eff} can be explained by the tip disrupting ordered, solid-like confined water layers.

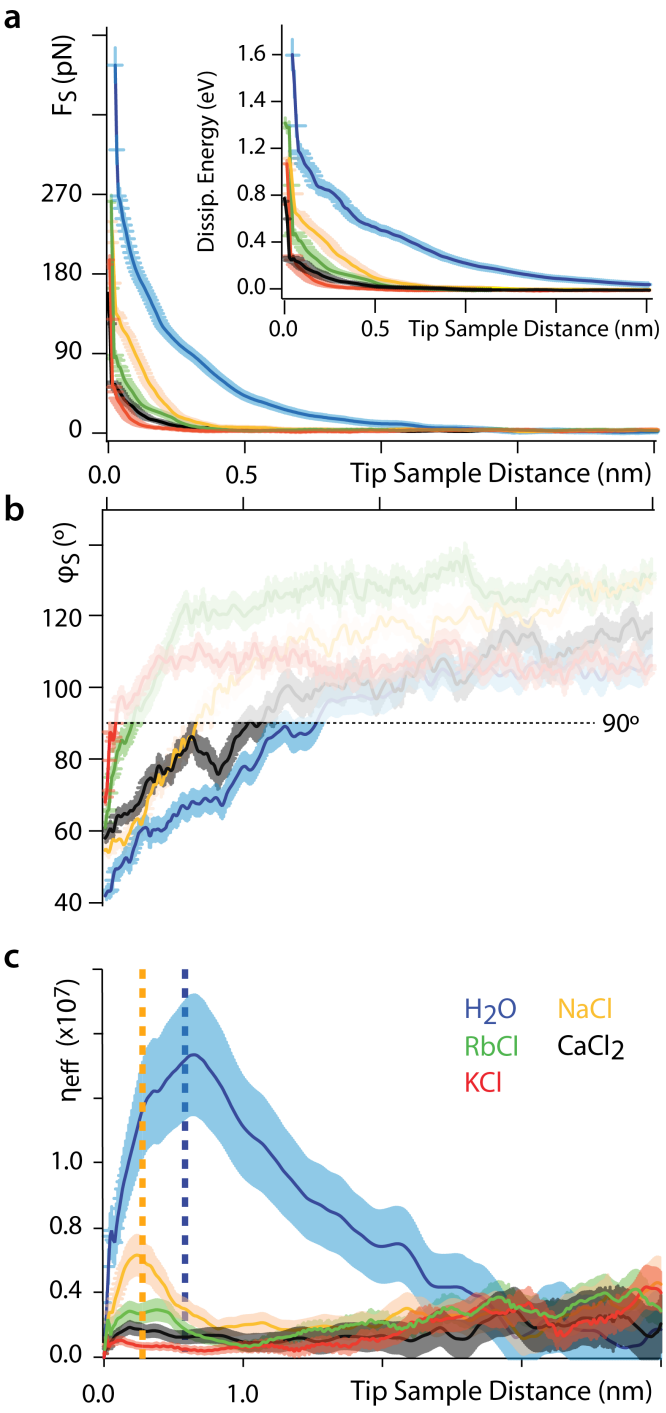

Fig. 4.5: Shear force (**a**), shear phase (**b**) and effective viscosity (**c**) as functions of the tip–sample distance. The force increases below distances of ~ 2 nm in pure water and ~ 0.5 nm in ionic solution. The inset in (**a**) shows the evolution of the energy dissipated per shear cycle. The response of nano-confined water induces a greater dissipation of energy than in ionic solutions. In (**b**) the shear phase is undefined at large tip-sample distance due to the shear amplitude and force being close to the noise level ($\phi_S > 90°$, semi-transparent region). (**c**) The effective viscosity of the interfacial liquid is normalised by the bulk solution viscosity, and increases by orders of magnitude in pure water, but changes in ionic solutions are close to the noise limit (except for NaCl). The yellow and blue dotted lines indicate regions where the confinement is smaller than one or two water molecules, respectively. For such small nanogaps, the assumption of continuous fluid implicit to Eq. 4.4 breaks down [18]. In the non-contact region, the shearing area is $A \sim 10$ nm^2. The slip length of mica is taken to be zero [30].

This is consistent with the significant elastic response of pure water, its glassy-like behaviour and the existence of long-range order in the hydrogen bond network.
The presence of ions markedly reduces η_{eff} that decreases only for nano-gaps thinner than a single water layer. This highlights the fact that the ions' lubricating properties originate from their ability to disrupt the ordered molecular arrangement of nano-confined water molecules, thereby inducing a greater fluidity of the liquid [52, 68–71].
Aside from calculating η_{eff}, it is also possible to derive the storage, G', and loss, G'', moduli of the confined liquid and then obtain an estimate of the system's relaxation time, τ [18]:

$$G'(d) = \frac{F_S\ d}{A\ A_t} cos\left(\phi_S\right) \tag{4.5}$$

$$G''(d) = \frac{F_S\ d}{A\ A_t} sin\left(\phi_S\right) \tag{4.6}$$

$$\tau = \frac{G'}{G''\omega_S} \tag{4.7}$$

where A is the tip-sample contact area, and A_t and ω_S are the shearing amplitude and frequency, respectively. The storage and loss moduli for all the aqueous solutions at pH 5.38 and 5 mM are shown in Fig. 4.6. It is clear that G'' always dominates over G', indicating that the confined liquid preserves its fluid nature. The significant storage modulus found for ultrapure water tends to confirm the hypothesized glassy behaviour under nano-confinement. Remarkably, the presence of ions within the system reduces the values of G' and G''. This further illustrates the lubricating properties of the ions, even when under weak confinement. τ describes the time needed for liquid molecules to relax, overcome the local solid-like order and reach the configuration of minimum free energy. Here, we find $\tau \sim$ 0.01 ms - 0.1 ms, several orders of magnitude slower than for bulk water, but slightly faster than the 60 ms dielectric relaxation time of supercooled water between 170 K and 210 K [18]. Similarly to supercooled water, the dynamics of a glass-forming liquid is governed by the collective motions of the molecules over the cooperative length [37]. In this framework, the relaxation timescale is related to reorientation dynamics of the confined water molecules when forming hydrogen bonds, preferentially parallel and perpendicular to the shearing direction [24]. This is in stark contrast with bulk water where no global preferred arrangements of dipole exists [38]. Adding cations helps break the global symmetry of the confined system, leading to a faster relaxation [32]. It is important to highlight that τ must be understood as an order of magnitude since it was not possible to explore different oscillation frequencies, ω_S.

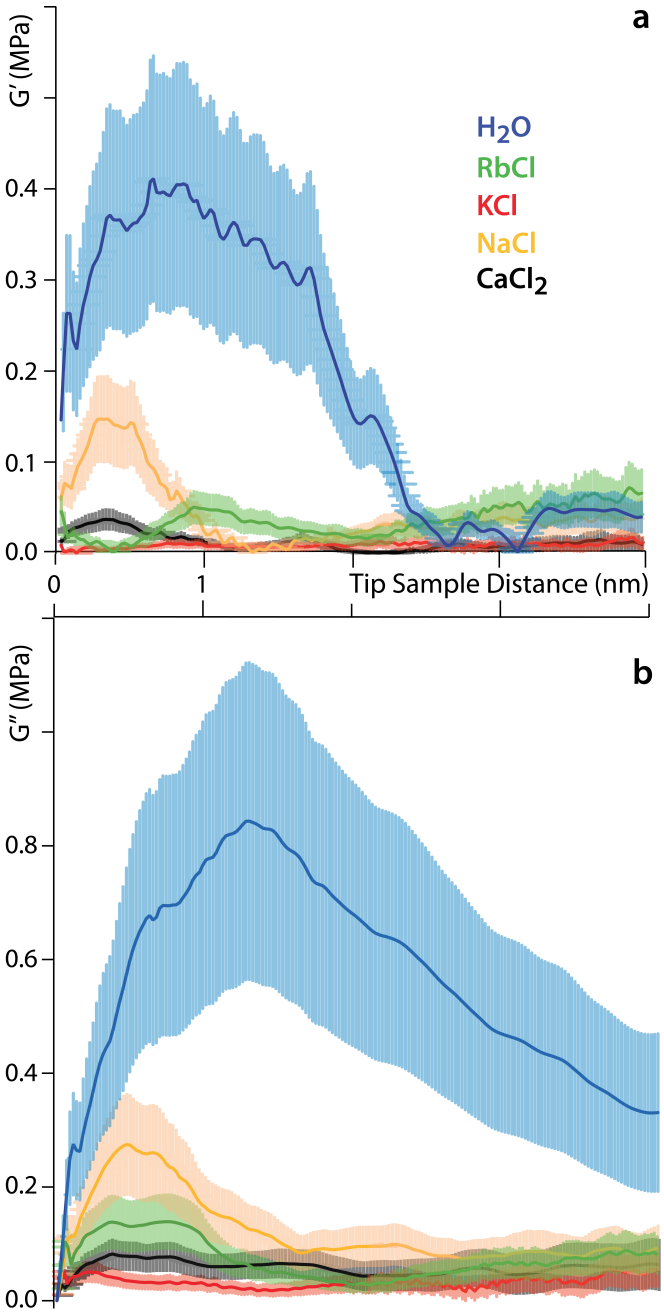

Fig. 4.6: (**a-b**) Behaviour of the storage modulus, G', and loss modulus, G'', as functions of the tip-sample distance. G'' is always larger than G', as expected for a fluid material. The shearing amplitude, A_t, is 0.5 nm. The area, A, is calculated to be 10 nm^2. The slip length of hydrophilic mica was taken to be zero [18]. All the ionic aqueous solutions are at pH 5.38 and 5.0 mM. The temperature is 298.0 ($\pm$ 0.1) K.

4.4.4 The effect of pH

One key aspect of measurements involving nano-confined water is the solution's pH. The hydronium ions compete with dissolved metal cations [24, 58, 79] and the dipole of the water molecules [24] for neutralising mica's negative surface charge. As a result, changes

in pH can have a marked effect on the molecular organisation and dynamics of interfacial water, often with consequences on the interface's tribological properties. At low pH, most of mica's surface charge is neutralised by strongly bound hydronium ions and metal ions tend to remain dissolved in the bulk solution due to their comparatively lower affinity for the mica surface [58]. To test this interpretation, shear experiments are conducted at three different pH for each of the ionic solutions investigated. In all cases, only HCl is used to adjust the pH with no buffering agent to avoid interference with the measurements [83]. The pH of the solution was checked before and after the measurements to ensure stability and no change was observed within experimental error ($\pm$ 0.07).

Results are shown in Figs 4.7-4.10. At low confining forces ($<$ 0.2 nN), the torsional coupling is often close to the noise level. This can result in the phase being undefined or assuming values greater than 90°. For completeness, shear phase values greater than 90° are reported but shadowed.

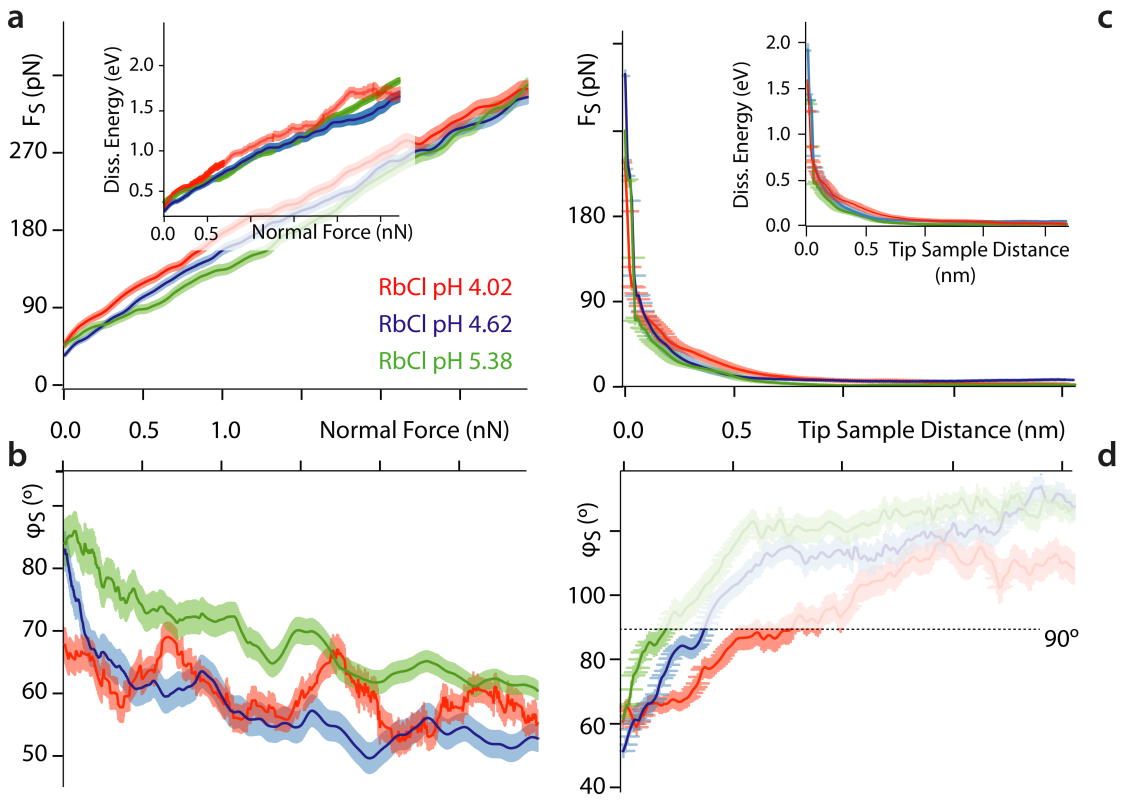

Fig. 4.7: Evolution of the shear force, F_S, energy dissipated per shear cycle and shear phase, ϕ_S, as functions of pH in RbCl. Results are shown for hard confinement (**a-b**) and soft confinement (**c-d**). The insets in (**a**) and (**c**) show the energy dissipated per shear cycle. The semi-transparent region in (**d**) indicates unreliable ϕ_S due to F_S being too small. The experiments are performed at 298.0 ($\pm$ 0.1) K.

Dissolved ions can alter the interfacial network, but this is dependent on the charge density of the confining surface itself, which is controlled by the pH. In general, for the ionic aqueous solutions probed here, both F_S and E_{diss} increase as the pH decreases, confirming

the replacement of metal cations by hydronium ions. This is further supported by ϕ_S values closer to 0° at low pH, showing a more pronounced elastic behaviour for the system. Specific differences in the hydration structure of the cations account for the diverse response to pH changes.

As shown in Fig. 4.7, the pH impact is clear but limited for RbCl. The trend can be explained taking into account two main factors. First, the relatively low charge density for Rb^+ results in a limited ability of this cation on restructuring the hydrogen-bond network of water [69–71] (see also Figs 4.2-4.3). Secondly, H_3O^+ ions are not able to markedly influence the local hydrogen bond network of water due to a very similar hydration structure [36] (see also Fig. 4.11).

The increase in F_S and E_{diss} at low pH is markedly greater for KCl (Fig. 4.8). Here, the evolution of the shear response with pH is consistent with hydronium ions competing with metal cations for binding sites on mica, thereby limiting the metal cations' ability to impact the water hydrogen-bond network and lubricate the system. This is further confirmed by a clear evolution of ϕ_S showing a greater elastic component when lowering the pH.

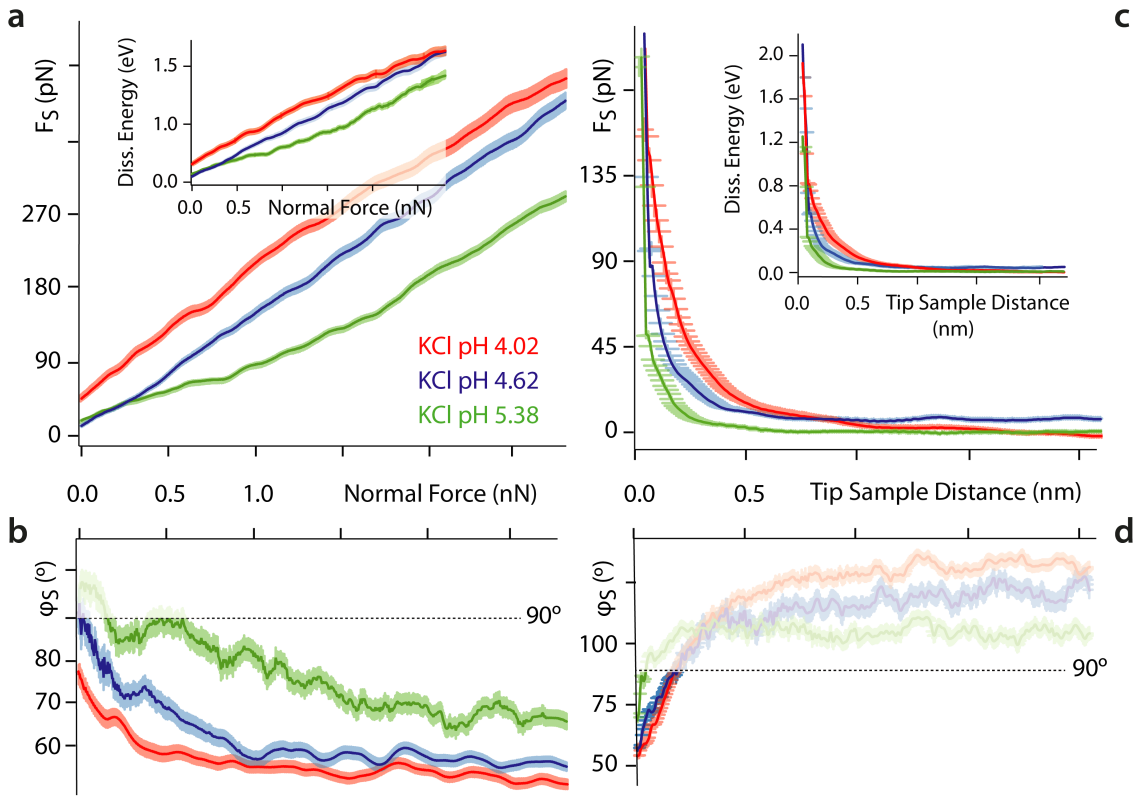

Fig. 4.8: Evolution of the shear force, F_S, energy dissipated per shear cycle and shear phase, ϕ_S, as functions of pH in KCl. Results are shown for hard confinement (**a-b**) and soft confinement (**c-d**). The insets in (**a**) and (**c**) show the energy dissipated per shear cycle. The hydronium ions interfere with the lubricating properties of the cations. In (**b**) and (**d**), ϕ_S is undefined at large tip-sample distance and small confining forces due to the F_S being close to the noise level ($\phi_S > 90°$, semi-transparent region). The experiments are performed at 298.0 (± 0.1) K.

In NaCl, the experiments consistently show an unusual behaviour with the results at pH 4.62 lying outside those obtained at pH 5.38 and pH 4.02 (see Fig. 4.9). This can be tentatively attributed to the complex adsorption profile of Na^+ and the presence of multiple solvation states which may be leading to a rapid dissolution of the initial geometric hydration arrangements [25, 63].

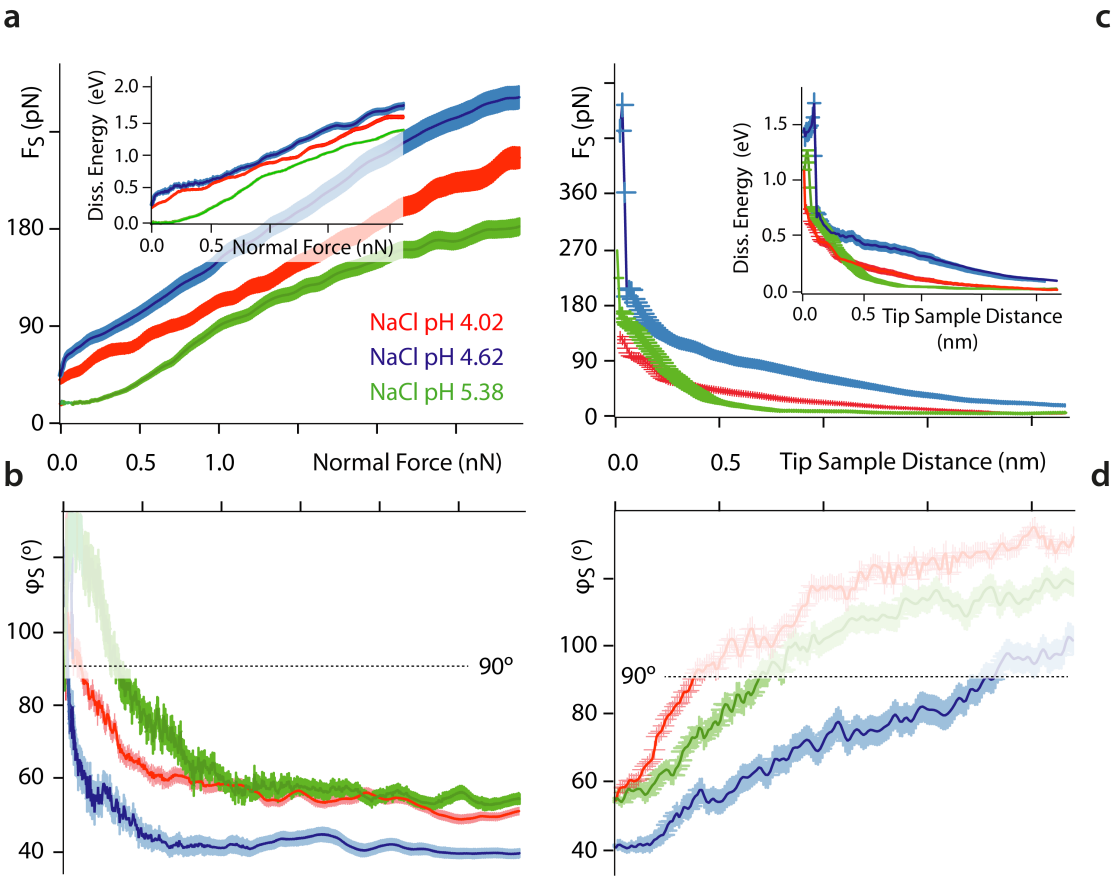

Fig. 4.9: Evolution of the shear force, F_S, energy dissipated per shear cycle and shear phase, ϕ_S, as functions of pH in NaCl. Results are shown for hard confinement (**a-b**) and soft confinement (**c-d**). The insets in (**a**) and (**c**) show the energy dissipated per shear cycle. The anomalous evolution of the shear response as a function of the pH is explained in light of high mobility and multiple solvation states for Na^+ [25, 63]. In (**b**) and (**d**), ϕ_S is undefined at large tip-sample distance and small confining forces due to the shear amplitude and hence force being close to the noise level ($\phi_S > 90°$, semi-transparent region). The experiments are performed at 298.0 ($\pm$ 0.1) K.

For $CaCl_2$ (Fig. 4.10), lowering the pH results in the expected increase in F_S and E_{diss} with ϕ_S showing a more pronounced elastic behaviour. The evolution is however similar at pH 4.62 and 4.02. At these pH values, hydronium ions seem to reach a plateau-like effect in displacing Ca^{2+} from the mica binding sites. This is tentatively explained due to the multiple hydration states and the adsorption of Ca^{2+} to both ditrigonal and interstitial sites [63].

In ultrapure water (Fig. 4.11), smaller changes in the shear response with pH are visible in

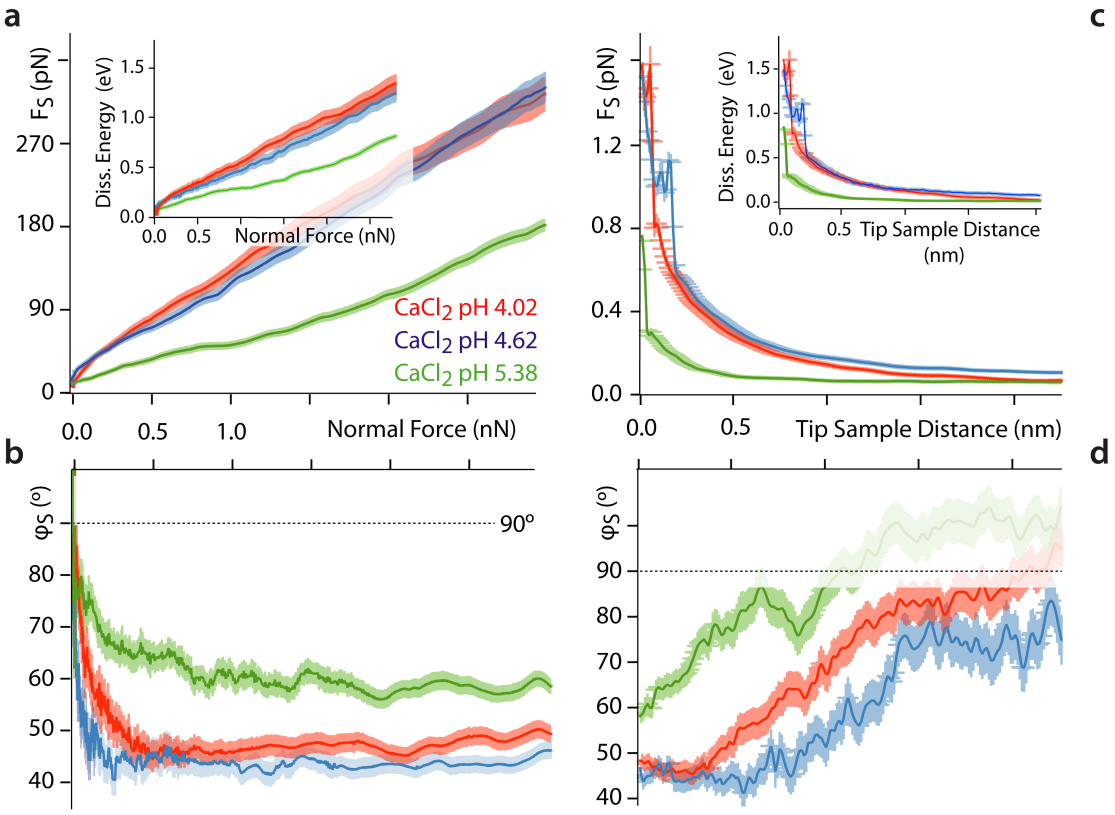

Fig. 4.10: Evolution of the shear force, F_S, energy dissipated per shear cycle and shear phase, ϕ_S, as functions of pH in $CaCl_2$. Results are shown for hard confinement (**a-b**) and soft confinement (**c-d**). The insets in (**a**) and (**c**) show the energy dissipated per shear cycle. In (**b**) and (**d**), ϕ_S is undefined at large tip-sample distance and small confining forces due to F_S being close to the noise level ($\phi_S > 90°$, semi-transparent region). The experiments are performed at 298.0 ($\pm$ 0.1) K.

comparison to the ionic aqueous solutions. This is however consistent with the hypothesis that the ions' size and concentration play a fundamental role in disrupting the glassy structure of the nano-confined liquid. The hydronium ion lies deep inside the ditrigonal cavities at the mica surface [72] and its hydrated radius may be too small to significantly affect the local hydrogen bond network.

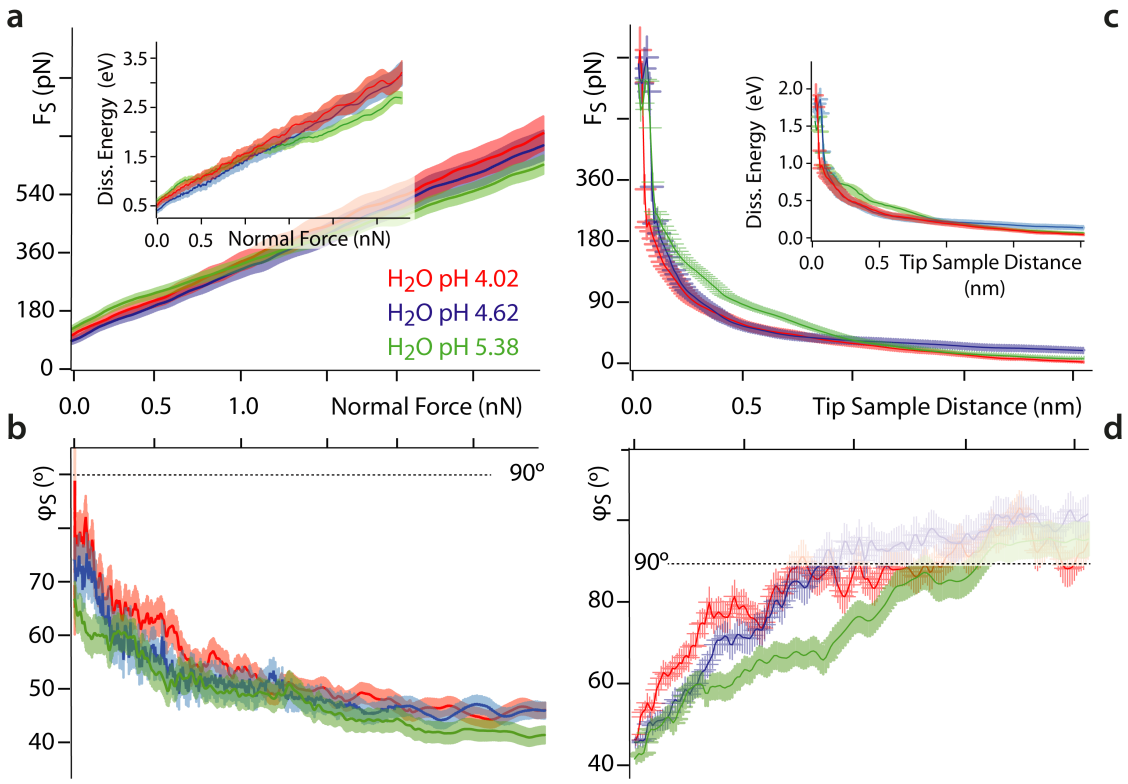

Fig. 4.11: Evolution of the shear force, F_S, energy dissipated per shear cycle and shear phase, ϕ_S, as functions of pH in pure water. Results are shown for hard confinement (**a-b**) and soft confinement (**c-d**). The absence of a clear trend is explained considering the similar hydration structures for H_3O^+ and pure water [36]. In (**b**) and (**d**), ϕ_S is undefined at large tip-sample distance and small confining forces due to F_S being close to the noise level ($\phi_S > 90°$, semi-transparent region). The experiments are performed at 298.0 ($\pm$ 0.1) K.

4.5 Summary

Within this Chapter, I have examined the nano-tribological properties of aqueous solutions under shear down to the single ion level. Results obtained in five different aqueous solutions (ultrapure water, RbCl, KCl, NaCl, and $CaCl_2$) and at different pH show that the behaviour of nano-confined water can be quantitatively interpreted in terms of the restructuring dynamics of its hydrogen bond network. Under strong confinement, the system is dominated by the thermally activated motion of ions between adjacent sites of the confining mica surface, with an energy barrier determined by the mica and the ions' hydration structures. The ions disrupt the otherwise ordered hydrogen bond network of the liquid and act as lubricants, whose effectiveness follows a direct Hofmeister series. Under softer confinement, the ions still disrupt water's hydrogen bond network, but ion-specificity is no longer obvious. Lowering the pH of the solution tends to replace adsorbed metal ions by hydronium, thereby rendering the system more elastic and increasing the

measured friction. High-resolution imaging reveals some mesoscopic ordering of ions within the Stern layer, suggesting that the nanoscale shear force measurements conducted here cannot be extrapolated directly from measurements involving larger confining areas and shear amplitudes. Further studies are needed to investigate the effect of the shearing velocity and extend the current findings to other ionic species, including for potential technological applications in the fields of energy and the design of the "ultimate green" water-based lubricants [13].

References: Chapter 4

[1] O. Bjorneholm et al., *Chemical Reviews* **2016**, *116*, 7698–7726.

[2] T. Li et al., *Physical Review B* **2007**, *75*, 115415.

[3] R. M. Berne et al., *Berne & Levy physiology*, Elsevier, **2008**.

[4] P. M. Wiggins, *Microbiology and Molecular Biology Reviews* **1990**, *54*, 432–449.

[5] R. Milke et al., *Contributions to Mineralogy and Petrology* **2007**, *154*, 519–533.

[6] M. Ricci et al., *Langmuir* **2013**, *29*, 2207–2216.

[7] T. Underwood et al., *Clays and Clay Minerals* **2016**, *64*, 472–487.

[8] S. Granick et al., *Physics* **2010**, *3*, 73.

[9] R. J. Mashl et al., *Nano Letters* **2003**, *3*, 589–592.

[10] F. Ridi et al., *Journal of Colloid and Interface Science* **2011**, *357*, 255–264.

[11] H. Stanley et al., *Journal of Physics: Condensed Matter* **2010**, *22*, 284101.

[12] D. Bradshaw et al., *Chemical Society Reviews* **2012**, *41*, 2344–2381.

[13] S. Liu et al., *Journal of Applied Physics* **2010**, *108*, 084315.

[14] N. Giovambattista et al., *Physical Review Letters* **2009**, *102*, 050603.

[15] E. Tombari et al., *The Journal of Chemical Physics* **2005**, *122*, 104712.

[16] R. Zangi, *Journal of Physics: Condensed Matter* **2004**, *16*, S5371.

[17] T. Mitsui et al., *Science* **2002**, *297*, 1850–1852.

[18] T. Li et al., *Physical Review Letters* **2008**, *100*, 106102.

[19] M. J. DelloStritto et al., *Langmuir* **2016**, *32*, 11353–11365.

[20] N. Giovambattista et al., *Physical Chemistry* **2012**, *63*, 179.

[21] S. Smirnov et al., *ACS Nano* **2010**, *4*, 5069–5075.

[22] L. Liu et al., *Physical Review Letters* **2005**, *95*, 117802.

[23] W. H. Briscoe et al., *Nature* **2006**, *444*, 191–194.

[24] M. Ricci et al., *Scientific Reports* **2017**, *7*, 1–12.

[25] M. Ricci et al., *Nature Communications* **2014**, *5*.

[26] K. Voitchovsky et al. in Colloidal Nanocrystals for Biomedical Applications VII, **2012**, 82320O.

[27] M. Ricci et al., *Journal of Non-Crystalline Solids* **2015**, *407*, 418–422.

[28] D. Argyris et al., *ACS Nano* **2010**, *4*, 2035–2042.

[29] U. Raviv et al., *Langmuir* **2004**, *20*, 5322–5332.

[30] D. Ortiz-Young et al., *Nature Communications* **2013**, *4*, 1–6.

[31] A. Malani et al., *The Journal of Chemical Physics* **2012**, *136*, 194701.

[32] A. Gaisinskaya-Kipnis et al., *Langmuir* **2016**, *32*, 4755–4764.

[33] A. Ulcinas et al., *Langmuir* **2011**, *27*, 10351–10355.

[34] G. Zhao et al., *The Journal of Chemical Physics* **2015**, *143*, 104705.

[35] I. Waluyo et al., *The Journal of Chemical Physics* **2011**, *134*, 064513.

[36] L. Cheng et al., *Physical Review Letters* **2001**, *87*, 156103.

[37] S. Cerveny et al., *The European Physical Journal Special Topics* **2007**, *141*, 49–52.

[38] W. Qi et al., *The Journal of Physical Chemistry B* **2013**, *117*, 7967–7971.

[39] H. Sakuma et al., *Physical Review Letters* **2006**, *96*, 046104.

[40] S. Perkin et al., *Faraday Discussions* **2009**, *141*, 399–413.

[41] C. Dushkin et al., *Colloids and Surfaces A* **1997**, *129*, 131–139.

[42] H. Kawai et al., *Review of Scientific Instruments* **2008**, *79*, 043701.

[43] U. Raviv et al., *Science* **2002**, *297*, 1540–1543.

[44] S. H. Khan et al., *Physical Review Letters* **2010**, *105*, 106101.

[45] T. Fukuma et al., *Applied Physics Letters* **2005**, *87*, 034101.

[46] D. Naumenko et al., *Analyst* **2013**, *138*, 5371–5383.

[47] A. Shiotari et al., *Nature Communications* **2017**, *8*, 1–7.

[48] E. J. Miller et al., *Journal of Visualized Experiments* **2016**, e54924.

[49] C. Cafolla et al., *Science Advances* **2020**, *6*, eaaz3673.

[50] J. Klein et al., *Journal of Physics: Condensed Matter* **2004**, *16*, S5437.

[51] J. Klein, *Friction* **2013**, *1*, 1–23.

[52] A. Gaisinskaya et al., *Faraday Discussions* **2012**, *156*, 217–233.

[53] Y. Leng et al., *Physical Review Letters* **2005**, *94*, 026101.

[54] A. Malani et al., *The Journal of Physical Chemistry B* **2009**, *113*, 13825–13839.

[55] S. S. Lee et al., *Nature Communications* **2017**, *8*, 1–9.

[56] I. Siretanu et al., *Scientific Reports* **2014**, *4*, 4956.

[57] F. H. van der Heyden et al., *Nano Letters* **2007**, *7*, 1022–1025.

[58] C. Park et al., *Langmuir* **2008**, *24*, 13993–14004.

[59] H.-J. Butt et al., *Nanotechnology* **1995**, *6*, 1.

[60] K. Voitchovsky et al., *Nature Nanotechnology* **2010**, *5*, 401–405.

[61] A. C. Fischer-Cripps, *Introduction to contact mechanics*, Springer, **2007**.

[62] T. Fukuma et al., *Physical Review Letters* **2010**, *104*, 016101.

[63] K. Kobayashi et al., *Langmuir* **2017**, *33*, 3892–3899.

[64] Y. Leng et al., *The Journal of Chemical Physics* **2006**, *124*, 074711.

[65] M. Odelius et al., *Physical Review Letters* **1997**, *78*, 2855.

[66] A. Verdaguer et al., *Chemical Reviews* **2006**, *106*, 1478–1510.

[67] P. Miranda et al., *Physical Review Letters* **1998**, *81*, 5876.

[68] J. S. Kim et al., *The Journal of Physical Chemistry B* **2008**, *112*, 1729–1735.

[69] B. Hribar et al., *Journal of the American Chemical Society* **2002**, *124*, 12302–12311.

[70] I. Topol et al., *The Journal of Chemical Physics* **1999**, *111*, 10998–11014.

[71] J. E. Combariza et al., *The Journal of Physical Chemistry* **1995**, *99*, 2717–2723.

[72] S. S. Lee et al., *Langmuir* **2012**, *28*, 8637–8650.

[73] H. Sakuma et al., *Geochimica et Cosmochimica Acta* **2011**, *75*, 63–81.

[74] S. Pintea et al., *Langmuir* **2016**, *32*, 12955–12965.

[75] K. Kimura et al., *The Journal of Chemical Physics* **2010**, *132*, 194705.

[76] E. Gnecco et al., *Journal of Physics: Condensed Matter* **2001**, *13*, R619.

[77] A. Vanossi et al., *Reviews of Modern Physics* **2013**, *85*, 529.

[78] A. Erbas et al., *Journal of the American Chemical Society* **2012**, *134*, 623–630.

[79] C. Park et al., *Physical review letters* **2006**, *97*, 016101.

[80] S. H. Khan et al., *Langmuir* **2016**, *32*, 10802–10807.

[81] J. Kestin et al., *Journal of Physical and Chemical Reference Data* **1978**, *7*, 941–948.

[82] T.-D. Li et al., *Review of Scientific Instruments* **2014**, *85*, 123707.

[83] L. Piantanida et al., *Biophysical Journal* **2017**, *113*, 426–439.

5.0 Lubricated friction around surface nano-defects

God made the bulk; the surface was invented by the devil.
Wolfgang Ernst Paul, as quoted in Growth, Dissolution, and Pattern Formation in Geosystems 1999

5.1 Overview

The lubrication properties of nanoconfined liquids underpin countless natural and industrial processes. Our current understanding of lubricated friction is still limited, especially for non-ideal interfaces exhibiting nanoscale chemical and topographical defects. In this Chapter, I use atomic force microscopy to explore the equilibrium and dynamical behaviour of a model lubricant, squalane, confined between a diamond tip and graphite in the vicinity of an atomic step. I combine high-resolution imaging of the interface with highly localized shear measurements at different velocities and temperatures to derive a quantitative picture of the lubricated friction around surface defects. The Chapter shows that defects tend to promote local molecular order and increase friction forces by reducing the number of stable molecular configurations in their immediate vicinity. The effect is general, can propagate over hundreds of nanometers, and can be quantitatively described by a semiempirical model that bridges the molecular details and mesoscale observations. The bulk of this Chapter has been published as an article: Lubricated friction around nanodefects. Science Advances 2020, 6: eaaz3673.

5.2 Introduction

Within Chapter 1, in particular Section 1.2, we have seen that friction plays a crucial role in many phenomena, ranging from the molecular diffusion of solutes within cells [1] and the function of our joints [2] to industrial machinery, car engines [3], and tectonic dynamics [4]. The ubiquitous importance of friction is perhaps best illustrated by the fact that

it accounts for more than 25% of the world's current energy consumption [3]. In most systems, friction forces can be reduced by the presence of a lubricant between the moving solid parts. The lubricant is typically arranged in a thin layer confined between the solids and modulates the magnitude and the dynamics of tribological contacts [3]. However, a comprehensive description of the molecular-level mechanisms underpinning lubricated friction is still lacking [5]. This is largely due to the fact that our understanding of friction and lubrication is based on semiempirical macroscopic models [6, 7], with no clear or direct links between molecular-level effects and the macroscopic forces they produce [7]. For lubricating films confined in nanoscale gaps, the behaviour of the lubricant tends to be dominated by that of the boundary layer directly in contact with the confining solid [8–10]. This boundary layer behaves very differently than the bulk fluid because of reduced configurational entropy. Furthermore, its interactions with the solid and nanoscale surface singularities can markedly alter the local fluid dynamics. Examples include local molecular segregation [11], superlubricity [9, 12, 13], and cooperative molecular effects [14], but the underpinning mechanisms are poorly understood. Molecular-level measurements are challenging [9, 11–13, 15–18], and often strongly depend on the precise nanoscale location probed [9, 11, 19]. Since most lubricated systems are imperfect with nanoscale roughness and chemical inhomogeneities at the surface of the solids [20], there is a critical need for *in situ* experimental investigations able to map the molecular details of the boundary layer around surface singularities and directly quantify the local lubrication behaviour at the nanoscale.

The present Chapter combines *in situ* experiments conducted locally with subnanometer precision and molecular dynamics (MD) computer simulations to investigate the molecular organization and dynamics of nanoconfined squalane near atomic steps of a graphite substrate. As shown in Fig. 5.1, squalane is a branched alkane with six methyl sidegroups [16] and is often used as a model lubricant in the formulation of engine oils [21] and in pharmaceutical products [22]. Because of the conformational constraints imposed

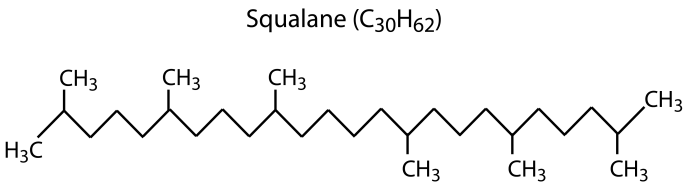

Fig. 5.1: Skeletal formula of squalane. IUPAC name: 2,6,10,15,19,23-hexamethyltetracosane [23].

by the side branches [24], squalane does not naturally form ordered layers but exhibits a pronounced interdigitation between adjacent molecules [25], enhancing its lubrication properties. Understandably, the nanoscale behaviour of squalane as a model lubricant has been extensively investigated with numerous techniques [11, 16–18, 24–35]. However,

as in the case of water discussed in Chapter 4 Section 4.2, the behaviour of squalane under confinement remains a matter of debate. Equilibrium surface force apparatus (SFA) experiments using two atomically smooth mica surfaces as confining solids [16–18] revealed no oscillatory force profile, suggesting a lack of ordered molecular arrangement. Shearing SFA measurements, however, yielded contradictory results [17, 18], and it is still not clear whether the lubricant molecules can realign along the shear direction or rather along the crystallographic directions of the solid [16]. In contrast, atomic force microscopy (AFM) measurements routinely identified an oscillatory solvation force profile when confining the squalane between a silicon tip and a smooth graphite surface [18, 36] with at least four layers visible [36]. The average layer thickness of ~ 0.6 nm is larger than would be expected for well-aligned squalane molecule, suggesting confined squalane to behave as an amorphous material with only short-range order. This view is also supported by He atom scattering, neutron scattering experiments, and x-ray reflectivity [31, 32]. It should be pointed out that the confinement pressure in AFM measurements is typically six orders of magnitude larger than in SFA because of the highly localized measurement [36]. In addition, the use of hydrophobic graphite may favour the formation of ordered squalane structures at its interface [18]. Lamellar structures have indeed been observed by scanning tunneling microscopy [28], and ordered structured of nanoconfined asymmetric molecules are also predicted by various theoretical studies based on molecular simulations [26, 37–39].
Together, these studies suggest a strong dependence of the squalane behaviour on the local nanoscale details of the confinement, with chemistry, geometry, and pressure all playing a role in the molecular arrangement of the lubricant. As highlighted in Chapter 4 Section 4.2, SFA experiments may average out localized effects [9, 18, 36], requiring measurements on the same scale as typical surface singularities of solids. To tackle this issue, high-resolution AFM measurements are conducted combining *in situ* molecular-level imaging and highly localized shearing measurements of squalane near and at atomic steps of highly orientated pyrolytic graphite (HOPG). AFM and complementary MD results help disentangle local surface effects from the altered thermodynamics of nanoconfined lubricants at interfaces and provide quantitative molecular-level insights into the impact of surface singularities. The impact of temperature and shearing velocity on the system are also explored to derive a simple molecular model that quantitatively explains the observations.

5.3 Experimental

5.3.1 Sample preparation

The experiments were performed on a freshly cleaved HOPG substrate (SPI Supplies, West Chester, PA). Further experiments were conducted using a freshly cleaved molybdenum

disulfide (MoS_2) substrate (SPI supplies, West Chester, PA, USA). MoS_2 and HOPG sheets were mounted on stainless steel disks, as described in Chapter 2 Section 2.3.1. High-performance liquid chromatography grade squalane with a purity of $\geq 99\%$ was purchased from Sigma-Aldrich and used without any further purification (St. Louis, MO, USA).

5.3.2 AFM measurements

Imaging and shear spectroscopy were conducted using a commercial Cypher ES AFM (Oxford Instruments, Santa Barbara, CA, USA), equipped with temperature control. All the experiments were conducted with a DLC-coated cantilevers (MikroMasch HQ:NSC18/HARD/AL BS, Apex Probes Ltd., UK) with nominal flexural spring constant, k_f, equal to 2.8 N/m (range 1.2 to 5.5 N/m). Each cantilever was calibrated using its thermal spectrum [40] and found to have typical stiffness within the nominal range and Q factor of 1.1 ± 0.2 in liquid. The method described in Chapter 3 was used to calibrate the torsional cantilever inverse optical lever sensitivity and spring constant, k_t, returning a value for $k_t = 92 \pm 2$ N/m [41].

Five cantilevers were randomly selected and imaged using scanning electron microscopy (SEM), either before or after conducting the experiments (including imaging and shear-force measurements). The cantilevers were not gold-coated before SEM imaging due to avoid overestimating the apex's size. The SEM analysis was performed with a commercial FEI Helios SEM system (Dawson Creek Drive Hillsboro, Oregon 97124 USA). Images were collected using a 3 kV electron beam in vacuum and the current set to 0.17 nA. Representative SEM images are shown in Fig. 5.2, further confirming the reliability of the AFM measurements with no significant change in the shape or radius of the probes after the experiments. Accurate calculation of the tip radius is challenging due to the fact that it is not perfectly spherical and the SEM image imperfect. To take this into account and determine a meaningful uncertainty, fitting of the apex was carried out with two different circles by either placing the weight on the very apex (smaller circle) or on the overall tip (larger circle). The average radius for all the cantilevers analyzed was found to lie between 34 nm and 43 nm.

All the AFM imaging and shear experiments were conducted at thermal equilibrium. Thermal equilibrium was assumed when the heating/cooling rates of the temperature control system had been constant for, at least, 15 min. Each series of experiments (including imaging and spectroscopy) was repeated, at least, three times so as to ensure reproducibility of the data.

An accurate cleaning procedure was performed so as to remove any possible sources of contamination (see Chapter 2 Section 2.3). The absence of contaminants was confirmed by subnanometric imaging of the area investigated [9, 42].

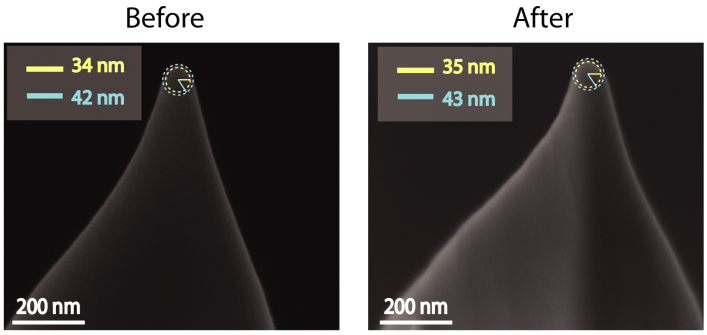

Fig. 5.2: Representative images of the AFM probes obtained by scanning electron microscopy (SEM) images. Randomly selected tips were analyzed either before or after the AFM measurements (including imaging and shear spectroscopy), with no significant changes visible. The tip radius is quantified by fitting the tip apex with a circle on the SEM image (dashed circles). To account for apex non-sphericity and uncertainties related to the SEM image quality, two limit cases are considered with a smallest and largest possible circle (yellow and blue, respectively). The resulting tip radius value in this image is the average of the extrema: 38 ± 4 nm.

Chapter 2 Sections 2.2 and 2.5 provided with a detailed description of the AFM imaging and shear spectroscopy techniques, as well as MD simulations. Hereafter, I will recall the aspects most relevant for the present Chapter.

Imaging

The AFM was operated in amplitude modulation, fully immersing the cantilever tip in liquid. In this mode, the cantilever was acoustically oscillated at a frequency close to its resonance, and the probe oscillation amplitude, A, was kept constant. The phase difference, ϕ, between the driving and the tip oscillation was allowed to vary freely. The ratio A/A_0, between the free amplitude, that is, away from the surface and the working amplitude, was optimized so as to keep it as high as possible, with A being between 0.8 and 1.5 nm. This allows resolving atomic details of the interface and any mesoscale structure [9, 42, 43].

Shear force spectroscopy

Shear force mode allows using the AFM as a nanoscopic linear rheometer so as to study the dynamic behaviour of the lubricant molecules under an applied shear [9, 11, 43]. The method has been extensively described in Chapter 2 Section 2.2.3. Also here, the sample was subjected to a lateral oscillation at 1.1 kHz, that is, below the resonance frequency of the scanner and the amplitude of the oscillation was 0.5 nm. For the experiments on the impact of shear velocity, the oscillation amplitude was set so as to achieve the desired speed. For each location explored, a minimum of 20 shear force spectroscopy curves were acquired and consequently averaged. The data were analyzed using homemade programs developed in Igor Pro (WaveMetrics, Lake Oswego, OR, USA) and Python. Before and after changing

location for force spectroscopy measurements, high-resolution imaging ensured that no shifts of the sample had taken place affecting the area under investigation.

5.3.3 MD simulations

MD simulations were performed as described in Chapter 2 Section 2.5.

5.4 Results and discussion

5.4.1 Molecular ordering near surface defects at equilibrium

The simplest and most common surface singularities at the surface of graphite are step edges. To examine the equilibrium organization of squalane molecules near an HOPG step, high-resolution amplitude modulation AFM imaging was conducted with both the imaging tip and the HOPG immersed into squalane (Fig. 5.3 and 5.4).

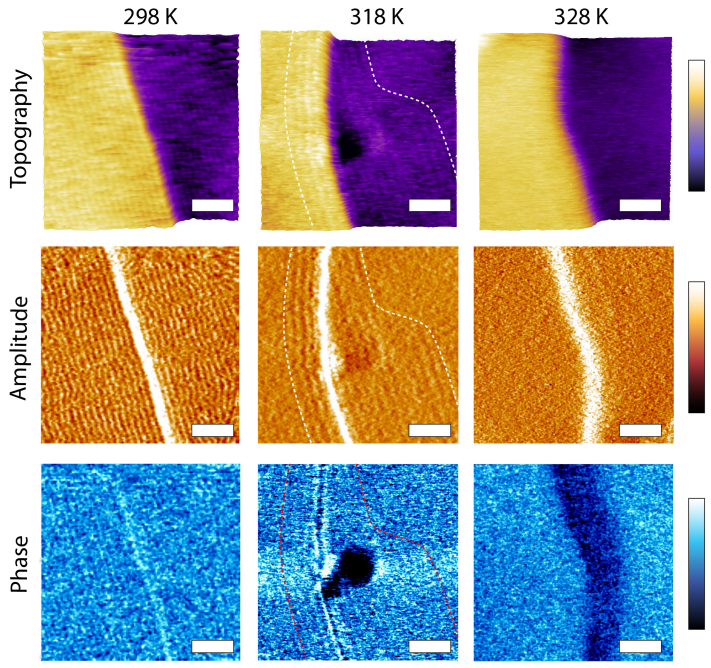

Fig. 5.3: High-resolution amplitude modulation AFM imaging of squalane molecules at the surface of HOPG near an atomic step at 298 K, 318 K, and 328 K. Topography, amplitude, and phase images are acquired simultaneously. At 298 K, periodic longitudinal structures running parallel to the step extend over the whole surface and are visible in all three channels. The darker region in phase suggests less mobile squalane molecules [11]. As the temperature increases, the squalane-based structures progressively retreat to within tens of nanometers of the step (highlighted by the dashed lines at 318 K) to lastly disappear completely at 328 K. Scale bars, 30 nm. The color bars for the topography, amplitude, and phase channels represent variations of 1.0 nm, 0.4 nm, and 2.0°, respectively.

High-resolution imaging of the squalane-HOPG interfaces shows that squalane molecules

tend to adopt a row-like equilibrium arrangement near step edges at room temperature. The arrangement is present both at the top and the bottom of the step but tends to progressively vanish when moving away from the step or when the temperature is increased, here, above 323 K (Fig. 5.3). This result is consistent with the squalane molecules progressively becoming more mobile away from step edges, rendering the ordered row-like molecular organization either invisible over the time scale of the AFM measurement ($\sim$ 100 s per image) or destroying it together.

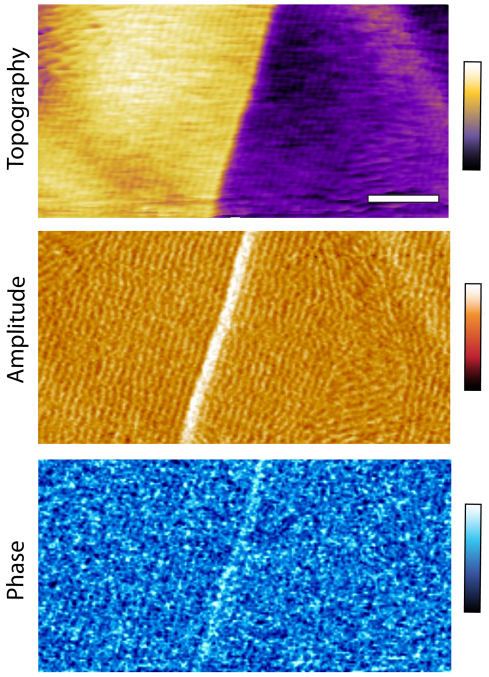

Fig. 5.4: High-resolution amplitude modulation AFM imaging of squalane molecules at 298 K, showing the formation of domains with different orientations close to surface defects. This is due to the step edge limiting the number of configurations the squalane molecules can explore. Epitaxial effects on HOPG determine the organization of domains at about at 60°. The scale bar is 50 nm in all the images. The color bars for the topography, amplitude, and phase channels represent variations of 1.0 nm, 0.4 nm, and 2.0°, respectively.

5.4.2 Spatial extent of the influence of defects on lubricated friction

To get a quantitative dynamical picture of the lubricant, it is necessary to go beyond high-resolution imaging of the interface at equilibrium. To achieve this, I have conducted highly localized shear measurements of the nanoconfined squalane molecules along the interface. This is achieved by using the AFM as a nanoscale linear shear rheometer with the tip oscillating laterally at a set distance from the surface. Using small shear amplitudes ($\sim$ 0.5 nm) and the nanopositioning system of the AFM to place the tip,

it is possible to conduct highly localized shear measurements at any desired location visible in the high-resolution image [9, 11, 43] (see Chapter 2 Section 2.2.3). Results of the shear measurements are presented in Fig. 5.5b and 5.5d as a function of the distance from the step edge, d_{se}. The shear force, F_S, is an absolute measurement of

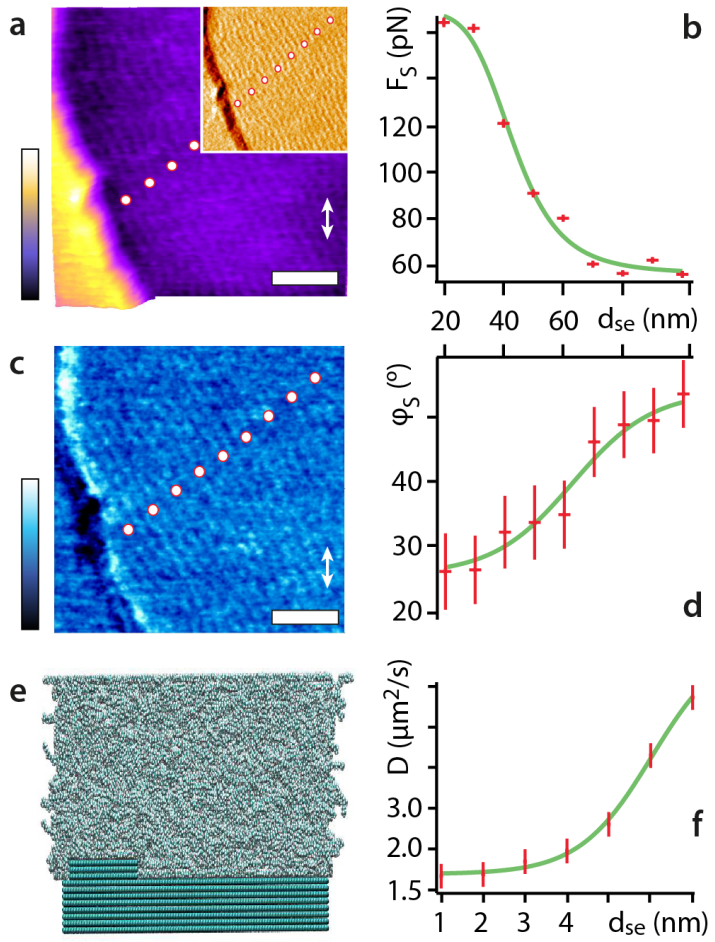

Fig. 5.5: Shear behaviour of squalane molecules near an HOPG step edge at 298 K. The row-like arrangement parallel to the edge is visible over the whole AFM images (**a** and **c**). The inset in (**a**) shows variations in the scanning amplitude where the contrast over the rows is clearer. Shear force spectroscopy measurements taken at set distances d_{se} from the step reveal a decrease in lubricated friction force (shear force, F_S) (**b**) and increase in the shear phase, ϕ_S, (**d**) when moving away from the step. F_S and ϕ_S are taken at an applied lateral force, F_L, $\sim$ 30 nN. The shear direction is illustrated by the white double-headed arrows in (**a**) and (**c**). Consistently, MD simulations (unit cell of 34.1 nm $\times$ 7.2 nm $\times$ 11.8 nm with $\sim$ 3000 squalane molecules) (**e**) show an increase in squalane diffusion constant, D, when moving away from the step edge at the interface (averaged within 1.2-nm layer above the HOPG surface) (**f**). Quantitative comparison between AFM and MD measurements is difficult because of limited size of the simulation box (see Chapter 2 Section 2.5.5 and in particular Fig. 2.14). The error on F_S, ϕ_S, and D is the standard error in each case. Using the z-piezo noise (nominal value $<$ 50 pm) and the error on the flexural spring constant k_f (see this Chapter Section 5.3), it is possible to derive the error on the deflection signal and on F_L [9]. Scale bars, 25 nm. The color bars in (**a**) and (**c**) represent height variations of 1.2 nm (0.6 nm for inset) and phase variations of 3.0°, respectively.

the average lubricated friction experienced by the tip, and the shear phase, ϕ_S, quantifies the viscoelastic properties of the confined lubricant (not to be confused with the imaging phase). With a confinement area of ~ 20 nm^2 [44] (see Fig. 5.2 for a detailed analysis on the AFM tips), F_S can be expressed also as a function of the confining pressure [9, 11, 43]. An increase of 1 nN in the applied load increases the confining pressure by ~ 50 MPa. This makes the present set-up suitable to probe the lubricant film in the high-pressure regime typical of mechanical applications [3]. Punctual shear measurements taken at different distances from the step edge show a progressive reduction in F_S and an increase in ϕ_S when moving away from the edge, both consistent with the hypothesis of squalane molecules becoming progressively more mobile and hence less able to resist the applied shear (Fig. 5.5b and 5.5d). The transition occurs over a relatively large distance (~ 100 nm), ruling out any tip or convolution effects at the step. This demonstrates that the increase in lubricated friction in proximity of a step edge is not a direct geometrical effect of the tip meeting a rougher area but rather the indirect result of a localized molecular ordering induced by the surface features of HOPG. As shown in Fig. 5.6, row-like domains can be found both at the bottom and at the top of the step edge, with a symmetrical behaviour of the lubricated friction as a function of distance from the singularity. This confirms that the molecular order is a general consequence of the existence of surface singularities and not specific to molecules being stabilized by the edge at the bottom of the step.

The measurements were conducted with diamond-like carbon (DLC)-coated AFM probes to ensure a system as symmetrical as possible with the model lubricant confined between two hydrophobic surfaces [45]. This ensures that molecular ordering of the lubricant is not due to a significant difference in the affinity between the squalane molecules and the confining surfaces. The use of DLC tips also offers other advantages over standard hydrophilic silicon tips [36] such as a high wear resistance and better reproducibility of the shear measurements [46]. Measurements with DLC-coated tips also better represent tribological contacts given the wide variety of DLC-coated components in mechanical systems [45, 46].

The behaviour observed experimentally at the HOPG step edge could be qualitatively reproduced using MD simulations, albeit on smaller distances from the step due to computational costs (34.1 nm $\times$ 7.2 nm $\times$ 11.8 nm simulation box with ~ 3000 squalane molecules and 8 layers of graphene; Fig. 5.5e). Despite being limited in size and duration, simulations offer a precious point of comparison for the AFM measurements because they are conducted without the AFM tip being present. Since the tip both imposes the confinement and quantifies its effect, examining the behaviour naturally adopted by unconfined squalane molecules near the step edge validates the interpretation of the molecular mechanisms at play in the experimental measurements. In addition, MD simulations allow the investigation of the step edge itself, a region difficult to

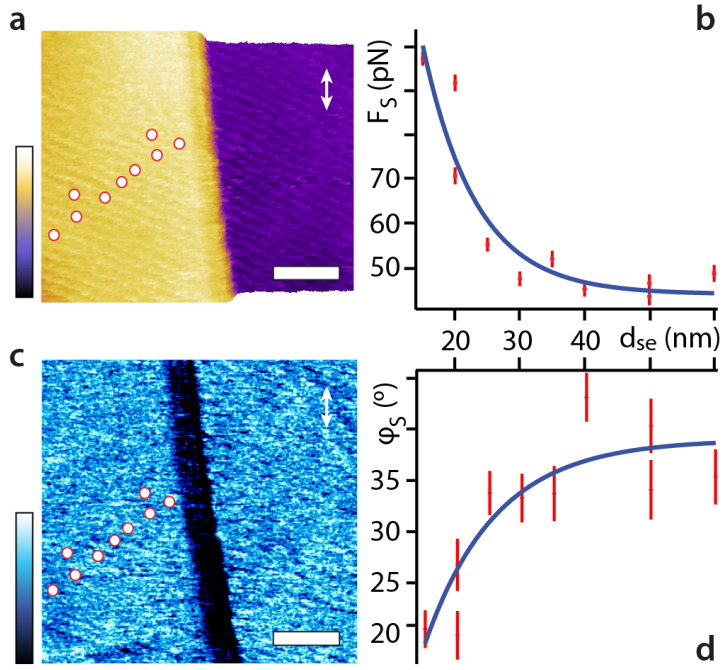

Fig. 5.6: Molecular ordering of squalane molecules at the top of the step edge. High-resolution amplitude modulation AFM images (**a-c**) show the organization of the molecules into row-like domains parallel to the step edge. Shear force spectroscopy measurements taken at set distances d_{se} from the step reveal a decrease in lubricated friction force (shear force, F_S) (**b**) and increase in the shear phase ϕ_S (**d**) when moving away from the step. F_S and ϕ_S are taken at an applied lateral force $F_L \sim 30$ nN. The shear direction is illustrated by the white arrow (**a-c**). The color bars in (**a**) and (**c**) represent height variations of 1.2 nm and phase variations of 3.0° respectively. The scale bar is 35 nm in all the images. The experiments were performed at 298 K.

unambiguously probe with AFM because of tip convolution effects, which could potentially affect the results. The translational mobility of the squalane molecules is quantified calculating their average diffusion constant, D, averaged over a 1.2 nm thick band above the HOPG surface (Fig. 5.5f). A significant increase in D can be observed from ~ 5 nm from the step edge and growing beyond the d_{se} distances simulated here. The threefold increase in the squalane diffusion coefficient matches remarkably well the magnitude of the reduction in F_S measured with AFM. The full spatial extent of the effect cannot be probed by MD simulation because of the finite size of the simulation box (see Chapter 2 Section 2.5.5 and the representative results shown in Fig. 2.14), but the MD results clearly confirm the fact that squalane molecules move more freely away from the step, along the x-y plane parallel to the step edge itself. The simulations also show an increase in the lateral layering of the squalane molecules close to the step edge, confirming the AFM observation that surface singularities promote molecular order (see Fig. 2.13 in Chapter 2 Section 2.5.5). Furthermore, the simulations show that the average orientation of squalane molecules tends to be aligned to the step edge when in close proximity but progressively lose this alignment at larger distances with no clear ordering for $d_{se} > 6$ nm (Fig. 2.15 in

Chapter 2 Section 2.5.5). This step-induced molecular orientation is consistent with the row-like features observed in AFM image (Figs. 5.3 - 5.6).

Overall, both the AFM and MD results show that a reduction of the lubricant's configurational entropy near surface singularities could provide an alternative molecular mechanism for the well-known increase in roughness-related friction routinely observed macroscopically between two solid surfaces [47–49]. In this framework, the roughness-induced increase in friction around surface defects could be an indirect effect in lubricated systems, a result of molecular ordering in the vicinity of surface singularities, and not dominated by direct solid-solid contacts at singularities. In such systems, the roughness of a solid would determine the density of singularities but not directly the friction force itself. Here, the more ordered squalane molecules have a reduced mobility, inducing larger lubricated friction force.

5.4.3 Impact of the precise molecular ordering around defects

The dominating role of the defect's "vicinity regions" in modulating the lubricated friction makes them particularly important to understand and model the process at the molecular level. Before examining the dynamical behaviour of the lubricant molecules in these regions, I have explored the impact of the local equilibrium molecular arrangement by performing shear measurements at locations exhibiting different row orientations around a same step (Fig. 5.7a-c). These regions could occasionally be found at lower temperature due to epitaxial effects on the HOPG and are typically orientated at 60° from each other (Fig. 5.7a-c; and also Figs 5.4 and 5.9). This also confirms the existence of row-like molecular arrangements both at the top and the bottom of the step near the edge (see also Figs 5.3, 5.4 and 5.6). When shearing parallel to the row-like features, the tip must disrupt a coherent molecular assembly along its whole path, whereas shearing at an angle allows the tip to "section" more easily the row-like features, hence limiting the experienced F_S (Fig. 5.7d). No significant differences in ϕ_S are observed (Fig. 5.8), but a viscoelastic response is always present, confirming that the AFM tip probes the shear response of the confined lubricant and not of the surface itself. These results confirm the importance of the vicinity regions to modulate friction, with the equilibrium molecular arrangement alone able to decrease F_S by more than 50% (Fig. 5.7d-e).

Figure 5.9 further confirms the impact of domain orientations on the lubrication friction force. Shear measurements conducted directly on the step edge show that lubricated friction force is no larger than on the well-ordered adjacent molecular domains, demonstrating that direct tribological contacts with the step and the tip do not dominate the friction. Here, lubricant molecules are arranged into rows both at the top and at the bottom of the step edge. Epitaxial effects on HOPG may also contribute to the domains

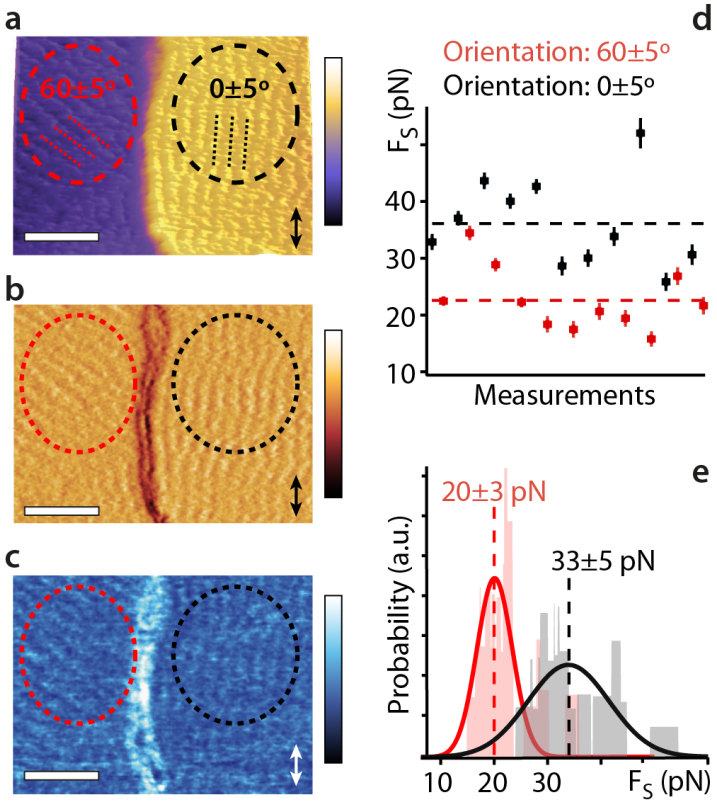

Fig. 5.7: Impact of the molecular ordering of squalane on the lubricated friction force. High-resolution topographic (**a**), amplitude (**b**), and phase (**c**) AFM images of the molecular arrangement of squalane at the interface with HOPG near a step. Domains with different row orientations are visible (dashed red and black circles). Shear force measurements show a clear sensitivity to the rows orientation with statistically higher F_S values when shearing parallel to the rows (**d-e**). Multiple measurements taken over the two regions (**a** to **c**) statistically confirm the dependence on the rows orientation (**e**). Scale bars, 25 nm. The imposed shear direction is indicated with a double-headed arrow (**a** to **c**). The dashed lines in (**d**) and (**e**) represent mean force values. The color bars represent total variations of 5.0 nm height (**a**), 0.2 nm (**b**), and 10.0° (**c**). The shear forces in (**d**) and (**e**) are taken at an applied load of F_L of 12 nN, and the measurements were performed at 298 K. a.u., arbitrary units.

being oriented at about at 60° from each other (Figure 5.9a-c). The lubricant domains oriented parallel to the shearing direction induce the largest shear (Figure 5.9d), larger than directly on the step edge. It should be pointed out that accurately probing the lubricated response on the step edge poses some challenges. Even if thermal stability is ensured (see Section 5.3 in this Chapter), there can be some drift of a few nanometers along the direction perpendicular to the shearing, leading to the tip also probing the geometry of the step itself or the ordered region close to the step. However, such problems would tend to increase the measured forces, confirming the dominating role played by molecular ordering.

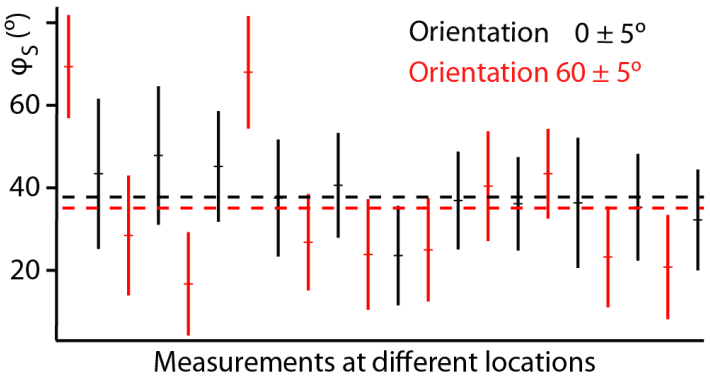

Fig. 5.8: Shear phase, ϕ_S, associated with the lubrication force presented in Fig. 5.7. ϕ_S values are taken at an applied load of 12 nN. No clear distinction can be seen between the two different row orientations, but ϕ_S values indicate that the interfacial lubricant is in a viscoelastic regime.

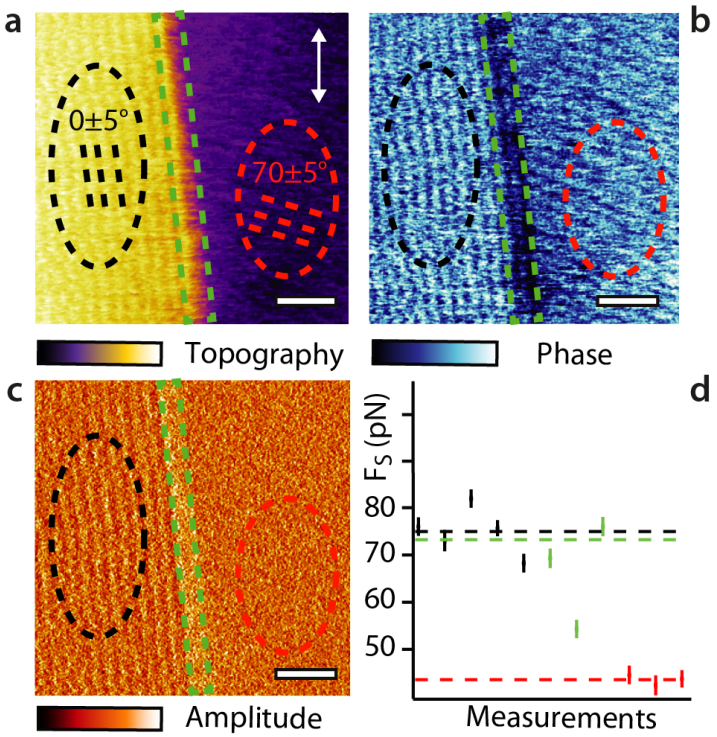

Fig. 5.9: High-resolution amplitude modulation AFM images. The topography (**a**), phase (**b**) and amplitude (**c**) images show, around the step edge, different row orientations for the lubricant molecules. The orientations result in significantly different lubricated friction forces as shown in (**d**). The imposed shearing direction is perpendicular to the image as shown by the arrows in (**a**). The scale bar is 20 nm in all the images. The color bars in (**a**), (**b**) and (**c**) represent variations of 1.0 nm, 2.0°, and 0.1 nm, respectively. The experiments were performed at 298 K.

5.4.4 Impact of shearing velocity and temperature on the lubrication force

Lubricated friction is, however, inherently a dynamical process, and insights into the local molecular dynamics are needed to capture the underpinning mechanisms at play. To quantitatively tackle this issue, I exploited the two distinct experimental handles on the lubricant's molecular dynamics offered by the AFM setup: the average shear velocity, v, of the AFM tip and the temperature, T, of the system. Both variables modulate the relaxation dynamics of the molecules under shear and hence the magnitude of F_S. Representative results showing the evolution of F_S with the applied load, F_L, are presented in Fig. 5.10a-b for different v values at $T = 308$ K. Similar curves can be obtained when varying temperature at a given shear velocity.

The curves exhibit a first regime characterized by a rapid increase in F_S, followed by a second regime where it reaches a plateau that increases slowly with F_L (Fig. 5.10a). The initial increase plays the role of a yield stress, Y_0, likely induced by the local destruction of the lubricant equilibrium molecular arrangement with the tip having to overcome strong cooperative interactions between the squalane molecules. This interpretation is also supported by ϕ_S exhibiting a close to elastic behaviour during the yielding process (Fig. 5.10b). The yield stress depends strongly on the shear velocity and temperature, as to be expected for the activated process of intermolecular bonds rupture [52]. As F_S further increases, the second plateau-like regime emerges, with a weak dependence on the applied load and a more viscous behaviour (Fig. 5.10a-b). When in this second regime and for a given applied load, F_S increases monotonically with the tip velocity, and the evolution can be empirically captured by a simple power law with an exponent $0 < \alpha < 1$ (Fig. 5.10c-d). This type of dependence on v has been previously reported for similar experiments conducted in other systems [53]. Here, it implies that $F_S \to 0$ when $v \to 0$, characteristic of the observed smooth sliding in this regime, with no apparent instabilities that could lead to a nonzero value for the low-velocity kinetic friction [9, 54]. Generally, the fact that F_S increases with v for all values of F_L is consistent with the idea that faster velocities allow less time for configurational relaxation of the sheared squalane molecules. This is also supported by ϕ_S, which becomes more elastic with increasing velocity because of a frustrated molecular relaxation (Fig. 5.10d). Generally, the shear behaviour of the nanoconfined lubricant is reminiscent of a modified Bingham model where the motion of the lubricant molecules is monotonic and close to Newtonian past an initial yield stress [55, 56].

When varying T for a given v, F_S follows an Arrhenius-like behaviour within error, with F_S decreasing exponentially as T increases (representative results are shown in Fig. 5.10e). Similarly to the experiments conducted at different shearing velocities, the

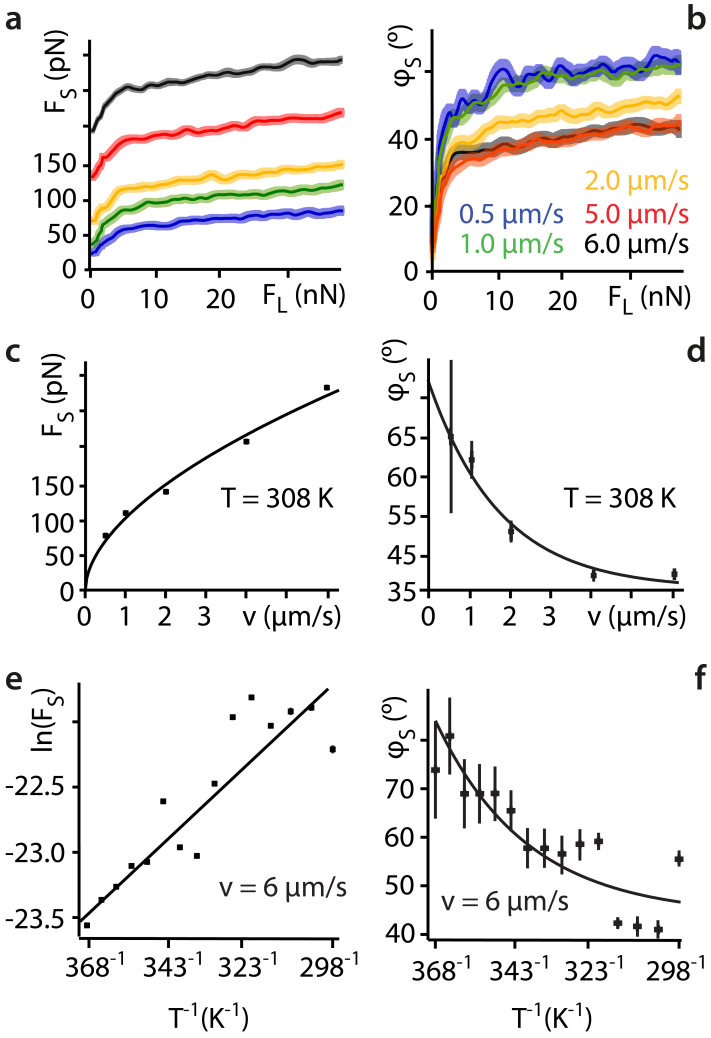

Fig. 5.10: Impact of the tip velocity, v, and the system's temperature, T, on the lubricated friction response. Representative shear force spectroscopy curves taken at 308 K for different shearing velocities (**a-b**) systematically show a two-regime behaviour of F_S with the applied load F_L. As F_L increases, F_S exhibits an initial rapid increase akin a yield stress, followed by a more regular plateau-like regime. The associated ϕ_S confirms the existence of a yield stress with a rapid transition from an initial elastic-like behaviour to a viscoelastic regime for larger F_L values (**b**). In the plateau-like regime, the evolution of F_S with v can be described by a power law at a given temperature (here, 308 K) (**c**). ϕ_S decreases monotonically as a function of v (**d**). For a given velocity (here, 6 μm/s), varying temperature shows F_S to follow an Arrhenius-like behaviour with a linear dependence of $ln(F_S)$ versus $1/T$ (**e**). Consistently, ϕ_S shows an increase in viscosity with temperature (**f**). The values of F_S and ϕ_S are taken at $F_L = 30$ nN in (**c**) to (**f**). The temperature is considered to be affected by an uncertainty of 0.1 K; even if the AFM temperature control system is one order of magnitude more precise, the error is overestimated so as to account for errors due to temperature gradients in the highly viscous liquid. The uncertainty on v is calculated using standard formulae for error propagation [50, 51], considering that the uncertainty on the tip oscillation amplitude and frequency are 0.05 nm and 10 Hz, respectively.

temperature dependence is consistent with the idea of a dynamical friction dominated by the configurational relaxation of the lubricant molecules. Higher temperatures favor

increased molecular mobility, faster relaxation time, and hence lower friction, together with a more viscous lubricant behaviour (Fig. 5.10f). As can be expected, no high-resolution images could be obtained above 318 K due to the increased molecular mobility preventing the formation of stable row structures (Fig. 5.3). This view is also supported by computer simulations and other experimental studies that indicate a melting of the solid interfacial squalane layer in contact with graphite between 325 and 338 K [28, 57].

The relaxation dynamics of the lubricant molecules is expected to have a marked impact on the lubricant's effective viscosity, η_{eff}, when nanoconfined [9, 15, 18]. However, accurately calculating η_{eff} poses some challenges, requiring some knowledge about the shearing boundary conditions, namely the slip length of the lubricant on the surface, b, and the contact area of confinement, A [9, 58]. Using Eqs 1.21 and 1.23 (see Chapter 1 Section 1.3.2), η_{eff} is indeed given by [9, 43, 58]:

$$\eta(d) = \frac{F_S \; sin\,(\phi_S) \;\; (d+b)}{A \; v} \tag{5.1}$$

where $F_S \; sin\,(\phi_S)$ is the viscous component of the shear force, d the tip-sample distance, and v the shearing velocity. From the SEM analysis of the tip (Fig. 5.2), a typical contact area was estimated to be ~ 20 nm^2 [44]. The slip length of squalane on HOPG is to the best of our knowledge not known. A no-slip condition would seem reasonable considering the apparent static organization of the lubricant molecules [9, 15], but this approximation may not hold true if molecules are able to escape their surroundings and move along the surface [55, 56]. A slip length of up to ~ 200 nm has been reported for squalane on sapphire [35]. To address this discrepancy, η_{eff} is calculated for a range of plausible slip lengths (0 to 50 nm) so as to derive an order of magnitude for η_{eff} (Fig. 5.11a). Unsurprisingly, higher effective viscosities correspond to smaller shearing velocities. Representative results calculated assuming a slip length of 20 nm (Fig. 5.11b) show a significant increase of η_{eff} for gaps smaller than 4 nm, consistent with the molecules arranging in ordered solid-like domains [9]. This is also supported by the existence of a maximum effective viscosity as the confining pressure increases (Fig. 5.11c). Here, the evolution of the viscosity is modelled as an exponential function of the pressure described by the Barus equation [55]: within this elasto-hydrodynamic model, the continuous film between two sliding surfaces is preserved even at high pressure thanks to an exponential rise in the viscosity. Such a viscosity increase prevents the flow of the fluid outside of the nano-confined gap [55]. A plateau regime appears for pressures larger than about 0.5 GPa, suggesting that piezo-viscous effects are limited by the molecules displaying more pronounced solid-like characteristics.

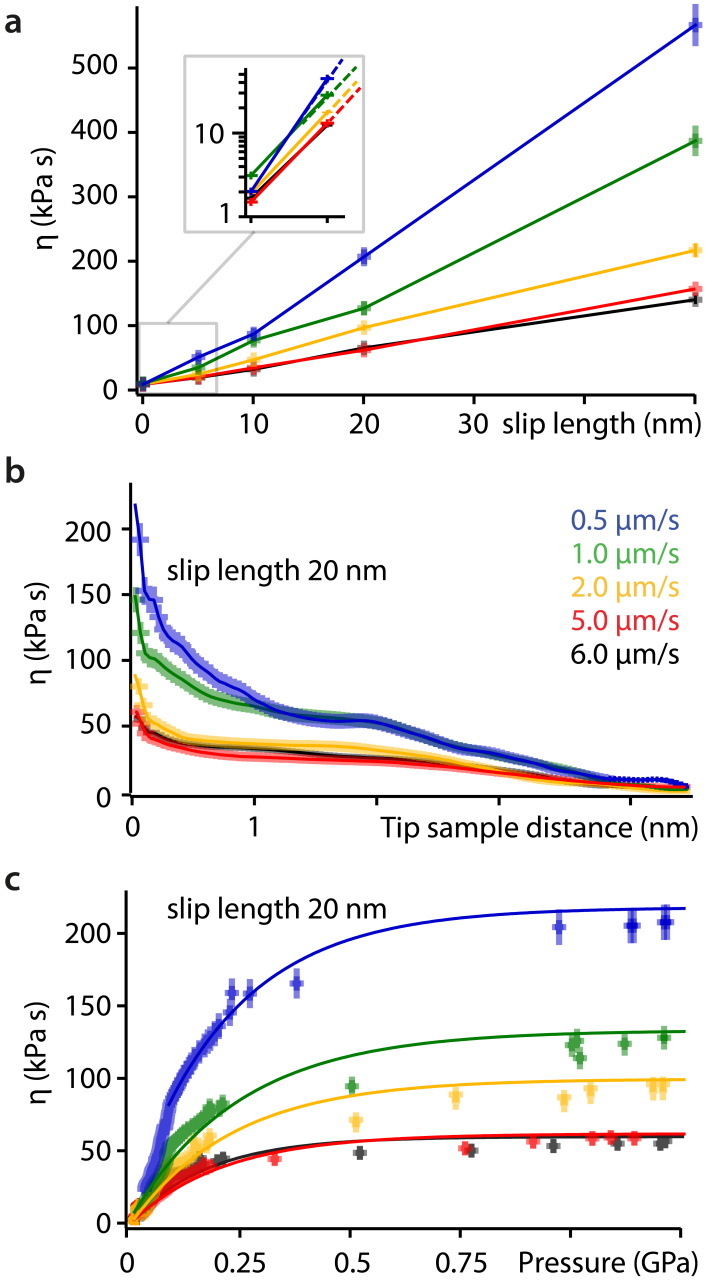

Fig. 5.11: Pressure dependence of the confined lubricant's viscosity. Effective viscosity calculated at 308 K and an applied pressure of 1.25 GPa for increasing values of slip length (**a**). The effective viscosity increases by orders of magnitude for tip-sample distance smaller than ~ 4 nm (**b**). The viscosity shows an exponential dependence on pressure (**c**), reaching a maximum value for confining pressures larger than ~ 0.5 GPa. This is consistent with the existence of solid-like ordered molecular domains of lubricant molecules.

5.4.5 A simple quantitative model

Together, these shearing experiments confirm the dominating role played by the lubricant's molecular relaxation and provide clues to modeling its behaviour. Building on this information, I have systematically explored the impact of temperature and shear velocity

on the resulting lubricated friction force, probing 14 different temperatures (between 298 and 368 K) and at least five different shear velocities at each temperature. For each measurement, at least 20 individual curves are acquired and subsequently averaged to ensure reliability of the results. The goal is to exploit this comprehensive set of measurements to develop a semi-empirical model able to quantitatively describe the dynamical response of the sheared lubricant in all the experiments. To simplify as much as possible the modeling and avoid any overfitting, the linear region of the shear force curves ($F_L \sim$ 10 to 30 nN; Fig. 5.10a) was fitted with a first-order polynomial. This strategy has two advantages. First, it exploits the most reproducible part of the data and extracts a single effective dynamical friction coefficient, μ_d, which can be understood as plastic viscosity in the modified Bingham plastic model. Second, it bypasses the difficulties associated with modeling the yield stress part of the curve ($F_L \leq$ 10 nN) where the shear curves tend to present irregular features and shapes. A poor reproducibility at lower loads is inevitable given the stochastic nature of intermolecular bond rupture and possible variations in the local nanoscale details of the squalane/tip system during the initial stages of the shearing. Using the proposed linear fitting, $Y_0(T, v)$ is simply the ordinate at origin:

$$F_S = Y_0(T, v) \; + \; \mu_d \; F_L \tag{5.2}$$

It should be pointed out that the fitting does not make any physical assumptions beyond the observed linear behaviour of F_S with F_L and generally provides good fitting (Fig. 5.12a) with residuals randomly distributed around the zero (Fig. 5.13). The effective yield stress represents an energy-activated process [9], and on the basis of the results presented in Fig. 5.12, the following dependence on T and v can be assumed:

$$Y_0(T, v) = A v^{\alpha} \; exp\left(-\frac{E_a}{k_B T}\right) \tag{5.3}$$

where A is a proportionality constant, E_a is the activation energy necessary to break intermolecular bonds, and k_B is the Boltzmann's constant. Equation 5.3 effectively combines the dependences of F_S on T and v evidenced in Fig. 5.12 and does not require any additional assumptions. Using Eq. 5.3, it is possible to fit globally $Y_0(T, v)$ over all the temperatures and velocities measured (Fig. 5.12a-b). Considering the small number of fitting parameters and the fact that they are global parameters (identical for all the curves), the quality of the fitting is generally good. Arguably, E_a is the most fundamental fitting parameter because it describes the energy necessary to break and make new intermolecular bonds. This activation energy effectively determines the stability of any molecular domains under confinement. The global fitting yields E_a = - 4.46 $\pm$ 0.07 $\times$ 10^{-20} J/molecule, representing $\sim$ - 11 $k_B T$ at room temperature (298 K). The negative sign is a consequence of Eq. 5.3 being formulated as a standard Arrhenius behaviour. Here, it implies lower

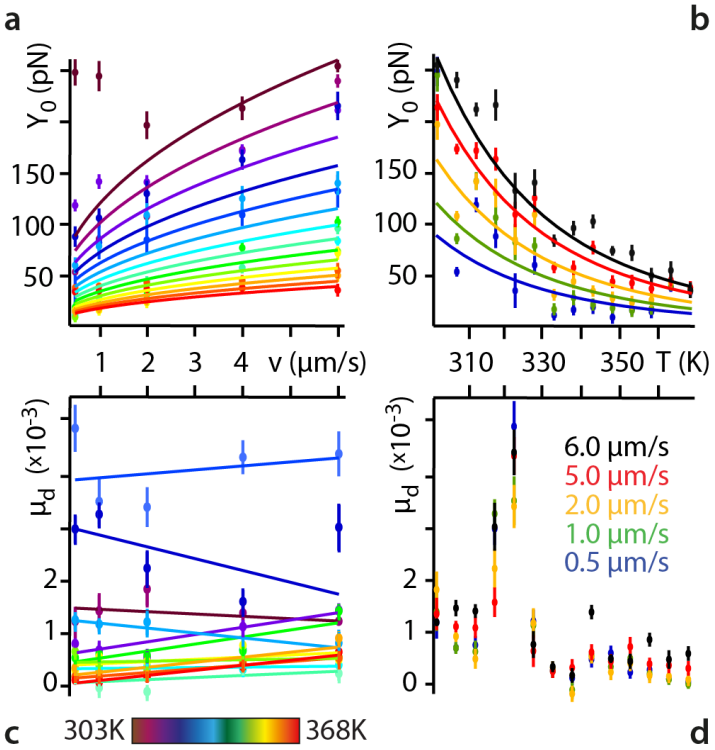

Fig. 5.12: Global analysis of the impact of T and v on the yield stress, Y_0, and the effective friction coefficient, μ_d. It is possible to globally fit Y_0 over the whole range of velocities (**a**) and temperatures (**b**) probed using Eq. 5.3. The residuals show no systematic error (Fig. 5.13) with significant outliers only at lower temperatures where interlayer digitation may affect the nanoshearing measurements [25]. Consequently, the data points at 298 K have been excluded. No clear dependence of μ_d on v (**c**) and T (**d**) is observed within experimental error, except for a local maximum around 323 K, which is ascribed to local melting instabilities in the confined squalane layer [28, 57]. Linear fitting of the data at each temperature yields no systematic trend (**c**). The same fitting coefficients are used for all the fits: $A = 1.0 \pm 0.2 \times 10^{-12}$ $(\mathrm{kg/s})^{-1/\alpha}$, $\alpha = 0.43 \pm 0.02$, and E_a = - 4.46 ± 0.07 × 10^{-20} J/molecule ($E_a \sim$ -11 k_BT at room temperature). The error on the natural logarithm of Y_0 and μ_d in the Arrhenius plots are calculated using standard formulae for error propagation [50, 51].

lubricated friction forces at higher temperatures. This is indeed the case (Fig. 5.12) with higher temperatures reducing the number of stable molecular configurations [59] and hence the lubricated friction forces. Within this framework, the motion of the squalane molecules can be understood as a limit case of boundary friction where the energy provided by the AFM tip allows the sheared squalane molecules to overcome E_a and explore neighbouring configurations as in the Prandtl-Tomlinson model [9, 54]. The activation energy being about 10 times greater than thermal fluctuations at room temperature, thermal contributions only facilitate the onset of motion, inducing a monotonic decrease of the yield stress with increasing temperature (Figs 5.10c-d and 5.12a-b). This interpretation is also supported by the power law dependence of lubricated friction on velocity (Figs 5.10c). In the range of velocities explored here, common analytical

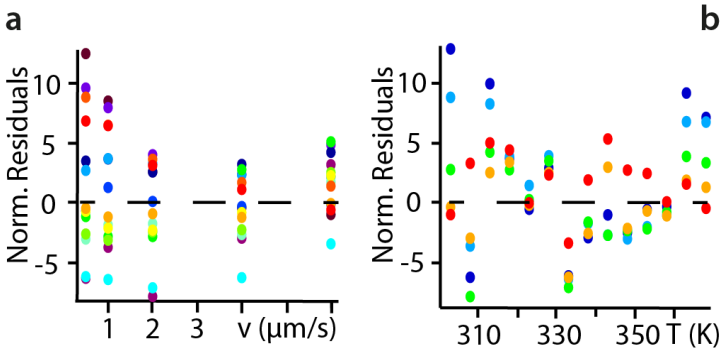

Fig. 5.13: Normalized residuals for the fits presented in Fig. 5.12a-b. The residuals do not show any pattern and appear randomly distributed around the zero, as expected for a suitable model [50, 51].

models predict a logarithmic dependence of the force on the velocity provided that the thermal energy is sufficient to overcome the initial barrier (i.e., $E_a \approx k_B T$) [53, 54, 60]. When this last condition is not fulfilled, a power law v^β behaviour is expected with $\beta = 2/3$ [53]. The present results suggest an intermediate scenario where E_a is larger than the thermal energy, but the latter is already able to facilitate molecular motion. This is consistent with the observed power law dependence of lubricated friction on velocity with an exponent $\alpha = 0.43 \pm 0.02$, smaller than β.

The magnitude of the activation energy can be compared with squalane's latent heat of vaporization, $\Delta H_v = 116.2$ kJ/mol ($\sim 19.3 \times 10^{-20}$ J/molecule) at 378 K [61]. ΔH_v represents the energy needed to fully remove a molecule from the bulk liquid and separate it from its neighbour. This is a more stringent process than the shearing-induced breaking of intermolecular bonds so ΔH_v is expected to be larger than E_a, but both quantities can be expected within the same order of magnitude. Here, $\Delta H_v \sim 4E_a$, consistent with the interpretation of E_a. Considering the fact that sheared squalane molecules at the interface with HOPG have fewer neighbours than in bulk squalane, the magnitude of E_a does suggest a local "vaporization" of the sheared molecules once past the yield stress. In other words, the magnitude of E_a may be sufficient to almost fully separate squalane molecules from their neighbours as the tip sets the solid-like interfacial layer into motion. This view also implies that once in motion, the molecules may be able to move individually, a bit like hard metal spheres rolling on a smooth flat surface. This shearing regime corresponds to the linear part of the shear curves (second regime; Fig. 5.10a) and is quantified by μ_d. The value of μ_d does not depend on T and v within experimental error (Fig. 5.12c-d), except for a local maximum around 323 K that may be ascribed to the local melting of the confined squalane [28, 57]. This finding supports the view that once in motion, the nanoconfined squalane molecules move either individually or in a very orderly and coordinated fashion so that the influence of the surrounding on any given molecule is minimal. The independence

of μ_d from v suggests a translational relaxation time scale, τ, for the molecules significantly slower than the regime probed here. τ describes the relaxation timescale associated with the translational dynamics of the molecules under shear. It is possible, however, to rearrange the expression for the yield stress in Eq. 5.3 so as to estimate an order of the magnitude for the relaxation time scale of the molecules when in the energy minima configurations. The analysis relies on expressing v in Eq. 5.3 as a function of oscillation amplitude and time, and then solving for the latter. This returns a timescale of 0.1-10 ms, in agreement with the literature reporting similar τ for organic molecules confined in nanogaps [62]. The reduction in configurational entropy due to confinement results in the molecules undergoing a structural transition into a more ordered phase with a dynamics orders of magnitude slower than the bulk fluid.

The magnitude of μ_d is also relatively low, consistently with typical friction coefficients observed at the limit between boundary lubrication and hydrodynamic friction [63]. Given the relatively strong squalane-squalane molecular interactions, a low μ_d value also supports the existence of a privileged shearing regime with particularly low friction. It should, however, be noted that the present work probes a limited range of temperatures and velocities; bulk squalane is liquid between 235 and 449 K at ambient pressure. It is therefore possible for μ_d to exhibit a stronger dependence on T and v outside the range probed here.

5.4.6 *Impact of other surface defects on lubricated friction*

The generality of the lubricated friction mechanisms remains to be fully explored beyond the present system and over different spatial scales, but the findings are not restricted only to step edges on HOPG. Lubrication experiments conducted with squalane nanoconfined between an amorphous silicon nitride AFM tip (Arrow UHF, Nanoworld, Switzerland) and a MoS_2 substrate reveal a comparable behaviour (Fig. 5.14). As visible in Fig. 5.14a, at room temperature, surface features such step edges and local dips promote molecular ordering of the lubricant just as for HOPG, also with domains forming at both the top and the bottom of a step edge. When the temperature increases, the lubricant molecules become more mobile and molecular domains can no longer be observed (Fig. 5.14b) inducing a significantly lubricated friction force than at room temperature (Fig. 5.14c). Overall, the experiments indicate that the hypothesis of lubricated friction being indirectly influenced by the surface features is also valid for MoS_2.

Similarly, mesoscale experiments taken over larger areas of the graphite's surface show a clear correlation between the apparent surface roughness and the resulting lubrication force despite the tip shearing over a variety of singularities (Fig. 5.14d-e). The actual shear measurements are conducted in an identical manner to those described in Figs 5.5 - 5.9 in terms of amplitude and frequency. However, picking randomly locations across larger areas

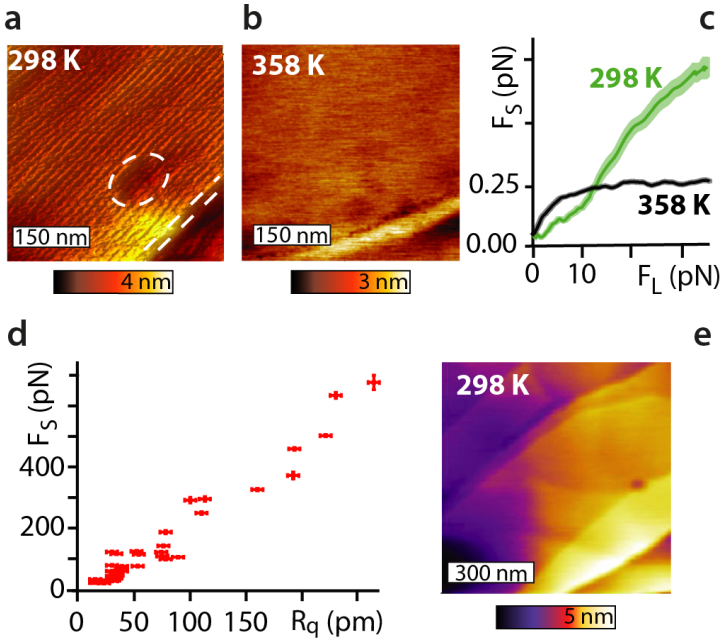

Fig. 5.14: High resolution imaging and shear behavior of squalane molecules near MoS_2 singularities, and impact of other HOPG singularities on the lubricated friction force. High-resolution topographic amplitude-modulation AFM images on MoS_2 reveal long-range ordering of the squalane molecules around surface defects at room temperature (298 K) (**a**). The dashed lines highlight some local surface singularities, here a concave depression and a step edge with the ordered squalane structures aligned along the step. When increasing the temperature to 358 K (**b**), no clear molecular details are visible due to an increased mobility of the squalane. Shear spectroscopy measurements (**c**) confirm the impact of the molecular organization on the lubricated friction force. To explore nano-lubrication around HOPG surface singularities other than a step edge, shear spectroscopy is performed on randomly selected locations (**d**) taken across larger areas of the HOPG region as exemplified in (**e**). No molecular order of the lubricant can be seen at this scale but features such as atomic steps or depressions are visible. A clear correlation between the lubrication force and the root mean square roughness is present (**d**).

statistically ensures that a variety of possible surface singularities are included and allows for multiple tip-asperities interactions. Given the large regions surveyed, molecular order cannot be seen (Fig. 5.14e). The measured lubricated friction force tends to increase almost linearly with the average root mean square roughness of the area probed, supporting the idea of group effects involving defect-induced organized molecular domains (Fig. 5.14d). However, the nanoscale AFM results cannot fully address the link between molecular-level effects and macroscopic friction, and complementary results also involving other techniques [19] are needed.

5.5 Summary

This Chapter has investigated the molecular details of lubricated friction in a well-established model system, squalane nanoconfined over a graphite surface. Combining high-resolution AFM imaging and subnanometric shear force spectroscopy, I have quantified the behaviour of squalane over a range of temperatures, shearing velocities, and degrees of confinement. The results, supported by MD simulations, show that surface features of the confining solids such as atomic steps locally organize the squalane lubricating molecules in their vicinity due to a loss of configurational entropy around the surface defects. These ordered regions can extend hundreds of nanometers away from the defect depending on the system's temperature, and the molecular ordering progressively vanishes as the distance from the step edge increases. Shear measurements conducted directly on step edges do not show any increase in the lubricated friction, but rather smaller values than on well-ordered domains, confirming the dominating role of the local molecular arrangement in modulating lubricated friction.

Interfacial regions with higher molecular order can markedly increase the shear force because of the reduced molecular mobility. The present results provide a molecular mechanism whereby roughness is able to affect lubricated friction indirectly and not only through the well-known solid-solid tribological contacts. In the context of this mechanism, surface singularities promote molecular order, which, in turn, reduces the molecular mobility of the squalane lubricant, resulting in increased lubricated friction forces by up to 50% in the present system. Further studies will determine the generality of this mechanism and its applicability to other systems.

I have also derived a quantitative model able to describe the lubrication mechanism over a range of temperatures and shearing velocities. The model parameters, determined by experimental observations, indicate that the main energy cost to lubrication comes from the rupture of the bonds between lubricant molecules that are resting at equilibrium. Once in motion under the shearing solid, the molecules move almost as if isolated and with limited influence from external parameters such as temperature and shear velocity.

The present Chapter offers fundamentally novel insights into lubricated friction, particularly the role played by the surface asperities typically present on all solids. While some of the results are likely to be system specific, the impact of interfacial domains with reduced molecular mobility and the proposed lubrication mechanism seem more general and may help with the rational design of lubricants.

References: Chapter 5

[1] O. Purrucker et al., *Physical Review Letters* **2007**, *98*, 078102.

[2] J. Seror et al., *Nature Communications* **2015**, *6*, 1–7.

[3] K. Holmberg et al., *Friction* **2017**, *5*, 263–284.

[4] D. A. Hanaor et al., *International Journal of Solids and Structures* **2015**, *59*, 121–131.

[5] W. H. Thompson, *The Journal of Chemical Physics* **2018**, *149*, 170901.

[6] J. Gao et al., *The Journal of Physical Chemistry B* **2004**, *108*, 3410–3425.

[7] B. Weber et al., *Nature Communications* **2018**, *9*, 1–7.

[8] O. Hod et al., *Nature* **2018**, *563*, 485–492.

[9] C. Cafolla et al., *Nanoscale* **2018**, *10*, 11831–11840.

[10] L. Bocquet et al., *Chemical Society Reviews* **2010**, *39*, 1073–1095.

[11] K. Voitchovsky, *Nanoscale* **2016**, *8*, 17472–17482.

[12] T. Han et al., *Langmuir* **2018**, *34*, 11281–11291.

[13] B. C. Donose et al., *Langmuir* **2005**, *21*, 1834–1839.

[14] B. Bhushan et al., *Nature* **1995**, *374*, 607–616.

[15] T.-D. Li et al., *Review of Scientific Instruments* **2014**, *85*, 123707.

[16] C. Drummond et al., *Physical Review E* **2001**, *63*, 041506.

[17] D. Gourdon et al., *Physical Review Letters* **2006**, *96*, 099601.

[18] S. J. O'Shea et al., *Japanese Journal of Applied Physics* **2010**, *49*, 08LA01.

[19] D. Petrova et al., *ACS Applied Materials & Interfaces* **2018**, *10*, 40973–40977.

[20] F. Robbe-Valloire et al., *Advances in Tribology* **2018**, *2018*.

[21] L. Montanari et al., *Applied Magnetic Resonance* **1998**, *14*, 345–356.

[22] S.-K. Kim et al. in *Advances in Food and Nutrition Research*, **2012**, pp. 223–233.

[23] A. C. Allison, *Methods* **1999**, *19*, 87–93.

[24] D. Fuhrmann et al., *The Journal of Chemical Physics* **2004**, *120*, 2439–2444.

[25] C. Drummond et al., *Macromolecules* **2000**, *33*, 4910–4920.

[26] C. J. Mundy et al., *Faraday Discussions* **1996**, *104*, 17–36.

[27] J. Gao et al., *The Journal of Chemical Physics* **1997**, *106*, 4309–4318.

[28] N. Gosvami et al., *Physical Review Letters* **2008**, *100*, 076101.

[29] G. Reiter et al., *The Journal of Chemical Physics* **1994**, *101*, 2606–2615.

[30] M. Doig et al., *Langmuir* **2014**, *30*, 186–195.

[31] D. Fuhrmann et al., *Surface Science* **2001**, *482*, 77–82.

[32] H. Mo et al., *Chemical Physics Letters* **2005**, *415*, 106–109.

[33] R. Lim et al., *Physical Review Letters* **2002**, *88*, 246101.

[34] Y. Zhu et al., *Physical Review Letters* **2004**, *93*, 096101.

[35] T. Schmatko et al., *Physical Review Letters* **2005**, *94*, 244501.

[36] E. Bonaccurso et al., *Current Opinion in Colloid & Interface Science* **2008**, *13*, 107–119.

[37] Y. Wang et al., *The Journal of Chemical Physics* **1994**, *100*, 3276–3285.

[38] M. Dijkstra, *The Journal of Chemical Physics* **1997**, *107*, 3277–3288.

[39] M. Tsige et al., *Chemical Physics Letters* **2008**, *457*, 357–361.

[40] H.-J. Butt et al., *Nanotechnology* **1995**, *6*, 1.

[41] C. Cafolla et al., *Journal of Applied Physics* **2018**, *124*, 154502.

[42] E. J. Miller et al., *Journal of Visualized Experiments* **2016**, e54924.

[43] C. Cafolla et al., *Science Advances* **2020**, *6*, eaaz3673.

[44] A. C. Fischer-Cripps, *Introduction to contact mechanics*, Springer, **2007**.

[45] D.-C. Sin et al. in *Coatings for Biomedical Applications*, Elsevier, **2012**, pp. 264–283.

[46] K. A. M. Aboua et al., *Tribology Letters* **2019**, *67*, 65.

[47] F. Svahn et al., *Wear* **2003**, *254*, 1092–1098.

[48] I. Krupka et al., *Tribology International* **2016**, *100*, 116–125.

[49] D. Feng et al., *Tribology Letters* **2017**, *65*, 10.

[50] A. A. Clifford, *Multivariate error analysis: a handbook of error propagation and calculation in many-parameter systems*, Applied Science Publications, **1973**.

[51] H. Ku, *Journal of Research of the National Bureau of Standards* **1966**, *706*, 263.

[52] A. Filippov et al., *Physical Review Letters* **2004**, *92*, 135503.

[53] C. Fusco et al., *Physical Review B* **2005**, *71*, 045413.

[54] A. Vanossi et al., *Reviews of Modern Physics* **2013**, *85*, 529.

[55] H. Spikes et al., *Tribology Letters* **2014**, *56*, 1–25.

[56] R. P. Chhabra et al., *Non-Newtonian flow and applied rheology: engineering applications*, Butterworth-Heinemann, **2011**.

[57] A. D. Enevoldsen et al., *The Journal of Chemical Physics* **2007**, *126*, 104703.

[58] D. Ortiz-Young et al., *Nature Communications* **2013**, *4*, 1–6.

[59] M. Mozurkewich et al., *The Journal of Physical Chemistry* **1984**, *88*, 6429–6435.

[60] E. Riedo et al., *Physical Review Letters* **2003**, *91*, 084502.

[61] R. M. Stephenson et al. in *Handbook of the Thermodynamics of Organic Compounds*, Springer, **1987**.

[62] C. M. Mate et al., *Tribology on the small scale*, Oxford University Press, **2019**.

[63] M. Woydt et al., *Wear* **2010**, *268*, 1542–1546.

6.0 Impact of water on the lubricating properties of hexadecane at the nanoscale

It was one of those humid days when the atmosphere gets confused. Sitting on the porch, you could feel it: the air wishing it was water.
Jeffrey Eugenides, Middlesex 2003

6.1 Overview

Fluid lubricants are routinely used to reduce friction in a wide range of applications, from car engines to machinery and hard-disk drives. However, their efficiency can be significantly influenced by the ambient conditions they are exposed to, in particular humidity. Our understanding of the molecular mechanisms responsible for the well-documented impact of water on lubrication remains limited, hindering the improvement of tribological formulations.

Here, atomic force microscopy (AFM) imaging and shear force spectroscopy are used to investigate the structural and dynamical behaviour of a model lubricant, hexadecane, confined between an AFM probe and a hydrophilic mica surface at different temperatures and humidities. The Chapter shows that both the nanoscale structure and the tribological behaviour of the system are dominated by the nucleation of water nanodroplets at the interface. The process is favoured at higher temperature and can be explained with classical nucleation theory whereby the droplets become stable when larger than 20 nm to 50 nm size, depending on the ambient conditions. Below this threshold, a molecularly thin film of water molecules coats the surface uniformly. Highly localised shear measurements demonstrate a detrimental impact of the nanodroplets on shear with a twofold increase in the lubricated friction force. However, this can be mitigated by the adjunction of an amphiphilic additive, here oleic acid.

The bulk of this Chapter has been published as an article: Impact of water on

the lubricating properties of hexadecane at the nanoscale Nanoscale 2020. DOI: 10.1039/D0NR03642K.

6.2 Introduction

Within the previous Chapters, we have discussed the negative impact tribological contacts may play in a wide range of biological phenomena [1–3] and technological applications [4, 5], from the flow of red blood cells in vessels and capilaries [2] and articulating cartilage surfaces [2], to the functioning of machinery [4] and wind turbines [5]. As shown in Chapter 5, one of the most common and effective approaches to reducing friction and wear is the use of lubricants [6]. Lubricants typically create thin mobile films, often in fluid form, adsorbed at the interface between moving parts. They allow the parts to slide easily and smoothly past each other by confining the shearing-induced molecular rearrangements to the lubricant layer [6, 7]. The efficiency of a lubricant depends on many different parameters such as the lubricant's molecular structure and intrinsic properties, the local topography and chemical characteristics of the sliding surfaces [8], and the operating parameters such as sliding speed [9, 10], contact pressure [11], and environmental factors (e.g. temperature [9] and humidity [8]). While many of these parameters can be kept to a particular operating regime, certain environmental parameters are significantly harder to control in real-life applications. The ambient humidity, for example, has a marked impact on lubricated friction [12, 13]. Atmospheric humidity can vary considerably and uncontrollably over short periods of time but its effects are not easily mitigated due to the fact that the moving parts in most devices do not operate in a controlled atmosphere [14, 15]. Water molecules can usually enter the lubricant through several sources including condensation and adsorption from a humid environment, leakage from heat exchangers or as a by-product of chemical reactions [16, 17]. The effect of water on the properties of lubricants are often detrimental [16, 17], especially when preventing the adsorption of organic lubricant molecules at the relevant interfaces. The ability of water to displace organic lubricants is particularly pronounced for interfaces involving a hydrophilic solid such as the metal oxide surfaces of most industrial machinery and engines [13, 18]. Water can impede the formation of an effective lubricating and protective layer between the sliding surfaces [16, 19–21]. Since the thickness of the lubrication film can be as thin as a few nanometers [22], even trace quantities of water may be detrimental, resulting in increased friction and damage to the moving parts.

Water can bind to the oxygen groups of both the main lubricant molecules and additives [16, 19–21]. Aside from displacing organic compounds [23], water adsorption can lead to the formation of free-radicals which affect the tribochemistry of the interface, in particular for systems involving metal oxides [19] lubricated by alkane-based products [13]. A broad

spectrum of fluid lubricant formulations are currently based on alkanes [13, 24–28], but a full understanding of the impact of humidity on lubricated friction is still elusive due to nanoscale nature of the problem: the adsorption of water molecules and the subsequent impact on lubrication are processes difficult to observe *in situ*, at the molecular level, in a controlled environment (humidity, temperature), all while tracking the system's evolution over relevant periods of time [8, 20, 29].

This is precisely the goal of the present Chapter that combines nanoscale atomic force microscopy (AFM) experiments with macroscopic contact angle (CA) measurements all conducted in controlled atmosphere. To make the results as relevant as possible while ensuring a clear interpretation, the investigations focused on the hexadecane-mica model system. Hexadecane is a model mineral base oil and one of the basic components of most commercial organic lubricants [13, 24–26]. Mica is a hydrophilic aluminosilicate that acts here as a model metal oxide surface [11]. Mica has been extensively used as a model substrate to study the fundamental aspects of lubricated friction, including real-life applications. Studies have explored lubricants as diverse as commercial additives [30], hydrated metal ions [11], ionic liquids [31] and liquid crystals intended as the new generation of lubricants [32]. Here, using mica has three main advantages. First, its layered structure makes it easy to obtain clean, atomically flat surfaces. This makes mica ideal to study the molecular-level details of lubrication because chemical variations across the interface can be clearly differentiated from topographical or roughness effects such as tribological contacts between asperities [11, 23, 29, 33]. Second, mica being an aluminosilicate, it is hydrophilic and contains many of the atoms often present in typical machinery and engines (Al, Si, O) [11]. This allows conducting experiments that partly replicate the hydrophilic surface chemistry of "real" systems while discriminating between lubricant and topographical effects. Finally, the fact that mica is a well-established model system for lubrication ensures a more robust interpretation of the experimental results in light of existing literature. Previous experimental studies on mica suggest an orientation of the interfacial hexadecane molecules parallel to the substrate [34]. This is also supported by molecular dynamics and Monte Carlo simulations that reveal well-ordered hexadecane structures when nanoconfined between two mica surfaces [35, 36]. The existence of in-plane order and interlayer correlation may result in long-range correlations in the confined film [33] with humidity adversely affecting the hydrocarbon adsoprtion [37]. However, no study to date has been able to clearly visualise water adsorption/desorption due to the high mobility of the water molecules [37, 38]. Furthermore, it is still unclear how physically adsorbed water molecules and their distribution on the sliding surfaces may affect the shear response of the lubricant [29]. This is because most current experimental techniques average over large regions of the interface [8, 29].

This Chapter combines *in situ* high-resolution AFM imaging of the interfaces as it evolves

with nano-rheological shear measurements at multiple temperature and humidities. This allows quantitatively linking the nanoscale organisation of water and lubricant at the interface with the resulting changes in lubricated friction in response to environmental variations. The results at the nanoscale are further complemented with contact angle measurements so as to gain a full insight, at different length and time scales, into the mechanisms behind the impact of humidity on the interfacial properties of model lubricants.

6.3 Experimental

6.3.1 Samples

The experiments were conducted on high-quality V1 muscovite mica discs with controls on highly orientated pyrolytic graphite (HOPG) substrates. The mica and HOPG substrates were glued to steel plates as described in Chapter 2 Section 2.3.1. The substrates were freshly cleaved before any experiment. High-performance liquid chromatography-grade hexadecane and oleic acid both with a purity $\geq 99\%$ were used without any further purification.

6.3.2 AFM measurements

As in the previous Chapters, also here the measurements were performed on a Cypher ES AFM system equipped with temperature control. The AFM probes used were Arrow UHF silicon nitride cantilevers (Nanoworld, Switzerland). Control experiments were performed using AD-2.8AS diamond coated silicon cantilevers (Adama Innovations LTD, Dublin, Ireland). The flexural calibration of each cantilever was performed using its thermal spectrum [39]. Arrow cantilevers were found to have a stiffness, k_f, in the range 1.6-5.0 N/m, a Q-factor of 3.1 ± 0.3 and a resonance frequency of 1900 ± 1 kHz in hexadecane. The diamond-coated cantilevers had a typical stiffness of 2.2 ± 0.5 N/m (in agreement with the nominal value of 2.8 N/m); the Q-factor and resonance frequency in hexadecane were 3.3 ± 0.5 and 255 ± 1 kHz, respectively. The torsional resonance frequencies are higher than the flexural resonances, and are hence not relevant for the shear measurements which are conducted at 1.1 kHz. Calibration of the cantilevers' inverse optical lever sensitivity (InvOLS) and torsional spring constant, k_t, was achieved using the method described in Chapter 3. k_t was found to be 230 ± 30 N/m and 90 ± 4 N/m for the Arrow UHF and the AD-2.8AS, respectively. The values are consistent with the literature [40].

Following the experimental procedure applied in the previous Chapters, also here five randomly selected cantilevers were analysed by scanning electron microscopy (SEM) either

before or after the AFM experiments (including imaging and shear-force measurements). Before SEM imaging, the AFM probes were sputtered with a 15 nm thick gold-coating in order to reduce any charge accumulation. The SEM analysis was carried out with a commercial FEI Helios SEM system (Dawson Creek Drive Hillsboro, Oregon 97124 USA). The machine operated at 3 kV electron beam in vacuum with a current set to 0.17 nA. Representative images in Fig. 6.1 do not show any significant changes before and after the experiments.

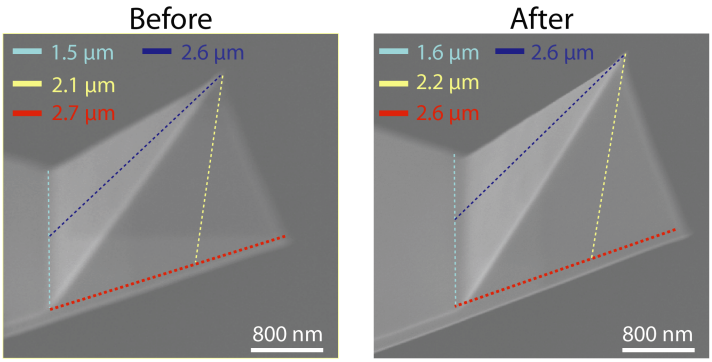

Fig. 6.1: Representative scanning electron microscopy images of the AFM probes. Randomly selected cantilevers were studied either before or after the AFM measurements (including imaging and shear-force spectroscopy). No clear changes are visible. The contact area is quantified by fitting the base and apothem for the faces of the triangular probe with the dashed lines. The estimated value of the contact area is 100 ± 10 nm^2 [41].

All the AFM imaging and shear-force spectroscopy experiments were conducted at thermal equilibrium. This was achieved ensuring that the cooling/heating rate of the temperature control system within the AFM was constant for at least 15 minutes. Relative humidity was controlled with nitrogen flux and monitored with a commercial Fluke 971 Thermo-hygrometer (Fluka Corporation, Washington, USA) placed inside the AFM chamber. Within each set of experiments, the variations in relative humidity, RH, were ensured to be $< 2\%$. Each set of experiments (including imaging and spectroscopy) was repeated at least three times in order to confirm data reproducibility. Accurate cleaning procedures were implemented to avoid any source of contamination (see Chapter 2 Section 2.3).

AFM imaging

High-resolution imaging was conducted in amplitude-modulation with the AFM probe completely immersed in hexadecane. The cantilever was acoustically driven at a frequency close to its resonance due to the limitations of photothermal excitation in viscous organic solvents. The details of the technique have been discussed in Chapter 2 Section 2.2.3. Here, it is important to highlight that this imaging mode allows probing primarily the

interfacial liquid with little direct contact between the tip and the surface of the solid [11, 27, 42, 43].

AFM shear-force spectroscopy

Shear-force spectroscopy was used to gain quantitative dynamical insights into the behaviour of the lubricant. The method allows probing determined locations of the interface with nanometer lateral precision and a shear force resolution in the pN range [11, 27, 42]. For each set of experiments, shear-force measurements were acquired over at least 5 locations, with at least 20 force curves per location. The results were then averaged. The details of the method have been discussed in Chapter 2 Section 2.2.3.

6.3.3 Contact angle measurements

Contact angle measurements were conducted in a home-made polycarbonate glove box. The relativity humidity was controlled with a nitrogen flux and monitored with a thermos-hygrometer (Fluka Corporation, Washington, USA) placed within the glove box. The temperature was kept constant using a hot plate (Thermo Fisher Scientific, Waltham, Massachusetts, USA) and monitored with the thermos-hygrometer. Experiments were performed once thermal stability was achieved (temperature and RH variations smaller than 0.1 K and 2% over at least 30 minutes, respectively). The mica was first cleaved and preconditioned to the desired temperature and RH. Wettability measurements were then carried out by placing a drop (5 μl) of hexadecane on the preconditioned mica while recording its evolution over time in a movie captured with a portable digital microscope Dino-Lite Edge camera (AnMo Electronics Corporation, Taiwan). Simultaneous side-view images of the drop allowed for contact angle quantification. The experiments were repeated two times. Data analysis was conducted using the ImageJ/Fiji free software [44] with the Contact Angle plugin [45]. Further analysis was performed with homemade routines developed in Igor Pro (Wavemetrics, Lake Oswego, OR, USA) and Python.

6.4 Results and discussion

6.4.1 Evolution of the mica-hexadecane interface at the nanoscale

I start by exploring the impact of ambient humidity on the nanoscale evolution of the mica-hexadecane interface using high-resolution AFM imaging. A cyclic change in temperature between 298 K and 368 K is imposed to the system so as to mimic the typical working conditions of lubricated mechanical systems. A representative set of AFM images taken

at different temperatures is presented in Fig. 6.2. As the temperature increases, small round protrusions begin to appear at the interface past 308 K (arrows in Fig. 6.2) and increase in number, eventually spreading homogeneously across the surface of mica at 368 K. Interestingly, a hysteresis behaviour can be observed when cooling the system back down to temperatures below 308 K with the different protrusions not disappearing, but merging instead into larger protrusions tens of nanometres across (Fig. 6.2). The mobile nature of the protrusions and their ability to coalesce suggest liquid nano-droplets nucleating at the interface. Given the fact that the only two liquid present are hexadecane

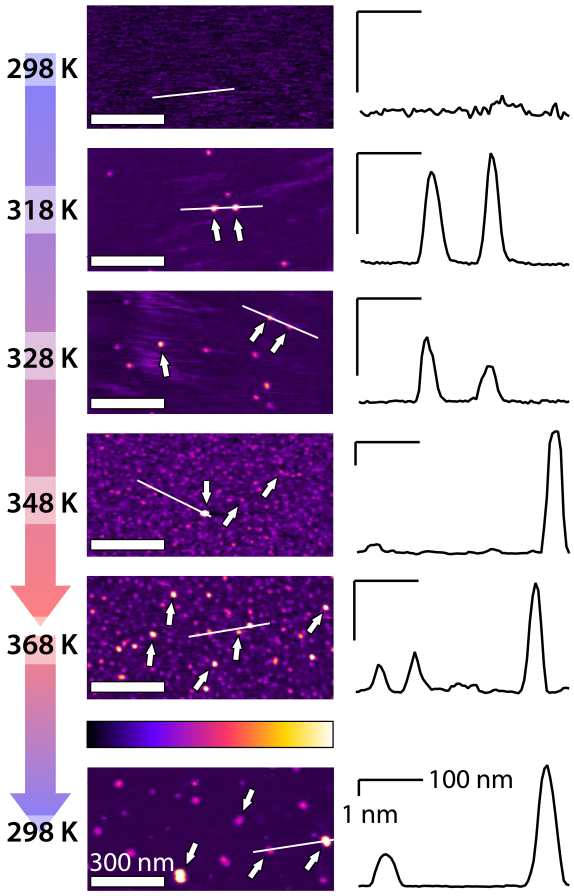

Fig. 6.2: Impact of temperature on the hexadecane-mica interface at ambient humidty. High-resolution amplitude-modulation AFM images of the hexadecane-mica interface exposed to the ambient atmosphere reveals a smooth and regular interface at 298 K. As the temperature increases, hemi-spherical protrusions interpreted as water nanodroplets progressively populate the interface (arrows). These nanodroplets are typically 20-50 nm wide and 1-5 nm tall (profiles) with the highest coverage at 368 K. Upon subsequently lowering the temperature back down to 298 K, the nano-droplets coalesce into fewer, larger droplets. The experiments were performed at RH = 42 ± 2%. Further heating was prevented from experimental equipment limitations with temperatures > 368 K interfering with the system electronics.

and traces of water from the ambient humidity, the protrusions are interpreted as interfacial water nanodroplets. This interpretation is also consistent with the fact that the surface

of mica initially carries a uniform nanoscopic layer of water when first immersed into the hexadecane. This is due to the strong hydrophilicity of the mica surface where a water layer between 0.4-2 nm thick builds up spontaneously and almost instantaneously when mica is cleaved in ambient conditions [37, 38, 46].

6.4.2 Molecular impact of water on lubricated friction

It is well-known that water can alter the shear response of a lubricant [23, 47]. Water can interfere with the hexadecane molecular packing and self-organisation, and thus reduce the smooth sliding of the AFM probe on the alkane layer [48, 49]. Additionally, water molecules create surface singularities where the AFM tip can be subject to pinning [42]. Here, the AFM-based experimental setup allows for precise quantification of the interface's lubrication properties with nanometre lateral resolution. This makes it possible to directly compare areas of uniform hexadecane-mica interface with regions where water nanodroplets are present within a same experiment. Measurements taken directly on nanodroplets exhibit a twofold increase in shear force, F_S, for any applied load compared to a uniform hexadecane interface in identical conditions (Fig. 6.3). The associated shear phases, ϕ_S, show the expected viscoelastic behaviour, but with little difference between both situations (Fig. 6.3b), at least for the shear rate used here. This suggests water to modify primarily the properties of the shearing surfaces, with the viscoelastic behaviour of the confined liquid being dominated by the hexadecane. Indeed, shearing in pure water tends to induce a very different phase behaviour [11] (see for example Fig. 4.3 in Chapter 4 Section 4.4.2). To confirm this hypothesis, shear measurements were conducted at different temperatures. In pure liquids, F_S usually decreases with increasing temperature [27, 42] and the lubricant tends to become more viscous (ϕ_S closer to 90°). Here, more nanodroplets are expected to nucleate at the interface when the temperature is raised, hence inducing an increase in F_S. Since the AFM measurements are highly localised, for each temperature probed at least 140 force curves were acquired, taken over 7 randomly selected locations and subsequently averaged. The results confirm the increase in F_S with temperature (Fig. 6.3c-d), reflecting the associated higher probability to shear over a water nanodroplet. The effect is non-monotonic with temperature, showing little evolution in F_S and ϕ_S between the water and the hexadecane below 328 K (yellow curve in Fig. 6.3c-d). This reflects the low probability for the AFM tip to randomly encounter a water nanodroplet.

The significant but localised impact of water nanodroplets on lubrication can be reduced with an amphiphilic molecule so as to decrease the interfacial energy of the system. Here, this is done using oleic acid, known for its surfactant properties and its ability to form supramolecular structure between water and hexadecane [50, 51]. The polar head of oleic acid binds to water, whereas its carbon chain is attracted to hexadecane molecules, thus

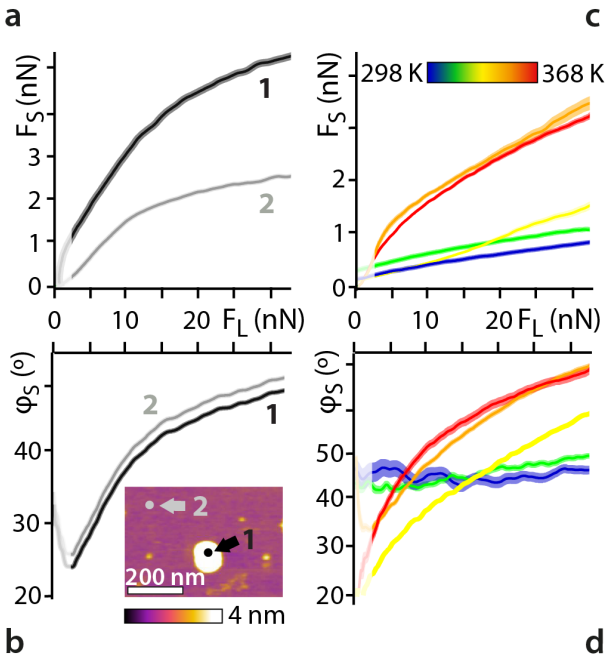

Fig. 6.3: Impact of water nanodroplets on lubricated friction. Representative shear spectroscopy measurements (**a**) conducted either on a water nanodroplet (**b**, inset location 1) or on a homogeneous hexadecane-mica interface (**b**, inset location 2). Water nanodroplets induce large changes in the lubricated friction force, F_S, for a given applied load. The associated shear phase, ϕ_S, appears much less sensitive to the location probed (**b**). Shear measurements were also conducted at different temperatures (**c-d**), averaging results over 7 randomly selected locations for each temperature. F_S increases with temperature due to a larger interface coverage with water nanodroplets (**c**). ϕ_S also tends to increase at higher temperatures (**d**), reflecting the interfacial liquids becoming more fluid (viscous). For low confining forces (< 2 nN), the shear amplitude nears to the experimental noise level and the data is deemed unreliable (semi-transparent region). The temperature in (**a-b**) is 368 K. The experiments were performed at RH $= 40 \pm 2\%$.

effectively preventing the latter from displacing the former. The impact of oleic acid is examined on both the nucleation of water droplet at the interface with temperature, and the resulting changes in lubricated friction forces. The results are presented in Fig. 6.4 and 6.5. The addition of only 0.01% of oleic acid to the hexadecane (molar concentration) before deposition on the mica surface already decreases the nucleation of water nanodroplets by more than 50% at any temperature explored. Further increasing the molar concentration of the amphiphilic acid to 0.1% results in a fourfold decrease in water nanodroplets when compared with pure hexadecane. If we assume a saturated oleic acid layer standing upright at the interface between the mica surface and the hexadecane, a 0.1% oleic acid molecular concentration would approximately represent a hundred-fold excess to the minimum number of molecules needed to cover the interface. This is shown by the following calculations for the surface coverage by oleic molecules.

The mica substrate is a disc of 12 mm diameter, with a total area of ~ 113 mm^2. The oleic acid being at the interface between the water film on the surface of mica and the

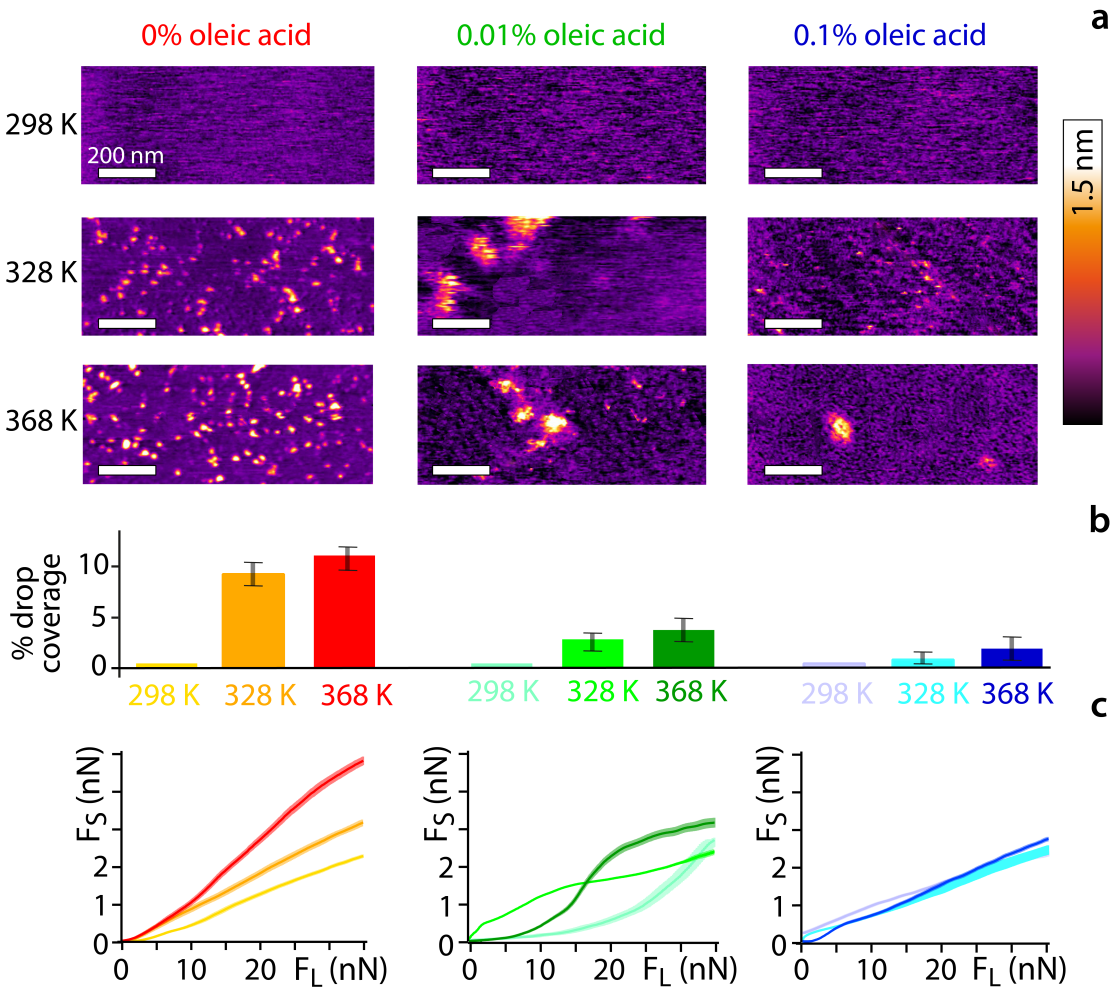

Fig. 6.4: Reducing the impact of water nanodroplets on lubrication. High-resolution amplitude-modulation AFM imaging of hexadecane-mica interface shows the expected presence of water nano-droplets as the temperature rises (0% oleic acid) (**a**). However, adding small amounts of oleic acid limits the formation of nanodroplets, with an effect already visible at 0.01 molar percentage. The impact of added oleic acid can be quantified by measuring the percentage of the interface covered with water nanodroplets using a thresholding approach (**b**). The reduction in interfacial nanodroplets also reduces the shear force and its anomalous behaviour with temperature (**c**) (see Fig. 6.5 for the associated phase). All the experiments were performed at RH = 45 ± 2%.

hexadecane, the oleic acid molecules are assumed to be standing upright so as to minimise the interfacial energy. This hypothesis is further supported by previous adsorption studies of oleic acid on iron oxide where the molecules were found to adsorb in an upright position and with a molecular surface area of ~ 0.45 nm^2 per molecule at saturation [52]. Using this value, the number of molecules N in an oleic acid layer covering the whole mica surface is given by $N \sim 113 \times 10^{12}$ nm^2 / 0.45 nm^2 $\sim 2.5 \times 10^{14}$. This value is an approximation but it provides a good indication of the order of magnitude for N. For comparison, a 100 μl drop (volume of the experiment) of hexadecane with a 0.1% molar concentration of oleic acid would approximately contain $N \sim 2 \times 10^{16}$ oleic acid molecules in the solution [53]:

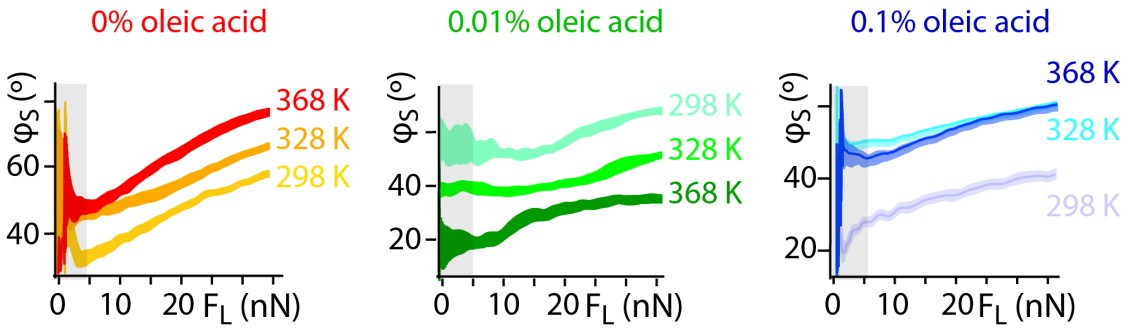

Fig. 6.5: Shear phase, ϕ_S, associated with the lubrication force presented in Fig. 6.4. In the absence of any oleic acid, ϕ_S values confirm a viscoelastic behaviour for all the different temperatures probed with a more pronounced viscous component as the temperature increases. Adding 0.01% oleic acid appears to reverse the trend, with higher temperatures appearing more elastic. This anomalous behaviour could be due to a partially compensated effect of the water nanodroplets which may create pinning points for the AFM tip [11]. At 0.1% oleic acid, the behaviour is back to a more usual trend with temperature, but without a regular progression. At low confining forces (< 5 nN), the shear amplitude and hence force are close to the experimental noise level. ϕ_S is hence undefined (semi-transparent region). Experiments were performed at RH $= 45 \pm 2\%$.

$N \sim 10^{-4} \times 10^{-4}$ litre $\times$ 0.77 $\times$ 10^3 g litre^{-1} / 226 g mol^{-1} $\times$ 6 $\times$ $10^{23} \sim 2 \times 10^{16}$.

The calculations suggest that 1/100 oleic acid molecules are at the interface to create a cohesive layer. Given the entropic costs associated with having all the acid molecules at the interface, a ratio of 1/100 indicates a strong affinity of the acid for the interface if a full layer can form. Considering the fact that the molecules are not bound at the interface and the system entropy will inevitably retain some of the oleic acid in the solution, no oleic acid aggregates are likely to be present within the nanoconfined hexadecane but instead form a regular layer. Such a layer would also be favoured by the amphiphilic nature of the acid. In addition, the interaction between oleic acid molecules is relatively long ranged [52], thus not necessarily requiring a full coverage of the initial water layer to be effective. Indeed, 0.01% of acid has already a significant effect on the interface (Fig. 6.4a-b). The impact of oleic acid on the structural organisation of the water/hexadecane interface has crucial consequences on the shear response of the system. The average lubricated friction markedly decreases as a function of oleic acid concentration (Fig. 6.4c). The lubrication process also appears to change, with a close to linear dependence of the lubricated friction force on the applied load. This behaviour can be observed in aqueous solutions [11] but is unusual in organic lubricants [27]. This suggests the particular arrangement of the oleic acid at the interface to play a dominating role in reducing friction, not only by removing the water nanodroplets, but also by forming a passivation layer protecting the AFM tip from pinning and playing a lubricating role.

It is worth mentioning that the carboxylic group of oleic acid may react with the potassium ions adsorbed on the mica surface forming a chemisorbed carboxylate film [54]. However,

given the strong hydrophilic nature of mica, this is unlikely to occur in humid environments, where most of the potassium ions are dissolved in the water layers naturally built up on mica after cleavage. Instead, carboxylate film formation is expected to be favoured in a situation where the carboxylic acids are deposited onto mica in the absence of any liquid water. Hence, the arrangement of the amphipathic molecules at the interface between water and hexadecane seems the most likely mechanism behind the observed reduction in water nanodroplets.

6.4.3 Impact of humidity on interfacial water nanodroplets

In order to unambiguously establish the role of water in the model system, further experiments were carried out at different RH. The mica disc and the AFM chamber were flushed with pure nitrogen for 48 hours so as to reach RH = 0% within experimental error (± 2%). After depositing hexadecane on the mica substrate, the AFM chamber was sealed. The AFM experiments were then conducted without the nitrogen flow to avoid acoustic perturbations, resulting in RH < 10% throughout the measurements (low humidity). The RH was measured inside the AFM isolating enclosure protecting the sealed AFM chamber. Hence the RH inside the sealed AFM chamber was likely to be even lower than 10%. In this case, no nanodroplets appeared at the interface, even after increasing the temperature up to 368 K (Fig. 6.6).

High humidity experiments were performed equilibrating the mica substrate at RH > 75% for 2 hours and then depositing hexadecane on mica. After sealing the AFM chamber, the RH humidity was measured inside the AFM isolating enclosure. This ensured that the experiments were performed at constant humidity level. In the case of high humidity, nanodroplets were already present at room temperature. Such a high RH was achieved by saturating the AFM chamber with water vapour. The nucleation of water nanodroplets at the interface has a dramatic influence on the lubricated friction. At low RH, F_S reveals a standard thermal behaviour [27, 42] with the lubricated friction force decreasing with temperature. This is no longer true at higher RH where temperature increases the lubricated friction force due to the presence of nanodroplets at the interface.

6.4.4 Control experiments to rule out contamination effects

In order to rule out the possibility of the AFM observations of nanodroplets being the result of contamination, each experiment was performed 5 times using different batches of hexadecane and mica discs and consistently showing interfacial nanodroplets. Control experiments were also carried out using a silicon nitride AFM probe and a hydrophobic substrate, HOPG. The hydrophobic nature of HOPG prevents the formation of a stable water layer in ambient conditions [11] while favouring the adsorption of

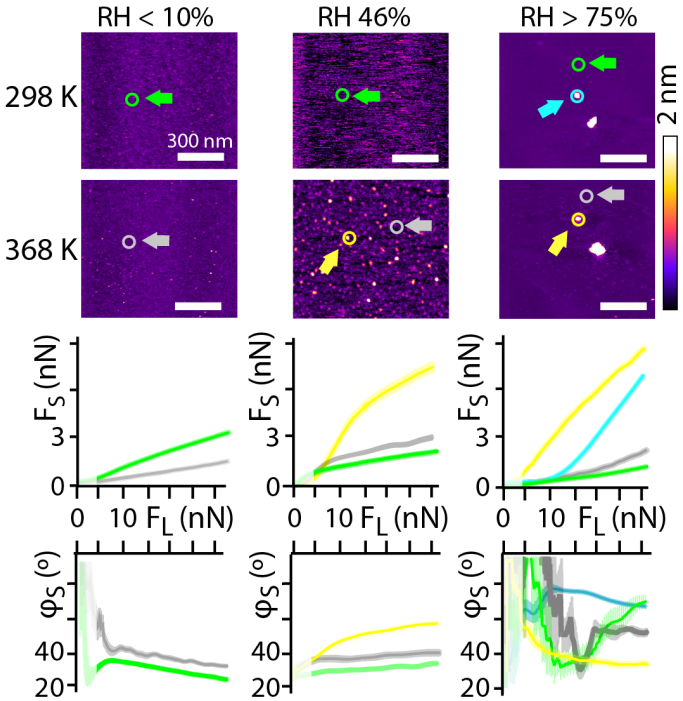

Fig. 6.6: Nanoscale impact of relative humidity on lubrication. High-resolution amplitude-modulation AFM imaging of hexadecane at the interface with mica (top). At low RH, no water nanodroplets appear at the interface and the lubricated friction force (shear force, F_S) decreases with increasing temperature. As the RH increases, water nanodroplets begin to appear with a significant impact on F_S. For RH of 46% (ambient conditions) and 75%, F_S is dramatically influenced by the presence of nanodroplets. This results in an anomalous thermal behaviour of F_S with temperature. For low and intermediate RH, the shear phase, ϕ_S, values indicate a viscoelastic regime with a weak evolution towards a more viscous behaviour as the temperature increases. At intermediate RH, the presence of nanodroplets create a more viscous shearing, consistent with the behaviour of water under shear [11]. At higher RH, nanodroplets tend to dominate the shear response of the lubricant. At low confining forces (< 5 nN), F_S is close to the experimental noise level, and the associated ϕ_S is undefined (semi-transparent regions). For all the RHs probed, the green and cyan force curves are taken respectively on areas of uniform hexadecane-mica interface and nano-droplets at 298 K; the grey and yellow curves are taken respectively on areas of uniform hexadecane-mica interface and nano-droplets at 368 K. The RH was measured inside the AFM isolating enclosure, and the error on the RH was $\pm$ 2%. The experiments were however likely to be affected by smaller variations as the measurements were conducted in the sealed AFM chamber placed within the isolating enclosure.

organic contaminants and should therefore not allow for water nanodroplets to form. Representative images (Fig. 6.7) confirm the absence of nanodroplets regardless of temperature.

In the absence of water, the shear response of the lubricant is dominated by surface nano-defects as already known from other model systems [42]. Interestingly, even close to the surface singularities, the lubricated friction force is significantly smaller than that induced by water nanodroplets (Fig. 6.3-6.4) This highlights the dominating role of interfacial water and the need of a hydrophilic surface such as mica for the nanodroplets to form.

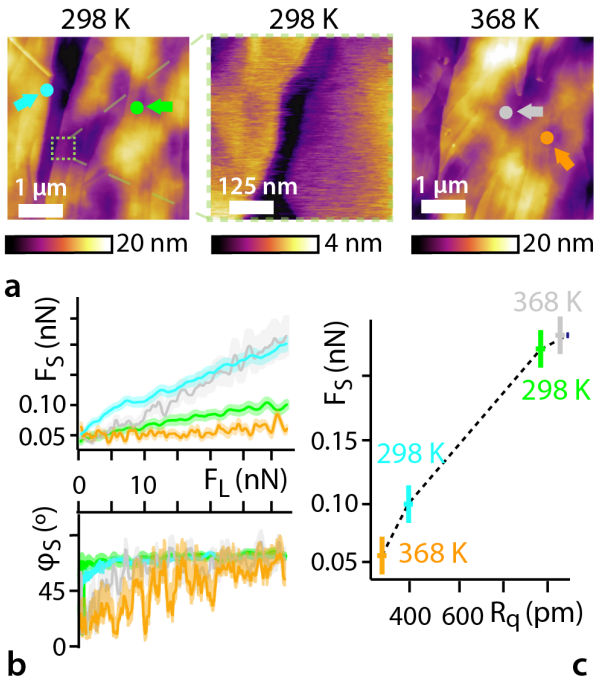

Fig. 6.7: AFM imaging and shear behaviour of hexadecane molecules at the surface of HOPG. Topography images (top) clearly show step edges and molecular layers, but no nanodroplets similar to those in Figs 6.2, 6.3 and 6.4. Experiments were performed at RH = 45 ± 2%. (**a**) Shear force spectroscopy measurements reveal a standard decrease of the lubricated friction force (shear force, F_S) with temperature. (**b**) The confined hexadecane layer shows a consistent viscoelastic behaviour as confirmed by the shear phase, ϕ_S. (**c**) The friction force is primarily affected by surface singularities such as steps and roughness, as shown by the clear correlation between the lubrication force and the root mean square roughness (R_q) of the HOPG.

In contrast, the chemical characteristics of the AFM probe do not seem to play a major role with the droplets being present on mica regardless of whether a hydrophilic (Fig. 6.2) or hydrophobic (Fig. 6.8) AFM tip is used. The fact that the flat interface dominates the observation instead of the cantilever-liquid interface is also consistent with previous AFM studies [55–57].

6.5 Rationalising the effect of temperature

In the proposed interpretation of the AFM observations, increasing the temperature stimulates the condensation into nano-droplets of the nanoscopic water film [37, 38] that initially covers the mica surface uniformly (Fig. 6.9). The underlying mechanism can be described in terms of a thermodynamic competition between hexadecane and water molecules for the mica's surface. Thermodynamics considerations about the most likely configurations of the different molecular species at the interface all hinge on the interfacial energies at play, with the work of adhesion and the spreading coefficient being the most

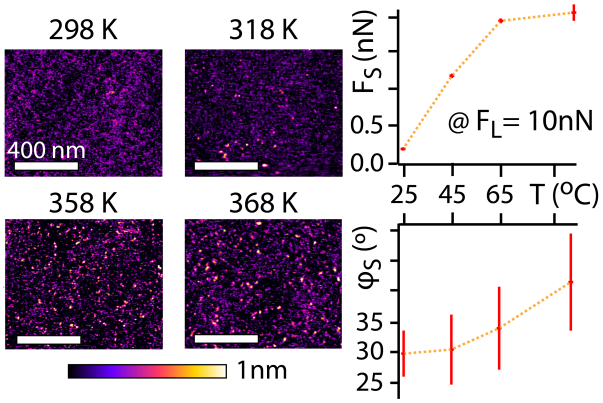

Fig. 6.8: High resolution AFM imaging and shear behaviour of the hexadecane-mica interface measured with a diamond AFM tip. Topographic images of the interface show the density of nanodroplets increases with temperature. At each temperature, the shear force, F_S, and phase, ϕ_S, are averaged over at least 5 locations to show the average impact of the nanodroplets, revealing the unusual increase of F_S with temperature. The associated ϕ_S shows a viscoelastic response of the sheared lubricant with no obvious temperature effect. F_S and ϕ_S displayed correspond to an applied load, F_L, equal to 10 nN. Experiments were performed at RH = 45 ± 2%.

important observables to characterise the system. Hereafter, I will introduce the most relevant aspects of these thermodynamic quantities and then discuss the consequences for the hexadecane-water-mica system.

Work of adhesion

The affinity between both liquids and the mica surface is best quantified by their respective work of adhesion W. The work of adhesion $W_{1,2}$ between the media 1 and 2 is related to the interfacial energy through the Dupré equation [58–60]:

$$\gamma_{1,2} = \gamma_1 + \gamma_2 - W_{1,2} \tag{6.1}$$

where γ_1 and γ_2 are respectively the surface energies of the media. The definition can be extended for interfaces exposed to a third medium (e.g. air) so that the work of adhesion between a solid and a liquid in the presence of a gas can be written as [58]:

$$W_{S,G,L} = \gamma_{S,G} + \gamma_{L,G} - \gamma_{S,G,L} \tag{6.2}$$

with $\gamma_{S,G} \sim \gamma_S$ the surface energy of the solid, $\gamma_{L,G}$ the surface tension (or surface energy) of the liquid measured in the presence of the gas and $\gamma_{S,G,L}$ the interfacial energy between the solid and the liquid in ambient conditions (not sealed from the atmosphere). From this last equation and the values given in Table 6.1, it is possible to estimate the following works of adhesion:

- Mica-water in air: $W_{m,a,w}$= 162 mN/m
- Mica-hexadecane in air: $W_{m,a,h}$= 146 mN/m

The values are estimates and carry an uncertainty of $\sim$ 10% (measured values).

Interface	γ (mN/m)
hexadecane-air [61]	27.42
hexadecane-mica$*$	53.90
hexadecane-water [62, 63]	53.30
water-air [53]	71.97
water-mica [64, 65]	83.00
mica-air [64]	173.00

Tab. 6.1: Interfacial energies between the different materials present in the system at 298 K. $*$ Experimentally determined in this study from contact angle measurements.

Spreading coefficient

The spreading coefficient, S, for a given liquid on the surface characterises the tendency of the liquid to spread on the solid, with spreading spontaneously occurring if $S > 0$. In the presence of a gas, S is simply derived from the Young's equation [66] assuming a null contact angle:

$$S_{L,G,S} = \gamma_{S,G} - \gamma_{L,G} - \gamma_{S,L} \tag{6.3}$$

where $\gamma_{S,G}$, $\gamma_{L,G}$, $\gamma_{S,L}$ correspond to the different interfacial energies between the solid, the liquid and the gas (S, L and G respectively). For water and hexadecane over mica in air, and using the values of Table 6.1, we get:

- $S_{w,a,m}$= 18 mN/m
- $S_{h,a,m}$= 92 mN/m

Also these values are estimates and carry an uncertainty of $\sim$ 10% (measured values). The difference between $W_{m,a,w}$ and $W_{m,a,h}$ is relatively small, in the order of 10%. Hexadecane furthermore exhibits a spreading coefficient S almost 5 times larger than water on mica. These values indicate that hexadecane and water are in close competition for the mica surface in ambient conditions, despite the mica being strongly hydrophilic. It is important to note that freshly cleaved mica can react with atmospheric CO_2 and other carbon contaminants [37, 67, 68], enhancing the affinity of hexadecane. Within this framework and the experimental observations on the role of temperature (Fig. 6.2), the evolution of the water nanodroplets can be understood in terms of a thermally activated process. Simple energy calculations allow quantifying this process.

6.5.1 Calculation of the total interfacial energy for a uniform water film vs a nanodroplet

At the beginning of each experiment, the mica surface is covered with a thin layer of water, typically 2 to 10 molecules thick (0.4 nm to 2 nm) depending on the ambient humidity [37, 46]. After immersion of the system into hexadecane, the layer may condense into discrete nanodroplets. Hereafter, I will calculate and compare the free energy associated with a same area A of the interface covered by either (i) a uniform water layer of thickness w or (ii) a single nanodroplet with the shape of a spherical cap as shown in Fig. 6.9. The total volume of water and hexadecane is conserved between the two situations, but the area of the different interfaces changes.

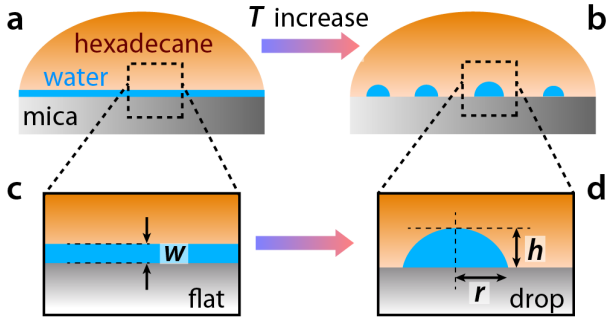

Fig. 6.9: A cartoon representation of the interface shows the temperature-stimulated transition from a nanoscopic water film covering the mica surface uniformly inside the hexadecane (**a**) to nanodroplets of water with hexadecane partially reaching the mica surface (**b**). It is possible to compare the total interfacial energy associated with a set area of the interface containing either a water nanodroplet (**c**) or a uniform water film of same volume (**d**).

Using the notation given in Fig. 6.9, the free energy E_{flat} associated with the uniform (flat) interface is given by:

$$E_{flat} = A\,\gamma_{m,w} \;+\; A\,\gamma_{h,w} \tag{6.4}$$

where the indices m, w and h stand for mica, hexadecane and water, respectively. To calculate the free energy E_{drop} associated with the interface containing the water droplet, it is necessary to first calculate the area of the droplet in contact with the mica and with the hexadecane. Assuming a spherical cap shape, the area covered by the water-hexadecane interface is given by $\pi(r^2+h^2)$, the area of water-mica contact is the base of the cap (πr^2) and the hexadecane-mica area is simply given by $A-\pi r^2$. This leads to the following expression:

$$E_{drop} = \pi r^2\,\gamma_{m,w} \;+\; \left(A-\pi r^2\right)\,\gamma_{m,h} \;+\; \pi(r^2+h^2)\,\gamma_{h,w} \tag{6.5}$$

Finally, both Eqs. 6.4 and 6.5 can be made independent of the area A of the interfacial region considered by assuming a conservation of the water volume:

$$Aw = \frac{1}{6}\pi h\left(3r^2 + h^2\right) \tag{6.6}$$

where the left term of the equality is the volume of water contained in the flat layer and the right-hand side term the volume of the cap making the water nanodroplet. Combining Eqs 6.4-6.6 and the interfacial energies given in Table 6.1, it is straightforward to calculate the ratio E_{flat}/E_{drop} as a function of r, h and w. As shown in Figs 6.10 and 6.11a, the ratio is calculated for :

- r ranging between 0.2 nm (1 water molecule) and 15 nm (30 nm diameter droplet, seen experimentally)
- h ranging between 0.2 nm (1 water molecule) and 5 nm (larger droplets observed experimentally)
- w = 2, 4, 6, 8 and 10 water layers so that 0.4 nm $\leq$ w $\leq$ 2 nm

In all cases, if $E_{flat}/E_{drop} < 1$, the uniform water film is thermodynamically favoured. These regions of the parameter space appear as blue in Fig. 6.10. If $E_{flat}/E_{drop} > 1$, water droplets are favoured with the associated regions of the parameter space appearing red in Fig. 6.10. The boundary between the two configurations is simply given by $E_{flat}/E_{drop} = 1$. Figure 6.11a compares the nucleation thresholds for the different w values of the initial water layer.

Under these circumstance, the free energy calculations show that the growth of interfacial water nanodroplets from the initial water film is thermodynamically favoured, provided that the nanodroplets reach a size comparable to that observed in Fig. 6.2. This indicates that the water nanodroplets form through a nucleation process requiring overcoming an initial interfacial energy barrier. This explanation is also consistent with the dependence on temperature: nucleation being an activated process, its probability usually follows an Arrhenius behaviour [69] and is hence proportional to $exp\left(-\frac{A}{k_B T}\right)$ where A is the activation energy and k_B the Boltzmann's constant. Consistently with classical nucleation theory, once the water nanodroplets are formed, they are stable and tend only to grow through ripening. This is visible in the hysteresis behaviour observed when the temperature is brought back down to 298 K (Fig. 6.2) with fewer, larger droplets being present at the interface.

I have also examined the evolution of the van der Waals interactions between water, hexadecane and mica with temperature. While the interface thermodynamics is the likely driving force for the nanodroplets nucleation, van der Waals interactions are also likely to play a role here given the high dieletric constant of mica [77, 78]. As shown in Chapter 2

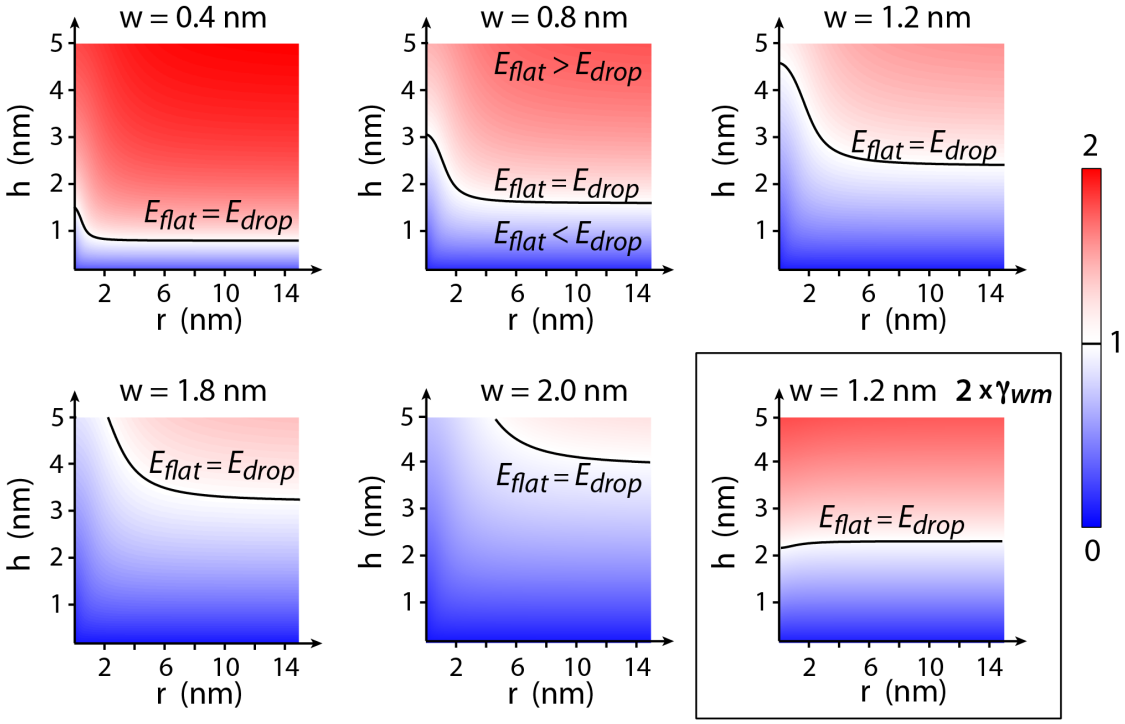

Fig. 6.10: Energy landscape of the interface. The energy ratio E_{flat}/E_{drop} is plotted as a function of r and h for different w values reflecting typical experimental conditions. The regions appearing in blue favour a uniform water layer to cover the mica surface whereas red regions favour the formation of discrete water droplets. Higher humidity conditions (larger w values) favour larger droplets and flatten the energy landscape. Increasing by a factor of two the interfacial energy between water and the solid (hence lowering the water-solid affinity) tends to shift the equilibrium to smaller droplets and reduce the influence of h, rendering their nucleation more likely.

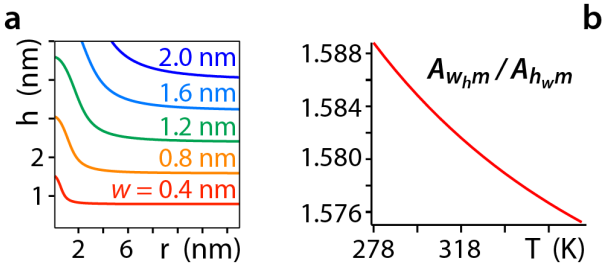

Fig. 6.11: Thermodynamics of hexadecane and water at the mica interface. Smaller droplets are unstable, consistent with classical nucleation theory. The ambient humidity affects the thickness w of the initial water film and hence the nucleation threshold (**a**). The temperature dependence of the ratio between the Hamaker constants describing water-mica interactions in hexadecane $H_{w,h,m}$ and hexadecane-mica interactions in water $H_{h,w,m}$ (**b**) supports the idea that a temperature increase comparatively reinforces the van der Walls interactions between the hexadecane and the mica through the interfacial water [70–76].

Section 2.2.4, for two media 1 and 2, separated by a distance L through a third medium

3, the van der Waals potential is described by [79]:

$$U_{vdw} = -\frac{H_{132}}{12\pi L^2} \tag{6.7}$$

with H_{132} being:

$$H_{132} = \frac{3k_BT}{4}\frac{\epsilon_1-\epsilon_3}{\epsilon_1+\epsilon_3}\frac{\epsilon_2-\epsilon_3}{\epsilon_2+\epsilon_3} + \frac{3h\nu_\epsilon}{8\sqrt{2}}\frac{\left(n_1^2-n_3^2\right)\left(n_2^2-n_3^2\right)}{\sqrt{n_1^2+n_3^2}\,\sqrt{n_2^2+n_3^2}\left(\sqrt{n_1^2+n_3^2}+\sqrt{n_2^2+n_3^2}\right)} \tag{6.8}$$

where k_B, T, h, ν_ϵ, ϵ_i and n_i are the Boltzmann constant, the temperature, the Planck constant, the electronic absorption frequency, the dielectric constant and the refractive index, respectively [73, 79]. The ϵ_i and n_i values for all the interfacial components are shown in Table 6.2. Air is taken to have dielectric constant of 1 [73] and the electronic absorption frequency for hexadecane and water is taken to be 3 x 10^{15} Hz [72].

Medium	ϵ_i	n_i
Air	1.0 [73]	1.000 [73]
Hexadecane	2.1 [72]	1.423 [71, 72]
Mica	7.0 [77, 78]	1.598 [80, 81]
Water	80.0 [71, 72]	1.333 [71, 72]

Tab. 6.2: Dielectric constant and refractive index values for the different components of the model system under investigation.

As expected, the Hamaker constant describing the van der Waals interaction between hexadecane and mica through water, $H_{h,w,m}$, and that describing the interaction between water and mica through hexadecane, $H_{w,h,m}$, both increase with temperature. However, the increase rate is higher for $H_{h,w,m}$ so that the ratio $H_{w,h,m}/H_{h,w,m}$ decreases with temperature (Fig. 6.11b). While the effect is small, this further supports the idea that a temperature increase of the system comparatively reinforces the van der Walls interactions between hexadecane molecules and mica surface through interfacial water.

6.5.2 The macroscopic equilibrium perspective

While AFM measurements provide nanoscale insights into the evolution of the interface, the interpretation of the results rely on macroscopic concepts such as the interfacial energies between the different materials constituting the system. I have therefore conducted macroscopic measurements of the static contact angle formed by hexadecane and mica at different relative humidiy (Fig. 6.12). To allow for comparison, all the experiments are conducted with the same volume of hexadecane, over a same, freshly cleaved mica surface and at the same temperature. At RH = 0%, hexadecane spreads rapidly over mica. The spreading kinetics can be well described with an exponential convergence to the maximum

coverage, yielding a single timescale of 35 ± 5 s (Fig. 6.12a). Hexadecane is fully wetting with a contact angle close to 0° as for pure water on mica (Fig. 6.12b). When the relative humidity increases, hexadecane retains its ability to spread rapidly, at least initially. In all cases, hexadecane strongly wets the interface with a contact angle $< 10°$ (Fig. 6.12b-d) even at saturated humidity (RH = 100%) where the water layer initially present on the mica surface is ~ 2 nm thick [46]. At RH = 100%, hexadecane spreading kinetics can also be modelled with a single exponential convergence to the maximum coverage (Fig. 6.12a), returning a slightly slower timescale of 55 ± 5 s compared to RH = 0%. The similarity is not surprising considering the very similar interfacial energies γ for hexadecane-mica ($\gamma_{h,m} = 53.90$ mN/m) and hexadecane-water ($\gamma_{h,w} = 53.30$ mN/m) (see Table 6.1).

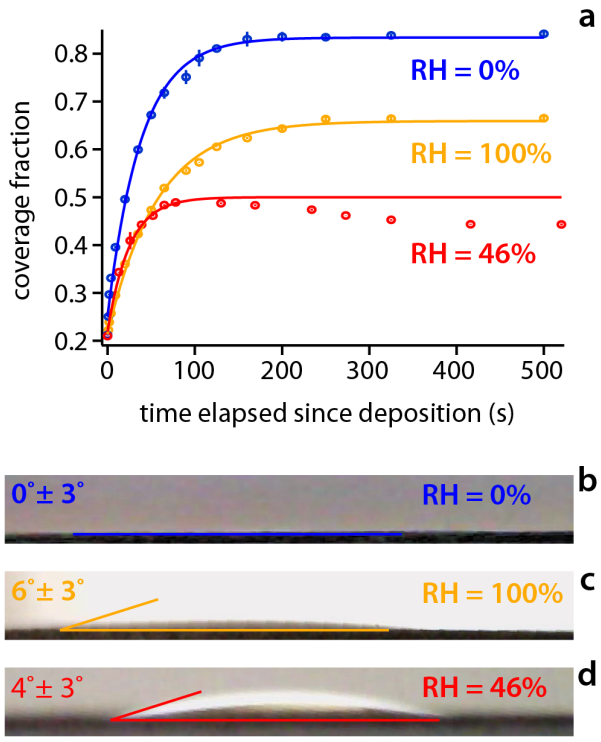

Fig. 6.12: Wetting dynamics for hexadecane on mica as a function of the relative humidity. (**a**) The time evolution of the hexadecane surface coverage fraction is tracked for dry (RH = 0%), humidity saturated (RH = 100%) and ambient (RH = 46%) conditions. Each set of kinetic data behaves as a simple exponential convergence to the maximum coverage achieved (solid lines fit) except for RH = 46% where the hexadecane recedes past 100 s. Snapshots of the movies tracking the evolution of the hexadecane drops provide estimate of the contact angle in each case (**b-d**). The error on the RH is ± 2%. All the experiments were performed at 298 K with the mica disc first equilibrated for 30 minutes in the desired conditions before depositing a 5 μl hexadecane drop and immediately recording its evolution.

This suggests that hexadecane uniformly spreads over the unaltered initial water layer, experiencing a thermodynamic situation almost identical to that in a completely dry atmosphere. This is also consistent with thermodynamics considerations whereby the thick

water layer present in saturated conditions [46] renders the nucleation of water nanodroplets less favourable (Fig. 6.6 and 6.11a). The final coverage reached over the timescale of the experiment is lower than for RH = 0% simply due to the higher contact angle. The situation is however different for the intermediate relative humidity (RH = 46%) that does not follow the trend. First, its maximum coverage is the lowest despite an intermediate contact angle value. Second, the kinetics is unusual with an initial rapid expansion comparable to that at RH = 0% (timescale of 25 ± 5 s) followed by a slow receding of the hexadecane spread, occurring over hundreds of seconds. This slow recess, highlighted by the exponential fitting (Fig. 6.12a), points to new interfacial effects absent in the other cases. Given the moderate relative humidity, the water layer initially covering the mica surface is not as thick as for RH = 100% but typically less than 1 nm [37, 38]. Occasional water nanodroplets are therefore likely to nucleate over the course of the experiment. However, given the relatively low temperature of the system (298 K), the nucleation rate is slow and only few droplets nucleate, progressively growing into large droplets by absorbing the surrounding water layer. This effect may render the interface inhomogeneous and hamper even the spreading of the hexadecane into a uniform layer. The small number of interfacial water droplets would also explain the fact that none were observed by AFM in these conditions with their effect only visible at the macroscale when the whole interface is considered.

The possibility of air-born water microdroplets bringing down hydrocarbons from the glove box walls onto the mica surface cannot be excluded, including species containing hydrophilic groups [67, 82]. Such molecules could create a bridge between the adsorbed water layer on mica and hexadecane, enhancing the hexadecane spreading at high humidity. However, the consistency of the nucleation interpretation for macroscopic and molecular-level AFM results suggest the later explanation to be the most likely interpretation.

6.6 Summary

In this Chapter, I have investigated the nanoscale details of the impact of ambient humidity on lubricated friction in a well-established model system. The experiments, combining high-resolution AFM imaging and nano-localised shear-force measurements, show that increasing the temperature of the system stimulates the nucleation of water nanodroplets at the hydrophilic interface. A fine balance of interfacial energies between mica, water and hexadecane determines the nucleation threshold, and water nanodroplets become stable for sizes in the range 20-50 nm, depending on the ambient humidity. Interestingly the same thermodynamics calculations used to estimate the nucleation threshold indicate a nucleation threshold with smaller droplets on the less hydrophilic metal oxide typical of engines. This would render the nucleation of water droplets more likely considering the

stochastic nature of the nucleation process. Water nanodroplets are highly detrimental to the lubrication properties of the interface by modifying the wetting properties of the shearing surfaces and creating local pinning points. The presence of droplets in engines and machinery that are typically made of metal are likely to exacerbate this effect. The issues can be however mitigated through the adjunction of amphiphilic molecules such as oleic acid to the lubricant, here hexadecane. With its hydrophilic groups, oleic acid binds to the water layer adsorbed on mica, whereas its hydrophobic chain has a strong affinity for the overlying hexadecane fluid. This prevents hexadecane from competing and displacing water molecules from the mica's surface, considerably reducing the average lubricated friction force. Overall, the present results provide a nanoscale description of the different processes at play and help explain the macroscale observations: humidity markedly limits the efficiency of oil-based lubricants on hydrophilic substrates such as the metal surfaces often used in car engines and industrial machinery. The present results may contribute to the rational design of optimal tribological solutions for technological applications.

References: Chapter 6

[1] M. Urbakh et al., *Nature* **2004**, *430*, 525–528.

[2] H. Turlier et al., *Nature Physics* **2016**, *12*, 513–519.

[3] G. D. Jay et al., *Matrix Biology* **2014**, *39*, 17–24.

[4] K. Lormes et al., *MTZ Worldwide* **2018**, *79*, 50–53.

[5] A. Greco et al., *Wear* **2011**, *271*, 1754–1760.

[6] D. Berman et al., *Materials Today* **2014**, *17*, 31–42.

[7] K. Holmberg et al., *Tribology International* **2012**, *47*, 221–234.

[8] Z. Chen et al., *Lubricants* **2018**, *6*, 74.

[9] A. Filippov et al., *Physical Review Letters* **2004**, *92*, 135503.

[10] T. E. Fischer et al., *Wear* **1988**, *124*, 133–148.

[11] C. Cafolla et al., *Nanoscale* **2018**, *10*, 11831–11840.

[12] K. Hasz et al., *Physical Review Materials* **2018**, *2*, 126001.

[13] M. Lapuerta et al., *Wear* **2014**, *309*, 200–207.

[14] B. Basu et al., *Acta materialia* **2000**, *48*, 2461–2471.

[15] Q. Wei et al., *RSC Advances* **2018**, *8*, 12540–12546.

[16] S. Soltanahmadi et al., *Tribology International* **2017**, *107*, 184–198.

[17] A. Arcifa et al., *ACS Applied Materials & Interfaces* **2016**, *8*, 2961–2973.

[18] J. Zhang et al., *Surface and Coatings Technology* **2016**, *304*, 530–536.

[19] J. Lancaster, *Tribology International* **1990**, *23*, 371–389.

[20] H. Cen et al., *Tribology international* **2012**, *56*, 47–57.

[21] K. Jacques et al., *Tribology Letters* **2019**, *67*, 105.

[22] A. Jabbarzadeh et al., *The Journal of Chemical Physics* **1999**, *110*, 2612–2620.

[23] F. Tian et al., *Langmuir* **1999**, *15*, 244–249.

[24] R. Pit et al., *Physical Review Letters* **2000**, *85*, 980.

[25] A. Jabbarzadeh, *Tribology International* **2016**, *97*, 108–115.

[26] C. Kajdas et al., *Lubrication Science* **2006**, *18*, 255–263.

[27] K. Voitchovsky, *Nanoscale* **2016**, *8*, 17472–17482.

[28] N. Maeda et al., *The Journal of Physical Chemistry B* **2001**, *105*, 5906–5913.

[29] O. Y. Fajardo et al., *ACS Nano* **2017**, *11*, 6825–6831.

[30] Y. Zhu et al., *Tribology Letters* **2003**, *15*, 127–134.

[31] X. Gong et al., *Advanced Engineering Materials* **2018**, *20*, 1700617.

[32] P. K. Jana et al., *Physical Chemistry Chemical Physics* **2018**, *20*, 18737–18743.

[33] S. Ohnishi et al., *Langmuir* **2002**, *18*, 6140–6146.

[34] M.-D. Krass et al., *Tribology Letters* **2018**, *66*, 87.

[35] S. Cui et al., *The Journal of Chemical Physics* **2001**, *114*, 6464–6471.

[36] S. Balasubramanian et al., *The Journal of Chemical Physics* **1995**, *103*, 3184–3195.

[37] X. Gong et al., *Chemical Science* **2015**, *6*, 3478–3482.

[38] K. Xu et al., *Science* **2010**, *329*, 1188–1191.

[39] H.-J. Butt et al., *Nanotechnology* **1995**, *6*, 1.

[40] C. Cafolla et al., *Journal of Applied Physics* **2018**, *124*, 154502.

[41] A. C. Fischer-Cripps, *Introduction to contact mechanics*, Springer, **2007**.

[42] C. Cafolla et al., *Science Advances* **2020**, *6*, eaaz3673.

[43] K. Voitchovsky et al., *Nature Nanotechnology* **2010**, *5*, 401–405.

[44] J. Schindelin et al., *Nature Methods* **2012**, *9*, 676–682.

[45] M. Brugnara, *University of Trento Trento Italy* **2010**.

[46] T. Arai et al., *Scientific Reports* **2017**, *7*, 1–11.

[47] M. Binggeli et al., *Journal of Vacuum Science & Technology B* **1995**, *13*, 1312–1315.

[48] G. Graziano, *Chemical Physics Letters* **2011**, *511*, 262–265.

[49] Y. Qiu et al., *Crystals* **2017**, *7*, 86.

[50] H. Fang et al., *RSC Advances* **2015**, *5*, 23578–23585.

[51] D. WU et al., *Chemical Engineering Communications* **1999**, *172*, 85–106.

[52] M. H. Wood et al., *Langmuir* **2016**, *32*, 534–540.

[53] J. A. Dean, *Lange's handbook of chemistry*, McGraw-Hill, **1999**.

[54] S. Campen et al., *Tribology Letters* **2015**, *57*, 18.

[55] T. Fukuma et al., *Physical Review Letters* **2010**, *104*, 016101.

[56] M. Ricci et al., *Nature Communications* **2014**, *5*.

[57] S.-H. Loh et al., *Langmuir* **2010**, *26*, 9176–9178.

[58] J. N. Israelachvili, *Intermolecular and surface forces*, Academic Press, **2015**.

[59] R. A. L. Jones et al., *Soft condensed matter*, Oxford University Press, **2002**.

[60] A. Dupre, *Theorie mecanique de la chaleur*, Gauthier-Villars, **1869**.

[61] D. D. Bank, Surface Tension of Hexadecane, **2020**, http://www.ddbst.com/en/EED/PCP/SFT_C516.php (visited on 05/08/2020).

[62] G. M. Kontogeorgis et al., *Introduction to applied colloid and surface chemistry*, John Wiley & Sons, **2016**.

[63] R. Aveyard et al., *Transactions of the Faraday Society* **1965**, *61*, 2255–2261.

[64] J. Drelich et al., *Journal of Colloid and Interface Science* **2004**, *280*, 484–497.

[65] A. I. Bailey et al., *Proceedings of the Royal Society of London* **1967**, *301*, 47–56.

[66] T. Young in Philosophical Transactions of the Royal Society, *Vol. 95*, **1805**, pp. 65–87.

[67] Z. Li et al., *ACS Nano* **2016**, *10*, 349–359.

[68] H. K. Christenson et al., *Surface Science Reports* **2016**, *71*, 367–390.

[69] P. G. Debenedetti, *Metastable liquids: concepts and principles*, Princeton University Press, **1996**.

[70] H. D. Ackler et al., *Journal of Colloid and Interface Science* **1996**, *179*, 460–469.

[71] C. J. Van Oss et al., *Chemical Reviews* **1988**, *88*, 927–941.

[72] I. Lee, *Journal of Materials Science* **1995**, *30*, 6019–6022.

[73] F. L. Leite et al., *International Journal of Molecular Sciences* **2012**, *13*, 12773–12856.

[74] R. M. Pashley et al., *Applied colloid and surface chemistry*, John Wiley & Sons, **2004**.

[75] J. H. Masliyah et al., *Electrokinetic and colloid transport phenomena*, John Wiley & Sons, **2006**.

[76] W. M. Haynes, *CRC handbook of chemistry and physics*, CRC Press, **2014**.

[77] C. G. Low et al., *Small* **2014**, *10*, 4213–4218.

[78] C. G. Low et al., *Small* **2012**, *8*, 2178–2183.

[79] J. M. Fernandez-Varea et al., *Journal of Colloid and Interface Science* **2000**, *231*, 394–397.

[80] A. I. Bailey et al., *British Journal of Applied Physics* **1965**, *16*, 39.

[81] S.-L. Guo et al. in *Handbook of Radioactivity Analysis*, Elsevier, **2020**, pp. 307–407.

[82] A. Verdaguer et al., *Chemical Reviews* **2006**, *106*, 1478–1510.

7.0 Conclusions and outlook

It doesn't matter how beautiful your theory is. If it doesn't agree with experiment, it's wrong.
Richard Feynmann, The Character of Physical Law, 1964

7.1 Summary

Friction is central to several natural and technological processes, from machinery brakes to solid state drive memories [1]. In most of the scenarios, friction is however detrimental as it involves wearing of surfaces in contact and marked waste of energy. Hence, the need to develop efficient lubricating solutions so as to allow the surfaces in contact to smoothly slide over each other [2]. This is crucial at the nano and mesoscale giving the growing importance of nanotechnologies and miniaturised devices [3]. The standard models, based on Amontons-Coulomb's laws, cannot fully capture the organisation and dynamics of lubricants at such scales, as these methods tend to average phenomena over large length and time scales without elucidating the specific molecular interactions [4]. Furthermore, a better understanding of the mechanisms behind lubricated friction at the nano and mesoscale would help to fill in the current gap between atomistic models and observed macroscale phenomena with the ultimate goal of developing efficient tribological solutions for real-life systems, including for example car engines.
In this thesis, using high-resolution AFM imaging and nano-rheological measurements as the main investigation tools, I have contributed to unravelling the fundamental physical processes at the basis of lubricated friction at the nano and mesocale, also providing some novel insights into macroscopically observed phenomena. The key results from this project and their importance are briefly summarised as follows:

- Chapter 3 reports a non-invasive and non-destructive *in situ* calibration method to determine the torsional spring constants of AFM cantilevers in viscous environments. AFM lateral and shear measurements are becoming increasingly popular for their ability to investigate in-plane forces with nanoscale precision, for example in nano-

lubrication studies. However, existing methods able to calibrate the torsional spring constant of microcantilevers typically rely on measuring their Q-factor at torsional resonance, a quantity difficult to measure accurately. Measurements of cantilevers Q-factor are particularly sensitive to the viscosity of the environment, potentially leading to large calibration errors. I present a method that does not require quantification of any Q-factor. The method is validated by comparing it to the common "Sader method" for different cantilevers immersed in six different liquids. The results demonstrate a higher precision, in particular for highly viscous liquids. This method has allowed extracting quantitative measurements from the experiments conducted in the thesis.

- Chapter 4 investigates the behaviour of confined ionic aqueous solutions. AFM is used to locally interrogate only a small number of liquid molecules at a mica interface, and with single ion resolution. This allows unambiguously quantifying the equilibrium and dynamic behaviour of dissolved metal ions at interfaces. The key results show that, in pure water, long-range order of the hydrogen bond network at the interface creates a slow and glassy behaviour of the liquid, with an effective viscosity several orders of magnitude higher than that of bulk water. At small ionic concentration (< 20 mM), single hydrated ions act as an efficient lubricant when diluted; they move between adsorption sites of the solid via a thermally activated process that can be quantitatively modeled (Prandt-Tomlinson). However, at high salt concentrations the model breaks down due to ion-ion interactions that create mesoscale ordered domains (5-20 nm), directly imaged at the interface. The results provide a clear molecular-level basis for explaining the unusual properties of aqueous solutions near interfaces.

- Chapter 5 combines AFM-based experiments with computer simulations to investigate the organization and dynamics of a model lubricant (squalane) near an atomic step of graphite. Surface defects locally promote molecular order in the lubricant due to a reduction in the number of stable molecular configurations near the step. This local ordering is correlated with a reduction in mobility of the lubricant and can propagate across hundreds of nanometers, depending on the intermolecular interactions and temperature. Significantly, it is this local reduction in the lubricant's mobility that dominates the friction forces, and not direct tribological contacts between solids at the step. This represents a radical change in paradigm for understanding lubricated friction because it demonstrates that roughness acts indirectly, by promoting molecular order in the lubricant. To fully explore this new paradigm, extensive molecular-level rheological measurements are conducted at different shearing velocities and temperatures. This allows developing a semi-

empirical model able to quantitatively describe the findings based on molecular interactions within the lubricant.

- Chapter 6 uses contact angle measurements with AFM imaging and highly localized nano-rheology to track *in situ* the behaviour of a model organic lubricant (hexadecane) when exposed to ambient humidity. It is well-established that water is detrimental to the efficiency of oil-based lubricants with serious consequences for the energy consumption of industrial machinery and engines. However, a clear picture of the pathway enabling ambient humidity to affect the performance of devices is still lacking. The results show that real-life conditions promote the formation, at the lubricant-solid interface, of water nanodroplets from ambient humidity. This does not occur on intrinsically hydrophobic materials, but on the hydrophilic surfaces typically found in engines and industrial machinery. The nanodroplets appear through a thermally-nucleated process and dramatically impact the lubricating properties of the system: measurements conducted on single nanodroplets reveal an increase in excess of 100% for the lubricated friction force with any applied load. As a result, the system exhibits poorer lubricating properties at higher temperatures, a highly unusual behaviour. The detrimental impact of humidity on lubrication can be fully mitigated by addition of small amounts of surfactant (here oleic acid) to the oil. Not only does the surfactant curtail the formation of water nanodroplets, but it also enhances the lubrication of the system allowing for a linear dependence of lubricated friction force on load.

7.2 General discussion

The findings of the thesis confirm the hypothesis formulated throughout Chapter 1: a top to down approach is inadequate to characterise lubricated friction at the nano and mesoscale. Macroscale models do not hold true at these length scales, where cooperative interactions among molecules due to topographical and chemical singularities cannot be accurately predicted by theories averaging out the properties of the sliding surfaces and the confined lubricant. Thus, the need for the investigations of this thesis which can interrogate a small number of molecules with a precision down to the pN range and are able to characterise both their structural and dynamic behaviour. After developing a method to accurately quantifying the measurements (Chapter 3), the thesis uses a number of model systems: first aqueous solutions at the interface with hydrophilic and atomistically flat surfaces (Chapter 4); then organic lubricants confined on a hydrophobic surface with well-defined topographical defects (Chapter 5); finally a combined water-organic mixture at the interface with both hydrophobic rough surfaces and hydrophilic flat substrates

(Chapter 6). The results indicate some common threads in the nanoscale behaviour of the different systems, in particular lubricated friction can be interpreted as a thermally activated process. The thesis also shows that a bottom-up approach should preferred for its potential in shining some light on macroscale phenomena. For example, in Chapter 6, the well-known negative impact of humidity on the efficiency of organic lubricants was studied at the nanoscale and then extended to the macroscale providing an insightful explanation for the detrimental role of water.
Here, I will discuss the main results of the thesis and their wider significance. Before discussing these aspects, it appears useful to reflect on the investigation methods, and particularly on the rationale behind their choice.

7.2.1 Methods used

Throughout the thesis, AFM has represented the main tool to study the molecular organisation and dynamic response of lubricants under shear at the solid/liquid interface. AFM-based investigations offer the advantage of, almost simultaneously, *in situ* probing the interfacial interactions determining the structural arrangement of nanoconfined fluids, and characterising the resulting reaction to a perturbing force (shear in our case).
In particular, amplitude modulation (AM) AFM imaging allowed studying the lubricant/solid interface as gently as possible reducing to a mininum any perturbations to the system. This imaging mode allowed accessing, with high spatial resolution, both the molecular details of lubricant re-ordering under nano-confinement and the mesoscale picture of the solid/liquid interface. The former was investigated for example in Chapter 5: the evolution of lubricant solid-like domains at surface defects was tracked with nanometric precision as a function of the distance from the singularity. In Chapter 4, it was possible to visualise how the hydration structure of metal cations in solutions was consistently correlated to a mesoscale reorganisation of the surrounding water.
Alongside imaging the lubricant ordering within nanogaps, AFM-based nano-rheological measurements directly probed the shear response of a highly localised area of the solid/liquid interface. A small number of fluid lubricant molecules were interrogated thus obtaining information on both the magnitude and the nature (elastic vs viscous) of the dynamic response under an applied shear. The calibration method for the torsional spring constant presented in Chapter 3 allowed accurately quantifying the information obtained by shear spectroscopy. The relevance of the calibration method goes beyond the thesis as it may significantly contribute to the field of nano and mesoscale tribology: AFM spectroscopic investigations are expected to benefit from a rapid and non-invasive approach to precisely measure friction forces. The potential of accurately calibrated nano-rheological measurements emerges clearly, for example, in Chapter 6. In this Chapter, it was possible

to distinguish the shear response of the adsorbed organic lubricant and the interfering water nano-droplets, thus decoupling the single contributions to the overall friction of the system. Combining the methodology with the ability of finely tuning shear velocity and temperature allowed developing quantitative models for lubricated friction at the nano and mesoscale (Chapters 4 and 5).

The AFM tip being both the measuring device and one of the interacting surfaces, AFM measurements are potentially limited by bias due to changes in the probe characteristics while scanning. Thus, complementary SEM was conducted in all the research studies of this thesis so as to rule out any deformations in the AFM tip apex. Furthermore, using SEM-based analysis of the AFM tips, it was possible to estimate the confining area and consequently the applied pressure to the confined lubricant. This confirmed the potential relevance of the results for applications in engines and industrial machinery, where components are subject to confining pressure of the order of hundreds of MPa as explored in this thesis.

MD simulations were occasionally used to further complement the AFM investigations with two main goals. The first was to study a region of just a few nanometers in close proximity of a surface defect, an area difficult to unambiguously probe via AFM. Second, MD simulations confirmed the experimental findings and ruled out any tip-correlation effects, thus further supporting SEM in excluding any significant probe related bias in the results.

7.2.2 General behaviour of aqueous and organic lubricants in nanogaps

One of the fundamental goals of the thesis highlighted in Chapter 1 (Section 1.5) was to contribute to solving the current debate on whether confined fluids would show different properties at nano-confinement. As shown in Chapter 2 Section 2.2.4, the liquid structure is expected to undergo a transition from being ordered in close proximity of the solid (typically for distances below a few nanometers) to being disordered in the bulk. The ordering would be primarily influenced by the geometry of the molecules and their consequent packing within the nanogap. The rearrangement would result in fluid layering and showing solid-like properties, such as an increase in viscosity by orders of magnitude in comparison with the bulk value [5]. However, experimental research based on surface force apparatus (SFA) and some theoretical studies have reported that some fluids, for example water and squalane, may retain their bulk-like fluidity [6–11]. The unexpected behaviour has been interpreted in terms of fast rotational and translation dynamics and consequent short relaxation time scale even under extreme conditions [6–9].

The results of this thesis confirm that, under nanoconfinement, both aqueous solutions

(Chapter 4) and organic fluids (Chapter 5) present a transition into an ordered phase with solid-like or glassy characteristics. This can be interpreted as follows. The constrained geometry results in a reduction in the available configurations the fluid molecules can probe, thus increasing the relaxation time scale. The liquid structural transition is particularly clear both when imaging the organisation of the fluids at equilibrium and when probing their dynamic properties. High resolution AM-AFM imaging shows an ice-like arrangement of water molecules at the interface of mica. Here, water ordering is enhanced by the confinement induced by the AFM tip and by the approximate lattice matching between the mica substrate and the hexagonal ice basal plane. Even in the absence of strong epitaxial effects (squalane confined on amorphous HOPG, Chapter 5), the lubricant organises into solid-like domains under the combined effect of vertical and lateral confinement. The ordered structure of the fluid molecules results in an increase in lubricated friction, and in viscosity by several orders of magnitude. As shown in Chapter 5, layering of the fluid molecules into solid-like structures is further confirmed by piezo-viscous effects limited for confining pressures greater than 0.5 GPa as a consequence of the lubricant "solidification". Fluid ordering at the solid interface is not limited to mica and HOPG substrates, but experiments with squalane confined on MoS_2 suggest a general effect independent from the particular system probed. Increasing, through thermal energy, the mobility of the lubricant molecules (Chapter 5), the order disappears, at least within the experimental time scale. The computational approach performed in Chapter 5 on a model squalane/HOPG system provided a good foundation for further understanding the molecular basis of liquid ordering as a phenomenon originating at close contact with the confining surface and then propagating by hundreds of nanometers as suggested by AFM imaging.
The experimental and computational results of the thesis hence show that the liquid structure transition would result from a combined effect of limited molecular mobility, and strong confinement reducing configurational entropy. This would explain the experimental observations provided by SFA where the confining pressure is six order of magnitude smaller than AFM. Overall, the results of the study may contribute to solving discrepancies between the existing bodies of SFA and AFM evidence.

7.2.3 Chemical and physical characteristics of the substrate-the role of singularities

As shown in Chapters 4, 5 and 6, surface singularities and boundary effects prevent any mean field simplifications, thus confirming that, at the nano and mesoscale, lubricated friction cannot be predicted by macroscale models. Specific chemical and physical properties of the confining surfaces may be generalised within the concept of singularities preventing a smooth sliding of the two solids in contact. Even if this framework is not

completely new, the thesis has brought a novel perspective for the underlying mechanisms. For example, Chapter 5 explored the nanoscale origins of roughness impact on lubricated friction. Asperities are generally interpreted as detrimental to smooth sliding of lubricated surfaces. According to the current models (see Chapter 1 Sections 1.3.1 and 1.3.2), the negative impact of roughness would be mainly due to elastic and plastic deformation in proximity of the contacting junctions, with adhesion and plowing forces generating a high friction force squeezing out the lubricant films. The investigations presented in Chapter 5 compared the behaviour of lubricated friction forces both directly on single asperities (shearing the tip on the step edge) and on lubricant ordered domains in proximity of the defects. The results show that the shear response is significantly greater in the latter case where the fluid lubricant undergoes a solid-like transition. The structural transition is induced by surface defects, and progressively disappears over hundreds of nanometers. Thus, the results of the thesis have introduced a new framework for roughness, indirectly affecting lubricated friction through an enhancement in fluid lubricant ordering.

This was also the case for the findings reported in Chapter 6 where the role of humidity was investigated *in situ* tracking the adsorption and evolution of water nano-droplets at the interface with hydrophilic and hydrophobic surfaces. The detrimental role of water is not due to its mere presence in a system lubricated by an organic lubricant (hexadecane, in our case), but by its specific distribution on the solid surface. On surfaces with a similar affinity for both the model lubricant and polar fluids, the two liquids may compete for adsorption on the substrate. Thus, water creates singularities in the uniform coverage of the surface by the organic lubricant. These singularities would represent pinning points for the sliding surfaces, as well as interfering elements for the packing of the organic molecules. The last mechanism clearly resembles the role of HOPG surface defects discussed in Chapter 5.

While the wide variety of specific mechanisms influencing lubricated friction may prevent simple theories, the common aspects present in the model systems investigated in the thesis suggest that the ordering of lubricant molecules is a key parameter to elucidate lubricated friction. Interface properties and environmental factors may become particularly relevant when representing singularities influencing the lubricant re-arrangement.

This framework would also explain the role of metal ions concentration in aqueous solutions (Chapter 4): in the case of small cation concentration (< 75 mM), the ions exert lubricating properties on the system by disrupting the hydrogen-bond network of the water molecules, thus reducing their ice-like behaviour. Past this concentration, multiple layers of ions would form on the substrate and interfere with a smooth sliding of the AFM probe. Thus, for relatively small concentrations, metal ions may be thought as singularities, or point-perturbations for the water structural transition into a solid-like system. For high concentrations, the cations are no longer a defect in the system but become the main feature.

7.2.4 Common threads in lubricated friction at the nano and mesoscale. A thermally activated process

Another common element emerges from the variety of systems analysed in this thesis: the role of temperature in modulating lubricated friction forces. Temperature is known to influence lubricated friction by increasing the lubricant mobility (see for example Chapter 1 Section 1.3.2). The thesis has however contributed to confirming the generality of this process showing that this holds true for both polar (Chapter 4) and non-polar lubricants (Chapters 5 and 6). Furthermore, the framework of a thermally activated process at the nano and mesoscale has been shown to follow an adapted Prandtl-Tomlinson model. The modelling was explicitly applied in Chapter 4 for hydrated metal cations. Their motion was described in terms of two competing contributions: the AFM tip provides energy to the ions so as to overcome an energy barrier, with the latter depending on the hydration structure of the ions themselves and their interactions with the surface. Ions can be thought as hard spheres and hydrodynamic friction as a limit case of boundary friction. Also, in the case of non-polar lubricants (for example, squalane, Chapter 5), the model holds true, with the AFM probe setting the fluid molecules into motion by allowing them to overcome the activation energy due to their strong cooperative interactions.
The dynamic behaviour of the lubricants explored in the thesis shows further common features. In most of the cases, the shear force shows an almost linear behaviour for the applied load as it were expected for macroscale friction according to Amontons-Coulomb's laws. This is the case for both ionic aqueous solutions (Chapter 4) and hexadecane (Chapter 6) that can be considered in the framework of the Prandtl-Tomlinson (see for example, the calculations in Chapter 4 Section 4.4.2). Overall, the results contribute to bridging the gap between the atomistic models and the phenomena observed at the macroscale. Specific interfacial interactions and system-specific singularities may however introduce particular elements to this general framework. For example, the strong cooperative interactions among squalane molecules and their confinement on both the vertical and lateral direction account for a non-zero effective yield stress (Chapter 5), whereas hexadecane molecules can be "more easily" set into motion on a hydrophlic substrate. This does not limit the validity of nano and mesoscale lubricated friction as a thermally activated process, but highlights the need for models at these scales to take into full account the specific physical-chemical interactions at the interface. Further experiments are however needed so as to confirm the results of this thesis and their full generality on real-life substrates and lubricants. This will be discussed in the following section.

7.3 Further work

This thesis has provided novel insights into nano and mesoscale lubricated friction as a thermally activated process, with the interpretation valid in aqueous and organic model fluids adsorbed on both atomistically flat and rough surfaces. Further work will be needed to address the generality of the findings, and to explore pressing aspects which currently limit the performances of available lubricants. Hereafter, I will review some of these key questions.

- The present findings on organic lubricants should be tested on systems closer to real-life applications such as metal oxides surfaces, routinely used in engines and machinery [12, 13]. At the nanoscale, lubricated friction is likely to result from the combined effects of the molecular arrangement around hydrophilic nano-domains and at topographical defects [4] which may favour the specific pinning of certain molecules. Exploring multiple substrates would also help extend the generality of the hypothesis of roughness influencing lubrication through the density of surface defects and consequently through a reduction in configurational entropy. In this sense, the thesis presents some encouraging but idealised results conducted on larger spatial scales (see Fig. 5.14 in Chapter 5). Ultimately, the goal should be to translate the findings at the nano and mesoscale to real multi-asperity contacts. This would require examining the same lubricant-surface system by combining our nanoscale experimental approach with macroscale investigation tools. The latter methods may include for example 3D fluorescent microscopy which is able to provide information on both lubricant thickness and deformation of surface roughness for length scales > 100 μm [14, 15]. Such a combined approach would provide a direct link between findings at different length scales. This would allow developing robust models to predict macroscale effects from nanoscale features.

- Investigations should be ultimately performed using currently available lubricants rather than pure fluids, or simple binary mixtures [5]. Such an ambitious goal may be achieved by studying firstly the single lubricant components and then their combined effect. Some preliminary experiments along this route are conducted in Chapter 6 when investigating the role of water nanodroplets on the lubricating properties of hexadecane. The focus of Chapter 6 is on the impact of humidity on model organic lubricants adsorbed to hydrophilic surfaces. We can however think of water and hexadecane as a binary mixture, whose behaviour has been studied analysing the role of each of the two components and assessing the overall response of the system. Such an approach may be similarly extended to realistic liquid lubricants containing a base oil ($\sim 90\%$), and additives ($\sim 10\%$) such as antioxidants, corrosion inhibitors,

antifoaming and anti-wear agents [16].

- Rising concerns about the environmental impact of fossil fuels have been pushing the demand for renewable green energy sources. Thus, we suggest exploring also the tribological performances of lubricants based on aqueous solutions containing polymer brush [17] and vegetable oils [18, 19]. These lubricants are characterised by their biodegradation, thus reducing problems related to waste management. Vegetable oils have been suggested as a promising candidate given their lubricating and anticorrosion properties, alongside a high flash point [18, 19]. The encouraging results achieved with oleic acid surfactants in reducing the impact of humidity (Chapter 6) would suggest to further investigate lubricants and additives derived from vegetable oils.

  This type of lubricants however presents some disadvantages mainly due to high melting point and filter-clogging tendency, and above all poor oxidative stability [20]. Natural antioxidants, such as propyl gallate and ascorbic acid, have been shown to improve the performance of biolubricant formulations. Still the efficiency is not always comparable to mineral oil based lubricants [21]. Further improvements may be achieved fully elucidating the molecular mechanisms by which the different stages of oxidation impact lubrication. For example, it is still unclear whether polymerisation induced by oxidative cyclisation is an undesirable aspect leading to the formation of deposits, or may be actually beneficial in the case of boundary lubrication [22]. Combining AFM experiments and MD simulations may offer a nanoscale insight into these questions, tracking the time evolution of the lubricant organisation and dynamical response as a function of the oxidative process. The study would highly benefit from the ability in controlling external parameters (e.g. temperature, pressure and humidity as shown in this thesis). Controlling these factors, the oxidative process may be tuned while real-time imaging lubricant re-arrangement and quantifying the lubricating efficiency.

References: Conclusions and outlook

[1] M. Urbakh et al., *Nature* **2004**, *430*, 525–528.

[2] B. N. Persson et al., *Physics of sliding friction*, Springer Science & Business Media, **2013**.

[3] J. Gao et al., *The Journal of Physical Chemistry B* **2004**, *108*, 3410–3425.

[4] C. Cafolla et al., *Science Advances* **2020**, *6*, eaaz3673.

[5] C. M. Mate et al., *Tribology on the small scale*, Oxford University Press, **2019**.

[6] J. Klein, *Friction* **2013**, *1*, 1–23.

[7] Y. Leng et al., *Physical Review Letters* **2005**, *94*, 026101.

[8] A. Malani et al., *The Journal of Physical Chemistry B* **2009**, *113*, 13825–13839.

[9] C. Drummond et al., *Physical Review E* **2001**, *63*, 041506.

[10] D. Gourdon et al., *Physical Review Letters* **2006**, *96*, 099601.

[11] S. J. O'Shea et al., *Japanese Journal of Applied Physics* **2010**, *49*, 08LA01.

[12] M. Lapuerta et al., *Wear* **2014**, *309*, 200–207.

[13] J. Zhang et al., *Surface and Coatings Technology* **2016**, *304*, 530–536.

[14] D. Petrova et al., *ACS Applied Materials & Interfaces* **2018**, *10*, 40973–40977.

[15] A. Azushima, *Wear* **2006**, *260*, 243–248.

[16] D. M. Pirro et al., *Lubrication fundamentals, revised and expanded*, CRC Press, **2016**.

[17] P. C. Nalam et al., *Tribology Letters* **2010**, *37*, 541–552.

[18] J. Salimon et al., *European Journal of Lipid Science and Technology* **2010**, *112*, 519–530.

[19] C. J. Reeves et al., *Tribology International* **2015**, *90*, 123–134.

[20] H. Mobarak et al., *Renewable and Sustainable Energy Reviews* **2014**, *33*, 34–43.

[21] L. A. Quinchia et al., *Journal of Agricultural and Food Chemistry* **2011**, *59*, 12917–12924.

[22] N. Fox et al., *Tribology international* **2007**, *40*, 1035–1046.

8.0 Professional Experience during the PhD

8.1 Full list of publications

- **Cafolla C**, Voitchovsky K. Impact of water on the lubricating properties of hexadecane at the nanoscale **Nanoscale 2020.** DOI: 10.1039/D0NR03642K.

- Li W, Zhu B., Zhu R, Wang Q, Lu P, **Cafolla C** et al. Atomic-scale control of electronic structure and ferromagnetic insulating state in perovskite oxide superlattices by long range tuning. **Advanced Functional Materials 2020**, 2001984.

- **Cafolla C**, Foster W, Voitchovsky K. Lubricated friction around nanodefects. **Science Advances 2020**, 6: eaaz3673

- Wang Y, He Q, Ming W, Du MH, Lu N, **Cafolla C** et al. Robust ferromagnetism in highly strained $SrCoO_3$ thin films. **Physical Review X 2020 Accepted**

- Alisi L, **Cafolla C**, Gentili A et al. Vitamin K concentration and cognitive status in elderly patients on anticoagulant therapy: a pilot study. **Journal of Ageing Research 2020**, 2020: 9695324. **Co-first author**

- **Cafolla C**, Payam A, Voitchovsky K. A non-destructive method to calibrate the torsional spring constant of atomic force microscope cantilevers in viscous environments. **Journal of Applied Physics 2018**, 124: 154502. **Editor's Pick & Highlighted in SciLight**

- **Cafolla C**, Voitchovsky K. Lubricating properties of single metal ions at interfaces. **Nanoscale 2018**, 10: 11831. **2018 Nanoscale Hot Article Collection**

- Ricci M, Trewby W, **Cafolla C**, Voitchovsky K. Direct observation of the dynamics of single metal ions at the interface with solids in aqueous solutions. **Nature Scientific Reports 2017**, 7: 43234

- **Cafolla C**, Mathew RS, Edge AC et al. SS Cancri: the shortest modulation-period Blazhko RR Lyrae. **Information Bulletin on Variable Stars 2017**, 63: 6213.
- Miller EJ, Trewby W, Payam AF, Piantanida L, **Cafolla C**, Voitchovsky K. Sub-nanometer resolution imaging with amplitude-modulation atomic force microscopy in liquid. **Journal of Visualized Experiments 2016**, 118: e54924
- Cafolla A, Gentili A, **Cafolla C** et al. Plasma vitamin K1 levels in Italian patients receiving oral anticoagulant therapy for mechanical heart prosthesis: a case-control study. **American Journal of Cardiovascular Drugs 2016**, 16: 267-274.
- Snopok B, Laroussi A, **Cafolla C**, Voitchovsky K, Snopok T, Mirsky V. Gold surface cleaning by etching polishing: optimization of polycrystalline film topography and surface functionality for biosensing. **Journal of Materials Chemistry B 2020, review stage.**
- **Cafolla C**, Voitchovsky K. A novel atomic force microscopy based diagnostic tool to detect nanovescicles in biological fluids. **In preparation**.
- **Cafolla C**, Rattray J. A pilot study on a tutorial model to support the transition from A-levels to University Physics. **In preparation**
- Nicholson B, **Cafolla C**, Kinane CJ, Mora-Hernandez A, Caruana A, Hindmarch AT. Control of proximity induced magnetism by using interface roughness. **In preparation**

8.2 Presentations and Talks at Professional Conferences

- **Talk. ACS Fall 2019**. *San Diego, USA*. August 2019
- **Poster. ACS Fall 2019**. *San Diego, USA*. August 2019
- **Poster. ACS Fall Science Mix 2019**. *San Diego, USA*. August 2019.
- **Poster. Royal Microscopy Society- Microscience Microscopy Congress 2019**. *Manchester, UK*. July 2019
- **Poster. International Biennial Gordon Research Conference on Tribology**. *Lewiston, USA*. June 2018
- **Invited seminar. Nanofluidics Workshop**. *Durham University, UK*. September 2017

- **Poster. International Conference on Nanotribology**. *SISSA Trieste, Italy.* **Poster Award.** June 2017
- **Poster. North Energy Materials Symposium.** *Durham University, UK.* April 2017

8.3 Scholarships and Awards

- **Graham Russell Prize** for outstanding overall performance in applied Physics. *Durham University, UK.* May 2020.
- **Physics Department Award for Excellence.** Nomination for outstanding commitment to teaching. *Durham University, UK.* Sept 2019
- **North East Polymer Association Sponsorship** (£ 500) Financial support to organise an interdisciplinary conference. *Durham University, UK.* Sept 2019
- **Bruker Bursary** Microscience Microscopy Congress. *Royal Microscopical Society, UK.* July 2019
- **Institute of Advanced Studies grant** (£ 4000) Highly competitive grant to organise an interdisciplinary conference. *Durham University, UK.* May 2019
- **Junior Visiting Fellow, St John's College** Conferred upon academics to support College Strategy. *St John's College, Durham University, UK.* Dec 2018
- **Physics Department Award for Excellence** Awarded for outstanding commitment to teaching. *Durham University, UK.* Sept 2018
- **Financial Support- Conference Participation** Tribology GRC, *Lewiston, USA* June 2018
- **Poster award**. International Conference on Trends in Nanotribology 2017. *International Center for Theoretical Physics, Trieste, Italy.* June 2017
- **Financial Support**. International Conference on Trends in Nanotribology 2017. *International Center for Theoretical Physics, Trieste, Italy.* June 2017

8.4 International Collaborations and Sponsored Research Visits

- **Beamtime at Diamond Light Source.** Didcot, UK. 7-14 May 2019

- **Collaboration with the Supramolecular Chemistry & Nanofabrication group.** University of Twente, The Netherlands. January 2019 - current
- **Beamtime at Diamond Light Source.** Didcot, UK. 18-25 Sept 2018
- **Collaboration with the Driscoll Research Group.** University of Cambridge, UK. May 2018 - current
- **International Collaboration with Asylum Research - Oxford Instruments.** Santa Barbara, USA. May 2017 - current
- **Member of the Skyrmion Project** Durham University, UK. May 2017 - current
- **BP Castrol**. iCase PhD Industrial Sponsor. UK. Oct 2016 - current
- **Collaboration with Haematology, Cellular Biotechnology & Chemistry Depts.** Sapienza University of Rome, Italy. Sept 2016 - current

8.5 Contributions to departmental teaching

Feb 2020 - June 2020	L4 Adv. Condensed Matter Physics Demonstrator
Oct 2019 - June 2020	L3 High Energy Physics Lab Demonstrator
Oct 2018 - June 2020	L1 Foundations of Physics Tutor
Aug 2017 - Aug 2019	Demonstrator, Sutton Trust Summer School
May 2017 - Jan 2020	Exam Invigilator
Oct 2016 - June 2018	L3 & L4 Adv. Physics Workshop Demonstrator
Oct 2016 - June 2018	L1 Discovery Skills Excel Workshop Demonstrator

8.6 Service to the Profession and Broader Professional Engagement

- **Main organiser of an International Conference on Nanolubrication.** Durham University, UK. July 2020

- **Development Coach for the Durham Inspired Award.** Durham University, UK. Nov 2019 - current
- **Main organiser of an industrially sponsored pub quiz.** Durham University, UK. Nov 2019
- **Helping supervise MSc Student in Strongly Correlated Electron Systems** Physics Department, Durham University, UK. Oct 2019 - June 2020
- **PGCert in Academic Practice.** Durham University, UK. March - Dec 2019
- **Saturday Morning Science: outreach event.** Durham University, UK. March 2019
- **Helping supervise MPhys Students in Soft Condensed Matter Physics.** Physics Department, Durham University, UK. Oct 2018 - May 2019
- **Postgraduate and International Resident Tutor.** St John's College, Durham University, UK. Sept 2018 - current
- **Reviewer for Hindawi Scanning.** Aug 2018 - current
- **In charge of weekly Academic Support Drop in Sessions.** St John's College, Durham University, UK. July 2018 - current
- **Fellow of the Higher Education Academy.** Durham University, UK. July 2018
- **Helping supervise MPhys Students in Soft Condensed Matter Physics.** Physics Department, Durham University, UK. Oct 2016 - current
- **Main organiser of monthly Café Scientifique talks.** St John's College, Durham University, UK. Oct 2016 - current
- **Pastoral Tutor.** St John's College, Durham University, UK. Oct 2016 - current
- **Active Member of the Durham Center for Doctoral Training in Energy.** Durham University, UK. Oct 2016 - Sept 2020
- **Active Member of the Durham Center for Soft Matter.** Durham University, UK. Oct 2016 - Sept 2020
- **Elected Member of the Postgraduate Students - Staff Consultative Committee.** Physics Department, Durham University, UK. Oct 2016 - Sept 2020